On the Statics and Dynamics of Microphase Separation in a Colloidal System with Tunable Competing Interactions

Dissertation
der Mathematisch-Naturwissenschaftlichen Fakultät
der Eberhard Karls Universität Tübingen
zur Erlangung des Grades eines
Doktors der Naturwissenschaften
(Dr. rer. nat.)

vorgelegt von
Kevin Marolt
aus Reutlingen

Tübingen
2021

Gedruckt mit Genehmigung der Mathematisch-Naturwissenschaftlichen Fakultät der Eberhard Karls Universität Tübingen.

Tag der mündlichen Qualifikation:	28.09.2021
Dekan:	Prof. Dr. Thilo Stehle
1. Berichterstatter	Prof. Dr. Roland Roth
2. Berichterstatter	Prof. Dr. Martin Oettel

Zusammenfassung

Thermodynamische Systeme kolloidaler Teilchen, welche mit einer starken, kurzreichweitigen Anziehung und einer schwachen, langreichweitigen Abstoßung wechselwirken, weisen ein ungewöhnliches Phasenverhalten auf. Anstatt unter bestimmten Bedingungen in eine gasförmige und eine flüssige Phase makroskopischen Ausmaßes zu separieren wie es bei rein attraktiven Kräften der Fall ist, führt die zusätzliche repulsive Komponente zu einer modulierten Teilchendichteverteilung welche durch die Ausbildung verschiedener mikro- oder mesoskopischer Strukturen wie etwa Tröpfchen, Streifen und Bläschen in Erscheinung tritt. Theoretische Studien haben gezeigt, dass diese sogenannten Mikrophasen – hervorgerufen durch konkurrierende Wechselwirkungen – einen stabilen thermodynamischen Gleichgewichtszustand darstellen können, und dass das entsprechende Dichteprofil eines unendlich großen Systems ohne äußeres Potential ein periodisch wiederkehrendes Muster besitzen würde. Entgegen dieser Vorhersagen konnten solch hochsymmetrische Strukturen experimentell jedoch nie nachgewiesen werden; stattdessen wurden oftmals willkürlich anmutende Konfigurationen beobachtet, die eine nennenswerte Ordnung vermissen lassen. Es existiert noch keine abschließende Erklärung für diese Diskrepanz zwischen Theorie und Experiment.

In der Bemühung, tiefere Einblicke in die Mechanik der Mikrophasenseparation und somit ein besseres Verständnis für das Auseinanderklaffen der beiden Welten zu erlangen, stellt die vorliegende Arbeit ein effektiv zweidimensionales Modellsystem vor, in welchem die konkurrierenden Wechselwirkungen auf eine relativ bequeme Art und Weise kontrolliert werden können. Der Aufbau besteht aus Siliziumdioxidkolloiden mit einem paramagnetischen Kern, welche in einem kritischen Gemisch aus Wasser und 2,6-Lutidin suspendiert sind. Die Teilchen sedimentieren durch die Schwerkraft auf den Grund einer Glaszelle und bilden dort eine Monolage. Die Zelle befindet sich in einem äußeren Magnetfeld, welches senkrecht zu dieser Monolage ausgerichtet ist. Knapp unterhalb der kritischen Entmischungstemperatur des Wasser-Lutidin-Gemisches sorgt die divergierende Korrelationslänge für eine anziehende kritische Casimirkraft zwischen den Kolloiden. Gleichzeit induziert das Magnetfeld ein Dipolmoment in den Teilchen, sodass sich diese gegenseitig abstoßen. Der attraktive und der repulsive Beitrag zur Wechselwirkung lassen sich somit *in situ* durch das Variieren der Temperatur bzw. der Stärke des Magnetfeldes unabhängig voneinander einstellen. Damit ist es nun möglich, durch eine geeignete Wahl der äußeren Parameter ein Wechselwirkungspotential zu erzeugen, welches eine Mikrophasenseparation hervorruft.

Zunächst führen wir eine Analyse des statischen Phasenverhaltens dieses Systems basierend auf der Dichtefunktionaltheorie durch. Wir bestimmen die für die makroskopische Phasenseparation relevante Binodale und Spinodale, als auch die λ-Linie/Fläche, welche jenes Gebiet im Phasendiagramm einschließt, in dem in es zur Mikrophasenseparation kommen muss. Anschließend entwickeln wir eine approximative Landau-Theorie, mit der wir uns einen groben Überblick über die Struktur der verschiedenen Mikrophasen sowie deren Lage im Phasendiagramm verschaffen. Da sich jedoch die Genauigkeit dieser Theorie als eher fragwürdig erweist, benutzen wir zusätzlich die Methode der freie Minimierung, um präzise Gleichgewichtsdichteverteilungen und Phasendiagramme zu berechnen. Im idealisierten Fall eines unendlich großen Systems finden wir drei thermodynamisch stabile Mikrophasen mit zunehmender mittlerer Dichte: eine mit hexagonal angeordneten Tröpfchen, eine weitere mit parallelen Streifen und eine letzte mit hexagonal angeordneten Bläschen. Bei schwachen Magnetfeldern beobachten wir dabei eine mesoskopische Phasenseparation, bei der diese periodischen Strukturen aus klar definierten gasförmigen und flüssigen Domänen aufgebaut sind. Falls das Systems hingegen in einer quadratische Zelle mit einer Kantenlänge von 20 oder 30 Kolloiddurchmessern eingeschlossen ist, so entdecken wir eine Mikrophase bestehend aus vier Tröpfchen, und ein andere mit einer Ringstruktur.

Zu guter Letzt studieren wir die Dynamik dieses endlichen Systems mittels dynamischer Dichtefunktionaltheorie. Wir untersuchen, wie das Dichteprofil auf Änderungen der Temperatur und des Magnetfeldes reagiert und sich zeitlich entwickelt. Es stellt sich dabei heraus, dass sich das System sehr leicht in einem metastabilen Zustand verfangen kann, wenn sich die Zielparameter innerhalb des Mikrophasenregimes befinden. Dies könnte einer der Gründe dafür sein, weshalb sich die wirklich stabilen Konfigurationen so selten in Experimenten manifestieren. Wir zeigen jedoch, dass es – zumindest in der Theorie – möglich ist, durch die Wahl eines geeigneten Pfades im Parameterraum das System von einer stabilen Mikrophase in die andere zu überführen.

Abstract

Thermodynamic systems of colloidal particles that interact via a strong, short-ranged attraction and a weak, long-ranged repulsion exhibit an unusual phase behavior. Rather than separating into a gaseous and a liquid phase of macroscopic extent under certain circumstances as it is the case with purely attractive forces, the additional repulsive component leads to a modulated particle density distribution which manifests itself in the development of various micro- or mesoscopic structures such as droplets, stripes or bubbles. Theoretic studies have shown that these so-called microphases – brought about by competing interactions – can represent a stable thermodynamic equilibrium state, and that the corresponding density profile of an infinitely large system with no external potential would possess a periodically recurring pattern. In contrast to predictions, however, such highly symmetric structures have never been detected experimentally; instead, only seemingly haphazard configurations were observed that lacked any notable order. There does not yet exist a definitive explanation for this discrepancy between theory and experiment.

In an effort of gaining deeper insights into the mechanics of microphase separation and thus a better understanding for the disparity of the two worlds, the thesis at hand presents an effectively two-dimensional model system in which the competing interactions can be controlled in a quite convenient manner. The setup consists of silica colloids with a paramagnetic core which are suspended in a critical mixture of water and 2,6-Lutidine. Under the force of gravity, the particles sediment toward the bottom of a confining glass cell and form a monolayer. The cell is placed inside an external magnetic field that is aligned perpendicularly to this monolayer. Slightly below the critical demixing temperature of the water–Lutidine mixture, the diverging correlation length causes an attractive critical Casimir force between the colloids. The magnetic field simultaneously induces a dipole moment within the particles so that they repel each other. The attractive and repulsive contribution to the interaction can therefore be adjusted *in situ* and independently from each other by varying the temperature and the strength of the magnetic field, respectively. In this way, it is possible through a suitable choice of the external parameters to create an interaction potential that brings about microphase separation.

Initially, we perform an analysis of the static phase behavior of this system on the basis of density functional theory. We determine the binodal and spinodal relevant for macroscopic phase separation, as well as the λ-line/surface enclosing that region in the phase diagram where microphase separation must occur. Afterwards, we develop an approximate Landau-type theory

with which we can obtain a rough overview of the structure of the different microphases and also their location in the phase diagram. Because the accuracy of this theory turns out to be rather questionable, we additionally make use of the method of free minimization to calculate precise equilibrium density distributions and phase diagrams. In the idealized case of an infinitely large system, we find three thermodynamically stable microphases with increasing average density: one with hexagonally arranged droplets, a second with parallel stripes and a third with hexagonally arranged bubbles. At weak magnetic fields, we observe a mesoscopic phase separation where these periodic structure are constructed out of clearly defined gaseous and liquid domains. If the system is confined to a square cell with a side length of 20 or 30 colloid diameters, however, we discover a microphase consisting of four droplets, and another featuring a ring structure.

Finally, we study the dynamics of this finite system by means of dynamic density functional theory. We investigate how the density profile reacts to changes of the temperature and the magnetic field, and how it evolves over time. It turns out that the system can easily become stuck in a metastable state if the target parameters are inside the microphase regime. This could be one of the reasons why the truly stable configurations manifest themselves so rarely in experiments. We show, however, that is – at least in theory – possible to guide the system from one stable microphase to another if a suitable path through parameter space is chosen.

Contents

1. Introduction **1**

2. Fundamental Concepts **9**

2.1. Thermodynamics . . . 9

2.1.1. Internal energy . . . 10

2.1.2. Entropy and thermodynamic equilibrium . . . 11

2.1.3. Thermodynamic potentials . . . 12

2.2. Statistical mechanics . . . 13

2.2.1. Canonical ensemble . . . 15

2.2.2. Grand canonical ensemble . . . 16

2.2.3. Ideal gas . . . 17

2.3. Density functional theory . . . 20

2.3.1. Ideal gas . . . 23

2.3.2. Hard disks . . . 24

2.3.3. Random phase approximation . . . 29

2.4. Critical phenomena . . . 31

2.4.1. Universal behavior . . . 33

2.4.2. Fluctuations and correlations . . . 35

2.4.3. Critical Casmir effect . . . 39

3. Model system **47**

4. Statics **51**

4.1. Bulk system . . . 52

4.1.1. Binodal, spinodal and λ-line . . . 52

4.1.2. Landau-type theory . . . 63

4.1.3. Free minimization . . . 76

4.2. Confined system . . . 93

4.2.1. Methodology . . . 93

4.2.2. Hexagonal and rectangular cells . . . 95

4.2.3. Square cells . . . 97

5. Dynamics **103**
5.1. Brownian motion and the Langevin equation . . . 103
5.2. Dynamic density functional theory . . . 107
5.2.1. Derivation . . . 107
5.2.2. Integration . . . 110
5.2.3. Implementation . . . 112
5.3. Dynamics of microphase separation . . . 114
5.3.1. Fluid → ring . . . 117
5.3.2. Fluid → droplets . . . 119
5.3.3. Droplets ⇄ ring . . . 122

6. Conclusion **127**

Acknowledgments **131**

Appendix **133**
A. Decomposition of the Mayer f-function for hard disks . . . 133
B. A relationship between chemical potential and pressure . . . 136
C. Derivation of the Ornstein–Zernike relation . . . 136
D. Fourier transforms in two dimensions . . . 138
D.1. Bessel and Struve functions . . . 138
D.2. Hard disk weight functions . . . 142
D.3. Competing interaction potential . . . 144
E. Autostereograms of the λ-surface . . . 145

References **147**

1. Introduction

One and the same substance can exist in various states of matter, depending on the external conditions such as temperature and pressure. We are well aware of this phenomenon from our everyday experience with water. At standard atmospheric pressure and room temperature, we encounter water in its liquid phase, where the molecules are moderately bound to each other and form a fluid that is nearly incompressible but still able to adept its shape. If the liquid water is heated above the boiling point, it undergoes a phase transition into a gaseous vapor, where the molecules are dissociated from another due to their increased kinetic energy and therefore free to occupy the entire volume available to them. If, on the other hand, water is cooled below the freezing point, it turns into solid ice that is neither compressible nor deformable. This rigidity is a consequence of the molecules' arrangement into a crystal lattice in which the bonds between neighboring molecules are so strong that they can no longer perform any motion relative to each other. In contrast to liquid or gaseous water, ice exhibits a highly symmetric structure that can extend even to macroscopic length scales; the spatial modulation of the density profile, however, has a period on the order of the size of the individual molecules.

Right at the melting point, both ice and liquid water are thermodynamically stable and can coexist alongside one another. The same is true for vapor and liquid water at the boiling point, as can be observed by the emergence of vapor bubbles in boiling water that under the influence of gravity rise to the top due to the lower density of the gas. The coexistence of two phases requires the formation of an interfacial layer between them, which always incurs an energy cost that increases with the area of the interface. As such, the system usually aims to minimize the interfacial area by separating into two large contiguous regions where either one or the other phase is prevalent. In the case of gas–liquid coexistence, this means that the density distribution is roughly uniform in each region, and only varies across the thin interface.

However, this reasoning appears to break down under certain circumstances. A variety a two- and three-dimensional systems are known to defy the urge to segregate into coexisting phases in the aforementioned radical manner. Instead, the phase regions actually alternate in space over mesoscopic length scales and form curious patterns [1]. Indeed, these so-called *microphases* can be thermodynamically stable; and when they are, they usually offer a periodic order with a high degree of symmetry. While seemingly similar to the microscopic structure of a crystal, the difference is that a crystal features a strict arrangement of *individual* molecules, whereas *entire domains* of molecules are involved in the formation of a microphase.

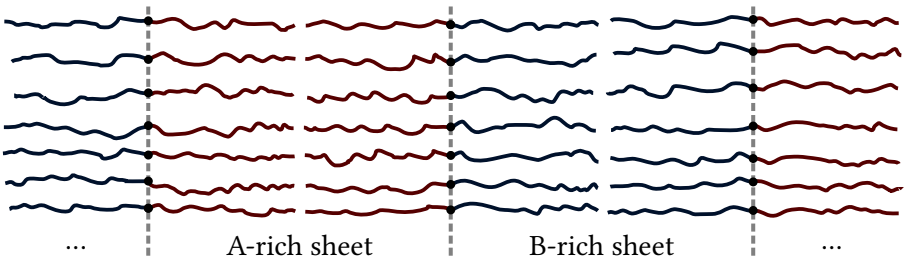

Figure 1.1.: Sketch of the lamellar phase formed by a system of diblock copolymers after microphase separation. The chains of type A (red) and type B (blue) monomers demix and self-assemble into alternating A-rich and B-rich sheets.

There are multiple mechanisms that can lead to the emergence of modulated phases. One is exemplified by diblock copolymers [2], which are macromolecules made up of a chain of monomers of type, say, A, that is covalently bound to another chain of monomers of type, say, B. A typical diblock copolymer might be

A–A–A–A–A–A–A–A–A—B–B–B–B–B–B–B–B–B–B–B–B

for instance. If the A and B monomers are incompatible with each other, demixing occurs at sufficiently low temperatures. However, because the A and B chains are interconnected, the system is unable to segregate into macroscopic A- and B-rich regions; it instead microphase separates into smaller A and B domains that border on each other. The size of these domains are on the order of the chain lengths, and the their equilibrium morphology is determined by the length ratio of the A and B chains. If the A chains are much shorter than the B chains, the former clump into spherical clusters that lie on a cubic lattice, while the latter fill the intermediary space. When the A chains are about half as long as the B chains, they assemble into parallel cylinders arranged in a hexagonal pattern. In the case that the A and B chains are roughly equal in length, they form alternating lamellar sheets as sketched in Fig. 1.1. When the B chains are shorter than the A chains, it is the B chains that aggregate into clusters or cylinders [3, 4].

In a system of diblock copolymers, the origin of microphase separation is the orientation dependent forces between the molecules due to the immiscibility of the blocks. Interestingly though, even isotropic interactions are capable of provoking the development of inhomogeneous density profiles, as demonstrated by amphiphilic monolayers at a flat air–water interface [5]. Amphiphiles, such as the phospholipids that cell membranes are built out of, consist of a polar head and an apolar tail. Because of their polarity, the heads are hydrophilic and get drawn below the water surface. The apolar tails, on the other hand, are hydrophobic and point the opposite way. The amphiphiles thus align themselves roughly perpendicularly to the interface like dabbling ducks searching for food: with heads submerged under water and tails exposed to the air, as depicted in Fig. 1.2. The force between the molecules is governed by (at least) three major contributions that are all radially symmetric within the monolayer: (i) for extremely small

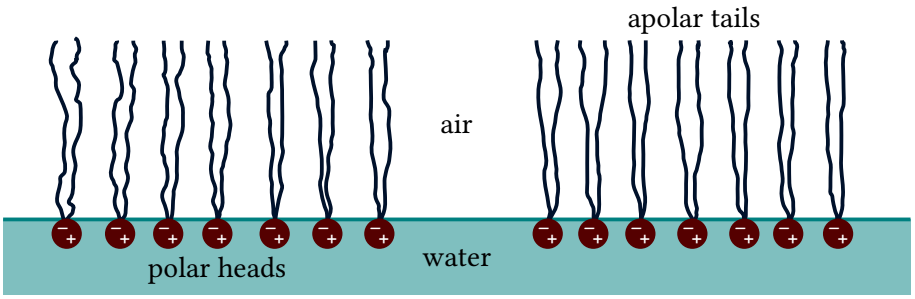

Figure 1.2.: Schematic depiction of an amphiphilic monolayer at an air–water interface. The polar heads are submerged under water and the apolar tails exposed to the air. The competition between short-ranged attractive London dispersion forces and long-ranged repulsive electrostatic dipole interactions can cause the the amphiphiles to form dense domains separated by thinly populated regions.

separations, the very strong repulsion of the electron shells due to the Pauli exclusion principle essentially prohibits the amphiphiles from "overlapping"; (ii) for intermediate separations, fluctuations of the electron distribution lead to an instantaneous mutual polarization of the molecules that gives rise to attractive London dispersion forces; (iii) for larger separations, the parallel orientation of the polar head groups causes an electrostatic dipole repulsion. If these *competing interactions* are suitably balanced, they result in a so-called SALR (short-ranged attraction, long-ranged repulsion) or mermaid (attractive head, repulsive tail) potential, similar to the one shown in Fig. 1.3. Because of the short-ranged attraction, the molecules preferably gather into denser regions. Once these regions reach a certain size, however, the long-ranged repulsive forces exerted on a molecule at the edge by those not within its vicinity become, in sum, dominant and prevent further growth. Hence, the system develops finite-sized liquid domains that are sepa-

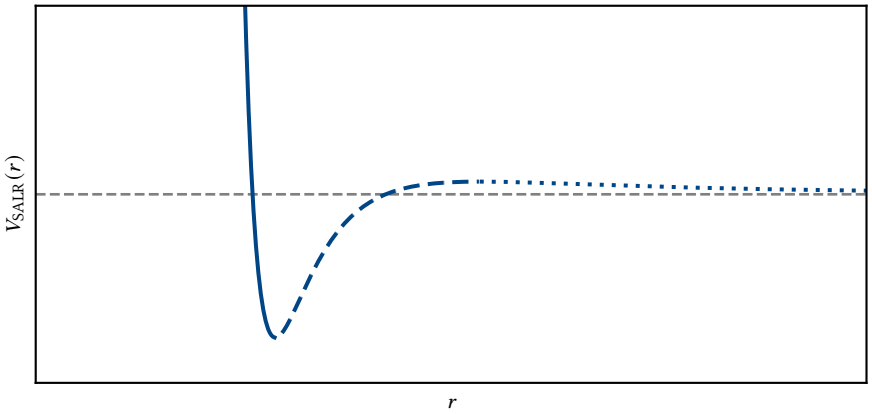

Figure 1.3.: The typical form of a SALR or mermaid potential V_{SALR} as a function of the inter-particle distance r. Strongly repulsive for small r (solid line), moderately attractive for intermediate values of r (dashed line), and weakly repulsive for large r (dotted line).

rated by a thinly populated gas. In (effectively) two-dimensional systems such as amphiphilic monolayers, one usually finds the following structures as the mean surface density is increased: circular liquid droplets forming a hexagonal pattern, alternating lamellar stripes of higher and lower density, and finally a hexagonal arrangement of circular gaseous bubbles surrounded by a denser liquid [6].

Competing interactions represent a rather practical and flexible means of inducing self-assembly as they can also be realized in other systems. A natural target are colloidal suspensions, which consist of nano- to micrometer sized particles, e. g., hard spheres made out of silica, polystyrene or acrylic glass, that are suspended in a molecular solvent. Colloids are still small enough to feel the collisions with the much tinier solvent molecules and perform a random walk through space, also known as Brownian motion [7, 8]; they are therefore subject to thermal fluctuations and behave like a thermodynamic system. Yet, colloids are also large enough to be imaged via confocal [9] or electron [10] microscopy, making their direct observation possible. For these reasons, and because the interaction between the colloids can be rather easily altered by preparing them in a certain way (equipping them with an electric charge or paramagnetic core, grafting or coating their surface, etc.) or choosing a specific solvent, colloidal suspensions have become an important model for atomic liquids and solids that is very accessible to experimental and theoretical studies alike.

Theoretical evidence for the emergence of microphase separation in colloidal systems is quite conclusive. Monte Carlo simulations by Archer and Wilding [11] as well as density functional theory calculations by Edelmann and Roth [12] and Pini and Parola [13], who investigated three-dimensional hard spheres with a competing double-Yukawa interaction, found the same periodic cluster, cylinder and sheet structures that diblock copolymers are known to form. This is also true for a square well fluid with a linear repulsion, as shown by Zhuang et al. using a thermodynamic integration scheme [14, 15]. Considering the vastly different interaction potentials and mechanisms that drive the self-assembly in these systems, the similarity of their phase diagrams is rather striking. An explanation for this was given by Ciach et al., who demonstrated that microphase separation in colloidal suspensions and diblock copolymers can be described by the same Landau-type theory [16], which in turn predicts a universal sequence of stable modulated phases [17]. The findings in two dimensions have been equally encouraging. Imperio et al. performed Monte Carlo simulation of a colloidal monolayer with competing exponentially-decaying pair potentials and obtained droplet, stripe and bubble patterns [18–22]. Archer was able to confirm the stability of these structures in a subsequent density functional theory study of the same system [23].

From an experimental standpoint, the case is unfortunately less clear. Ghezzi et al. prepared a monolayer of spherical latex particles by trapping them at an air–water interface and reported the formation of irregular cluster, foam-like and bubble structures; however, they found these to

eventually dissolve into a homogeneous film and thus to be at most metastable [24, 25]. Similar observations have also been made by Ruiz-García et al. for a comparable system [26–28]. Because the distance between the particles within those structures turned out to be on the order of several colloid diameters, both Ghezzi et al. and Ruiz-García et al. postulated a more complicated competing interaction potential, with an additional secondary minimum that lies further out than the primary one. The metastability of the structures could then be explained by a relatively shallow depth of the secondary minimum. Sear et al. demonstrated that silver nanocrystals deposited at an air–water interface spontaneously self-assembled into circular and lamellar domains for lower and higher densities, respectively [29]. Even though this experiment is probably among those that offer the best qualitative agreement with theoretical predictions, the emerging patterns are still lacking symmetry: the droplets are distributed arbitrarily and vary considerably in size, whereas the stripes meander aimlessly and form intricate mazes. While the situation in quasi-two-dimensional systems is somewhat mixed (to say the least), it is even drearier in three dimensions. There was hope that charged colloids suspended in a non-adsorbing polymeric solvent would undergo microphase separation since short-ranged attractive depletion and long-ranged repulsive electrostatic forces were expected to give rise to an SALR potential. Stradner et al. saw proof for competing interactions in the formation of mobile equilibrium clusters (due to the short-raged attraction) that did not grow beyond a certain size (due to the long-ranged repulsion) [30]. For lower colloid densities, Campbell et al. observed such a cluster fluid as well; with increasing density, the clusters grew into elongated chains that eventually linked together into percolated, gel-like network that is dynamically arrested [31]. Klix et al. also reported the emergence of a cluster glass, i. e., an amorphous state of compact clusters that become caged due to the long-ranged repulsion between them [32]. Although one might perceive a slight resemblance with the cluster crystal that would be thermodynamically stable according to theory, the cluster glass is again missing any periodicity and uniformity of cluster sizes. Indeed, no ordered phases have been detected in experiments with colloidal suspensions at all to date, and also not even disordered ones featuring cylindrical or lamellar structures.

The reasons for these glaring discrepancies between theory and experiment are not clear and the subject of an ongoing discussion. Depending on the relative strength of the long-ranged repulsion, Zhuang and Charbonneau predict different phase diagrams for a colloidal systems with an SALR interaction [33]; see Fig. 1.4. If there is no or only a very weak repulsion, the phase behavior is identical to that of a monatomic substance, with homogeneous low-density gas, medium-density liquid and high-density solid phases that are separated by regions of gas–liquid or fluid–solid coexistence. Above the critical temperature, gas and liquid unify into a supercritical fluid since coexistence, and thus discrimination, of the two phases is no longer possible. For a moderate repulsion, gas–liquid coexistence is expected to give way to periodic microphases. Just outside the microphase regime, computer simulations suggest the existence of a cluster fluid for

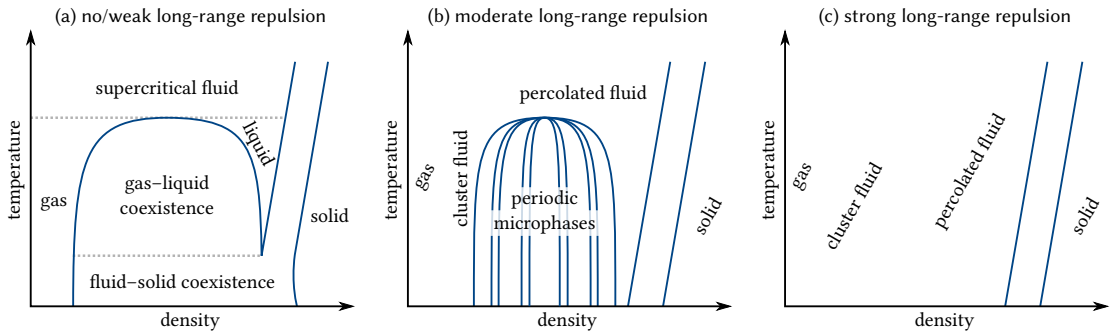

Figure 1.4.: Phase diagrams predicted by Zhuang and Charbonneau [33] for a colloidal system with an SALR interaction, depending on the relative strength of the long-ranged repulsion. In the case of no or only a very weak repulsion (a), the phase diagram resembles that of a monatomic substance with a gas, liquid, solid and supercritical fluid phase. For a moderate repulsion (b), gas–liquid coexistence comes in the form of periodic microphases. Just outside the microphase regime, the system is a cluster or percolated fluid. If the repulsion becomes too strong (c), periodic microphases might vanish again.

lower, and a percolated fluid for higher densities [14]. If the repulsion becomes very strong, periodic microphases might vanish completely in favor of the cluster and the percolated fluid.

In a review of several experiments studying the effects of competing interactions in colloidal suspensions, Royall comes to the conclusion that the electrostatic repulsion indeed appears to be unexpectedly high in some cases [34], potentially preventing microphase separation. Furthermore, even if the repulsion were appropriately tuned by adjusting the charge of the colloids or the dielectric constant of the solvent, its description as a radially symmetric Yukawa potential seems to actually break down when the colloids clump together: Klix et al. argue that free ions in the solvent condense preferably in the narrow space between two adjacent colloids, resulting in an inhomogeneous surface charge distribution and hence an anisotropic interaction; they speculate that this could have a profound impact on the growth of clusters and more elaborate structures [35]. These issues are essentially experimental in nature and present obstacles for the realization of mermaid potentials in colloidal suspensions.

However, there may also exist more fundamental difficulties. In view of the frequent emergence of the disordered cluster and percolated fluid, one might hypothesize that the kinetic slowdown observed to accompany these states becomes so dramatic in the vicinity of the ordered microphase region (which they presumably surround) that the system effectively freezes into a arrested glass or gel and is no longer able to rearrange into periodic structures. Using molecular dynamics simulations, de Candia et al. investigated whether a colloidal suspension with competing interactions could transition from a completely disordered state at high temperatures to an ordered one following a quench into to microphase regime [36]. Unsurprisingly, they found that the colloids would initially aggregate into clusters which then evolved into chains that later connected to form a network; eventually, though, the chains indeed spontaneously self-assembled into a hexagonal arrangement of parallel cylindrical columns. Interestingly, at

densities for which the lamellar phase was deemed to be stable, no ordering occurred during the simulation runs, suggesting a much slower transformation. Ironically, the situation was reversed in a similar study by Zhuang and Charbonneau where the colloids managed to form lamellae but not cylinders (or any other periodic phases) [37]. Nonetheless, they likewise observed that the transition time varied significantly, depending on the temperature after the quench and the colloid density. While these findings show that the system can in principle go from a disordered to an ordered state, this process can take so long in practice that it will not complete over the course of a typical experiment. Tarzia and Coniglio suspect that a complex free energy landscape with many local minima and large barriers in between is the reason why colloids interacting via an SALR potential tend to suffer slow dynamics or even get stuck in a metastable state [38].

This raises the question whether there are any techniques that can help to safely navigate this free energy landscape or make it less treacherous so that the ordering transition becomes faster and more reliable. Since non-equilibrium dynamics appears to play a crucial role in the process of forming periodic structures, it would be reasonable to assume that the way in which the external conditions are altered over time in order to bring the system into the microphase regime can have a large impact on the final state. A report by Helm and Möhwald supports this idea, who found that a rapid compression of a phospholipid monolayer into the cluster phase led to a wider range of cluster sizes than a slower one [39]. Would it be therefore also better, for example, to lower the temperature gradually instead of performing an abrupt quench as often done? How does the system behave if it is simultaneously compressed *and* cooled in some complicated manner? Unfortunately, research into this matter with regard to microphase separation seems to be scarce.

With the aim of making progress on some of the aforementioned issues, we shall concern ourselves in the following with an effectively two-dimensional system of colloids in which competing interactions are realized in a novel way: the short-ranged attraction is a consequence of critical Casimir forces mediated by the solvent, whereas the long-ranged repulsion stems from magnetic dipole interactions induced by an external magnetic field. The compelling feature of this setup is that both the attraction and the repulsion can be tuned easily and independently from each other via the temperature and the strength of the magnetic field, respectively. This opens up exciting possibilities, because we gain a fine control over the interaction potential and can investigate how its shape affects the phase behavior and the structure of the system. Furthermore, it allows the interaction between the colloids to be varied *in situ*, and therefore also during a phase transition, which might prove useful for guiding the system from one state to another.

The hope is, of course, that the attraction and repulsion can be balanced in such a way that they yield a true SALR potential. In that case, this system has the chance of becoming an important model colloidal microphase former with the prospect of narrowing the gap between experiment and theory. Experimentally, monolayers of colloids under the influence of either magnetic dipole

[40, 41] or critical Casimir [42] forces have already been realized. Combining both interactions should not be too difficult, but this has apparently not been pursued yet. However, even if an attempt to do so were made, the experimenters would likely consider the large parameter space a curse rather then a blessing at first, for it seems futile to blindly guess in advance which choice of temperature, magnetic field and colloid density gives rise to interesting behavior. A more systematic approach might not fare much better, since experiments tend to be rather expensive and time-consuming – and, as we have seen, also somewhat recalcitrant when it comes to microphase separation. In view of these anticipated experimental challenges, prior theoretical analysis would certainly be welcome and will be presented in the remainder of this thesis, which is structured as follows:

In Chapter 2, we introduce the fundamental concepts of thermodynamics, statistical mechanics and density functional theory that form the groundwork upon which our methodology is going to be built. We also give an overview of critical phenomena and how these lead to the critical Casimir effect. In Chapter 3, we describe the setup of our proposed model system and how competing interactions are realized therein. In Chapter 4, we determine and discuss the phase behavior of this system in great detail. With an initial focus on the infinite bulk, we calculate the binodal and spinodal that play an important role for macroscopic gas–liquid phase separation, and we compute the so-called λ-line (or, more precisely, the λ-surface) that surrounds the region in the phase diagram where periodic microphases are thermodynamically stable. To ascertain the structure of these microphases, we first devise an approximate Landau-type theory and subsequently an accurate free minimization algorithm that we implemented on a workstation. Afterwards, we use the latter technique to investigate what happens when the system is confined to a finite cell. Then, in Chapter 5, we study the dynamics of the system by employing dynamic density functional theory to find out how the density profile responds to a change of the competing interaction potential (as a consequence of varying the temperature and the magnetic field) and how it evolves over time. Finally, in Chapter 6, we draw our conclusion.

This thesis represents an expansion on the following publications:

- K. Marolt, M. Zimmermann and R. Roth, "Microphase separation in a two-dimensional colloidal system with competing attractive critical Casimir and repulsive magnetic dipole interactions," Phys. Rev. E **100**, 052602 (2019).

- K. Marolt and R. Roth, "Statics and dynamics of a finite two-dimensional colloidal system with competing attractive critical Casimir and repulsive magnetic dipole interactions," Phys. Rev. E **102**, 042608 (2020).

2. Fundamental Concepts

2.1. Thermodynamics

From classical mechanics we know that a d-dimensional system of N particles has $2dN$ degrees of freedom and that its state at some arbitrary time t can be fully specified by dN coordinates $\boldsymbol{q}(t) = (q_1(t), \ldots, q_{dN}(t))$ and dN momenta $\boldsymbol{p}(t) = (p_1(t), \ldots, p_{dN}(t))$. Given the system's Hamiltonian $\mathcal{H}$, which is usually just the sum of the potential energy $\mathcal{V}$ and the kinetic energy $\mathcal{T}$,

$$\mathcal{H}(\boldsymbol{q}, \boldsymbol{p}) = \mathcal{V}(\boldsymbol{q}) + \mathcal{T}(\boldsymbol{p}), \tag{2.1}$$

it is possible to uniquely determine the future (and even the past) trajectories of the particles by solving a set of $2dN$ coupled ordinary differential equations called Hamilton's equations of motion:

$$\frac{\mathrm{d}q_i(t)}{\mathrm{d}t} = \left.\frac{\partial \mathcal{H}(\boldsymbol{q}, \boldsymbol{p})}{\partial p_i}\right|_{\substack{\boldsymbol{q}=\boldsymbol{q}(t) \\ \boldsymbol{p}=\boldsymbol{p}(t)}}, \qquad \frac{\mathrm{d}p_i(t)}{\mathrm{d}t} = -\left.\frac{\partial \mathcal{H}(\boldsymbol{q}, \boldsymbol{p})}{\partial q_i}\right|_{\substack{\boldsymbol{q}=\boldsymbol{q}(t) \\ \boldsymbol{p}=\boldsymbol{p}(t)}} \tag{2.2}$$

for $i \in \{1, \ldots, dN\}$.

Unfortunately, this very quickly becomes very difficult as the number of particles increases. Already for the seemingly simple case of three bodies interacting via gravitational forces there exists no general analytical solution and one has to resort to numerical approximations. Even though computers have gotten incredibly powerful and are nowadays capable of simulating thousands or millions of individual atoms, that is still a far cry from the macroscopic systems we encounter on a daily basis. For example, calculating the trajectories of all 10^{25} H_2O molecules in a glass of water is entirely unfeasible. Moreover, such large systems typically display a chaotic behavior, which means that even minute uncertainties about the initial state will grow exponentially as time progresses. Thus, predicting the future would require the precise simultaneous measurement of all coordinates and momenta. This is not only exceptionally challenging from an experimental point of view, it is actually fundamentally impossible according to the laws of quantum mechanics.

However, in many-particle systems, the complicated interplay on the microscopic level gives rise to universal collective properties on the macroscopic scale that are a lot more accessible and relevant in practice. This observation led to the development of thermodynamics, a phenomeno-

logical theory that essentially describes such systems in terms of their ability to store various forms of energy and to perform useful work. Gaining an understanding of these concepts and learning to harness them had a tremendous impact on human history for it enabled the construction of ever more efficient steam engines which powered locomotives, propelled ships and heralded the advent of the Industrial Revolution.

2.1.1. Internal energy

Consider a macroscopic system – say, a gas – of N particles confined to a volume V. Due to the interaction of the particles, the system will have a certain internal energy U that will depend, amongst others, on V and N. In order to compress the gas and reduce its volume by an infinitesimal amount $\mathrm{d}V$, we have to perform some mechanical work δW_{mech} on the system, thus increasing U. It follows from the conservation of energy that

$$\delta W_{\mathrm{mech}} = U(V + \mathrm{d}V, N, \dots) - U(V, N, \dots) = -P\,\mathrm{d}V, \tag{2.3}$$

where $P = -\partial U(V, N, \dots)/\partial V$ is the pressure of the system. Likewise, adding a small number $\mathrm{d}N$ of particles into the volume V requires the chemical work

$$\delta W_{\mathrm{chem}} = U(V, N + \mathrm{d}N, \dots) - U(V, N, \dots) = \mu\,\mathrm{d}N \tag{2.4}$$

with the chemical potential $\mu = \partial U(V, N, \dots)/\partial N$. However, we know from experience that there is another important type of energy which we can transfer to the system: heat. Since we can do so without changing V or N, we need to postulate a third quantity, the entropy S, on which U depends. The portion of heat necessary to effect a tiny increase $\mathrm{d}S$ in entropy is then given by

$$\delta Q = U(V, N, S + \mathrm{d}S) - U(V, N, S) = T\,\mathrm{d}S, \tag{2.5}$$

where $T = \partial U(V, N, S)/\partial S$ denotes the temperature of the system. The total infinitesimal change in internal energy can therefore be written as

$$\mathrm{d}U(V, N, S) = \delta W_{\mathrm{mech}} + \delta W_{\mathrm{chem}} + \delta Q = -P\,\mathrm{d}V + \mu\,\mathrm{d}N + T\,\mathrm{d}S. \tag{2.6}$$

Note that V, N, S and U are extensive quantities. This means that if the system were divided into n subsystems, then $V = \sum_{i=1}^{n} V_i$, $N = \sum_{i=1}^{n} N_i$, $S = \sum_{i=1}^{n} S_i$ and

$$U\left(\textstyle\sum_{i=1}^{n} V_i, \sum_{i=1}^{n} N_i, \sum_{i=1}^{n} S_i\right) = U(V, N, S) = \displaystyle\sum_{i=1}^{n} U_i = \sum_{i=1}^{n} U(V_i, N_i, S_i). \tag{2.7}$$

By extension, if the size of the system were scaled by some number λ so that $V_\lambda = \lambda V$, $N_\lambda = \lambda N$

and $S_\lambda = \lambda S$, then $U(\lambda V, \lambda N, \lambda S) = U(V_\lambda, N_\lambda, S_\lambda) = U_\lambda = \lambda U(V, N, S)$ and therefore

$$\begin{aligned} U(V,N,S) &= \left[\frac{\partial}{\partial\lambda}\left\{\lambda U(V,N,S)\right\}\right]_{\lambda=1} = \left[\frac{\partial}{\partial\lambda}U(\lambda V,\lambda N,\lambda S)\right]_{\lambda=1} \\ &= \left.\frac{\partial U(\lambda V,\lambda N,\lambda S)}{\partial(\lambda V)}\right|_{\lambda=1} V + \left.\frac{\partial U(\lambda V,\lambda N,\lambda S)}{\partial(\lambda N)}\right|_{\lambda=1} N + \left.\frac{\partial U(\lambda V,\lambda N,\lambda S)}{\partial(\lambda S)}\right|_{\lambda=1} S \\ &= -PV + \mu N + TS. \end{aligned} \tag{2.8}$$

2.1.2. Entropy and thermodynamic equilibrium

Now, imagine two systems that are brought into thermal contact, but are otherwise isolated from each other and the environment. Because the internal energy of the combined system will remain constant, any heat δQ that flows out of the first system must be completely absorbed by the second. Hence $\delta Q_2 = \delta Q = -\delta Q_1$. The change in total entropy is then given by

$$\mathrm{d}S = \mathrm{d}S_1 + \mathrm{d}S_2 = \frac{\delta Q_1}{T_1} - \frac{\delta Q_2}{T_2} = -\left(\frac{1}{T_1} - \frac{1}{T_2}\right)\delta Q. \tag{2.9}$$

Considering that it was never observed that heat would be transferred from the colder to the hotter system, we must conclude that $T_1 > T_2$ if $\delta Q > 0$ and $T_1 < T_2$ if $\delta Q < 0$. Thus, we find that

$$\mathrm{d}S \geq 0. \tag{2.10}$$

It is the central insight of thermodynamics that the entropy of an isolated system does not decrease. Either the system is in a stationary state of maximum entropy called thermodynamic equilibrium where $\mathrm{d}S = 0$, or irreversible processes take place that increase the entropy until said equilibrium is reached.

Let us suppose that the wall is also movable and permeable, so that the two systems are able to exchange mechanical and chemical energy. Since the total internal energy $U_{\mathrm{tot}} = U_1 + U_2$, volume $V_{\mathrm{tot}} = V_1 + V_2$ and particle number $N_{\mathrm{tot}} = N_1 + N_2$ cannot change,

$$0 = \mathrm{d}U_{\mathrm{tot}} = \mathrm{d}U_1 + \mathrm{d}U_2, \quad 0 = \mathrm{d}V_{\mathrm{tot}} = \mathrm{d}V_1 + \mathrm{d}V_2, \quad 0 = \mathrm{d}N_{\mathrm{tot}} = \mathrm{d}N_1 + \mathrm{d}N_2, \tag{2.11}$$

we have from Eq. (2.6) that in thermodynamic equilibrium,

$$\begin{aligned} 0 = \mathrm{d}S = \mathrm{d}S_1 + \mathrm{d}S_2 &= \frac{\mathrm{d}U_1 + P_1\mathrm{d}V_1 - \mu_1\mathrm{d}N_1}{T_1} + \frac{\mathrm{d}U_2 + P_2\mathrm{d}V_2 - \mu_2\mathrm{d}N_2}{T_2} \\ &= \left(\frac{1}{T_1} - \frac{1}{T_2}\right)\mathrm{d}U_1 + \left(\frac{P_1}{T_1} - \frac{P_2}{T_2}\right)\mathrm{d}V_1 - \left(\frac{\mu_1}{T_1} - \frac{\mu_2}{T_2}\right)\mathrm{d}N_1. \end{aligned} \tag{2.12}$$

This is fulfilled exactly when $T_1 = T_2$, $P_1 = P_2$ and $\mu_1 = \mu_2$, i. e., when both systems have equal temperature, pressure and chemical potential. It follows that if we were to divide an equilibrated system into arbitrarily many subsystems, each subsystem would have the same T, P and μ, which

means that these quantities do *not* scale with the size of the system and are therefore intensive properties.

2.1.3. Thermodynamic potentials

If a system is kept in thermodynamic equilibrium with a much larger bath, the latter will be hardly influenced by changes of the state of the former. Depending on the type of interface between them and the interactions it allows, the bath will thus impose its constant pressure, chemical potential and/or temperature on the system. In this case, we give up governance over some of the extensive variables in favor of the corresponding intensive ones, and it becomes practical to replace the internal energy with other thermodynamic potentials that contain the same information, but are functions of the quantities in our control.

Helmholtz free energy

If the system is in thermal contact with a bath but has a fixed volume and particle number, we can use a Legendre transformation of the internal energy to exchange the entropy for the temperature. This results in the Helmholtz free energy

$$F(V,N,T) = U - \frac{\partial U}{\partial S} S = U - TS = -PV + \mu N, \tag{2.13}$$

which indeed depends only on V, N and T since

$$\begin{aligned} \mathrm{d}F(V,N,T) &= \mathrm{d}U(V,N,S) - \mathrm{d}(TS) = (-P\,\mathrm{d}V + \mu\,\mathrm{d}N + T\,\mathrm{d}S) - (T\,\mathrm{d}S + S\,\mathrm{d}T) \\ &= -P\,\mathrm{d}V + \mu\,\mathrm{d}N - S\,\mathrm{d}T. \end{aligned} \tag{2.14}$$

Knowing F, we can easily extract the pressure, chemical potential and entropy via

$$P = -\frac{\partial F(V,N,T)}{\partial V}, \quad \mu = \frac{\partial F(V,N,T)}{\partial N}, \quad S = -\frac{\partial F(V,N,T)}{\partial T}. \tag{2.15}$$

Irreversible processes happening at constant temperature, $\mathrm{d}T = 0$, always lower the Helmholtz free energy of a system because

$$\mathrm{d}F = \mathrm{d}U - \mathrm{d}(TS) = -\mathrm{d}U_{\mathrm{bath}} - (T\,\mathrm{d}S + S\,\mathrm{d}T) = -T\,\mathrm{d}S_{\mathrm{bath}} - T\,\mathrm{d}S = -T\,\mathrm{d}S_{\mathrm{tot}} \leq 0. \tag{2.16}$$

In thermodynamic equilibrium, F is minimal.

Grand potential

When both heat and particles can flow from the system to the bath and vice versa, the thermodynamic potential of choice is the grand potential

$$\Omega(V,\mu,T) = U - \frac{\partial U}{\partial N}N - \frac{\partial U}{\partial S}S = U - \mu N - TS = -PV, \tag{2.17}$$

which is the Legendre transformation of U with respect to N and S. From

$$\begin{aligned} \mathrm{d}\Omega(V,\mu,T) &= \mathrm{d}U(V,N,S) - \mathrm{d}(\mu N) - \mathrm{d}(TS) \\ &= (-P\,\mathrm{d}V + \mu\,\mathrm{d}N + T\,\mathrm{d}S) - (\mu\,\mathrm{d}N + N\,\mathrm{d}\mu) - (T\,\mathrm{d}S + S\,\mathrm{d}T) \\ &= -P\,\mathrm{d}V - N\,\mathrm{d}\mu - S\,\mathrm{d}T \end{aligned} \tag{2.18}$$

it is clear that Ω is truly a function of V, μ and T, and that

$$P = -\frac{\partial\Omega(V,\mu,T)}{\partial V} = -\frac{\Omega(V,\mu,T)}{V}, \quad N = -\frac{\partial\Omega(V,\mu,T)}{\partial\mu}, \quad S = -\frac{\partial\Omega(V,\mu,T)}{\partial T}. \tag{2.19}$$

In systems where the chemical potential and temperature are held constant, $\mathrm{d}\mu = 0$ and $\mathrm{d}T = 0$, the grand potential is minimal in thermodynamic equilibrium since

$$\begin{aligned} \mathrm{d}\Omega &= \mathrm{d}U - \mathrm{d}(\mu N) - \mathrm{d}(TS) = -\mathrm{d}U_{\mathrm{bath}} - (\mu\,\mathrm{d}N + N\,\mathrm{d}\mu) - (T\,\mathrm{d}S + S\,\mathrm{d}T) \\ &= -\mu\,\mathrm{d}N_{\mathrm{bath}} - T\,\mathrm{d}S_{\mathrm{bath}} - \mu\,\mathrm{d}N - T\,\mathrm{d}S = -\mu\,\mathrm{d}N_{\mathrm{tot}} - T\,\mathrm{d}S_{\mathrm{tot}} = -T\,\mathrm{d}S_{\mathrm{tot}} \\ &\leq 0. \end{aligned} \tag{2.20}$$

2.2. Statistical mechanics

While thermodynamics is extremely successful in describing many-particle systems, it does not explain how the microscopic behavior determines macroscopic properties such as the pressure, chemical potential or temperature. By employing probabilistic methods, statistical mechanics allows us to establish precisely this connection between the small and the large scale. The idea is that the macrostate emerges through an averaging of certain observables of the microstate. As the microscopic state $(\boldsymbol{q}(t), \boldsymbol{p}(t))$ evolves in time according to Hamilton's equation of motion (2.2), an observable O will fluctuate about its time-averaged value

$$\langle O\rangle_{[t_0,\,t_1]} \equiv \frac{1}{t_1 - t_0}\int_{t_0}^{t_1} \mathrm{d}t\, O(\boldsymbol{q}(t), \boldsymbol{p}(t)) \tag{2.21}$$

in the interval $[t_0, t_1]$. For example, the total energy $\mathcal{H}$ of a many-particle system in thermal contact with its environment is not fixed because heat gets constantly exchanged. In the stationary state of thermodynamic equilibrium, however, we can expect that the variations are so imperceptibly small that the mean energy $\langle\mathcal{H}\rangle_{[t_0,\,t_1]}$ is essentially independent of t_0 and t_1, provided

that the averaging is performed over a period $t_1 - t_0$ that is much longer than the correlation time of the fluctuations. For this kind of observable, its average value is the relevant macroscopic quantity. Of course, calculating the time average as per Eq. (2.21) is not really an option since it would again require us to solve the microscopic dynamics, which is what we wanted to avoid in the first place.

The approach of statistical mechanics is to express the hypothetical all-time average $\langle O \rangle_{[-\infty,\infty]}$ as an average over all possible microstates,

$$\langle O \rangle_{[-\infty,\infty]} \overset{!}{=} \langle O \rangle_\varrho \equiv \frac{1}{h^{dN} N!} \int \mathrm{d}^{dN}\boldsymbol{q} \int \mathrm{d}^{dN}\boldsymbol{p}\, \varrho(\boldsymbol{q},\boldsymbol{p})\, O(\boldsymbol{q},\boldsymbol{p}), \tag{2.22}$$

where the probability distribution of some microstate $(\boldsymbol{q},\boldsymbol{p})$ is formally given by

$$\varrho(\boldsymbol{q},\boldsymbol{p}) = \lim_{\tau\to\infty}\left[\frac{h^{dN}N!}{2\tau}\int_{-\tau}^{\tau}\mathrm{d}t\,\delta(\boldsymbol{q}-\boldsymbol{q}(t))\,\delta(\boldsymbol{p}-\boldsymbol{p}(t))\right] \tag{2.23}$$

with the Planck constant $h \approx 6.63 \times 10^{-34}\,\mathrm{Js}$. The factor $h^{dN}N!$ accounts for the quantum-mechanical density of microstates in coordinate–momentum space and the fact that swapping two identical particles does not produce a different state. Since ϱ is still defined in terms of the time evolution of the system, this may not appear to give us any advantage. However, we are now able to reason about ϱ from a purely information-theoretical standpoint.

Our macroscopic knowledge of a system in thermodynamic equilibrium is usually limited to whether extensive properties such as the internal energy, the volume or the number of particles are constant, or whether they fluctuate about an average value due to interactions with its surroundings. Information theory now states that the most appropriate ϱ is the one that maximizes the information entropy

$$H[\varrho] \equiv -\langle \ln\varrho \rangle_\varrho = -\frac{1}{h^{dN}N!}\int \mathrm{d}^{dN}\boldsymbol{p}\int \mathrm{d}^{dN}\boldsymbol{q}\,\varrho(\boldsymbol{p},\boldsymbol{q})\,\ln\varrho(\boldsymbol{p},\boldsymbol{q}) \tag{2.24}$$

under the constraints that are known to hold [43, 44]. Since $H[\varrho]$ measures the degree of indifference of ϱ with regard to the individual microstates, any other probability distribution would suffer from an unwarranted bias. If the available information is expressed in terms of functionals $C_1,\ldots,C_n$ of ϱ that ought to evaluate to zero, then the equilibrium probability distribution ϱ_eq can be found with the method of Lagrange multipliers by solving

$$0 = \left[\frac{\delta}{\delta\varrho(\boldsymbol{q},\boldsymbol{p})}\left(H[\varrho] - \sum_{i=1}^{n}\lambda_i C_i[\varrho]\right)\right]_{\varrho=\varrho_\mathrm{eq}} = \left.\frac{\delta H[\varrho]}{\delta\varrho(\boldsymbol{q},\boldsymbol{p})}\right|_{\varrho=\varrho_\mathrm{eq}} - \sum_{i=1}^{n}\lambda_i \left.\frac{\delta C_i[\varrho]}{\delta\varrho(\boldsymbol{q},\boldsymbol{p})}\right|_{\varrho=\varrho_\mathrm{eq}} \tag{2.25}$$

for ϱ_eq such that $C_i[\varrho_\mathrm{eq}] = 0$ for $i \in \{1,\ldots,n\}$. It should come as no surprise that the information entropy H and the thermodynamic entropy S, which are both maximized in equilibrium, are actually proportional to each other: the Boltzmann constant $k_\mathrm{B} \approx 1.38 \times 10^{-23}\,\mathrm{JK}^{-1}$ links statis-

tical mechanics back to thermodynamics through the identity

$$S = k_\mathrm{B} H[\varrho_\mathrm{eq}]. \tag{2.26}$$

2.2.1. Canonical ensemble

Let us apply this principle of maximum entropy to determine the equilibrium probability distribution ϱ_can of the so-called *canonical ensemble*, which represents a macroscopic system with fixed volume V and particle number N that is held at a constant temperature T due to thermal equilibrium with a bath; this is the same situation as during the discussion of the Helmholtz free energy. At first, we need to specify which constraints ϱ_can has to satisfy. For one, as any proper probability distribution, ϱ_can should be normalized so that $C_1[\varrho_\mathrm{can}] = 0$ for

$$C_1[\varrho] \equiv \langle 1 \rangle_\varrho - 1 = \frac{1}{h^{dN} N!} \int \mathrm{d}^{dN}\boldsymbol{q} \int \mathrm{d}^{dN}\boldsymbol{p}\, \varrho(\boldsymbol{q},\boldsymbol{p}) - 1. \tag{2.27}$$

For another, although the total energy $\mathcal{H}$ of the system will fluctuate due to the exchange of heat with the bath, at least its average value should be equal to the internal energy U. Thus, we also have to demand that $C_2[\varrho_\mathrm{can}] = 0$ for

$$C_2[\varrho] \equiv \langle \mathcal{H} \rangle_\varrho - U = \frac{1}{h^{dN} N!} \int_V \mathrm{d}^{dN}\boldsymbol{q} \int \mathrm{d}^{dN}\boldsymbol{p}\, \varrho(\boldsymbol{q},\boldsymbol{p})\, \mathcal{H}(\boldsymbol{q},\boldsymbol{p}) - U. \tag{2.28}$$

Calculating the functional derivatives of H, C_1 and C_2, we find that

$$\frac{\delta H[\varrho]}{\delta \varrho(\boldsymbol{q},\boldsymbol{p})} = -\frac{\ln \varrho(\boldsymbol{q},\boldsymbol{p}) + 1}{h^{dN} N!}, \quad \frac{\delta C_1[\varrho]}{\delta \varrho(\boldsymbol{q},\boldsymbol{p})} = \frac{1}{h^{dN} N!}, \quad \frac{\delta C_2[\varrho]}{\delta \varrho(\boldsymbol{q},\boldsymbol{p})} = \frac{\mathcal{H}(\boldsymbol{q},\boldsymbol{p})}{h^{dN} N!}. \tag{2.29}$$

Thus, maximizing H under the constraints C_1 and C_2 according to Eq. (2.25), we have

$$0 = \left.\frac{\delta H[\varrho]}{\delta \varrho(\boldsymbol{q},\boldsymbol{p})}\right|_{\varrho=\varrho_\mathrm{can}} - \alpha \left.\frac{\delta C_1[\varrho]}{\delta \varrho(\boldsymbol{q},\boldsymbol{p})}\right|_{\varrho=\varrho_\mathrm{can}} - \beta \left.\frac{\delta C_2[\varrho]}{\delta \varrho(\boldsymbol{q},\boldsymbol{p})}\right|_{\varrho=\varrho_\mathrm{can}} = -\frac{\ln \varrho_\mathrm{can}(\boldsymbol{q},\boldsymbol{p}) + 1 + \alpha + \beta\mathcal{H}(\boldsymbol{q},\boldsymbol{p})}{h^{dN} N!} \tag{2.30}$$

which leads to

$$\varrho_\mathrm{can}(\boldsymbol{q},\boldsymbol{p}) = \exp(-1-\alpha) \exp[-\beta\mathcal{H}(\boldsymbol{q},\boldsymbol{p})]. \tag{2.31}$$

Using the normalization constraint

$$0 = C_1[\varrho_\mathrm{can}] = \frac{\exp(-1-\alpha)}{h^{dN} N!} \int_V \mathrm{d}^{dN}\boldsymbol{q} \int \mathrm{d}^{dN}\boldsymbol{p}\, \exp[-\beta\mathcal{H}(\boldsymbol{q},\boldsymbol{p})] - 1, \tag{2.32}$$

we can eliminate the Lagrange multiplier α and finally arrive at

$$\varrho_\mathrm{can}(\boldsymbol{q},\boldsymbol{p}) = \frac{\exp[-\beta\mathcal{H}(\boldsymbol{q},\boldsymbol{p})]}{\frac{1}{h^{dN} N!} \int_V \mathrm{d}^{dN}\boldsymbol{q}' \int \mathrm{d}^{dN}\boldsymbol{p}'\, \exp[-\beta\mathcal{H}(\boldsymbol{q}',\boldsymbol{p}')]} = \frac{\exp[-\beta\mathcal{H}(\boldsymbol{q},\boldsymbol{p})]}{\mathcal{Z}_\mathrm{can}} \tag{2.33}$$

with the canonical partition sum

$$\mathcal{Z}_{\text{can}} = \frac{1}{h^{dN} N!} \int_V \mathrm{d}^{dN}\boldsymbol{q} \int \mathrm{d}^{dN}\boldsymbol{p}\, \exp[-\beta \mathcal{H}(\boldsymbol{q}, \boldsymbol{p})]. \tag{2.34}$$

Employing the energy constraint, we see that the thermodynamic entropy is

$$\begin{aligned} S &= k_{\text{B}} H[\varrho_{\text{can}}] = -k_{\text{B}} \langle \ln \varrho_{\text{can}} \rangle_{\varrho_{\text{can}}} = -k_{\text{B}} \langle -\beta \mathcal{H} - \ln \mathcal{Z}_{\text{can}} \rangle_{\varrho_{\text{can}}} \\ &= k_{\text{B}} (\beta \langle \mathcal{H} \rangle_{\varrho_{\text{can}}} + \ln \mathcal{Z}_{\text{can}}) = k_{\text{B}} (\beta U + \ln \mathcal{Z}_{\text{can}}), \end{aligned} \tag{2.35}$$

and that the Lagrange multiplier β is directly related to the temperature T through

$$T \equiv \frac{\partial U}{\partial S} = \left(\frac{\partial S}{\partial U} \right)^{-1} = \frac{1}{k_{\text{B}} \beta}. \tag{2.36}$$

The Helmholtz free energy is therefore given by

$$\begin{aligned} F &= U - TS = U - k_{\text{B}} T (\beta U + \ln \mathcal{Z}_{\text{can}}) = -k_{\text{B}} T \ln \mathcal{Z}_{\text{can}} \\ &= -k_{\text{B}} T \ln \left[\frac{1}{h^{dN} N!} \int_V \mathrm{d}^{dN}\boldsymbol{q} \int \mathrm{d}^{dN}\boldsymbol{p}\, \exp\{-\beta \mathcal{H}(\boldsymbol{q}, \boldsymbol{p})\} \right] \end{aligned} \tag{2.37}$$

2.2.2. Grand canonical ensemble

The *grand canonical ensemble* describes a system with fixed volume V that is not only in thermal but also in chemical equilibrium with its surroundings. Thus, the total energy as well as the number of particles are subject to fluctuations. Since each microstate is now characterized by a particular particle number n in addition to dn coordinates $\boldsymbol{q} = (q_1, \ldots, q_{dn})$ and dn momenta $\boldsymbol{p} = (p_1, \ldots, p_{dn})$, the averaging of an observable O must also occur over all $n \in \mathbb{N}_0$, so that

$$\langle O \rangle_{\varrho} = \sum_{n=0}^{\infty} \frac{1}{h^{dn} n!} \int_V \mathrm{d}^{dn}\boldsymbol{q} \int \mathrm{d}^{dn}\boldsymbol{p}\, \varrho(n, \boldsymbol{q}, \boldsymbol{p})\, O(n, \boldsymbol{q}, \boldsymbol{p}). \tag{2.38}$$

Consequently, the information entropy of some grand canonical probability distribution ϱ is actually

$$H[\varrho] \equiv -\langle \ln \varrho \rangle_{\varrho} = \sum_{n=0}^{\infty} \frac{1}{h^{dn} n!} \int_V \mathrm{d}^{dn}\boldsymbol{q} \int \mathrm{d}^{dn}\boldsymbol{p}\, \varrho(n, \boldsymbol{q}, \boldsymbol{p})\, \ln \varrho(n, \boldsymbol{q}, \boldsymbol{p}). \tag{2.39}$$

As in the canonical ensemble, we require that the equilibrium probability distribution ϱ_{gc} is normalized and that $\langle H \rangle_{\varrho_{\text{gc}}} = U$. Furthermore, we demand that the macroscopic particle number N can be identified with the average particle number $\langle \mathcal{N} \rangle_{\varrho_{\text{gc}}}$, where $\mathcal{N}(n, \boldsymbol{q}, \boldsymbol{p}) \equiv n$. Thus,

$C_1[\varrho_{\mathrm{gc}}] = C_2[\varrho_{\mathrm{gc}}] = C_3[\varrho_{\mathrm{gc}}] = 0$ for

$$\begin{aligned} C_1[\varrho] &\equiv \langle 1\rangle_\varrho - 1 = \sum_{n=0}^{\infty} \frac{1}{h^{dn} n!} \int_V \mathrm{d}^{dn}\boldsymbol{q} \int \mathrm{d}^{dn}\boldsymbol{p}\, \varrho(n,\boldsymbol{q},\boldsymbol{p}) - 1, \\ C_2[\varrho] &\equiv \langle \mathcal{H}\rangle_\varrho - U = \sum_{n=0}^{\infty} \frac{1}{h^{dn} n!} \int_V \mathrm{d}^{dn}\boldsymbol{q} \int \mathrm{d}^{dn}\boldsymbol{p}\, \varrho(n,\boldsymbol{q},\boldsymbol{p})\, \mathcal{H}(n,\boldsymbol{q},\boldsymbol{p}) - U, \\ C_3[\varrho] &\equiv \langle \mathcal{N}\rangle_\varrho - N = \sum_{n=0}^{\infty} \frac{1}{h^{dn} n!} \int_V \mathrm{d}^{dn}\boldsymbol{q} \int \mathrm{d}^{dn}\boldsymbol{p}\, \varrho(n,\boldsymbol{q},\boldsymbol{p})\, \mathcal{N}(n,\boldsymbol{q},\boldsymbol{p}) - N. \end{aligned} \tag{2.40}$$

Maximizing H subject to these constraints, one finds that

$$\varrho_{\mathrm{gc}}(n,\boldsymbol{q},\boldsymbol{p}) = \frac{\exp[-\beta\{\mathcal{H}(n,\boldsymbol{q},\boldsymbol{p}) - \mu\mathcal{N}(n,\boldsymbol{q},\boldsymbol{p})\}]}{\mathcal{Z}_{\mathrm{gc}}} = \frac{\exp[-\beta\{\mathcal{H}(n,\boldsymbol{q},\boldsymbol{p}) - \mu n\}]}{\mathcal{Z}_{\mathrm{gc}}}, \tag{2.41}$$

where

$$\mathcal{Z}_{\mathrm{gc}} = \sum_{n=0}^{\infty} \frac{1}{h^{dn} n!} \int_V \mathrm{d}^{dn}\boldsymbol{q} \int \mathrm{d}^{dn}\boldsymbol{p}\, \exp[-\beta\{\mathcal{H}(n,\boldsymbol{q},\boldsymbol{p}) - \mu n\}]. \tag{2.42}$$

is the grand canonical partition sum. With the thermodynamic entropy given by

$$S = k_{\mathrm{B}} H[\varrho_{\mathrm{gc}}] = -k_{\mathrm{B}} \langle -\beta(\mathcal{H} - \mu\mathcal{N}) - \ln \mathcal{Z}_{\mathrm{gc}}\rangle_{\varrho_{\mathrm{gc}}} = k_{\mathrm{B}}[\beta(U - \mu N) + \ln \mathcal{Z}_{\mathrm{gc}}], \tag{2.43}$$

we find that $\beta = (k_{\mathrm{B}}T)^{-1}$ also in the grand canonical case and that because of

$$\frac{\partial S}{\partial N} = -k_{\mathrm{B}}\beta\mu = -\frac{\mu}{T}, \tag{2.44}$$

the Lagrange multiplier μ is indeed the chemical potential. Since V, μ and T are therefore the natural variables of the grand canonical ensemble, the relevant thermodynamic potential is the grand potential

$$\begin{aligned} \Omega &= U - \mu N - TS = U - \mu N - k_{\mathrm{B}}T[\beta(U - \mu N) + \ln \mathcal{Z}_{\mathrm{gc}}] = -k_{\mathrm{B}}T \ln \mathcal{Z}_{\mathrm{gc}}. \\ &= -k_{\mathrm{B}}T \ln \sum_{n=0}^{\infty} \frac{1}{h^{dn} n!} \int_V \mathrm{d}^{dn}\boldsymbol{q} \int \mathrm{d}^{dn}\boldsymbol{p}\, \exp[-\beta\{\mathcal{H}(n,\boldsymbol{q},\boldsymbol{p}) - \mu n\}] \end{aligned} \tag{2.45}$$

2.2.3. Ideal gas

To demonstrate the power of the formalism of statistical mechanics, we shall derive the macroscopic properties of the *ideal gas*, which is a theoretical system of identical point particles with mass m that do not interact with each other and are confined to a certain volume V. It represents an important reference model because it is both quite simple and describes the behavior of real

monatomic gases at high dilutions reasonably well. The Hamiltonian of the ideal gas is

$$\mathcal{H}(n,\boldsymbol{q},\boldsymbol{p}) = \sum_{j=1}^{n} \mathcal{V}^{\text{ext}}(\vec{q}_j) + \sum_{i=1}^{n} \frac{\vec{p}_i^{\,2}}{2m} = \sum_{j=1}^{n} \mathcal{V}^{\text{ext}}(\vec{q}_j) + \sum_{i=1}^{dn} \frac{p_i^2}{2m}, \tag{2.46}$$

where the sum over the particle coordinates is the potential energy due to an external potential $\mathcal{V}^{\text{ext}}$, and the sum over the particle momenta is the kinetic energy. For the grand canonical partition sum, we find that

$$\begin{aligned}
\mathcal{Z}_{\text{gc}} &= \sum_{n=0}^{\infty} \frac{1}{h^{dn} n!} \int_V \mathrm{d}^{dn}\boldsymbol{q} \int \mathrm{d}^{dn}\boldsymbol{p}\, \exp[-\beta\{\mathcal{H}(n,\boldsymbol{q},\boldsymbol{p}) - \mu n\}] \\
&= \sum_{n=0}^{\infty} \frac{1}{h^{dn} n!} \int_V \mathrm{d}^{dn}\boldsymbol{q} \int \mathrm{d}^{dn}\boldsymbol{p}\, \exp\left[-\beta\left\{\sum_{i=1}^{dn} \frac{p_i^2}{2m} + \sum_{j=1}^{n} \mathcal{V}^{\text{ext}}(\vec{q}_j) - \mu n\right\}\right] \\
&= \sum_{n=0}^{\infty} \frac{\exp(\beta\mu n)}{h^{dn} n!} \prod_{i=1}^{dn} \left[\int_{-\infty}^{\infty} \mathrm{d}p_i \exp\left(-\frac{\beta p_i^2}{2m}\right)\right] \prod_{j=1}^{n} \left[\int_V \mathrm{d}^d\vec{q}_j \exp\{-\beta\mathcal{V}^{\text{ext}}(\vec{q}_j)\}\right] \\
&= \sum_{n=0}^{\infty} \frac{\exp(\beta\mu n)}{n!} \left[\frac{1}{h}\int_{-\infty}^{\infty} \mathrm{d}p \exp\left(-\frac{\beta p^2}{2m}\right)\right]^{dn} \left[\int_V \mathrm{d}^d\vec{q} \exp\{-\beta\mathcal{V}^{\text{ext}}(\vec{q})\}\right]^n .
\end{aligned} \tag{2.47}$$

where we used that the integrals are independent of the indices i and j. If we define the *thermal wavelength* as

$$\Lambda \equiv \left[\frac{1}{h}\int_{-\infty}^{\infty} \mathrm{d}p \exp\left(-\frac{\beta p^2}{2m}\right)\right]^{-1} = \left(\frac{1}{h}\sqrt{\frac{2\pi m}{\beta}}\right)^{-1} = \frac{h}{\sqrt{2\pi m k_{\text{B}} T}} \tag{2.48}$$

and the single-particle configuration integral as

$$Q_1(V) \equiv \int_V \mathrm{d}^d\vec{r} \exp[-\beta\mathcal{V}^{\text{ext}}(\vec{r})], \tag{2.49}$$

we arrive at

$$\mathcal{Z}_{\text{gc}} = \sum_{n=0}^{\infty} \frac{1}{n!} \frac{\exp(\beta\mu n)}{\Lambda^{dn}} Q_1(V)^n = \sum_{n=0}^{\infty} \frac{1}{n!} \left[\frac{\exp(\beta\mu)}{\Lambda^d} Q_1(V)\right]^n = \exp\left[\frac{\exp(\beta\mu)}{\Lambda^d} Q_1(V)\right]. \tag{2.50}$$

The grand potential is therefore given by

$$\Omega = -k_{\text{B}} T \ln \mathcal{Z}_{\text{gc}} = -k_{\text{B}} T \frac{\exp(\beta\mu)}{\Lambda^d} Q_1(V) = -k_{\text{B}} T \frac{\exp(\beta\mu)}{\Lambda^d} \int_V \mathrm{d}^d\boldsymbol{r} \exp[-\beta\mathcal{V}^{\text{ext}}(\vec{r})] \tag{2.51}$$

as a function of the natural variables V, μ and T, from which the corresponding conjugate quantities are calculated to be

$$P = -\frac{\partial\Omega}{\partial V} = k_\mathrm{B}T\frac{\exp(\beta\mu)}{\Lambda^d}\mathcal{Q}_1'(V), \tag{2.52}$$

$$N = -\frac{\partial\Omega}{\partial\mu} = \frac{\exp(\beta\mu)}{\Lambda^d}\mathcal{Q}_1(V) = -\frac{\Omega}{k_\mathrm{B}T}, \tag{2.53}$$

$$S = -\frac{\partial\Omega}{\partial T} = k_\mathrm{B}\left(1+\frac{d}{2}-\beta\mu\right)\frac{\exp(\beta\mu)}{\Lambda^d}\mathcal{Q}_1(V) = -\left(1+\frac{d}{2}-\beta\mu\right)\frac{\Omega}{T}, \tag{2.54}$$

where

$$\mathcal{Q}_1'(V) \equiv \frac{\mathrm{d}\mathcal{Q}_1(V)}{\mathrm{d}V} = \frac{1}{A(V)}\int_{A(V)}\mathrm{d}^d\vec{r}\,\exp[-\beta\mathcal{V}^\mathrm{ext}(\vec{r})] \tag{2.55}$$

with $A(V)$ denoting the surface of the volume V.

Because statistical mechanics allows us to compute the average of any arbitrary function of the microscopic state, we can also make predictions about other quantities than the typical thermodynamic ones. Since we need to be able to determine the spatial structure of a system in order to study microphase separation, an important measure will be the local *(single-particle) density distribution*

$$\rho(\vec{r}) \equiv \langle\hat{\rho}_{\vec{r}}\rangle, \tag{2.56}$$

which is defined as the average of the *density operator*

$$\hat{\rho}_{\vec{r}}(n,\boldsymbol{q},\boldsymbol{p}) \equiv \sum_{i=1}^{n}\delta(\vec{r}-\vec{q}_i). \tag{2.57}$$

For the ideal gas in the grand canonical ensemble, we have

$$\begin{aligned}
\rho(\vec{r}) \equiv \langle\hat{\rho}_{\vec{r}}\rangle_{\varrho_\mathrm{gc}} &= \frac{1}{\mathcal{Z}_\mathrm{gc}}\sum_{n=0}^{\infty}\frac{1}{h^{dn}n!}\int_V\mathrm{d}^{dn}\boldsymbol{q}\int\mathrm{d}^{dn}\boldsymbol{p}\,\hat{\rho}_{\vec{r}}(n,\boldsymbol{q},\boldsymbol{p})\,\exp[-\beta\{\mathcal{H}(n,\boldsymbol{q},\boldsymbol{p})-\mu n\}] \\
&= \frac{1}{\mathcal{Z}_\mathrm{gc}}\sum_{n=1}^{\infty}\frac{1}{\Lambda^{dn}n!}\int_V\mathrm{d}^{dn}\boldsymbol{q}\,\sum_{i=1}^{n}\delta(\vec{r}-\vec{q}_i)\,\exp\left[-\beta\left\{\sum_{j=1}^{n}\mathcal{V}^\mathrm{ext}(\vec{q}_j)-\mu n\right\}\right] \\
&= \frac{1}{\mathcal{Z}_\mathrm{gc}}\sum_{n=1}^{\infty}\frac{1}{\Lambda^{dn}n!}\sum_{i=1}^{n}\int_V\mathrm{d}^{dn}\boldsymbol{q}\,\delta(\vec{r}-\vec{q}_n)\,\exp\left[-\beta\left\{\sum_{j=1}^{n}\mathcal{V}^\mathrm{ext}(\vec{q}_j)-\mu n\right\}\right] \\
&= \frac{1}{\mathcal{Z}_\mathrm{gc}}\sum_{n=1}^{\infty}\frac{1}{\Lambda^{dn}(n-1)!}\int_V\mathrm{d}^{d(n-1)}\boldsymbol{q}\,\exp\left[-\beta\left\{\sum_{j=1}^{n-1}\mathcal{V}^\mathrm{ext}(\vec{q}_j)+\mathcal{V}^\mathrm{ext}(\vec{r})-\mu n\right\}\right] \\
&= \frac{\exp[-\beta\{\mathcal{V}^\mathrm{ext}(\vec{r})-\mu\}]}{\Lambda^d}\frac{1}{\mathcal{Z}_\mathrm{gc}}\underbrace{\sum_{n=0}^{\infty}\frac{1}{\Lambda^{dn}n!}\int_V\mathrm{d}^{dn}\boldsymbol{q}\,\exp\left[-\beta\left\{\sum_{j=1}^{n}\mathcal{V}^\mathrm{ext}(\vec{q}_j)-\mu n\right\}\right]}_{=\mathcal{Z}_\mathrm{gc}}.
\end{aligned} \tag{2.58}$$

On the last line, we can identify the sum over n as the grand canonical partial sum $\mathcal{Z}_{\mathrm{gc}}$ of the ideal gas and therefore find that

$$\rho(\vec{r}) = \frac{\exp(\beta\mu)}{\Lambda^d} \exp[-\beta \mathcal{V}^{\mathrm{ext}}(\vec{r})]. \tag{2.59}$$

In the special case of a vanishing external potential, $\mathcal{V}^{\mathrm{ext}} = 0$, we have that $Q_1(V) = V$ and $Q_1'(V) = 1$. Consequently,

$$\Omega = -k_{\mathrm{B}}T \frac{\exp(\beta\mu)}{\Lambda^d} V \tag{2.60}$$

$$P = k_{\mathrm{B}}T \frac{\exp(\beta\mu)}{\Lambda^d} = -\frac{\Omega}{V}, \tag{2.61}$$

$$N = \frac{\exp(\beta\mu)}{\Lambda^d} V = -\frac{\Omega}{k_{\mathrm{B}}T}, \tag{2.62}$$

$$S = k_{\mathrm{B}} \left(1 + \frac{d}{2} - \beta\mu\right) \frac{\exp(\beta\mu)}{\Lambda^d} V = -\left(1 + \frac{d}{2} - \beta\mu\right) \frac{\Omega}{T}, \tag{2.63}$$

giving rise to the experimentally well-known relations

$$PV = Nk_{\mathrm{B}}T, \quad U = \Omega + \mu N + TS = \frac{d}{2} Nk_{\mathrm{B}}T. \tag{2.64}$$

The density distribution becomes uniform,

$$\rho(\vec{r}) = \frac{\exp(\beta\mu)}{\Lambda^d} = \frac{N}{V} \equiv \rho_{\mathrm{b}}, \tag{2.65}$$

where ρ_{b} is the *bulk density*, and solving Eq. (2.62) for the chemical potential yields

$$\mu = k_{\mathrm{B}}T \ln\left(\Lambda^d \frac{N}{V}\right) = k_{\mathrm{B}}T \ln\left(\Lambda^d \rho_{\mathrm{b}}\right). \tag{2.66}$$

2.3. Density functional theory

Although statistical mechanics in principle lets us calculate the grand potential of a system based on its microscopic description via Eq. (2.45), the infinite sum and high-dimensional integrals make it practically impossible to find an analytical expression for Ω in all but the simplest of cases, such as the ideal gas. For the same reasons, and also due to the usually erratic behavior of the exponential integrand, numerically computing an accurate result is just as unfeasible. Fortunately, the computational complexity can be vastly reduced by means of *density functional theory* (DFT) [45].

Let us define the *grand potential functional* for some normalized but otherwise arbitrary prob-

ability distribution ϱ as

$$\begin{aligned}\Omega[\varrho] &\equiv \langle \mathcal{H} - \mu\mathcal{N} - T\mathcal{S}_\varrho \rangle_\varrho \\ &= \sum_{n=0}^{\infty} \frac{1}{h^{dn} n!} \int \mathrm{d}^{dn}\boldsymbol{q} \int \mathrm{d}^{dn}\boldsymbol{p}\, \varrho(n,\boldsymbol{q},\boldsymbol{p}) \left[\mathcal{H}(n,\boldsymbol{q},\boldsymbol{p}) - \mu n - T\mathcal{S}_\varrho(n,\boldsymbol{q},\boldsymbol{p})\right]\end{aligned} \tag{2.67}$$

with $\mathcal{S}_\varrho(n,\boldsymbol{q},\boldsymbol{p}) \equiv -k_\mathrm{B} \ln \varrho(n,\boldsymbol{q},\boldsymbol{p})$. Rather then explicitly restricting the integral over the coordinates to the volume V, we demand that $\mathcal{H}(n,\boldsymbol{q},\boldsymbol{p}) = \infty$ if $\vec{q} \notin V$ for any $\vec{q} \in \boldsymbol{q}$. Using that the grand canonical equilibrium probability distribution ϱ_gc satisfies

$$k_\mathrm{B}T \ln \varrho_\mathrm{gc}(n,\boldsymbol{q},\boldsymbol{p}) = -k_\mathrm{B}T \ln \mathcal{Z}_\mathrm{gc} - \left[\mathcal{H}(n,\boldsymbol{q},\boldsymbol{p}) - \mu n\right] = \Omega - \left[\mathcal{H}(n,\boldsymbol{q},\boldsymbol{p}) - \mu n\right], \tag{2.68}$$

we see that

$$\begin{aligned}\Omega[\varrho] &= \sum_{n=0}^{\infty} \frac{1}{h^{dn} n!} \int \mathrm{d}^{dn}\boldsymbol{q} \int \mathrm{d}^{dn}\boldsymbol{p}\, \varrho(n,\boldsymbol{q},\boldsymbol{p}) \left[\mathcal{H}(n,\boldsymbol{q},\boldsymbol{p}) - \mu n + k_\mathrm{B}T \ln \varrho(n,\boldsymbol{q},\boldsymbol{p})\right] \\ &= \sum_{n=0}^{\infty} \frac{1}{h^{dn} n!} \int \mathrm{d}^{dn}\boldsymbol{q} \int \mathrm{d}^{dn}\boldsymbol{p}\, \varrho(n,\boldsymbol{q},\boldsymbol{p}) \left[\Omega - k_\mathrm{B}T \ln \varrho_\mathrm{gc}(n,\boldsymbol{q},\boldsymbol{p}) + k_\mathrm{B}T \ln \varrho(n,\boldsymbol{q},\boldsymbol{p})\right] \\ &= \Omega + k_\mathrm{B}T \sum_{n=0}^{\infty} \frac{1}{h^{dn} n!} \int \mathrm{d}^{dn}\boldsymbol{q} \int \mathrm{d}^{dn}\boldsymbol{p}\, \varrho(n,\boldsymbol{q},\boldsymbol{p}) \ln \frac{\varrho(n,\boldsymbol{q},\boldsymbol{p})}{\varrho_\mathrm{gc}(n,\boldsymbol{q},\boldsymbol{p})} \\ &= \Omega + k_\mathrm{B}T \sum_{n=0}^{\infty} \frac{1}{h^{dn} n!} \int \mathrm{d}^{dn}\boldsymbol{q} \int \mathrm{d}^{dn}\boldsymbol{p}\, \varrho_\mathrm{gc}(n,\boldsymbol{q},\boldsymbol{p})\, h\!\left(\frac{\varrho(n,\boldsymbol{q},\boldsymbol{p})}{\varrho_\mathrm{gc}(n,\boldsymbol{q},\boldsymbol{p})}\right),\end{aligned} \tag{2.69}$$

where $h(x) \equiv x \ln x - (x-1)$. Since $h'(x) \equiv \mathrm{d}h(x)/\mathrm{d}x = \ln x$, it follows that $h'(x) < 0$ for $0 \leq x < 1$ and $h'(x) > 0$ for $x > 1$, which implies that h has a global minimum at $x = 1$. Therefore, $h(x) > h(1) = 0$ for $x \neq 1$ and consequently

$$\Omega = \Omega[\varrho_\mathrm{gc}] < \Omega[\varrho] \tag{2.70}$$

for $\varrho \neq \varrho_\mathrm{gc}$. In other words, the grand potential functional (2.67) is minimized exclusively by the equilibrium probability distribution ϱ_gc, where it evaluates to the thermodynamic grand potential Ω of the system.

Let us now consider a Hamiltonian of the form $\mathcal{H} = \mathcal{H}_\mathrm{int} + \mathcal{H}_\mathrm{ext}$ with

$$\mathcal{H}_\mathrm{ext}(n,\boldsymbol{q},\boldsymbol{p}) \equiv \sum_{i=1}^{n} \mathcal{V}^\mathrm{ext}(\vec{q}_i) = \int \mathrm{d}^d\vec{r}\, \hat{\rho}_{\vec{r}}(n,\boldsymbol{q},\boldsymbol{p})\, \mathcal{V}^\mathrm{ext}(\vec{r}), \tag{2.71}$$

where $\mathcal{V}^\mathrm{ext}(\vec{r}) = \infty$ if $\vec{r} \notin V$ and $\mathcal{H}_\mathrm{int}$ is volume-independent. The grand potential function can

then be written as

$$\begin{aligned}\Omega[\varrho] &= \langle \mathcal{H} - \mu\mathcal{N} - T\mathcal{S}_\varrho \rangle_\varrho = \langle \mathcal{H}_{\text{int}} - T\mathcal{S}_\varrho \rangle_\varrho + \langle \mathcal{H}_{\text{ext}} - \mu\mathcal{N} \rangle_\varrho \\ &= \mathcal{F}[\varrho] + \int \mathrm{d}^d\vec{r}\, \langle \hat{\rho}_{\vec{r}} \rangle_\varrho \, [\mathcal{V}^{\text{ext}}(\vec{r}) - \mu] = \mathcal{F}[\varrho] - \int \mathrm{d}^d\vec{r}\, \langle \hat{\rho}_{\vec{r}} \rangle_\varrho \, \mu_{\text{int}}(\vec{r}),\end{aligned} \tag{2.72}$$

where $\mathcal{F}[\varrho] \equiv \langle \mathcal{H}_{\text{int}} - T\mathcal{S}_\varrho \rangle_\varrho$ is the *intrinsic free energy functional* and $\mu_{\text{int}}(\vec{r}) \equiv \mu - \mathcal{V}^{\text{ext}}(\vec{r})$ the *intrinsic chemical potential*. Note that a different intrinsic chemical potential $\mu'_{\text{int}} \equiv \mu_{\text{int}} + \Delta\mu_{\text{int}}$ with $\Delta\mu_{\text{int}} \neq 0$ would give rise to a different equilibrium probability distribution $\varrho'_{\text{gc}} \neq \varrho_{\text{gc}}$ since

$$\begin{aligned}\varrho'_{\text{gc}}(n, \boldsymbol{q}, \boldsymbol{p}) &= \frac{\exp\left[-\beta \left\{\mathcal{H}_{\text{int}}(n, \boldsymbol{q}, \boldsymbol{p}) - \sum_{i=1}^n \mu'_{\text{int}}(\vec{q}_i)\right\}\right]}{\mathcal{Z}'_{\text{gc}}} \\ &= \varrho_{\text{gc}}(n, \boldsymbol{q}, \boldsymbol{p}) \frac{\mathcal{Z}_{\text{gc}}}{\mathcal{Z}'_{\text{gc}}} \exp\left[\beta \sum_{i=1}^n \Delta\mu_{\text{int}}(\vec{q}_i)\right]\end{aligned} \tag{2.73}$$

and the term $(\mathcal{Z}_{\text{gc}}/\mathcal{Z}'_{\text{gc}}) \exp[\beta \sum_{i=1}^n \Delta\mu_{\text{int}}(\vec{q}_i)]$ cannot be identical to unity for all microstates $(n, \boldsymbol{q}, \boldsymbol{p})$. We can use this to show that a different intrinsic chemical potential also results in a different equilibrium density distribution $\rho'_{\text{eq}}(\vec{r}) \equiv \langle \hat{\rho}_{\vec{r}} \rangle_{\varrho'_{\text{gc}}} \neq \langle \hat{\rho}_{\vec{r}} \rangle_{\varrho_{\text{gc}}} \equiv \rho_{\text{eq}}(\vec{r})$. Because ϱ_{gc} minimizes the grand potential functional in Eq. (2.72) according to Eq. (2.70), we have that

$$\Omega[\varrho_{\text{gc}}] < \Omega[\varrho'_{\text{gc}}] = \mathcal{F}[\varrho'_{\text{gc}}] - \int \mathrm{d}^d\vec{r}\, \langle \hat{\rho}_{\vec{r}} \rangle_{\varrho'_{\text{gc}}} \, \mu_{\text{int}}(\vec{r}) = \Omega'[\varrho'_{\text{gc}}] + \int \mathrm{d}^d\vec{r}\, \rho'_{\text{eq}}(\vec{r})\, \Delta\mu_{\text{int}}(\vec{r}) \tag{2.74}$$

with $\Omega'[\varrho'] \equiv \mathcal{F}[\varrho'] - \int \mathrm{d}^d\vec{r}\, \langle \hat{\rho}_{\vec{r}} \rangle_{\varrho'} \, \mu'_{\text{int}}(\vec{r})$. Likewise, we find that

$$\Omega'[\varrho'_{\text{gc}}] < \Omega'[\varrho_{\text{gc}}] = \mathcal{F}[\varrho_{\text{gc}}] - \int \mathrm{d}^d\vec{r}\, \langle \hat{\rho}_{\vec{r}} \rangle_{\varrho_{\text{gc}}} \, \mu'_{\text{int}}(\vec{r}) = \Omega[\varrho_{\text{gc}}] - \int \mathrm{d}^d\vec{r}\, \rho_{\text{eq}}(\vec{r})\, \Delta\mu_{\text{int}}(\vec{r}). \tag{2.75}$$

By adding Eqs. (2.74) and (2.75), it follows that

$$\int \mathrm{d}^d\vec{r}\, [\rho'_{\text{eq}}(\vec{r}) - \rho_{\text{eq}}(\vec{r})]\, \Delta\mu_{\text{int}}(\vec{r}) > 0, \tag{2.76}$$

which implies that $\rho'_{\text{eq}} \neq \rho_{\text{eq}}$. Since every μ_{int} leads to a unique ϱ_{gc} and ρ_{eq}, we can in principle construct a mapping $\rho \mapsto \hat{\varrho}[\rho]$ that takes an equilibrium density distribution and returns the associated equilibrium probability distribution. This allows us to define a density functional $\mathcal{F}[\rho] \equiv \mathcal{F}[\hat{\varrho}[\rho]]$ of the intrinsic free energy of a system with a given $\mathcal{H}_{\text{int}}$ such that for any $\mu_{\text{int}}(\vec{r}) = \mu - \mathcal{V}^{\text{ext}}(\vec{r})$, and by extension also for any volume V implicitly incorporated into $\mathcal{V}^{\text{ext}}$, the corresponding density functional

$$\Omega[\rho] \equiv \Omega[\hat{\varrho}[\rho]] = \mathcal{F}[\rho] + \int \mathrm{d}^d\vec{r}\, \rho(\vec{r})\, [\mathcal{V}^{\text{ext}}(\vec{r}) - \mu] \tag{2.77}$$

of the grand potential is minimized solely by the equilibrium density distribution ρ_{eq}, where it

evaluates to the thermodynamic grand potential Ω. Thus,

$$\Omega = \Omega[\rho_{\mathrm{eq}}] < \Omega[\rho] \tag{2.78}$$

for $\rho \neq \rho_{\mathrm{eq}}$. Since the minimization of the density functional (2.77) is significantly simpler than the direct computation of (2.45), DFT gives us a considerable advantage. Furthermore, because we obtain the grand potential and the equilibrium density distribution in the same step, DFT is an immensely practical tool for studying the phase behavior and the structure of a system.

The DFT formalism is easily extended to mixtures of different particle species. For a ν-component system with density distribution $\boldsymbol{\rho} = (\rho_1, \ldots, \rho_\nu)$, the grand potential functional can be written as

$$\Omega[\boldsymbol{\rho}] = \mathcal{F}[\boldsymbol{\rho}] + \sum_{a=1}^{\nu} \int \mathrm{d}^d\vec{r}\, \rho_a(\vec{r})\, [\mathcal{V}_a^{\mathrm{ext}}(\vec{r}) - \mu_a], \tag{2.79}$$

where $\mathcal{V}_a^{\mathrm{ext}}$ denotes the external and μ_a the chemical potential of species a. This functional is again minimized by the equilibrium density distribution $\boldsymbol{\rho}_{\mathrm{eq}}$ so that $\Omega = \Omega[\boldsymbol{\rho}_{\mathrm{eq}}] < \Omega[\boldsymbol{\rho}]$ for $\boldsymbol{\rho} \neq \boldsymbol{\rho}_{\mathrm{eq}}$.

The actual challenge of DFT lies in determining the density functional $\mathcal{F}$ of the intrinsic free energy for a concrete $\mathcal{H}_{\mathrm{int}}$. An exact expression has only been found in a very few cases; however, it is often possible to devise quite accurate approximations for $\mathcal{F}$.

2.3.1. Ideal gas

For the ideal gas with $\mathcal{H}_{\mathrm{int}}(n, \boldsymbol{q}, \boldsymbol{p}) = \mathcal{T}(n, \boldsymbol{p}) \equiv \sum_{i=1}^{dn} p_i^2/(2m)$, it is trivial to derive the exact the intrinsic free energy functional. By comparing Eqs. (2.51) and (2.58), we immediately see that

$$\Omega_{\mathrm{id}}[\rho] = -k_{\mathrm{B}}T \int \mathrm{d}^d\vec{r}\, \rho(\vec{r}). \tag{2.80}$$

Using that $\mathcal{V}^{\mathrm{ext}}(\vec{r}) - \mu = -k_{\mathrm{B}}T \ln[\Lambda^d \rho(\vec{r})]$ according to (2.58), we then find that

$$\mathcal{F}_{\mathrm{id}}[\rho] = \Omega_{\mathrm{id}}[\rho] - \int \mathrm{d}^d\vec{r}\, \rho(\vec{r})\, [\mathcal{V}^{\mathrm{ext}}(\vec{r}) - \mu] = k_{\mathrm{B}}T \int \mathrm{d}^d\vec{r}\, \rho(\vec{r})\, [\ln\{\Lambda^d \rho(\vec{r})\} - 1]. \tag{2.81}$$

In the case of a ν-component mixture with masses $m_1, \ldots, m_\nu$, we consequently have

$$\mathcal{F}_{\mathrm{id}}[\boldsymbol{\rho}] = \sum_{a=1}^{\nu} \mathcal{F}_a^{\mathrm{id}}[\rho_a] = k_{\mathrm{B}}T \sum_{a=1}^{\nu} \int \mathrm{d}^d\vec{r}\, \rho_a(\vec{r})\, [\ln\{\Lambda_a^d \rho_a(\vec{r})\} - 1] \tag{2.82}$$

with $\Lambda_a \equiv h/\sqrt{2\pi m_a k_\mathrm{B} T}$. For other systems with

$$\mathcal{H}_\mathrm{int}(\boldsymbol{n}, \boldsymbol{q}, \boldsymbol{p}) = \mathcal{T}(\boldsymbol{n}, \boldsymbol{p}) + \mathcal{U}(\boldsymbol{n}, \boldsymbol{q}) = \sum_{a=1}^{\nu} \sum_{i=1}^{dn_a} \frac{p_{ai}^2}{2m_a} + \mathcal{U}(\boldsymbol{n}, \boldsymbol{q}), \tag{2.83}$$

the intrinsic free energy functional is usually written as $\mathcal{F} = \mathcal{F}_\mathrm{id} + \mathcal{F}_\mathrm{ex}$, where $\mathcal{F}_\mathrm{id}$ contains the contribution of the kinetic term $\mathcal{T}$ and the *excess free energy functional* $\mathcal{F}_\mathrm{ex}$ accounts for the interaction term $\mathcal{U}$.

2.3.2. Hard disks

Mixtures of hard particles are an important reference system due to the simplicity of their interaction and the ability to model them experimentally with colloids. Every species a has an associated radius $R_a > 0$, and two hard particles cannot interpenetrate each other so that their separation can never be smaller than the sum of their radii. The interaction potential is therefore given by

$$\mathcal{U}(\boldsymbol{n}, \boldsymbol{q}) = \frac{1}{2} \sum_{a=1}^{\nu} \sum_{\substack{b=1 \\ a \neq b \text{ or } i \neq j}}^{\nu} \sum_{i=1}^{n_a} \sum_{j=1}^{n_b} u_{ab}(\vec{q}_{ai} - \vec{q}_{bj}) \tag{2.84}$$

with the pair potential

$$u_{ab}(\vec{r}) = \begin{cases} \infty & \text{if } |\vec{r}| < R_a + R_b, \\ 0 & \text{otherwise.} \end{cases} \tag{2.85}$$

For one-dimensional hard rods ($d = 1$), the excess free energy functional is known exactly [46, 47] and can be expressed in terms of so-called *weighted densities*, which are convolutions of the density distribution with certain weight functions that characterize the fundamental geometric measures of the rods: their surface (the two endpoints) and their volume (the region between the endpoints). An approximate excess free energy functional with the same general structure has been constructed by Rosenfeld for three-dimensional hard spheres ($d = 3$) [48]. His basic approach – referred to as *fundamental measure theory* (FMT) – turned out to be extremely powerful and led to the development of ever more accurate excess free energy functionals for hard sphere mixtures.

We shall now follow Roth, Mecke and Oettel [49] to derive an excess free energy functional for a mixture of two-dimensional hard disk ($d = 2$) by means of FMT. As a starting point, we use that in the low-density limit, the excess free energy functional of any system with only pairwise

interactions can be expanded in powers of the density distributions as

$$\beta\mathcal{F}_{\text{ex}}[\boldsymbol{\rho}] = -\frac{1}{2}\sum_{a=1}^{\nu}\sum_{b=1}^{\nu}\int \mathrm{d}^d\vec{r}\int \mathrm{d}^d\vec{r}'\,\rho_a(\vec{r})\,\rho_b(\vec{r}')\,f_{ab}(\vec{r}-\vec{r}') + O(\boldsymbol{\rho}^3) \tag{2.86}$$

with the *Mayer f-function*

$$f_{ab}(\vec{r}) \equiv \exp[-\beta u_{ab}(\vec{r})] - 1. \tag{2.87}$$

For hard particles and u_{ab} given by Eq. (2.85), we have

$$f_{ab}(\vec{r}) = \begin{cases} -1 & \text{if } |\vec{r}| < R_a + R_b, \\ 0 & \text{otherwise.} \end{cases} \tag{2.88}$$

As shown in Appendix A, the Mayer f-function for hard disks can be decomposed into

$$-f_{ab} = \omega_a^2 \star \omega_b^0 + \omega_a^0 \star \omega_b^2 + \frac{1}{2\pi}\sum_{m=0}^{\infty} C_m\,\boldsymbol{\omega}_a^m \star \boldsymbol{\omega}_b^m, \tag{2.89}$$

where the *weight functions* are defined as

$$\omega_a^0(\vec{r}) \equiv \frac{\delta(R_a - |\vec{r}|)}{2\pi R_a}, \quad \omega_a^2(\vec{r}) \equiv \Theta(R_a - |\vec{r}|), \quad [\boldsymbol{\omega}_a^m(\vec{r})]_{i_1,\ldots,i_m} \equiv \frac{x_{i_1}\cdots x_{i_m}}{|\vec{r}|^m}\delta(R_a - |\vec{r}|) \tag{2.90}$$

for $\vec{r} = (x_1, x_2)$ and $i_1, \ldots, i_m \in \{1, 2\}$, and the coefficients are given by

$$C_0 = \frac{\pi}{2}, \quad C_1 = -1, \quad C_2 = -\frac{\pi}{4}, \quad C_m = -\frac{(m-3)!!}{m!!}C_{\text{mod}(m,2)} \tag{2.91}$$

for $m \geq 3$. The symbol "$\star$" denotes the cross-correlation

$$\begin{aligned} (\omega_a^k \star \omega_b^l)(\vec{r}) &\equiv \int \mathrm{d}^2\vec{r}'\,\omega_a^k(\vec{r}'-\vec{r})\,\omega_b^l(\vec{r}'), \\ (\boldsymbol{\omega}_a^m \star \boldsymbol{\omega}_b^m)(\vec{r}) &\equiv \int \mathrm{d}^2\vec{r}'\,\boldsymbol{\omega}_a^m(\vec{r}'-\vec{r})\cdot\boldsymbol{\omega}_b^m(\vec{r}'), \end{aligned} \tag{2.92}$$

and "$\cdot$" the dot product

$$\boldsymbol{\omega}_a^m(\vec{r})\cdot\boldsymbol{\omega}_b^m(\vec{r}') \equiv \sum_{i_1=1}^{2}\cdots\sum_{i_m=1}^{2}[\boldsymbol{\omega}_a^m(\vec{r})]_{i_1,\ldots,i_m}\,[\boldsymbol{\omega}_b^m(\vec{r}')]_{i_1,\ldots,i_m}. \tag{2.93}$$

If we insert Eq. (2.89) into (2.86), we encounter terms of the form

$$\begin{aligned}
&\sum_{a=1}^{\nu}\sum_{b=1}^{\nu}\int \mathrm{d}^d\vec{r}\int \mathrm{d}^d\vec{r}'\,\rho_a(\vec{r})\,\rho_b(\vec{r}')\,(\omega_a^k\star\omega_b^l)(\vec{r}-\vec{r}')\\
&\quad=\sum_{a=1}^{\nu}\sum_{b=1}^{\nu}\int \mathrm{d}^d\vec{r}\int \mathrm{d}^d\vec{r}'\,\rho_a(\vec{r})\,\rho_b(\vec{r}')\int \mathrm{d}^2\vec{r}''\,\omega_a^k(\vec{r}''-\vec{r}+\vec{r}')\omega_b^l(\vec{r}'')\\
&\quad=\int \mathrm{d}^2\vec{r}''\sum_{a=1}^{\nu}\int \mathrm{d}^2\vec{r}\,\rho_a(\vec{r})\,\omega_a^k(\vec{r}''-\vec{r})\sum_{b=1}^{\nu}\int \mathrm{d}^2\vec{r}'\,\rho_b(\vec{r}')\,\omega_b^l(\vec{r}''-\vec{r}')\\
&\quad=\int \mathrm{d}^2\vec{r}''\,w_{\boldsymbol{\rho}}^k(\vec{r}'')\,w_{\boldsymbol{\rho}}^l(\vec{r}'')
\end{aligned}\tag{2.94}$$

and analogously

$$\sum_{a=1}^{\nu}\sum_{b=1}^{\nu}\int \mathrm{d}^d\vec{r}\int \mathrm{d}^d\vec{r}'\,\rho_a(\vec{r})\,\rho_b(\vec{r}')\,(\boldsymbol{\omega}_a^m\star\boldsymbol{\omega}_b^m)(\vec{r}-\vec{r}')=\int \mathrm{d}^2\vec{r}''\,\boldsymbol{w}_{\boldsymbol{\rho}}^m(\vec{r}'')\cdot\boldsymbol{w}_{\boldsymbol{\rho}}^m(\vec{r}''),\tag{2.95}$$

where the *weighted densities*

$$\begin{aligned}
w_{\boldsymbol{\rho}}^k(\vec{r})&\equiv\sum_{a=1}^{\nu}(\rho_a\otimes\omega_a^k)(\vec{r})=\sum_{a=1}^{\nu}\int \mathrm{d}^2\vec{r}'\,\rho_a(\vec{r}')\,\omega_a^k(\vec{r}-\vec{r}'),\\
\boldsymbol{w}_{\boldsymbol{\rho}}^m(\vec{r})&\equiv\sum_{a=1}^{\nu}(\rho_a\otimes\boldsymbol{\omega}_a^m)(\vec{r})=\sum_{a=1}^{\nu}\int \mathrm{d}^2\vec{r}'\,\rho_a(\vec{r}')\,\boldsymbol{\omega}_a^m(\vec{r}-\vec{r}')
\end{aligned}\tag{2.96}$$

are convolutions of the density distributions with the weight functions. In the low-density limit, we therefore find that

$$\beta\mathcal{F}_{\mathrm{ex}}^{\mathrm{hd}}[\boldsymbol{\rho}]=\int \mathrm{d}^2\vec{r}\left[w_{\boldsymbol{\rho}}^2(\vec{r})w_{\boldsymbol{\rho}}^0(\vec{r})+\frac{1}{4\pi}\sum_{m=0}^{\infty}C_m\,\boldsymbol{w}_{\boldsymbol{\rho}}^m(\vec{r})\cdot\boldsymbol{w}_{\boldsymbol{\rho}}^m(\vec{r})\right]+O(\boldsymbol{\rho}^3).\tag{2.97}$$

The key assumption of FMT is that even for a general density distribution, the excess free energy functional can be written as

$$\beta\mathcal{F}_{\mathrm{ex}}^{\mathrm{hd}}[\boldsymbol{\rho}]=\int \mathrm{d}^2\vec{r}\,\phi_{\boldsymbol{\rho}}^{\mathrm{hd}}(\vec{r})=\int \mathrm{d}^2\vec{r}\,\phi^{\mathrm{hd}}(w_{\boldsymbol{\rho}}^0(\vec{r}),w_{\boldsymbol{\rho}}^2(\vec{r}),\boldsymbol{w}_{\boldsymbol{\rho}}^0(\vec{r}),\boldsymbol{w}_{\boldsymbol{\rho}}^1(\vec{r}),\boldsymbol{w}_{\boldsymbol{\rho}}^2(\vec{r}),\dots),\tag{2.98}$$

where ϕ^{hd} is a suitable function of the weighted densities. Since $\phi_{\boldsymbol{\rho}}^{\mathrm{hd}}(\vec{r})$ has to be a scalar with dimensions of $[\mathrm{length}]^{-2}$, Roth et al. made the *ansatz* that

$$\phi_{\boldsymbol{\rho}}^{\mathrm{hd}}(\vec{r})=f(w_{\boldsymbol{\rho}}^2(\vec{r}))w_{\boldsymbol{\rho}}^0(\vec{r})+\frac{1}{4\pi}\sum_{m=0}^{\infty}g_m(w_{\boldsymbol{\rho}}^2(\vec{r}))\,C_m\,\boldsymbol{w}_{\boldsymbol{\rho}}^m(\vec{r})\cdot\boldsymbol{w}_{\boldsymbol{\rho}}^m(\vec{r}).\tag{2.99}$$

In order to recover the low-density limit (2.97), the functions f and g_m for $m\in\mathbb{N}_0$ must have the

expansions

$$f(x) = x + O(x^2), \quad g_m(x) = 1 + O(x). \tag{2.100}$$

To determine these functions, let us consider the case of an infinitely large system without an external potential. At moderate bulk densities $\boldsymbol{\rho}_\mathrm{b} = (\rho_1^\mathrm{b}, \dots, \rho_\nu^\mathrm{b})$, the system is in a fluid state with uniform density distributions $\boldsymbol{\rho}(\vec{r}) = \boldsymbol{\rho}_\mathrm{b}$ in equilibrium. This means that the weighted densities are uniform as well and thus

$$\frac{\beta\mathcal{F}_\mathrm{ex}^\mathrm{hd}[\boldsymbol{\rho}_\mathrm{b}]}{V} = \phi_{\boldsymbol{\rho}_\mathrm{b}}^\mathrm{hd} = f(w_{\boldsymbol{\rho}_\mathrm{b}}^2) w_{\boldsymbol{\rho}_\mathrm{b}}^0 + \frac{1}{4\pi} \sum_{m=0}^{\infty} g_m(w_{\boldsymbol{\rho}_\mathrm{b}}^2)\, C_m\, \boldsymbol{w}_{\boldsymbol{\rho}_\mathrm{b}}^m \cdot \boldsymbol{w}_{\boldsymbol{\rho}_\mathrm{b}}^m \tag{2.101}$$

with

$$w_{\boldsymbol{\rho}_\mathrm{b}}^0 = \sum_{a=1}^{\nu} \rho_a^\mathrm{b}, \quad w_{\boldsymbol{\rho}_\mathrm{b}}^2 = \sum_{a=1}^{\nu} \pi R_a^2 \rho_a^\mathrm{b}, \quad [\boldsymbol{w}_{\boldsymbol{\rho}_\mathrm{b}}^m]_{i_1,\dots,i_m} = \int_0^{2\pi} \mathrm{d}\varphi\, (\vec{e}_\varphi)_{i_1} \cdots (\vec{e}_\varphi)_{i_m} \sum_{a=1}^{\nu} R_a \rho_a^\mathrm{b}, \tag{2.102}$$

where $\vec{e}_\varphi \equiv (\cos\varphi, \sin\varphi)$. Calculating the pressure P, we find that

$$\begin{aligned}
\beta P &= -\beta \frac{\partial \mathcal{F}^\mathrm{hd}[\boldsymbol{\rho}_\mathrm{b}]}{\partial V} = \beta P^\mathrm{id} - \beta \frac{\partial \mathcal{F}_\mathrm{ex}^\mathrm{hd}[\boldsymbol{\rho}_\mathrm{b}]}{\partial V} = \sum_{a=1}^{\nu} \beta P_a^\mathrm{id} - \frac{\partial (V \phi_{\boldsymbol{\rho}_\mathrm{b}}^\mathrm{hd})}{\partial V} \\
&= \sum_{a=1}^{\nu} \rho_a^\mathrm{b} - \phi_{\boldsymbol{\rho}_\mathrm{b}}^\mathrm{hd} - V \sum_{a=1}^{\nu} \frac{\partial \phi_{\boldsymbol{\rho}_\mathrm{b}}^\mathrm{hd}}{\partial \rho_a^\mathrm{b}} \frac{\partial \rho_a^\mathrm{b}}{\partial V} = w_{\boldsymbol{\rho}_\mathrm{b}}^0 - \phi_{\boldsymbol{\rho}_\mathrm{b}}^\mathrm{hd} - V \sum_{a=1}^{\nu} \sum_{w \in \mathbb{W}} \frac{\partial \phi_{\boldsymbol{\rho}_\mathrm{b}}^\mathrm{hd}}{\partial w_{\boldsymbol{\rho}_\mathrm{b}}} \frac{\partial w_{\boldsymbol{\rho}_\mathrm{b}}}{\partial \rho_a^\mathrm{b}} \left(-\frac{\rho_a^\mathrm{b}}{V} \right) \\
&= w_{\boldsymbol{\rho}_\mathrm{b}}^0 - \phi_{\boldsymbol{\rho}_\mathrm{b}}^\mathrm{hd} + \sum_{w \in \mathbb{W}} \frac{\partial \phi_{\boldsymbol{\rho}_\mathrm{b}}^\mathrm{hd}}{\partial w_{\boldsymbol{\rho}_\mathrm{b}}} \sum_{a=1}^{\nu} \frac{\partial w_{\boldsymbol{\rho}_\mathrm{b}}}{\partial \rho_a^\mathrm{b}} \rho_a^\mathrm{b} = w_{\boldsymbol{\rho}_\mathrm{b}}^0 - \phi_{\boldsymbol{\rho}_\mathrm{b}}^\mathrm{hd} + \sum_{w \in \mathbb{W}} \frac{\partial \phi_{\boldsymbol{\rho}_\mathrm{b}}^\mathrm{hd}}{\partial w_{\boldsymbol{\rho}_\mathrm{b}}} w_{\boldsymbol{\rho}_\mathrm{b}} \\
&= \left(\frac{\partial \phi_{\boldsymbol{\rho}_\mathrm{b}}^\mathrm{hd}}{\partial w_{\boldsymbol{\rho}_\mathrm{b}}^0} + 1 \right) w_{\boldsymbol{\rho}_\mathrm{b}}^0 + \frac{\partial \phi_{\boldsymbol{\rho}_\mathrm{b}}^\mathrm{hd}}{\partial w_{\boldsymbol{\rho}_\mathrm{b}}^2} w_{\boldsymbol{\rho}_\mathrm{b}}^2 + \sum_{m=0}^{\infty} \frac{\partial \phi_{\boldsymbol{\rho}_\mathrm{b}}^\mathrm{hd}}{\partial \boldsymbol{w}_{\boldsymbol{\rho}_\mathrm{b}}^m} \cdot \boldsymbol{w}_{\boldsymbol{\rho}_\mathrm{b}}^m - \phi_{\boldsymbol{\rho}_\mathrm{b}}^\mathrm{hd},
\end{aligned} \tag{2.103}$$

where $\mathbb{W} = \{w^0, w^2, \boldsymbol{w}^0, \boldsymbol{w}^1, \boldsymbol{w}^2, \dots\}$ denotes the set of all weighted densities. The excess chemical potential $\mu_a^\mathrm{ex} \equiv \mu_a - \mu_a^\mathrm{id}$ of species a is given by

$$\beta\mu_a^\mathrm{ex} = \beta \frac{\partial \mathcal{F}_\mathrm{ex}^\mathrm{hd}[\boldsymbol{\rho}_\mathrm{b}]}{\partial N_a} = \frac{\beta}{V} \frac{\partial \mathcal{F}_\mathrm{ex}^\mathrm{hd}[\boldsymbol{\rho}_\mathrm{b}]}{\partial \rho_a^\mathrm{b}} = \frac{\partial \phi_{\boldsymbol{\rho}_\mathrm{b}}^\mathrm{hd}}{\partial \rho_a^\mathrm{b}} = \sum_{w \in \mathbb{W}} \frac{\partial \phi_{\boldsymbol{\rho}_\mathrm{b}}^\mathrm{hd}}{\partial w_{\boldsymbol{\rho}_\mathrm{b}}} \frac{\partial w_{\boldsymbol{\rho}_\mathrm{b}}}{\partial \rho_a^\mathrm{b}}. \tag{2.104}$$

Since μ_a^ex represents the energy required to insert an impenetrable disk with radius R_a (at some fixed position) into the system, in the limit $R_a \to \infty$ it must be identical to the reversible work PV_a necessary to create a cavity with volume $V_a = \pi R_a^2$. Therefore, we also have

$$\beta P = \lim_{R_a \to \infty} \frac{\beta\mu_a^\mathrm{ex}}{V_a} = \sum_{w \in \mathbb{W}} \frac{\partial \phi_{\boldsymbol{\rho}_\mathrm{b}}^\mathrm{hd}}{\partial w_{\boldsymbol{\rho}_\mathrm{b}}} \cdot \lim_{R_a \to \infty} \left(\frac{1}{\pi R_a^2} \frac{\partial w_{\boldsymbol{\rho}_\mathrm{b}}}{\partial \rho_a^\mathrm{b}} \right) = \frac{\partial \phi_{\boldsymbol{\rho}_\mathrm{b}}^\mathrm{hd}}{\partial w_{\boldsymbol{\rho}_\mathrm{b}}^2}, \tag{2.105}$$

where we used that

$$\frac{\partial w^0_{\boldsymbol{\rho}^\mathrm{b}}}{\partial \rho^\mathrm{b}_a} = 1, \quad \frac{\partial w^2_{\boldsymbol{\rho}^\mathrm{b}}}{\partial \rho^\mathrm{b}_a} = \pi R_a^2, \quad \frac{\partial \boldsymbol{w}^m_{\boldsymbol{\rho}^\mathrm{b}}}{\partial \rho^\mathrm{b}_a} \propto R_a. \tag{2.106}$$

according to Eq. (2.102). Subtracting Eq. (2.105) from (2.103) gives us

$$\begin{aligned} 0 &= \left(\frac{\partial \phi^\mathrm{hd}_{\boldsymbol{\rho}_\mathrm{b}}}{\partial w^0_{\boldsymbol{\rho}_\mathrm{b}}} + 1\right) w^0_{\boldsymbol{\rho}_\mathrm{b}} + \frac{\partial \phi^\mathrm{hd}_{\boldsymbol{\rho}_\mathrm{b}}}{\partial w^2_{\boldsymbol{\rho}_\mathrm{b}}}(w^2_{\boldsymbol{\rho}_\mathrm{b}} - 1) + \sum_{m=0}^{\infty} \frac{\partial \phi^\mathrm{hd}_{\boldsymbol{\rho}_\mathrm{b}}}{\partial \boldsymbol{w}^m_{\boldsymbol{\rho}_\mathrm{b}}} \cdot \boldsymbol{w}^m_{\boldsymbol{\rho}_\mathrm{b}} - \phi^\mathrm{hd}_{\boldsymbol{\rho}_\mathrm{b}} \\ &= [1 - f'(w^2_{\boldsymbol{\rho}_\mathrm{b}})(1 - w^2_{\boldsymbol{\rho}_\mathrm{b}})]\, w^0_{\boldsymbol{\rho}_\mathrm{b}} + \sum_{m=0}^{\infty} [g_m(w^2_{\boldsymbol{\rho}_\mathrm{b}}) - g'_m(w^2_{\boldsymbol{\rho}_\mathrm{b}})(1 - w^2_{\boldsymbol{\rho}_\mathrm{b}})]\, C_m \boldsymbol{w}^m_{\boldsymbol{\rho}_\mathrm{b}} \cdot \boldsymbol{w}^m_{\boldsymbol{\rho}_\mathrm{b}}, \end{aligned} \tag{2.107}$$

leading to

$$f'(x) \equiv \frac{\mathrm{d}f(x)}{\mathrm{d}x} \stackrel{!}{=} \frac{1}{1-x}, \quad g'_m(x) \equiv \frac{\mathrm{d}g_m(x)}{\mathrm{d}x} \stackrel{!}{=} \frac{g_m(x)}{1-x}. \tag{2.108}$$

Integrating these derivatives yields

$$f(x) = C_f - \ln(1-x) = C_f + x + O(x^2), \quad g_m(x) = \frac{C_g}{1-x} = C_g + O(x), \tag{2.109}$$

with the integration constants $C_f = 0$ and $C_g = 1$ determined by demanding agreement with the expansions (2.100). Inserting these functions into the ansatz (2.99), we arrive at

$$\beta \mathcal{F}^\mathrm{hd}_\mathrm{ex}[\boldsymbol{\rho}] = \int \mathrm{d}^2\vec{r} \left(-w^0_{\boldsymbol{\rho}}(\vec{r}) \ln[1 - w^2_{\boldsymbol{\rho}}(\vec{r})] + \frac{\sum_{m=0}^{\infty} C_m \boldsymbol{w}^m_{\boldsymbol{\rho}}(\vec{r}) \cdot \boldsymbol{w}^m_{\boldsymbol{\rho}}(\vec{r})}{4\pi[1 - w^2_{\boldsymbol{\rho}}(\vec{r})]} \right). \tag{2.110}$$

It is possible to show that, for a uniform hard disk fluid with a single component ($\nu = 1$), this gives rise to the pressure

$$\beta P = \frac{\rho_\mathrm{b}}{(1 - \pi R^2 \rho_\mathrm{b})^2}, \tag{2.111}$$

which is in agreement with the equation of state that can be derived via scaled particle theory (SPT) [50]. Furthermore, in the so-called zero-dimensional limit where the volume of the system is so small that it can hold at most a single disk and the density distribution thus becomes $\rho_{0\mathrm{D}}(\vec{r}) = N\delta(\vec{r})$ with $N \leq 1$, the excess free energy functional correctly evaluates to the exact result

$$\beta \mathcal{F}_\mathrm{ex}[\rho_{0\mathrm{D}}] = N + (1 - N)\ln(1 - N). \tag{2.112}$$

The problem with Eq. (2.110) is that is cannot be used in a numerical context since it involves a sum over infinitely many weighted densities. For this reason, Roth et al. truncated the sum after

the first three terms, leading to

$$\beta\mathcal{F}_{\text{ex}}^{\text{hd}}[\boldsymbol{\rho}] = \int \mathrm{d}^2\vec{r}\left(-w_{\boldsymbol{\rho}}^0(\vec{r})\ln[1-w_{\boldsymbol{\rho}}^2(\vec{r})] + \frac{C_0\,\boldsymbol{w}_{\boldsymbol{\rho}}^0(\vec{r})\cdot\boldsymbol{w}_{\boldsymbol{\rho}}^0(\vec{r}) + C_1\,\boldsymbol{w}_{\boldsymbol{\rho}}^1(\vec{r})\cdot\boldsymbol{w}_{\boldsymbol{\rho}}^1(\vec{r}) + C_2\,\boldsymbol{w}_{\boldsymbol{\rho}}^2(\vec{r})\cdot\boldsymbol{w}_{\boldsymbol{\rho}}^2(\vec{r})}{4\pi[1-w_{\boldsymbol{\rho}}^2(\vec{r})]}\right). \tag{2.113}$$

Unfortunately, with the coefficients specified in Eq. (2.91), this functional satisfies neither the SPT equation of state nor the correct zero-dimensional limit. Instead, one finds

$$\beta P = \frac{\rho_{\text{b}}}{(1-\pi R^2\rho_{\text{b}})^2} + \left(C_0 + \frac{C_2}{2} - 1\right)\rho_{\text{b}}\frac{\pi R^2\rho_{\text{b}}}{(1-\pi R^2\rho_{\text{b}})^2} \tag{2.114}$$

and

$$\beta\mathcal{F}_{\text{ex}}[\rho_{0\text{D}}] = N + (1-N)\ln(1-N) + \frac{C_0+C_1+C_2}{4\pi}\int \mathrm{d}^2\vec{r}\,\frac{[\delta(R-|\vec{r}|)]^2}{1-N\Theta(R-|\vec{r}|)}. \tag{2.115}$$

To recover Eqs. (2.111) and (2.112), Roth et al. adjusted the coefficients so that $C_2 = 2-2C_0$ and $C_1 = -C_0 - C_2 = -C_0 - (2-2C_0) = C_0 - 2$. They then fixed $C_0 = 19/12$ via a least-squares fit of $\omega_a^2\star\omega_b^0 + \omega_a^0\star\omega_b^2 + \frac{1}{2\pi}\left[C_0\,\boldsymbol{\omega}_a^0\star\boldsymbol{\omega}_b^0 + (C_0-2)\,\boldsymbol{\omega}_a^1\star\boldsymbol{\omega}_b^1 + (2-2C_0)\,\boldsymbol{\omega}_a^2\star\boldsymbol{\omega}_b^2\right]$ to $(-f_{ab})$, which resulted in the final excess free energy functional

$$\beta\mathcal{F}_{\text{ex}}^{\text{hd}}[\boldsymbol{\rho}] = \int \mathrm{d}^2\vec{r}\left(-w_{\boldsymbol{\rho}}^0(\vec{r})\ln[1-w_{\boldsymbol{\rho}}^2(\vec{r})] + \frac{19\,\boldsymbol{w}_{\boldsymbol{\rho}}^0(\vec{r})\cdot\boldsymbol{w}_{\boldsymbol{\rho}}^0(\vec{r}) - 5\,\boldsymbol{w}_{\boldsymbol{\rho}}^1(\vec{r})\cdot\boldsymbol{w}_{\boldsymbol{\rho}}^1(\vec{r}) - 14\,\boldsymbol{w}_{\boldsymbol{\rho}}^2(\vec{r})\cdot\boldsymbol{w}_{\boldsymbol{\rho}}^2(\vec{r})}{48\pi[1-w_{\boldsymbol{\rho}}^2(\vec{r})]}\right). \tag{2.116}$$

For a single-component hard sphere *liquid* with bulk packing fractions $\eta_{\text{b}} \equiv \pi R^2\rho_{\text{b}} \lesssim 0.7$, Roth et al. found that DFT results obtained employing the functional (2.116) were in excellent agreement with Monte Carlo simulations.

2.3.3. Random phase approximation

Consider two systems whose intrinsic Hamiltonians $\mathcal{H}_0^{\text{int}}$ and $\mathcal{H}_1^{\text{int}}$ only differ in the pairwise interaction term, i. e., $\mathcal{H}_1^{\text{int}}(\boldsymbol{n},\boldsymbol{q},\boldsymbol{p}) = \mathcal{H}_0^{\text{int}}(\boldsymbol{n},\boldsymbol{q},\boldsymbol{p}) + \Delta\mathcal{U}(\boldsymbol{n},\boldsymbol{q},\boldsymbol{p})$ with

$$\begin{aligned}\Delta\mathcal{U}(\boldsymbol{n},\boldsymbol{q},\boldsymbol{p}) &\equiv \frac{1}{2}\sum_{a=1}^{\nu}\sum_{\substack{b=1\\ a\neq b \text{ or } i\neq j}}^{\nu}\sum_{i=1}^{n_a}\sum_{j=1}^{n_b}\Delta u_{ab}(\vec{q}_{ai},\vec{q}_{bj})\\ &= \frac{1}{2}\sum_{a=1}^{\nu}\sum_{b=1}^{\nu}\int \mathrm{d}^d\vec{r}\int \mathrm{d}^d\vec{r}\,'\,\hat{\rho}_{\vec{r},\vec{r}\,'}^{ab}(\boldsymbol{n},\boldsymbol{q},\boldsymbol{p})\,\Delta u_{ab}(\vec{r},\vec{r}\,'),\end{aligned} \tag{2.117}$$

where

$$\hat{\rho}^{ab}_{\vec{r},\vec{r}'}(\boldsymbol{n},\boldsymbol{q},\boldsymbol{p}) \equiv \sum_{\substack{i=1 \\ a\neq b \text{ or } i\neq j}}^{n_a}\sum_{j=1}^{n_b} \delta(\vec{r}-\vec{q}_{ai})\,\delta(\vec{r}'-\vec{q}_{bj}) \tag{2.118}$$

is the *two-point density operator* at points $\vec{r}$ and $\vec{r}'$ for the species a and b. We then find that the difference of the excess free energy functionals is given by

$$\begin{aligned}\mathcal{F}_1^{\text{ex}}[\boldsymbol{\rho}] - \mathcal{F}_0^{\text{ex}}[\boldsymbol{\rho}] &= \mathcal{F}_1[\hat{\varrho}[\boldsymbol{\rho}]] - \mathcal{F}_0[\hat{\varrho}[\boldsymbol{\rho}]] = \langle \mathcal{H}_1^{\text{int}} + T\mathcal{S}_{\hat{\varrho}[\boldsymbol{\rho}]}\rangle_{\hat{\varrho}[\boldsymbol{\rho}]} - \langle \mathcal{H}_0^{\text{int}} + T\mathcal{S}_{\hat{\varrho}[\boldsymbol{\rho}]}\rangle_{\hat{\varrho}[\boldsymbol{\rho}]} \\ &= \langle \Delta\mathcal{U}\rangle_{\hat{\varrho}[\boldsymbol{\rho}]} = \frac{1}{2}\sum_{a=1}^{\nu}\sum_{b=1}^{\nu}\int \mathrm{d}^d\vec{r}\int \mathrm{d}^d\vec{r}'\,\langle\hat{\rho}^{ab}_{\vec{r},\vec{r}'}\rangle_{\hat{\varrho}[\boldsymbol{\rho}]}\,\Delta u_{ab}(\vec{r},\vec{r}').\end{aligned} \tag{2.119}$$

If the system with $\mathcal{H}_0^{\text{int}}$ acts as a reference for which $\mathcal{F}_0^{\text{ex}}$ is known and we make the mean-field assumption that density correlations can be neglected in the sense that

$$\langle\hat{\rho}^{ab}_{\vec{r},\vec{r}'}\rangle_{\hat{\varrho}[\boldsymbol{\rho}]} \approx \langle\hat{\rho}^{a}_{\vec{r}}\,\rangle_{\hat{\varrho}[\boldsymbol{\rho}]}\langle\hat{\rho}^{b}_{\vec{r}'}\rangle_{\hat{\varrho}[\boldsymbol{\rho}]} = \rho_a(\vec{r})\,\rho_b(\vec{r}'), \tag{2.120}$$

we can approximate the excess free energy functional $\mathcal{F}_1^{\text{ex}}$ for the system of interest as

$$\mathcal{F}_1^{\text{ex}}[\boldsymbol{\rho}] \approx \mathcal{F}_0^{\text{ex}}[\boldsymbol{\rho}] + \frac{1}{2}\sum_{a=1}^{\nu}\sum_{b=1}^{\nu}\int \mathrm{d}^d\vec{r}\int \mathrm{d}^d\vec{r}'\rho_a(\vec{r})\,\rho_b(\vec{r}')\,\Delta u_{ab}(\vec{r},\vec{r}'). \tag{2.121}$$

This gives rise to the *random phase approximation* (RPA) for the *direct two-point correlation function*

$$c^{ab}_{2,1}(\vec{r},\vec{r}') \equiv -\beta\frac{\delta^2\mathcal{F}_1^{\text{ex}}[\boldsymbol{\rho}]}{\delta\rho_a(\vec{r})\,\delta\rho_b(\vec{r}')} \approx c^{ab}_{2,0}(\vec{r},\vec{r}') - \beta\Delta u_{ab}(\vec{r},\vec{r}'). \tag{2.122}$$

For a system with pair potential u, it is expected that $c_2(\vec{r},\vec{r}') \to -\beta u(\vec{r},\vec{r}')$ for $|\vec{r}-\vec{r}'| \to \infty$. Since $c^{ab}_{2,1}(\vec{r},\vec{r}') \to -\beta u^{ab}_0(\vec{r},\vec{r}') - \beta\Delta u_{ab}(\vec{r},\vec{r}') = -\beta u^{ab}_1(\vec{r},\vec{r}')$ for $|\vec{r}-\vec{r}'| \to \infty$, Eq. (2.122) at least offers the correct asymptotic behavior. This implies that Eq. (2.121) should be a reasonable approximation if Δu_{ab} represents a long-ranged perturbation to the pair potential u_0 of the reference system, whereas u_0, and by extension $\mathcal{F}_0^{\text{ex}}$, accounts for most of the short-ranged interaction.

If the reference system consists of hard particles, a more accurate approximation for the density correlations is given by

$$\langle\hat{\rho}^{ab}_{\vec{r},\vec{r}'}\rangle_{\hat{\varrho}[\boldsymbol{\rho}]} \approx \Theta[|\vec{r}-\vec{r}'| - (R_a+R_b)]\,\rho_a(\vec{r})\,\rho_b(\vec{r}') \tag{2.123}$$

as it accounts for the impenetrability of the particles. This then leads to

$$\mathcal{F}_1^{\text{ex}}[\boldsymbol{\rho}] \approx \mathcal{F}_0^{\text{ex}}[\boldsymbol{\rho}] + \frac{1}{2}\sum_{a=1}^{\nu}\sum_{b=1}^{\nu}\int \mathrm{d}^d\vec{r}\int_{|\vec{r}-\vec{r}'|>R_a+R_b} \mathrm{d}^d\vec{r}'\,\rho_a(\vec{r})\,\rho_b(\vec{r}')\,\Delta u_{ab}(\vec{r},\vec{r}'). \tag{2.124}$$

2.4. Critical phenomena

Let us study the phase behavior of a simple three-dimensional model liquid consisting of a single species of hard spheres with radius R that are subject to a long-ranged attractive pair potential $u_{\mathrm{lr}} < 0$ so that

$$\mathcal{F}[\rho] = \mathcal{F}_{\mathrm{hs}}[\rho] + \frac{1}{2}\int_V \mathrm{d}^3\vec{r} \int_{\substack{V \\ |\vec{r}-\vec{r}'|>2R}} \mathrm{d}^3\vec{r}'\rho(\vec{r})\,\rho(\vec{r}')\,u_{\mathrm{lr}}(|\vec{r}-\vec{r}'|), \tag{2.125}$$

according to Eq. (2.124), where $\mathcal{F}_{\mathrm{hs}}$ is the (unspecified) excess free energy functional of the hard sphere system. In the uniform bulk, we therefore have

$$\mathcal{F}[\rho_{\mathrm{b}}] = \mathcal{F}_{\mathrm{hs}}[\rho_{\mathrm{b}}] + \frac{1}{2}\rho_{\mathrm{b}}^2\int_V \mathrm{d}^3\vec{r} \int_{\substack{V \\ |\vec{r}-\vec{r}'|>2R}} \mathrm{d}^3\vec{r}'\,u_{\mathrm{lr}}(|\vec{r}-\vec{r}'|) = \mathcal{F}_{\mathrm{hs}}[\rho_{\mathrm{b}}] - V\rho_{\mathrm{b}}^2\alpha \tag{2.126}$$

with $\alpha \equiv -\frac{1}{2}\int_V \mathrm{d}^3\vec{r}\,u_{\mathrm{lr}}(|\vec{r}|)\,\Theta(|\vec{r}|-2R) > 0$. Using the Carnahan-Starling equation of state for the hard sphere system, the chemical potential is easily calculated as

$$\mu = \frac{1}{V}\frac{\delta\mathcal{F}[\rho_{\mathrm{b}}]}{\delta\rho_{\mathrm{b}}} = \mu_{\mathrm{hs}} - 2\rho_{\mathrm{b}}\alpha = k_{\mathrm{B}}T\ln(\Lambda^3\rho_{\mathrm{b}}) + k_{\mathrm{B}}T\,\frac{8\eta-9\eta^2+3\eta^3}{(1-\eta)^3} - 2\rho_{\mathrm{b}}\alpha \tag{2.127}$$

with the *bulk packing fraction* $\eta_{\mathrm{b}} \equiv (4\pi/3)R^3\rho_{\mathrm{b}}$.

If we plot the chemical potential versus the bulk density for various temperatures, we arrive at the phase diagram depicted in Fig. 2.1. Above a certain critical temperature $T_{\mathrm{c}} \approx 0.0225\,\alpha/(k_{\mathrm{B}}R^3)$, the chemical potential is a strictly increasing function of the bulk density so that for a any value of the chemical potential there exists precisely one corresponding bulk density. If the temperature falls below T_{c}, a van der Waals loop develops and the chemical potential is actually decreasing for a range of bulk densities, $\partial\mu/\partial\rho_{\mathrm{b}} < 0$. Using that

$$\frac{\partial P}{\partial\rho_{\mathrm{b}}} = \rho_{\mathrm{b}}\frac{\partial\mu}{\partial\rho_{\mathrm{b}}} \tag{2.128}$$

as shown in Appendix B, this implies a negative isothermal compressibility

$$\kappa_T \equiv -\frac{1}{V}\left(\frac{\partial V}{\partial P}\right)_T = \frac{1}{\rho_{\mathrm{b}}}\left(\frac{\partial\rho_{\mathrm{b}}}{\partial P}\right)_T = \frac{1}{\rho_{\mathrm{b}}^2}\left(\frac{\partial\rho_{\mathrm{b}}}{\partial\mu}\right)_T. \tag{2.129}$$

However, $\partial\mu/\partial\rho_{\mathrm{b}} < 0$ means that the uniform system is unstable and will immediately undergo a so-called *spinodal decomposition* into domains of different densities. Too see this, let us approximate the change in free energy when a separation into two equally-sized phases with bulk

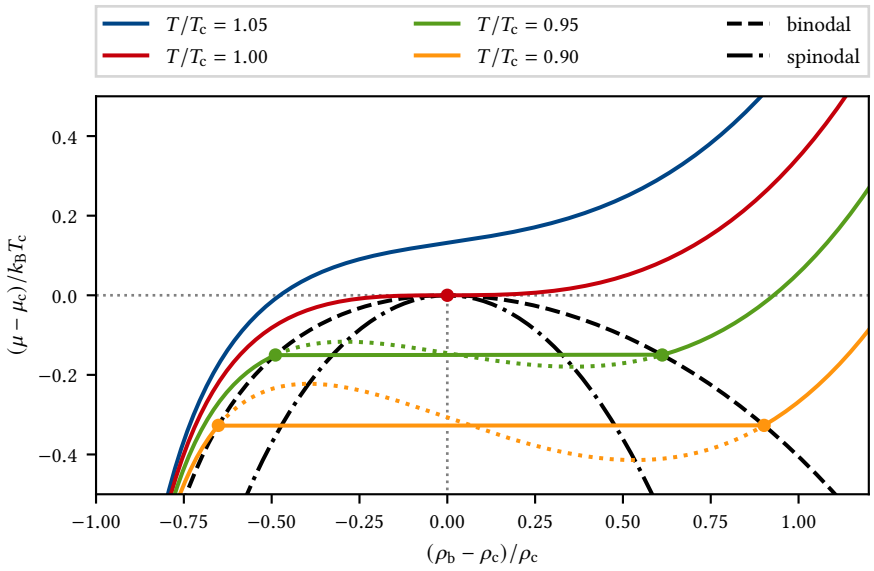

Figure 2.1.: Phase diagram of a model liquid consisting of a single species of hard spheres that are subject to a long-ranged attractive pair potential. The colored curves represent the chemical potential μ according to Eq. (2.127) as a function of the bulk density ρ_b for various temperatures T. Precisely at the critical temperature T_c, the curve has an inflection point point in (ρ_c, μ_c). For $T < T_c$, symbols mark those two states that lie on the binodal (dashed curve) and can therefore coexist because they have equal pressure P in addition to equal temperature and chemical potential. Inside the region enclosed by the binodal, the system phase separates into these states so that μ and P actually remain constant, as indicated by the horizontal lines connecting the symbols. If no phase separation were to occur, van der Waals loops (dotted curves) would develop. The spinodal (dashed-dotted curve) surrounds that part of the phase diagram where the uniform system would have a negative isothermal compressibility κ_T and thus be mechanically unstable; right on the spinodal (and consequently also at the critical point), κ_T diverges.

densities $\rho_- = \rho_b - \Delta\rho$ and $\rho_+ = \rho_b + \Delta\rho$ with $\Delta\rho \ll \rho_b$ occurs. A Taylor expansion gives us

$$\mathcal{F}[\rho_b \pm \Delta\rho] - \mathcal{F}[\rho_b] \approx \pm\frac{\delta\mathcal{F}[\rho_b]}{\delta\rho_b}\Delta\rho + \frac{1}{2}\frac{\delta^2\mathcal{F}[\rho_b]}{\delta\rho_b^2}(\Delta\rho)^2 = \pm V\mu\,\Delta\rho + \frac{V}{2}\frac{\partial\mu}{\partial\rho_b}(\Delta\rho)^2, \quad (2.130)$$

and it follows that

$$\begin{aligned}\Delta\mathcal{F}[\rho_b] &\equiv \frac{\mathcal{F}[\rho_-] + \mathcal{F}[\rho_+]}{2} - \mathcal{F}[\rho_b] = \frac{\mathcal{F}[\rho_b - \Delta\rho] + \mathcal{F}[\rho_b + \Delta\rho]}{2} - \mathcal{F}[\rho_b] \\ &\approx \frac{1}{2}\left(-V\mu\,\Delta\rho + \frac{V}{2}\frac{\partial\mu}{\partial\rho_b}(\Delta\rho)^2 + V\mu\,\Delta\rho + \frac{V}{2}\frac{\partial\mu}{\partial\rho_b}(\Delta\rho)^2\right) = \frac{V}{2}\frac{\partial\mu}{\partial\rho_b}(\Delta\rho)^2 < 0.\end{aligned} \quad (2.131)$$

Hence, decomposition is always energetically favored. In the phase diagram, the stable and unstable regions are separated from each other by the *spinodal* where $\partial\mu/\partial\rho_b = 0$ and $|\kappa_T| \to \infty$.

For $T < T_c$, there exists multiple pairs (ρ_g, ρ_l) of bulk densities outside the spinodal domain with equal chemical potential $\mu(T, \rho_g) = \mu(T, \rho_l)$. Among these, there is exactly one pair that also has equal pressure $P(T, \rho_g) = P(T, \rho_l)$; with Eq. (2.128) and integrating by parts, this condition

translates to

$$\begin{aligned} 0 = P(T,\rho_\mathrm{l}) - P(T,\rho_\mathrm{g}) &= \int_{\rho_\mathrm{g}}^{\rho_\mathrm{l}} \mathrm{d}\rho_\mathrm{b}\, \frac{\partial P(T,\rho_\mathrm{b})}{\partial \rho_\mathrm{b}} = \int_{\rho_\mathrm{g}}^{\rho_\mathrm{l}} \mathrm{d}\rho_\mathrm{b}\, \rho_\mathrm{b} \frac{\partial \mu(T,\rho_\mathrm{b})}{\partial \rho_\mathrm{b}} \\ &= \rho_\mathrm{l}\, \mu(T,\rho_\mathrm{l}) - \rho_\mathrm{g}\, \mu(T,\rho_\mathrm{g}) - \int_{\rho_\mathrm{g}}^{\rho_\mathrm{l}} \mathrm{d}\rho_\mathrm{b}\, \mu(T,\rho_\mathrm{b}) \end{aligned} \tag{2.132}$$

In the phase diagram, the points $(\rho_\mathrm{g}, \rho_\mathrm{l})$ that satisfy $\mu(T,\rho_\mathrm{g}) = \mu(T,\rho_\mathrm{l})$ and $P(T,\rho_\mathrm{g}) = P(T,\rho_\mathrm{l})$ define the *binodal*; they represent two different states – a gaseous phase with lower density ρ_g and a liquid phase with higher density ρ_l – that can coexist alongside each other since they are in thermodynamic equilibrium according to Eq. (2.12). Inside the binodal, the system will always aim to segregate into a gas with volume $V_\mathrm{g} = V(\rho_\mathrm{l} - \rho_\mathrm{b})/(\rho_\mathrm{l} - \rho_\mathrm{g})$ and into a liquid with volume $V_\mathrm{l} = V(\rho_\mathrm{b} - \rho_\mathrm{g})/(\rho_\mathrm{l} - \rho_\mathrm{g})$ because this results in the lowest Helmholtz free energy; hence, the chemical potential actually remains constant for bulk densities between ρ_g and ρ_l as indicated by the horizontal segments in the phase diagram.

Right at the critical temperature $T = T_\mathrm{c}$, the curve of the chemical potential has an inflection point at the critical bulk density $\rho_\mathrm{c} \approx 0.0311/R^3$ characterized by

$$\left(\frac{\partial \mu(T,\rho_\mathrm{b})}{\partial \rho_\mathrm{b}}\right)_\mathrm{c} = 0 = \left(\frac{\partial^2 \mu(T,\rho_\mathrm{b})}{\partial \rho_\mathrm{b}^2}\right)_\mathrm{c}. \tag{2.133}$$

As we will show in the following section, this has very remarkable consequences for the behavior of a system close to criticality.

2.4.1. Universal behavior

To understand the behavior near a critical point, we shall roughly follow Hansen and McDonald [51]. Using the condition (2.133), a Taylor expansion of the chemical potential around the critical temperature T_c and density ρ_c up to the lowest non-vanishing order in T and ρ_b gives

$$\mu(T,\rho_\mathrm{b}) = \mu_\mathrm{c} + \mu_\mathrm{c}^{(1,0)}\,(T - T_\mathrm{c}) + \mu_\mathrm{c}^{(1,1)}\,(T - T_\mathrm{c})\,(\rho_\mathrm{b} - \rho_\mathrm{c}) + \frac{1}{6}\mu_\mathrm{c}^{(0,3)}\,(\rho_\mathrm{b} - \rho_\mathrm{c})^3, \tag{2.134}$$

where $\mu_\mathrm{c} \equiv \mu(T_\mathrm{c},\rho_\mathrm{c})$ is the critical chemical potential and $\mu_\mathrm{c}^{(k,l)} \equiv [\partial^{k+l}\mu(T,\rho_\mathrm{b})/(\partial T^k\, \partial \rho^l)]_\mathrm{c}$. Thus,

$$\frac{1}{\kappa_T} = \rho_\mathrm{b}^2 \left(\frac{\partial \mu(T,\rho_\mathrm{b})}{\partial \rho_\mathrm{b}}\right)_T = \rho_\mathrm{b}^2 \left[\mu_\mathrm{c}^{(1,1)}(T - T_\mathrm{c}) + \frac{1}{2}\mu_\mathrm{c}^{(0,3)}(\rho_\mathrm{b} - \rho_\mathrm{c})^2\right]. \tag{2.135}$$

Suppose that the system is at the critical density, $\rho_\mathrm{b} = \rho_\mathrm{c}$, and slightly above the critical temperature, $T > T_\mathrm{c}$. If the temperature is lowered toward T_c, then

$$\frac{1}{\kappa_T} = \rho_\mathrm{c}^2 \mu_\mathrm{c}^{(1,1)} |T - T_\mathrm{c}| \tag{2.136}$$

from which we can deduce that the isothermal compressibility diverges as $\kappa_T \propto |T - T_c|^{-1}$. If the system is at $\rho_b = \rho_c$ but below the critical temperature, $T < T_c$, it will separate into a gaseous phase with density ρ_g and a liquid phase with density ρ_l. From the form of (2.134), it is clear that $\mu(T, \rho_g) = \mu(T, \rho_l)$ and $P(T, \rho_g) = P(T, \rho_l)$ can only be satisfied if ρ_g and ρ_l are symmetrical in the vicinity of ρ_c, i. e., $\rho_g = \rho_c - \Delta\rho$ and $\rho_l = \rho_c + \Delta\rho$ for some $\Delta\rho > 0$. Demanding

$$0 = \mu(T, \rho_c + \Delta\rho) - \mu(T, \rho_c - \Delta\rho) = 2\mu_c^{(1,1)}(T - T_c)\,\Delta\rho + \frac{1}{3}\mu^{(0,3)}(\Delta\rho)^3, \tag{2.137}$$

we can easily solve for $\Delta\rho$ and find that

$$|\rho_{g/l} - \rho_c| = \Delta\rho = \sqrt{6\frac{\mu_c^{(1,1)}}{\mu_c^{(0,3)}}|T - T_c|} \propto |T - T_c|^{1/2}. \tag{2.138}$$

Therefore,

$$\frac{1}{\kappa_T} = (\rho_c \pm \Delta\rho)^2 \left[\mu_c^{(1,1)}(T - T_c) + \frac{1}{2}\mu_c^{(0,3)}(\Delta\rho)^2\right] = 2\rho_c^2\mu_c^{(1,1)}|T - T_c| + O\left(|T - T_c|^{3/2}\right) \tag{2.139}$$

and again $\kappa_T \propto |T - T_c|^{-1}$.

We can see that close to the critical point, certain quantities such as κ_T or $|\rho_{g/l} - \rho_c|$ acquire a power-law dependence on the reduced temperature

$$T_* \equiv \frac{T - T_c}{T_c} \tag{2.140}$$

such that $\kappa_T \propto |T_*|^{-\gamma}$ and $|\rho_{g/l} - \rho_c| \propto |T_*|^{\beta}$ with suitable *critical exponents* γ and β. While the corresponding proportionality constants depend on the microscopic details, the critical exponents are actually shared by a whole set of systems that together form a *universality class*.

Interestingly, a universality class may even contain seemingly unrelated systems. For example, consider the phase diagram of the Ising model shown in Fig. 2.2, which plots the strength of an external magnetic field B versus the average magnetization M of the Ising spins for various temperatures. We see that there exists a critical temperature T_c such that $M_0 \equiv M(B = 0) = 0$ for $T \geq T_c$ and $M_0 \neq 0$ for $T < T_c$. For $T = T_c$, B has an inflection point at $M = 0$. This is essentially equivalent to the phase diagram of our model liquid (Fig. 2.1) if we associate $B \mathrel{\hat{=}} \mu - \mu_c$, $M \mathrel{\hat{=}} \rho - \rho_c$, $M_0 \mathrel{\hat{=}} \rho_{g/l} - \rho_c$ and $\chi_T \equiv (\partial M/\partial B)_T \mathrel{\hat{=}} \kappa_T$. Near the critical point, one indeed finds with the same reasoning that $|M_0| \propto |T_*|^{1/2}$ and $\chi_T \propto |T_*|^{-1}$, i. e., the Ising and fluid model belong to the same universality class.

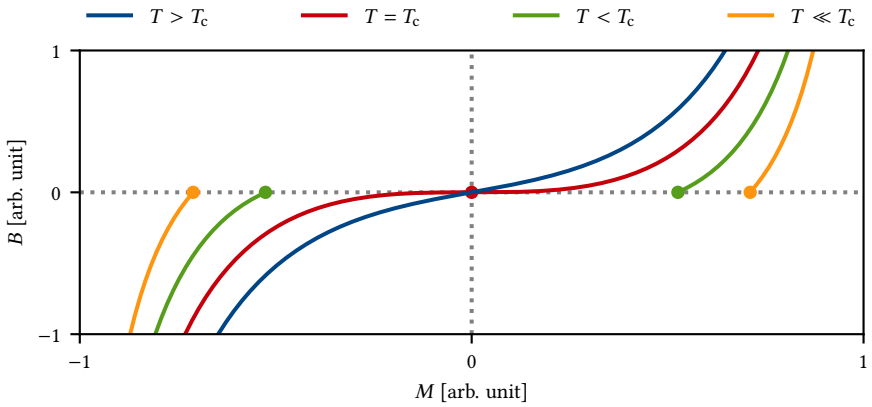

Figure 2.2.: Schematic phase diagram of the Ising model, plotting the strength B of an external magnetic field versus the average magnetization M of the Ising spins. There exists a critical temperature T_c such that $M_0 \equiv M(B = 0) = 0$ for $T \geq T_c$ and $M_0 \neq 0$ for $T < T_c$. For $T = T_c$, B has an inflection point at $M = 0$. Note the similarities to the phase diagram of the model liquid (Fig. 2.1) if we associate $B \mathrel{\hat{=}} \mu - \mu_c$ and $M \mathrel{\hat{=}} \rho - \rho_c$.

2.4.2. Fluctuations and correlations

The isothermal compressibility κ_T is linked to the particle number fluctuations $\langle (\mathcal{N} - N)^2 \rangle$ via

$$\begin{aligned}
\rho_b k_B T \kappa_T &= \frac{k_B T}{\rho_b} \frac{\partial \rho_b}{\partial \mu} = \frac{k_B T}{N} \frac{\partial N}{\partial \mu} = \frac{k_B T}{N} \frac{\partial^2 \Omega}{\partial \mu^2} = \frac{(k_B T)^2}{N} \frac{\partial^2 \ln \mathcal{Z}_{gc}}{\partial \mu^2} \\
&= \frac{(k_B T)^2}{N} \left[\frac{1}{\mathcal{Z}_{gc}} \frac{\partial^2 \mathcal{Z}_{gc}}{\partial \mu^2} - \left(\frac{1}{\mathcal{Z}_{gc}} \frac{\partial \mathcal{Z}_{gc}}{\partial \mu} \right)^2 \right] = \frac{(k_B T)^2}{N} \left[\beta^2 \langle \mathcal{N}^2 \rangle - (\beta \langle \mathcal{N} \rangle)^2 \right] \\
&= \frac{\langle \mathcal{N}^2 \rangle - N^2}{N} = \frac{\langle (\mathcal{N} - N)^2 \rangle}{N}.
\end{aligned} \tag{2.141}$$

Let us now define the *total two-point correlation function* as

$$h_2(\vec{r}, \vec{r}\,') \equiv \frac{\langle \hat{\rho}^{(2)}_{\vec{r},\vec{r}\,'} \rangle}{\langle \hat{\rho}_{\vec{r}} \rangle \langle \hat{\rho}_{\vec{r}\,'} \rangle} - 1 = \frac{\rho^{(2)}(\vec{r}, \vec{r}\,')}{\rho(\vec{r}) \rho(\vec{r}\,')} - 1, \tag{2.142}$$

where $\rho^{(2)}(\vec{r}, \vec{r}\,') \equiv \langle \hat{\rho}^{(2)}_{\vec{r},\vec{r}\,'} \rangle$ and

$$\hat{\rho}^{(2)}_{\vec{r},\vec{r}\,'}(n, \boldsymbol{q}, \boldsymbol{p}) \equiv \sum_{i=1}^{n} \sum_{\substack{j=1 \\ j \neq i}}^{n} \delta(\vec{r} - \vec{q}_i)\, \delta(\vec{r}\,' - \vec{q}_j) = \hat{\rho}_{\vec{r}}(n, \boldsymbol{q}, \boldsymbol{p}) \left[\hat{\rho}_{\vec{r}\,'}(n, \boldsymbol{q}, \boldsymbol{p}) - \delta(\vec{r} - \vec{r}\,') \right] \tag{2.143}$$

is identical to the two-point density operator (2.118) if the system consists of only one species. Furthermore, let

$$c_2(\vec{r}, \vec{r}\,') \equiv -\beta \frac{\delta^2 \mathcal{F}_{ex}[\rho]}{\delta \rho(\vec{r}\,') \delta \rho(\vec{r})}. \tag{2.144}$$

be the *direct two-point correlation function*. As shown in Appendix C, h_2 and c_2 are connected through the Ornstein–Zernike relation

$$h_2(\vec{r},\vec{r}') = c_2(\vec{r},\vec{r}') + \int \mathrm{d}^d\vec{r}''\, c_2(\vec{r},\vec{r}'')\,\rho(\vec{r}'')\,h_2(\vec{r}'',\vec{r}'). \tag{2.145}$$

In the uniform bulk with $\rho = \rho_\mathrm{b}$, we can expect that $h_2(\vec{r},\vec{r}')$ and $c_2(\vec{r},\vec{r}')$ only depend on the relative vector $\vec{r}-\vec{r}'$, i. e., $h_2(\vec{r},\vec{r}') = h_2(\vec{r}-\vec{r}')$ and $c_2(\vec{r},\vec{r}') = c_2(\vec{r}-\vec{r}')$, in which case Eq. (2.145) can be written as

$$\begin{aligned} h_2(\vec{r}-\vec{r}') &= c_2(\vec{r}-\vec{r}') + \rho_\mathrm{b}\int \mathrm{d}^d\vec{r}''\, c_2(\vec{r}-\vec{r}'')\,h_2(\vec{r}''-\vec{r}') \\ &= c_2(\vec{r}-\vec{r}') + \rho_\mathrm{b}(c_2\otimes h_2)(\vec{r}-\vec{r}'), \end{aligned} \tag{2.146}$$

where "$\otimes$" denotes convolution. Employing the convolution theorem, this translates to the simple expression

$$\tilde{h}_2(\vec{k}) = \tilde{c}_2(\vec{k}) + \rho_\mathrm{b}\tilde{c}_2(\vec{k})\tilde{h}_2(\vec{k}) \tag{2.147}$$

in Fourier space, which can be easily solved for either $\tilde{c}_2$ or $\tilde{h}_2$ to give

$$\tilde{c}_2(\vec{k}) = \frac{\tilde{h}_2(\vec{k})}{1+\rho_\mathrm{b}\tilde{h}_2(\vec{k})}, \quad \tilde{h}_2(\vec{k}) = \frac{\tilde{c}_2(\vec{k})}{1-\rho_\mathrm{b}\tilde{c}_2(\vec{k})}. \tag{2.148}$$

If we define the Fourier transform of the *static structure factor* as

$$\tilde{S}(\vec{k}) \equiv 1+\rho_\mathrm{b}\tilde{h}_2(\vec{k}) = \frac{1}{1-\rho_\mathrm{b}\tilde{c}_2(\vec{k})} \tag{2.149}$$

and make use of

$$\begin{aligned} \int \mathrm{d}^d\vec{r}\int \mathrm{d}^d\vec{r}'\,\rho^{(2)}(\vec{r},\vec{r}') &= \int \mathrm{d}^d\vec{r}\int \mathrm{d}^d\vec{r}'\langle\hat{\rho}_{\vec{r}}[\hat{\rho}_{\vec{r}'}-\delta(\vec{r}-\vec{r}')]\rangle \\ &= \langle\textstyle\int \mathrm{d}^d\vec{r}\hat{\rho}_{\vec{r}}\int \mathrm{d}^d\vec{r}'\hat{\rho}_{\vec{r}'}\rangle - \langle\int \mathrm{d}^d\vec{r}\hat{\rho}_{\vec{r}}\int \mathrm{d}^d\vec{r}'\delta(\vec{r}-\vec{r}')]\rangle \\ &= \langle\mathcal{N}^2\rangle - N = N(\rho_\mathrm{b}k_\mathrm{B}T\kappa_T - 1 + N), \end{aligned} \tag{2.150}$$

we find that

$$\begin{aligned} \tilde{S}(0) &= 1+\rho_\mathrm{b}\tilde{h}_2(0) = 1+\rho_\mathrm{b}\int \mathrm{d}^d\vec{r}\,h_2(\vec{r}) = 1+\frac{\rho_\mathrm{b}}{V}\int \mathrm{d}^d\vec{r}\int \mathrm{d}^d\vec{r}'\,h_2(\vec{r},\vec{r}') \\ &= 1+\frac{\rho_\mathrm{b}^2}{N}\int \mathrm{d}^d\vec{r}\int \mathrm{d}^d\vec{r}'\left[\frac{\rho^{(2)}(\vec{r},\vec{r}')}{\rho_\mathrm{b}^2}-1\right] = 1+\frac{\rho_\mathrm{b}^2}{N}\left[\frac{N(\rho_\mathrm{b}k_\mathrm{B}T\kappa_T-1+N)}{\rho_\mathrm{b}^2}-V^2\right] \\ &= \rho_\mathrm{b}k_\mathrm{B}T\kappa_T. \end{aligned} \tag{2.151}$$

The interpretation of this result is straightforward: if κ_T diverges, then so does $\tilde{S}(0)$, which means that the density correlations quantified by h_2 must become sufficiently long-ranged so that $\int \mathrm{d}^d\vec{r}\, h_2(\vec{r}) \to \infty$.

Let us now determine how h_2 behaves asymptotically for large arguments. In the uniform bulk, we can actually make the even stronger assumption that h_2 and c_2 are radially symmetric, i. e., $h_2(\vec{r},\vec{r}') = h_2(|\vec{r}-\vec{r}'|)$ and $c_2(\vec{r},\vec{r}') = c_2(|\vec{r}-\vec{r}'|)$. Consequently, $\tilde{h}_2(\vec{k}) = \tilde{h}_2(|\vec{k}|)$ and $\tilde{c}_2(\vec{k}) = \tilde{c}_2(|\vec{k}|)$. Using Eq. (2.148), the inverse Fourier transform from $\tilde{h}_2$ back to h_2 for a three-dimensional system is given by

$$\begin{aligned} h_2(r) &= \frac{1}{(2\pi)^3}\int_0^{2\pi}\mathrm{d}\varphi\int_0^{\pi}\mathrm{d}\vartheta\int_0^{k}\mathrm{d}k\,k^2\sin\vartheta\exp(\mathrm{i}kr\cos\vartheta)\,\tilde{h}_2(k) \\ &= \frac{1}{4\pi^2\mathrm{i}r}\int_0^{\infty}\mathrm{d}k\,k\,[\exp(\mathrm{i}kr)-\exp(-\mathrm{i}kr)]\,\tilde{h}_2(k) = \frac{1}{4\pi^2\mathrm{i}r}\int_{-\infty}^{\infty}\mathrm{d}k\,k\exp(\mathrm{i}kr)\,\tilde{h}_2(k) \\ &= \frac{1}{4\pi^2\mathrm{i}r}\int_{-\infty}^{\infty}\mathrm{d}k\,\frac{k\exp(\mathrm{i}kr)\,\tilde{c}_2(k)}{1-\rho_\mathrm{b}\tilde{c}_2(k)} = \frac{1}{4\pi^2\mathrm{i}r}\int_{\partial\mathbb{C}_+}\mathrm{d}k\,\frac{k\exp(\mathrm{i}kr)\,\tilde{c}_2(k)}{1-\rho_\mathrm{b}\tilde{c}_2(k)}. \end{aligned} \tag{2.152}$$

In the last step, we expressed the integral as a contour integral around the upper complex half-plane $\mathbb{C}_+ \equiv \{z\in\mathbb{C} : \mathrm{Im}(z) > 0\}$. Assuming that $\tilde{c}_2$ is an analytic function, we can use the residue theorem to evaluate this integral to

$$h_2(r) = -\frac{1}{2\pi r}\sum_{k_0\in\mathbb{K}}\frac{k_0\exp(\mathrm{i}k_0r)\tilde{c}_2(k_0)}{\rho_\mathrm{b}\tilde{c}_2'(k_0)} = -\frac{1}{2\pi r}\sum_{k_0\in\mathbb{K}}\frac{k_0\exp(\mathrm{i}k_0r)}{\rho_\mathrm{b}^2\tilde{c}_2'(k_0)}, \tag{2.153}$$

where $\mathbb{K} \equiv \{k_0\in\mathbb{C}_+ : 1-\rho_\mathrm{b}\tilde{c}_2(k_0) = 0\}$. For large r, the dominant contribution comes from the $k_0\in\mathbb{K}$ which has the smallest imaginary part, since that one is associated with the slowest exponential decay. It therefore makes sense to perform a Taylor expansion of $\tilde{c}_2$ around $k = 0$,

$$\tilde{c}_2(k) = \tilde{c}_2(0) + \frac{1}{2}\tilde{c}_2''(0)\,k^2 + O(k^4), \tag{2.154}$$

where terms with odd powers of k vanish due to the radial symmetry of c_2. Demanding that

$$0 = 1-\rho_\mathrm{b}\tilde{c}_2(\mathrm{i}k_0) = 1-\rho_\mathrm{b}\tilde{c}_2(0) - \rho_\mathrm{b}\frac{1}{2}\tilde{c}_2''(0)(\mathrm{i}k_0)^2 = 1-\rho_\mathrm{b}\tilde{c}_2(0) + \rho_\mathrm{b}\frac{1}{2}\tilde{c}_2''(0)\,k_0^2, \tag{2.155}$$

we have $\mathbb{K} = \{\mathrm{i}k_0\}$ with

$$k_0 = \sqrt{-2\frac{1-\rho_\mathrm{b}\tilde{c}_2(0)}{\rho_\mathrm{b}\tilde{c}_2''(0)}} = \sqrt{-\frac{2}{\rho_\mathrm{b}\tilde{S}(0)\tilde{c}_2''(0)}} = \sqrt{\frac{2}{\rho_\mathrm{b}^2 k_\mathrm{B}T|\tilde{c}_2''(0)|\kappa_T}}. \tag{2.156}$$

Note that we require $\tilde{c}_2''(0) < 0$ in order to satisfy $\mathrm{i}k_0\in\mathbb{C}_+$. Inserting this into Eq. (2.153), we arrive at

$$h_2(r) \to -\frac{\exp(-k_0r)}{2\pi r\rho_\mathrm{b}^2\tilde{c}_2''(0)} = \frac{1}{2\pi\rho_\mathrm{b}^2|\tilde{c}_2''(0)|}\frac{\exp(-r/\xi)}{r} \quad \text{for } r\to\infty, \tag{2.157}$$

where

$$\xi \equiv \frac{1}{k_0} = \sqrt{\frac{1}{2}\rho_\mathrm{b}^2 k_\mathrm{B} T |\tilde{c}_2''(0)| \kappa_T} \tag{2.158}$$

is the *correlation length* which diverges as $\xi \propto \sqrt{\kappa_T} \propto \sqrt{|T - T_\mathrm{c}|^{-1}} = |T - T_\mathrm{c}|^{-1/2} \propto |T_*|^{-\nu}$ with $\nu \equiv 1/2$. This agrees with our hypothesis that the density correlations become long-ranged and that $\int \mathrm{d}^3\vec{r}\, h_2(\vec{r}) \to \infty$ as $\kappa_T \to \infty$.

Experimental evidence of the increasing density fluctuations on approaching the critical point can be observed with the naked eye. If the temperature of a liquid at critical density is lowered towards T_c, a precursor of macroscopic phase separation progressively sets in where the liquid forms small fluid or vaporous droplets whose diameters are on the order of the correlation length ξ. As $T \to T_\mathrm{c}$, these droplets will grow because $\xi \to \infty$ and eventually become comparable in size to the wavelength of visible light, at which point they start to scatter the light that passes through them. As a consequence, the liquid appears milky and iridescent near the critical point: a phenomenon which is known as *critical opalescence* [52].

At the end of the day, the divergence of the correlation length near the critical point is the fundamental reason behind the similarity of the critical behavior of systems belonging to the same universality class. As ξ increases, it becomes the only significant length scale of these systems and the relevance of the microscopic details diminishes. This implies a scale-invariance in the sense that a "coarse-grained" picture of the system with a reduced number of degrees of freedom should be self-similar to the microscopic one, which has led to the development of scaling concepts by Widom [53] and Kadanoff [54].

It should be noted that the critical exponents derived so far ($\beta = 1/2$, $\gamma = 1$, $\nu = 1/2$) are not accurate for d-dimensional systems with $d < 4$. This is due to the negligence of correlations inherent in the mean-field approximation (2.125), which is not appropriate in the critical regime. It is possible to overcome this issue within the renormalization group theory introduced by Wilson, who shows that the mean-field exponents are actually correct for $d \geq 4$ and provides an expansion for the critical exponents in powers of $(4 - d)$ that can be used to extrapolate the results for $d = 4$ to lower dimensions [55]. Up to second order in $(4 - d)$ one finds that

$$\begin{aligned}
\beta_d &\approx \frac{1}{2} - \frac{(4-d)}{6} + \frac{(4-d)^2}{162} &&\rightsquigarrow \quad \beta_3 \approx 0.34, \\
\gamma_d &\approx 1 + \frac{(4-d)}{6} + \frac{25\,(4-d)^2}{324} &&\rightsquigarrow \quad \gamma_3 \approx 1.24, \\
\nu_d &\approx \frac{1}{2} + \frac{(4-d)}{12} + \frac{7\,(4-d)^2}{162} &&\rightsquigarrow \quad \gamma_3 \approx 0.63,
\end{aligned} \tag{2.159}$$

which is in very good agreement with experimental results.

2.4.3. Critical Casmir effect

Imagine two uncharged, perfectly conducting parallel plates with surface area A separated by a distance L inside a vacuum. One might be tempted to think that the plates will not interact with each other (except through gravity). Surprisingly however, as postulated by Casimir in 1948 [56] and finally confirmed almost half a century later in experiments by Lamoreaux [57], the plates are indeed subject to another force that arises due to the always present quantum and/or thermal fluctuations of the electromagnetic field. Because the plates impose certain boundary conditions on the field, only very specific eigenmodes are allowed in between them. This then effectively leads to a reduction of the average energy $\langle E(L)\rangle$ of the system that becomes more pronounced as L decreases, and is in the limit $A \to \infty$ given by

$$\langle E(L)\rangle = \begin{cases} \langle E(\infty)\rangle - A\dfrac{\pi}{1440}\dfrac{hc}{L^3} & \text{if } T = 0, \quad (2.160a) \\ \langle E(\infty)\rangle - A\dfrac{\zeta(3)}{8\pi}\dfrac{k_\mathrm{B}T}{L^2} & \text{if } k_\mathrm{B}T \gg \frac{hc}{L}, \quad (2.160b) \end{cases}$$

where h is the Planck constant, c the speed of light in vacuum and $\zeta(3) \approx 1.202$ [58]. It follows that there exists a *Casimir force* $K_\mathrm{cas}(L) \equiv -\mathrm{d}\langle E(L)\rangle/\mathrm{d}L < 0$ that pushes the plates together.

In 1978, Fisher and de Gennes predicted a thermodynamic analog of this phenomenon when two plates are immersed in a binary mixture that is near its critical point [59]. A binary mixture consists of two different liquids that, depending on their composition c and the temperature T, either blend to form a homogeneous solution, or separate into two coexisting phases rich in one or the other component. Such a mixture may have both a lower and an upper critical temperature. Below (above) the lower (upper) critical temperature, the mixture is homogeneous for all compositions; above (below), it will phase separate if the composition is within a certain range. The lower (upper) critical temperature has a corresponding critical composition that marks the minimum (maximum) of the binodal in a c–T phase diagram; see Fig. 2.3. In the following

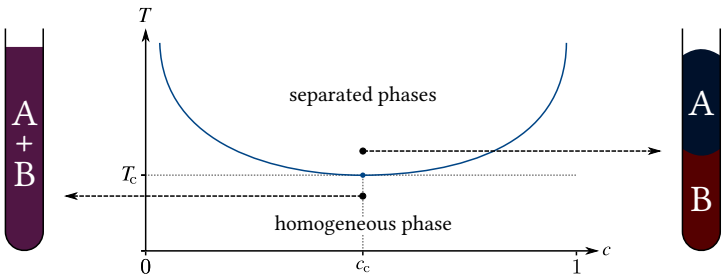

Figure 2.3.: Schematic phase diagram of a binary mixture, consisting of liquids A and B, near its lower critical temperature T_c. Below T_c, the mixture is homogeneous for all compositions c; above T_c, it will separate into an A-rich and B-rich phase if the composition lies within the coexistence region enclosed by the binodal (solid blue curve). The minimum of the binodal defines the lower critical point $(c_\mathrm{c}, T_\mathrm{c})$.

discussion, we shall – without loss of generality – only focus on the lower critical point (T_c, c_c).

We can essentially picture the demixing process of a binary mixture as both components undergoing a liquid–vapor separation simultaneously, during which the liquid phase of one component merges with the vapor phase of the other. From this point of view it should be clear that the critical behavior of a binary mixture is qualitatively identical to that of a pure substance, and that both systems must therefore belong to the same universality class. In particular, the composition fluctuations in a binary mixture become long-ranged as $T \longrightarrow T_c$ and the associated correlation length diverges as $\xi \sim \xi_0 |T_*|^{-\nu}$ with a material constant ξ_0 and $\nu \approx 0.63$ in three dimensions.

Let us now think about how the Helmholtz free energy F changes when we insert two parallel plates into a homogeneous binary mixture at critical composition, $c = c_c$, and below the critical temperature, $T < T_c$. Due to the interaction of the plates with the surrounding particles, we would expect a correction term that is proportional to the surface area A; the corresponding conjugate quantity is the *surface tension* γ which depends on the specific mixture and surface properties. Thus, in the general case that the plates are made out of different materials, we have

$$F_{||} = F_b + A\,\gamma_1 + A\,\gamma_2, \tag{2.161}$$

where F_b denotes the bulk Helmholtz free energy of the binary mixture. This appears like a reasonable assumption – at least if the plate separation L is much larger than the mixture's molecules so that depletion effects are negligible.

Depending on the material, the plates will typically show an adsorption preference for one or the other component of the binary mixture, which means that the concentration of the favored component will be significantly higher in the vicinity of the plate. Under normal circumstances, the resulting local deviation of the concentration profile from the bulk is very short-ranged and quickly decays. However, as the temperature approaches T_c and the correlation length diverges, the plates' influence on the medium will be increasingly far-reaching so that they eventually start to feel each other's presence and can no longer be considered independent entities. This fluctuation-induced interaction between the plates is known as the *critical Casimir effect* and has to be incorporated into $F_{||}$ through an additional contribution F_{cas}. From the universal character of critical behavior, we can infer that F_{cas} must be universal itself and cannot depend on microscopic details. Right at the critical point where ξ is infinite, the only macroscopic measures that can factor into F_{cas} are A, L, $k_B T$ and a universal, dimensionless *Casimir amplitude*

$$\Delta_{||} \equiv \begin{cases} \Delta_{||}^{\pm\pm} & \text{if both surfaces favor the same component,} \\ \Delta_{||}^{\pm\mp} & \text{otherwise,} \end{cases} \tag{2.162}$$

that accounts for the adsorption preference of the surfaces [60]. Since we can expect that F_{cas}

increases linearly with A and decreases with L, the only viable combination with the correct dimensions of energy is

$$F_{||}^{\mathrm{cas}}(L) = k_{\mathrm{B}}T\frac{A}{L^2}\Delta_{||}. \tag{2.163}$$

Adding this term to (2.161), we find that

$$F_{||}(L) = F_{\mathrm{b}} + A\,\gamma_1 + A\,\gamma_2 + F_{||}^{\mathrm{cas}}(L) = F_{||}(\infty) + k_{\mathrm{B}}T_{\mathrm{c}}\frac{A}{L^2}\Delta_{||}, \tag{2.164}$$

in complete analogy to Eq. (2.160b) for the quantum-mechanical Casimir effect.

Slightly below the critical temperature, ξ is finite but large and therefore another macroscopic quantity that enters into $F_{||}^{\mathrm{cas}}$. Due to scale-invariance, $F_{||}^{\mathrm{cas}}$ should only depend on ξ through some scaling function $\Theta_{||}$ of the dimensionless ratio L/ξ, so that [61]

$$F_{||}^{\mathrm{cas}}(L) = k_{\mathrm{B}}T\frac{A}{L^2}\Theta_{||}\left(\frac{L}{\xi}\right) = k_{\mathrm{B}}T\frac{A}{L^2}\Theta_{||}\left(\frac{L}{\xi_0|T_*|^{-\nu}}\right) = k_{\mathrm{B}}T\frac{A}{L^2}\Theta_{||}\left(\frac{L}{\xi_0}\left|\frac{T-T_{\mathrm{c}}}{T_{\mathrm{c}}}\right|^{\nu}\right). \tag{2.165}$$

To recover Eq. (2.163) for $T = T_{\mathrm{c}}$ and $F_{||}^{\mathrm{cas}} = 0$ for $T \ll T_{\mathrm{c}}$, we require that $\Theta_{||}(0) = \Delta_{||}$ and $\Theta_{||}(x) \to 0$ for $x \to \infty$. Like the Casimir amplitude $\Delta_{||}$, the scaling function $\Theta_{||}$ is dependent on the boundary conditions imposed by the surfaces. In the critical regime, the Helmholtz free energy thus amounts to

$$F_{||}(L) = F_{\mathrm{b}} + A\,\gamma_1 + A\,\gamma_2 + F_{||}^{\mathrm{cas}}(L) = F_{||}(\infty) + k_{\mathrm{B}}T\frac{A}{L^2}\Theta_{||}\left(\frac{L}{\xi_0}\left|\frac{T-T_{\mathrm{c}}}{T_{\mathrm{c}}}\right|^{\nu}\right), \tag{2.166}$$

which gives rise to the critical Casimir force

$$K_{||}^{\mathrm{cas}}(L) \equiv -\frac{\mathrm{d}F_{||}(L)}{\mathrm{d}L} = k_{\mathrm{B}}T\frac{A}{L^3}\theta_{||}\left(\frac{L}{\xi}\right) = k_{\mathrm{B}}T\frac{A}{L^3}\theta_{||}\left(\frac{L}{\xi_0}\left|\frac{T-T_{\mathrm{c}}}{T_{\mathrm{c}}}\right|^{\nu}\right) \tag{2.167}$$

with $\theta_{||}(x) \equiv 2\Theta_{||}(x) - x\Theta'_{||}(x)$. The sign of $K_{||}^{\mathrm{cas}}$ ultimately depends on the scaling function $\Theta_{||}$ and hence on the boundary conditions; it turns out that plates which favor the same component experience an attraction, whereas those with opposite adsorption preferences repel each other.

Obtaining theoretical predictions for the scaling functions is a non-trivial task for which several different approaches have been devised. As already mentioned, the critical behavior in four or more dimensions can be exactly described with mean-field theory, which allows the derivation of exact expressions for the scaling functions [62]. The critical Casimir effect can also be observed in the Ising model, which belongs to the same universality class as a simple fluid or a binary mixture and therefore shares the same scaling functions; in two dimensions, these can be determined exactly using transfer-matrix methods [63]. In three dimensions, numerical approximations of the scaling functions have been computed via Monte Carlo simulations of the Ising model in combination with a thermodynamic integration scheme [64].

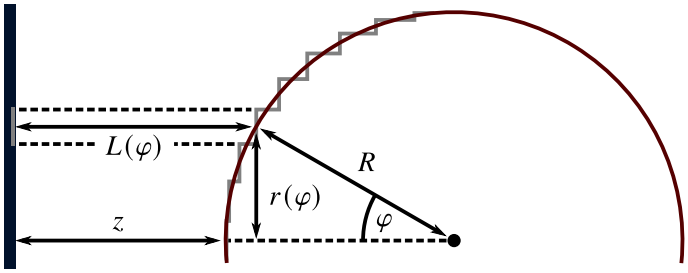

Figure 2.4.: Illustration of the Derjaguin approximation for the critical Casimir interaction between a flat plate (blue) and a sphere (red) with radius R. The surface of the sphere is decomposed into thin annuli (indicated in gray) that lie parallel to the plate. Each annulus is assumed to interact with a corresponding annulus on the plate's surface (also in gray) according to Eq. (2.165). One then takes the limit of infinitesimally thin annuli and integrates over all contributions, leading to Eq. (2.169).

The parallel plate geometry is only a special case that is nonetheless very important from a theoretical standpoint because the critical Casimir interaction is particularly easy to describe due to the symmetry of the setup. Of course, critical Casimir forces will in general act between all kinds of surfaces with a potentially complicated dependence on their shape, orientation and adsorption preferences. Since parallel plates are very difficult to realize in practice, experimental studies of the critical Casimir effect usually involve either a sphere in front of a flat surface, or two spheres. For these two situations, we can use the *Derjaguin approximation* to derive an expression for the critical Casimir interaction if the scaling function $\Theta_{||}$ of the parallel plate geometry is known [65].

Let us first consider a sphere with radius R whose center is a distance $R + z$ away from a flat plate. The idea of the Derjaguin approximation is to decompose the curved surface of the sphere into infinitely many, infinitesimally thin annuli that lie parallel to the plate; see Fig. 2.4. For every angle $\varphi \in [0, 2\pi]$ there is an associated annulus that has a radius $r(\varphi) = R\sin\varphi$, an area $\mathrm{d}A(\varphi) = \mathrm{d}[\pi r(\varphi)^2] = 2\pi R\sin\varphi\cos\varphi\,\mathrm{d}\varphi$ and a separation $L(\varphi) = z + (1-\cos\varphi)R$ to the plate. We now make the assumption that each of these annuli interacts with a corresponding annulus on the plate's suface, and that this contribution to the Helmholtz free energy is

$$\mathrm{d}F^{\mathrm{cas}}_{|\bigcirc}(\varphi) = k_{\mathrm{B}}T\frac{\mathrm{d}A(\varphi)}{L(\varphi)^2}\,\Theta_{||}\left[\frac{L(\varphi)}{\xi}\right] = k_{\mathrm{B}}T\frac{2\pi R^2\sin\varphi\cos\varphi}{[z+(1-\cos\varphi)R]^2}\,\Theta_{||}\left[\frac{z+(1-\cos\varphi)R}{\xi}\right]\mathrm{d}\varphi \quad (2.168)$$

as per Eq. (2.165). Integrating over φ then gives the total contribution of all annuli,

$$F^{\mathrm{cas}}_{|\bigcirc} = k_{\mathrm{B}}T\frac{2\pi R^2}{z^2}\int_0^{\pi/2}\mathrm{d}\varphi\,\frac{\sin\varphi\cos\varphi}{[1+(1-\cos\varphi)(R/z)]^2}\,\Theta_{||}\left[\frac{z}{\xi}\left\{1+(1-\cos\varphi)\frac{R}{z}\right\}\right]. \quad (2.169)$$

Due to the denominator, the integrand is small for $\varphi \gg 0$. We can therefore choose an upper integration limit $\varphi_{\max} > 0$ such that $\varphi_{\max} \ll \pi/2$. Then, defining $l(\varphi) \equiv 1 + (\varphi^2/2)(R/z)$ and

using that $\sin\varphi \approx \varphi$ and $\cos\varphi \approx 1 - \varphi^2/2$ for $\varphi \in [0, \varphi_{\max}]$, we have

$$\begin{aligned} F_{|\bigcirc}^{\mathrm{cas}} &\approx k_{\mathrm{B}}T\frac{2\pi R^2}{z^2}\int_0^{\varphi_{\max}} \mathrm{d}\varphi\, \frac{\varphi}{[1+(\varphi^2/2)(R/z)]^2}\Theta_{||}\left(\frac{z}{\xi}\left\{1+\frac{\varphi^2}{2}\frac{R}{z}\right\}\right) \\ &= k_{\mathrm{B}}T\frac{2\pi R}{z}\int_0^{\varphi_{\max}} \mathrm{d}\varphi\, \frac{\mathrm{d}l(\varphi)}{\mathrm{d}\varphi}\frac{\Theta_{||}(l(\varphi)z/\xi)}{l(\varphi)^2} = k_{\mathrm{B}}T\frac{2\pi R}{z}\int_{l(0)}^{l(\varphi_{\max})} \mathrm{d}l\, \frac{\Theta_{||}(lz/\xi)}{l^2}. \end{aligned} \tag{2.170}$$

Finally, recognizing that $l(0) = 1$ and $l(\varphi_{\max}) = 1 + \varphi_{\max}^2(R/z) \to \infty$ in the limit $R/z \to \infty$ regardless of the specific choice of $\varphi_{\max}$, we find that

$$F_{|\bigcirc}^{\mathrm{cas}}(z) \approx k_{\mathrm{B}}T\frac{R}{z}\Theta_{|\bigcirc}\left(\frac{z}{\xi}\right) = k_{\mathrm{B}}T\frac{R}{z}\Theta_{|\bigcirc}\left(\frac{z}{\xi_0}\left|\frac{T-T_{\mathrm{c}}}{T_{\mathrm{c}}}\right|^{\nu}\right) \quad \text{for } R \gg z \tag{2.171}$$

with the plate–sphere scaling function

$$\Theta_{|\bigcirc}(x) \equiv 2\pi\int_1^{\infty} \mathrm{d}l\, \frac{\Theta_{||}(xl)}{l^2}. \tag{2.172}$$

The critical Casimir force between the sphere and the plate is therefore

$$K_{|\bigcirc}^{\mathrm{cas}}(z) \equiv -\frac{\mathrm{d}F_{|\bigcirc}^{\mathrm{cas}}(z)}{\mathrm{d}z} \approx k_{\mathrm{B}}T\frac{R}{z^2}\theta_{|\bigcirc}\left(\frac{z}{\xi}\right) = k_{\mathrm{B}}T\frac{R}{z^2}\theta_{|\bigcirc}\left(\frac{z}{\xi_0}\left|\frac{T-T_{\mathrm{c}}}{T_{\mathrm{c}}}\right|^{\nu}\right) \quad \text{for } R \gg z \tag{2.173}$$

with $\theta_{|\bigcirc}(x) \equiv \Theta_{|\bigcirc}(x) - x\Theta'_{|\bigcirc}(x)$.

For the critical Casimir interaction between two spheres with the same radius R and center-to-center distance $2R+z$, the Derjaguin approximation works exactly the same, except that now, $L(\varphi) = z + 2(1-\cos\varphi)R$. In the end, this only results in an additional factor $1/2$ so that

$$F_{\bigcirc\bigcirc}^{\mathrm{cas}}(z) = \frac{1}{2}F_{|\bigcirc}^{\mathrm{cas}}(z) \approx k_{\mathrm{B}}T\frac{R}{2z}\Theta_{|\bigcirc}\left(\frac{z}{\xi}\right) = k_{\mathrm{B}}T\frac{R}{2z}\Theta_{|\bigcirc}\left(\frac{z}{\xi_0}\left|\frac{T-T_{\mathrm{c}}}{T_{\mathrm{c}}}\right|^{\nu}\right) \quad \text{for } R \gg z \tag{2.174}$$

and

$$K_{\bigcirc\bigcirc}^{\mathrm{cas}}(z) = \frac{1}{2}K_{|\bigcirc}^{\mathrm{cas}}(z) \approx k_{\mathrm{B}}T\frac{R}{2z^2}\theta_{|\bigcirc}\left(\frac{z}{\xi}\right) = k_{\mathrm{B}}T\frac{R}{2z^2}\theta_{|\bigcirc}\left(\frac{z}{\xi_0}\left|\frac{T-T_{\mathrm{c}}}{T_{\mathrm{c}}}\right|^{\nu}\right) \quad \text{for } R \gg z. \tag{2.175}$$

In Fig. 2.5, the plate–sphere scaling functions $\Theta_{|\bigcirc}$ and $\theta_{|\bigcirc}$ based on Refs. [64] and [65] are shown for equal ($\pm\pm$) and opposite ($\pm\mp$) boundary conditions. Since $\theta_{|\bigcirc}^{\pm\pm} < 0$ and $\theta_{|\bigcirc}^{\pm\mp} > 0$, it is clear that the critical Casimir force between a plate and a sphere or between two spheres is attractive if the surfaces preferentially adsorb the same component, and repulsive otherwise.

Experimentally, a major breakthrough in the study of the critical Casimir effect was reported by Hertlein et al. in 2008 [66] (see also Ref. [65] by Gambassi et al. for a more detailed account), who were able to directly measure the critical Casimir force between a spherical particle and planar substrate by means of total internal reflection microscopy (TIRM). As particles, they used polystyrene colloids with a diameter of a few microns that have been immersed in a mixture of

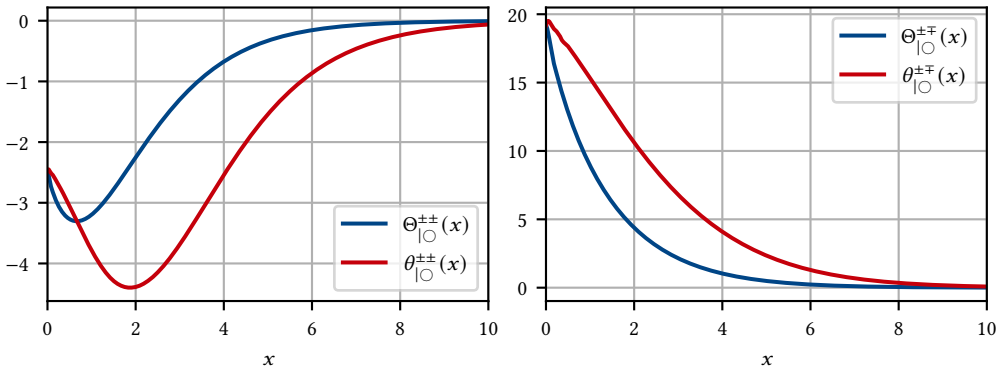

Figure 2.5.: The Derjaguin approximation of the critical Casimir scaling functions $\Theta_{|\bigcirc}$ and $\theta_{|\bigcirc}$ for the plate–sphere geometry with equal ("±±"; left panel) or opposite ("±∓"; right panel) adsorption preferences. Since $\theta_{|\bigcirc}^{\pm\pm} < 0$ and $\theta_{|\bigcirc}^{\pm\mp} > 0$, it follows that the critical Casimir force (2.173) is attractive if the surfaces favor the same component of the binary mixture, and repulsive otherwise. Based on Refs. [64] and [65].

water and 2,6-Lutidine. The water–2,6-Lutidine mixture has a lower critical (demixing) point at temperature $T_c \approx 307\,\mathrm{K} \approx 34\,^\circ\mathrm{C}$ and 2,6-Lutidine mass fraction $c_c^L \approx 0.286$. The colloids either favored 2,6-Lutidine ("+" boundary condition) if they had a low surface charge density, or water ("−" boundary condition) in case of a high surface charge density. The mixture and the colloids were contained within a cell made out of silica glass. The adsorption preference of the cell's surface was adjusted by coating it either with hexamethyldisilazane (HMDS) or NaOH, resulting in an affinity for 2,6-Lutidine (+) or water (−) respectively. Thus, all possible boundary conditions (++, +−, −+, −−) could be realized. Using an optical tweezer, a single colloid was captured and held in place in the lateral direction, but still allowed to move perpendicular to the bottom of the cell. From below the cell, a polarized laser beam was then directed at the point of the cell–mixture interface just below the colloid at such a flat angle that it was totally reflected. As a consequence, an evanescent electromagnetic field penetrated into the mixture and was scattered by the colloid. Since an evanescent field decays exponentially with increasing distance from the interface, the intensity of the scattered light depended sensitively on the height of the colloid above the interface. Via a measurement of this intensity, the vertical position of the colloid could then be accurately determined. Finally, by recording the thermal fluctuations of the colloid's height over some period of time, it was possible to infer the substrate–colloid interaction potential. Near the critical point, after subtraction of the gravitational and electrostatic contribution, the potential was found to be in excellent agreement with the theoretical prediction (2.171) for the critical Casimir plate–sphere interaction.

In another type of experiment, Zvyagolskaya et al. investigated the behavior of a binary mixture of silica colloids immersed in water–2,6-Lutidine at critical composition [42, 67]. The col-

loids sedimented toward the bottom of the containing cell into a plane monolayer, therefore effectively forming a two-dimensional system of hard disks. While one colloid species favored water (−) due to a high surface charge density, the other was rendered hydrophobic (+) through a functionalization with silane. After increasing the temperature above $T_c - 0.4\,\mathrm{K}$, the hitherto homogeneous colloid mixture was observed to segregate into domains rich in either one or the other species. The ensuing coarsening of the system's structure only became more pronounced as T_c was approached. This clearly suggest the presence of an attractive critical Casimir force between colloids of the same species (and thus the same adsorption preferences), and a repulsive critical Casimir force between colloids of different species (and thus opposite adsorption preferences). The experimental results proved to be consistent with a theoretic model of hard disks interacting via $K_{\bigcirc\bigcirc}^{\mathrm{cas}}$ as given by Eq. (2.175).

The critical Casimir effect presents an intriguing means of significantly altering the interaction between colloidal particles through minute changes of the temperature. In the next chapter, we will use this instrument to devise a colloidal model system with competing interactions, wherein the attraction and repulsion can be tuned easily and independently from each other.

3. Model system

We shall now direct our attention to the task of designing a novel model system that promises to offer intriguing possibilities and freedoms in the study of competing interactions and microphase separation. Ideally, this system would possess the following desirable properties:

(i) *Experimental realizability:* The model can be studied experimentally and, preferably, only requires slight modifications of experiments that have already been successfully conducted. Furthermore, the system can be directly imaged to reveal its structure.

(ii) *Theoretical accessibility:* The model can be analyzed theoretically in order to make predictions about its behavior that can guide experimentalists and that can also be compared with experimental results. In particular, the interactions between the particles are well-understood.

(iii) *Tunable competing interactions:* The particles interact via a typical SALR potential (Fig. 1.3) with a strong repulsion for small, a moderate attraction for intermediate, and a weak repulsion for larger particle separations. The strength of the attraction and the long-ranged repulsion can be tuned independently from each other by adjusting two easily controllable external variables.

Keeping this list in mind, consider the setup shown in Fig. 3.1. A single species of spherical silica colloids with a paramagnetic core and a diameter a of a few microns are immersed in a mixture of water and 2,6-Lutidine at critical composition. This suspension is confined to a temperature-controlled glass cell in which the colloids sediment toward the bottom under the force of gravity and form an essentially flat monolayer – provided that the mass of the colloids

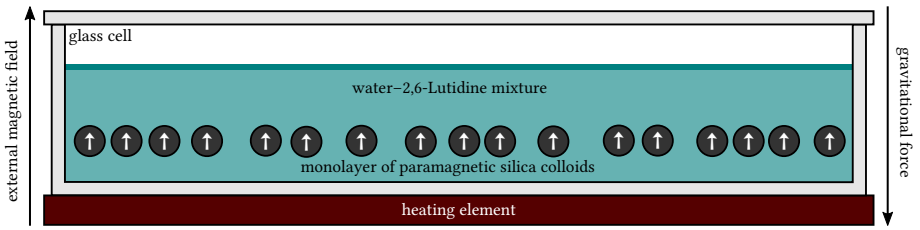

Figure 3.1.: Schematic side view of the experimental setup. Spherical silica colloids (dark circles) with a paramagnetic core are suspended in a water–2,6-Lutidine mixture (blue) at critical composition. The suspension is confined to a glass cell (light gray) in which the colloids sediment toward the bottom under the force of gravity and form an essentially flat monolayer. For temperature control, the cell sits on top of a heating element (red). Within the colloids, a magnetic dipole moment (white arrows) is induced by a homogeneous external magnetic field perpendicular to the monolayer.

is sufficiently high so that variations of their vertical position due to thermal fluctuations are negligible. Finally, the cell is placed inside the homogeneous magnetic field of, say, a copper coil, such that the field is perpendicular to the monolayer.

Silica surfaces in contact with an aqueous solvent acquire a negative charge through the dissociation of silanol groups ($SiOH \longrightarrow SiO^- + H^+$) [68]. One consequence of this is a screened electrostatic (Yukawa) repulsion between the colloids given by the pair potential

$$u_{\mathrm{el}}(r) = \frac{Q^2}{\varepsilon} \frac{\exp(\kappa a)}{(1+\kappa a/2)^2} \frac{\exp(-\kappa r)}{r}, \tag{3.1}$$

where r is the center-to-center distance between two colloids, Q their electric charge, ε the dielectric constant of the solvent and κ^{-1} the Debye screening length [69]. Since $\kappa^{-1} \approx 12\,\mathrm{nm}$ for water–2,6-Lutidine [66] and therefore $\kappa \ll a$, this repulsion is extremely short-ranged and can thus be well approximated as a hard core interaction with an effective diameter $\sigma > a$ [42],

$$u_{\mathrm{el}}(r) \approx \begin{cases} \infty & \text{if } r < \sigma, \\ 0 & \text{otherwise.} \end{cases} \tag{3.2}$$

We shall henceforth use $a = 3\,\mu\mathrm{m}$ and $\sigma = 3.1\,\mu\mathrm{m}$ as in Ref. [42].

Another consequence of the negative surface charge of the colloids is the preferential adsorption of water. Close to the critical temperature $T_\mathrm{c} \approx 307\,\mathrm{K}$ of the water–2,6-Lutidine mixture, the divergence of the correlation length $\xi = \xi_0 \left(|T - T_\mathrm{c}|/T_\mathrm{c}\right)^{-\nu}$, where $\xi_0 \approx 0.2\,\mathrm{nm}$ [66] and $\nu \approx 0.63$, will lead to a critical Casimir attraction between two *isolated* colloids that is, according to Eq. (2.174), described by the pair potential

$$u_{\mathrm{cas}}(r) = \frac{k_\mathrm{B}T}{4} \frac{a}{r-a} \Theta^{\pm\pm}_{|\bigcirc}\left(\frac{r-a}{\xi}\right) = \frac{k_\mathrm{B}T}{4} \frac{a}{r-a} \Theta^{\pm\pm}_{|\bigcirc}\left(\frac{r-a}{\xi_0} \left|\frac{T-T_\mathrm{c}}{T_\mathrm{c}}\right|^{\nu}\right). \tag{3.3}$$

However, if these colloids are *not* isolated but, as in the present case, part of a collective, this is no longer necessarily true. Because additional colloids will affect the concentration fluctuations of the mixture that mediate the critical Casimir force, the interaction between two colloids will in general also be influenced by the other colloids in their neighborhood [70–72]. Dang et al. attribute discrepancies between the experimentally determined and theoretically predicted phase diagram of a colloidal suspension close to the critical point to the non-additivity of the critical Casimir potential [73], and Paladugu et al. were able to directly measure the deviations from Eq. (3.3) when a third colloid was nearby. While such many-body effects are certainly nor irrelevant, they are unfortunately also notoriously hard to quantify and to incorporate because of their usually very complicated dependence on the relative position, orientation and geometry of the surfaces; there does not even exist a comprehensive description of the critical Casimir interaction between three identical spherical objects. For this reason, we are forced to assume pairwise

additivity of u_{cas} in our analysis and neglect many-body effects of higher order. Although this approximation might diminish the *quantitative* accuracy of our theoretical predictions in comparison to possible experiments, it is unlikely to have a considerable impact on the *qualitative* behavior. Note that $u_{\mathrm{cas}}(r) \to -\infty$ as $r \to a$, which means that two colloids would in principle become inseparably stuck to each other if their proper surfaces came into contact. In practice, however, this should not a problem since measurements show [66, 74] that the electrostatic repulsion typically beats the critical Casimir attraction for very small colloid separations (which further justifies approximating the former as a hard core interaction).

The homogeneous external magnetic field $\vec{B}$ induces a magnetic dipole moment $\vec{M} = \chi\vec{B}$ within the paramagnetic core of the colloids, where χ is their magnetic susceptibility. Each colloid, in turn, produces itself a magnetic dipole field given by

$$\vec{B}_{\mathrm{col}}(\vec{r}) = \frac{\mu_0}{4\pi}\left[\frac{3\,(\vec{M}\cdot\vec{r})\,\vec{r}}{|\vec{r}|^5} - \frac{\vec{M}}{|\vec{r}|^3}\right] \tag{3.4}$$

with the vacuum permeability $\mu_0 \simeq 1.257 \times 10^{-6}\,\mathrm{TmA}^{-2}$. The induced magnetic dipole of any other colloid will interact with this field; using that $\vec{M}\cdot\vec{r} = 0$ since the colloids lie in a flat monolayer perpendicular to $\vec{B}$, this results in a magnetic dipole–dipole repulsion described by the potential

$$u_{\mathrm{mag}}(r) = -\vec{M}\cdot\vec{B}_{\mathrm{col}}(\vec{r}) = \frac{\mu_0}{4\pi}\frac{|\vec{M}|^2}{r^3} = \frac{\mu_0}{4\pi}\frac{\chi^2 B^2}{r^3}. \tag{3.5}$$

Colloids with a paramagnetic core inside an external magnetic field have been experimentally studied, among others, by Zahn et al. [40] and Bubeck et al. [41]. In the following, we shall assume that $\chi = 7.62\,\mathrm{Am}^2\mathrm{T}^{-1}$ as in Ref. [40].

Combining all contributions to the colloid–coloid interaction, we arrive at the pair potential

$$u(r) = u_{\mathrm{el}}(r) + u_{\mathrm{cas}}(r) + u_{\mathrm{mag}}(r) \tag{3.6}$$

with a very strong short-ranged electrostatic repulsion u_{el}, a medium-ranged critical Casimir attraction u_{cas} depending on the temperature T, and a long-ranged magnetic dipole repulsion u_{mag} that increases with the magnitude B of the external magnetic field. The remaining question is whether we can choose T and B in such a way that u truly has the shape of an SALR potential. As we can see in Fig. 3.2, where $u(r)$ is plotted for several combinations of T and B versus the colloid separation r, this is indeed the case. For large r, $u_{\mathrm{mag}}(r)$ dominates and causes a weak repulsion between the colloids. As r becomes smaller, the critical Casimir force at some point quite abruptly grows significantly in strength and forms a deep trench for $r \in (\sigma, r_*)$, where r_* denotes the separation at which the magnetic and critical Casimir forces balance each other out and u attains its maximum. For $r < \sigma$, $u(r)$ is infinite due to the hard core interaction. Figure 3.2(a)

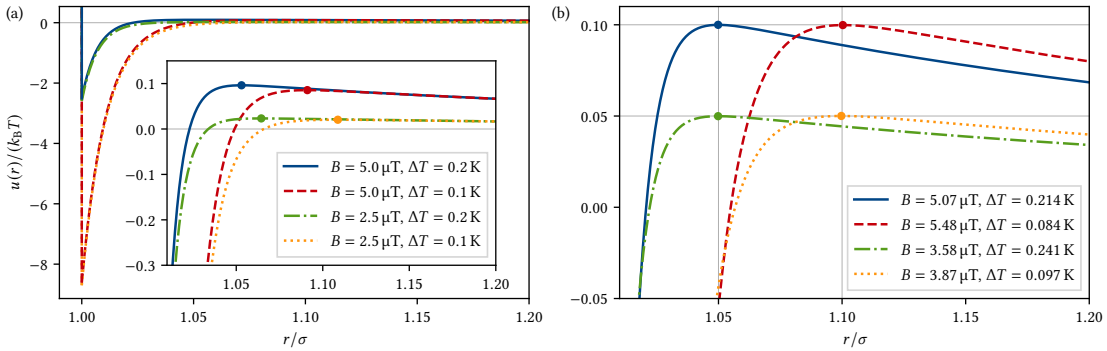

Figure 3.2.: The pair potential $u(r) = u_{el}(r) + u_{cas}(r) + u_{mag}(r)$ as a function of the colloid separation r for different combinations of the magnetic field B and the temperature $\Delta T \equiv T_c - T$ that give rise to a typical SALR shape. Symbols mark the maxima of u. Panel (a) shows how u responds to changes of either B or T. The inset displays a more detailed view of the maxima. Panel (b) demonstrates that we can precisely set the maximum of u by choosing suitable values for B and T.

shows how a change of either T or B affects the pair potential, while Fig. 3.2(b) demonstrates that the ability to tune u_{mag} and u_{cas} independently from each other allows one to, e. g., precisely set the location r_* and height $u(r_*)$ of the potential's maximum through an appropriate choice of T and B.

Briefly recalling the list from the beginning of this chapter, we find that our model system checks off all three items: (i) The experimental realizability of the model has, for all intents and purposes, already been demonstrated because the setup is essentially just a blending of the one by Zvyagolskaya et al. [42, 67] with that by Zahn or Bubeck et al. [40, 41]. Furthermore, as an effectively two-dimensional colloidal system, it is relatively easy to image via microscopy. (ii) Except for critical Casimir many-body effects, we know which forces are acting on the colloids and how to quantify them. Describing the colloids as two-dimensional hard disks with diameter $\sigma > a$ through the excess free energy functional (2.116) and treating the remaining long-ranged "tail" $u_{ci} = u_{cas} + u_{mag}$ of the interaction potential as a perturbation to this hard disk reference system by employing the random phase approximation (2.124) should yield a fairly accurate density funcional theory for the model. (iii) We have clearly established that the colloidal interaction potential has an attractive critical Casimir component that can be tuned by varying the temperature, and a repulsive magnetic dipole component that can be controlled by adjusting an external magnetic field. Together with a strong short-ranged electrostatic repulsion, they give rise to an SALR potential for suitable values of T and B.

For the remainder of the thesis, we shall study theoretically the statics and dynamics of this model with a focus on the question: Will the system undergo microphase separation?

4. Statics

Let us start by studying the statics of our model system presented in the previous chapter, i. e., the phase behavior in thermodynamic equilibrium. We shall employ DFT to develop several approaches that are increasingly involved and expensive, but in return also become more accurate and powerful. These nicely complement each other since the simpler methods allow us to quickly identify interesting situations that we can then investigate in greater depth with the more complex ones.

To describe the system, we use the intrinsic free energy functional $\mathcal{F} = \mathcal{F}_{\mathrm{id}} + \mathcal{F}_{\mathrm{hd}}^{\mathrm{ex}} + \mathcal{F}_{\mathrm{ci}}^{\mathrm{ex}}$, which is composed of an ideal gas, an excess hard disk and an excess competing interactions contribution. According to Eq. (2.81), the ideal gas functional is given by

$$\beta\mathcal{F}_{\mathrm{id}}[\rho] = \int_V \mathrm{d}^2\vec{r}\,\rho(\vec{r})\,[\ln\{\Lambda^2\rho(\vec{r})\} - 1] = \int_V \mathrm{d}^2\vec{r}\,\phi_{\mathrm{id}}(\rho(\vec{r})) \tag{4.1}$$

with $\phi_{\mathrm{id}}(\rho) = \rho\,[\ln(\Lambda^2\rho) - 1]$. For the hard disk part, we choose the FMT functional (2.116) by Roth, Mecke and Oettel which can be written as

$$\beta\mathcal{F}_{\mathrm{hd}}^{\mathrm{ex}}[\rho] = \int_V \mathrm{d}^2\vec{r}\,\phi_{\mathrm{hd}}\Big(w_\rho^0(\vec{r}), w_\rho^2(\vec{r}), \boldsymbol{w}_\rho^0(\vec{r}), \boldsymbol{w}_\rho^1(\vec{r}), \boldsymbol{w}_\rho^2(\vec{r})\Big) \tag{4.2}$$

with

$$\phi_{\mathrm{hd}}(w_\rho^0, w_\rho^2, \boldsymbol{w}_\rho^0, \boldsymbol{w}_\rho^1, \boldsymbol{w}_\rho^2) = -w_\rho^0\ln(1 - w_\rho^2) + \frac{19\,\boldsymbol{w}_\rho^0\cdot\boldsymbol{w}_\rho^0 - 5\,\boldsymbol{w}_\rho^1\cdot\boldsymbol{w}_\rho^1 - 14\,\boldsymbol{w}_\rho^2\cdot\boldsymbol{w}_\rho^2}{48\pi(1 - w_\rho^2)}. \tag{4.3}$$

Since we have only a single species ($\nu = 1$) of hard spheres with radius $R = \sigma/2$, the weighted densities reduce to

$$w_\rho^k(\vec{r}) = \int_V \mathrm{d}^2\vec{r}\,'\,\rho(\vec{r}\,')\,\omega^k(\vec{r} - \vec{r}\,'), \quad \boldsymbol{w}_\rho^m(\vec{r}) = \int_V \mathrm{d}^2\vec{r}\,'\,\rho(\vec{r}\,')\,\boldsymbol{\omega}^m(\vec{r} - \vec{r}\,') \tag{4.4}$$

with the weight functions

$$\omega^0(\vec{r}) = \frac{\delta(R - |\vec{r}|)}{2\pi R}, \quad \omega^2(\vec{r}) = \Theta(R - |\vec{r}|), \quad [\boldsymbol{\omega}^m(\vec{r})]_{i_1,\ldots,i_m} = \frac{x_{i_1}\cdots x_{i_m}}{|\vec{r}|^m}\delta(R - |\vec{r}|) \tag{4.5}$$

for $\vec{r} = (x_1, x_2)$ and $i_1, \ldots, i_m \in \{1, 2\}$. We incorporate the competing critical Casimir and mag-

netic dipole interactions through the RPA (2.121),

$$\beta\mathcal{F}_{\mathrm{ci}}^{\mathrm{ex}}[\rho] = \frac{1}{2}\int_V \mathrm{d}^2\vec{r}\int_V \mathrm{d}^2\vec{r}'\,\rho(\vec{r})\,\rho(\vec{r}')\,\beta u_{\mathrm{ci}}(|\vec{r}-\vec{r}'|), \tag{4.6}$$

where $u_{\mathrm{ci}} = u_{\mathrm{cas}} + u_{\mathrm{mag}}$ with

$$u_{\mathrm{cas}}(r) = \frac{k_{\mathrm{B}}T}{4}\frac{a}{r-a}\,\Theta_{|\bigcirc}^{\pm\pm}\left(\frac{r-a}{\xi_0}\left|\frac{T-T_{\mathrm{c}}}{T_{\mathrm{c}}}\right|^{\nu}\right), \quad u_{\mathrm{mag}}(r) = \frac{\mu_0}{4\pi}\frac{\chi^2 B^2}{r^3}. \tag{4.7}$$

However, $\mathcal{F}_{\mathrm{ci}}^{\mathrm{ex}}$ is actually ill-defined because $u_{\mathrm{cas}}(r)$ is not valid for $r \leq a$ and $u_{\mathrm{mag}}(r) \to \infty$ as $r \to 0$. A potential remedy has already been discussed in Sec. 2.3.3, where it was suggested that for a hard core reference system (as in the present case), it is beneficial to restrict the integration domains of $\vec{r}$ and $\vec{r}'$ such that $|\vec{r}-\vec{r}'| > \sigma$, or, equivalently, to artificially set $u_{\mathrm{ci}}(r) = 0$ for $r \leq \sigma$. Although this would solve the problem, it unfortunately tends to lead to an underestimation of the correlations. As an empirical correction, we instead extend the (finite) value $u_{\mathrm{ci}}(\sigma)$ into the hard core, resulting in

$$u_{\mathrm{ci}}(r) = \begin{cases} u_{\mathrm{cas}}(\sigma) + u_{\mathrm{mag}}(\sigma) & \text{if } r \leq \sigma, \\ u_{\mathrm{cas}}(r) + u_{\mathrm{mag}}(r) & \text{otherwise.} \end{cases} \tag{4.8}$$

Note: In the following discussion, the Fourier transforms of several quantities that either factor into or stem from the intrinsic free energy functional $\mathcal{F}$ will become important. For the sake of a clearer presentation, their derivation is deferred to Appendix D.

4.1. Bulk system

4.1.1. Binodal, spinodal and λ-line

Initially, we are going to concern ourselves with the bulk system, which is characterized by an infinite volume, $V \to \infty$, and a vanishing external potential, $\mathcal{V}^{\mathrm{ext}} = 0$. Before taking a look at microphase separation, it will prove insightful to first study the coexistence between the "regular" uniform gas and liquid phases (in a similar manner as in Section 2.4), where the density distribution is constant and identical to the bulk density, $\rho(\vec{r}) = \rho_{\mathrm{b}}$.

For the ideal gas contribution to the free energy density, we find

$$\frac{\beta\mathcal{F}_{\mathrm{id}}[\rho_{\mathrm{b}}]}{V} = \frac{1}{V}\int_V \mathrm{d}^2\vec{r}\,\phi_{\mathrm{id}}(\rho_{\mathrm{b}}) = \rho_{\mathrm{b}}\,[\ln(\Lambda^2\rho_{\mathrm{b}}) - 1]. \tag{4.9}$$

The hard disk contribution simplifies significantly to

$$\frac{\beta\mathcal{F}_{\mathrm{hd}}^{\mathrm{ex}}[\rho_{\mathrm{b}}]}{V} = \frac{1}{V}\int_V \mathrm{d}^2\vec{r}\,\phi_{\mathrm{hd}}(w_{\rho_{\mathrm{b}}}^0, w_{\rho_{\mathrm{b}}}^2, \boldsymbol{w}_{\rho_{\mathrm{b}}}^0, \boldsymbol{w}_{\rho_{\mathrm{b}}}^1, \boldsymbol{w}_{\rho_{\mathrm{b}}}^2) = \rho_{\mathrm{b}}\left[\frac{\pi R^2\rho_{\mathrm{b}}}{1-\pi R^2\rho_{\mathrm{b}}} - \ln(1-\pi R^2\rho_{\mathrm{b}})\right], \tag{4.10}$$

where we used that $w^0_{\rho_\mathrm{b}} = \rho_\mathrm{b}, w^2_{\rho_\mathrm{b}} = \pi R^2 \rho_\mathrm{b}, \boldsymbol{w}^0_{\rho_\mathrm{b}} = 2\pi R \rho_\mathrm{b}, \boldsymbol{w}^1_{\rho_\mathrm{b}} = 0$, and $\boldsymbol{w}^2_{\rho_\mathrm{b}} = \pi R \rho_\mathrm{b} \left(\begin{smallmatrix} 1 & 0 \\ 0 & 1 \end{smallmatrix}\right)$. Lastly, the competing interactions contribution is

$$\frac{\beta \mathcal{F}^\mathrm{ex}_\mathrm{ci}[\rho_\mathrm{b}]}{V} = \frac{1}{2V} \int_V \mathrm{d}^2\vec{r} \int_V \mathrm{d}^2\vec{r}\,' \rho_\mathrm{b}^2 \, \beta u_\mathrm{ci}(|\vec{r} - \vec{r}\,'|) = \frac{1}{2} \rho_\mathrm{b}^2 \int_V \mathrm{d}^2\vec{r} \, \beta u_\mathrm{ci}(|\vec{r}|) = -\rho_\mathrm{b}^2 \alpha \tag{4.11}$$

with the interaction parameter

$$\alpha \equiv -\frac{1}{2} \int_V \mathrm{d}^2\vec{r} \, \beta u_\mathrm{ci}(|\vec{r}|) \longrightarrow -\frac{1}{2} \beta \tilde{u}_\mathrm{ci}(0) \tag{4.12}$$

which, in the limit $V \to \infty$, can be expressed in terms of the two-dimensional Fourier transform of u_ci,

$$\tilde{u}_\mathrm{ci}(\vec{k}) = \int \mathrm{d}^2\vec{r} \, u_\mathrm{ci}(|\vec{r}|) \exp(-\mathrm{i}\vec{k} \cdot \vec{r}). \tag{4.13}$$

The total free energy density in the bulk is therefore given by

$$\frac{\beta \mathcal{F}[\rho_\mathrm{b}]}{V} = \rho_\mathrm{b} \left[\ln \frac{\Lambda^2 \rho_\mathrm{b}}{1 - \pi R^2 \rho_\mathrm{b}} + \frac{\pi R^2 \rho_\mathrm{b}}{1 - \pi R^2 \rho_\mathrm{b}} - \rho_\mathrm{b} \alpha - 1 \right]. \tag{4.14}$$

With this, we can calculate the pressure via

$$\beta P(\rho_\mathrm{b}) = \rho_\mathrm{b} \frac{\partial}{\partial \rho_\mathrm{b}} \frac{\beta \mathcal{F}[\rho_\mathrm{b}]}{V} - \frac{\beta \mathcal{F}[\rho_\mathrm{b}]}{V} = \frac{\rho_\mathrm{b}}{(1 - \pi R^2 \rho_\mathrm{b})^2} - \rho_\mathrm{b}^2 \alpha, \tag{4.15}$$

and the chemical potential as

$$\beta \mu(\rho_\mathrm{b}) = \frac{\partial}{\partial \rho_\mathrm{b}} \frac{\beta \mathcal{F}[\rho_\mathrm{b}]}{V} = \ln \frac{\Lambda^2 \rho_\mathrm{b}}{1 - \pi R^2 \rho_\mathrm{b}} + 3 \frac{\pi R^2 \rho_\mathrm{b}}{1 - \pi R^2 \rho_\mathrm{b}} + \left(\frac{\pi R^2 \rho_\mathrm{b}}{1 - \pi R^2 \rho_\mathrm{b}} \right)^2 - 2 \rho_\mathrm{b} \alpha. \tag{4.16}$$

Demanding that

$$\left(\frac{\partial \mu(\rho_\mathrm{b})}{\partial \rho_\mathrm{b}} \right)_{\substack{\alpha = \alpha_c \\ \rho_\mathrm{b} = \rho_\mathrm{c}}} = 0 = \left(\frac{\partial^2 \mu(\rho_\mathrm{b})}{\partial \rho_\mathrm{b}^2} \right)_{\substack{\alpha = \alpha_c \\ \rho_\mathrm{b} = \rho_\mathrm{c}}} \tag{4.17}$$

we find a critical bulk density ρ_c, interaction parameter α_c and pressure P_c of

$$\pi R^2 \rho_\mathrm{c} = \frac{\sqrt{7} - 2}{3} \approx 0.215, \quad \frac{\alpha_\mathrm{c}}{\pi R^2} = \frac{108 + 27\sqrt{7}}{1724 - 640\sqrt{7}} \approx 5.84, \quad \pi R^2 \beta P_\mathrm{c} \approx 0.0789. \tag{4.18}$$

For $\alpha > \alpha_c$, coexistence of a gaseous phase with density $\rho_\mathrm{g} < \rho_\mathrm{c}$ and a liquid phase with density $\rho_\mathrm{l} > \rho_\mathrm{c}$ is possible when $\mu(\rho_\mathrm{g}) = \mu(\rho_\mathrm{l})$ and $P(\rho_\mathrm{g}) = P(\rho_\mathrm{l})$; we defined the pairs $(\rho_\mathrm{g}, \rho_\mathrm{l})$ that satisfy this condition as the binodal. We recall that states with $\partial \mu(\rho_\mathrm{b}) / \partial \rho_\mathrm{b} < 0$ have a negative isothermal compressibility κ_T and are therefore unstable; these are enclosed by the spinodal for which $\partial \mu(\rho_\mathrm{b}) / \partial \rho_\mathrm{b} = 0$ and $|\kappa_T| \to \infty$. The binodal and spinodal with respect to the interaction

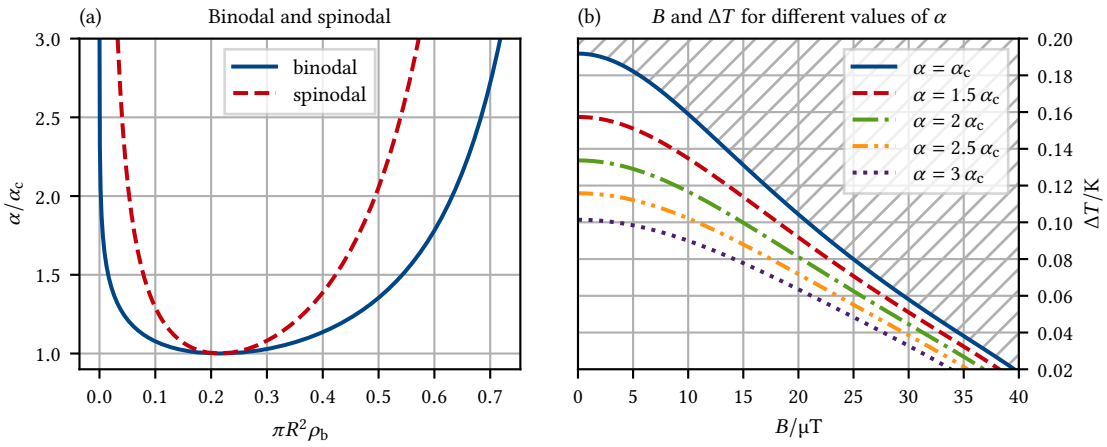

Figure 4.1.: (a) The binodal and spinodal of our model system with respect to the interaction parameter α. For $\alpha > \alpha_c$, uniform gas and liquid phases can coexist. (b) The combinations of B and ΔT that correspond to certain values of α. In the hatched region, $\alpha < \alpha_c$ so that gas–liquid coexistence is not possible.

parameter α are shown in Fig. 4.1(a). Bear in mind that α, through u_{ci}, depends on the magnetic field B and the temperature T. In Fig. 4.1(b) we can see which combinations of B and $\Delta T \equiv T_c - T$ correspond to certain values of α. At $B = 20\,\mu T$ and $\Delta T = 0.09\,K$, for instance, we find that $\alpha \approx 1.6\,\alpha_c$, which implies coexistence of a gas with density $\pi R^2\rho_g \approx 0.01$ and a liquid with density $\pi R^2\rho_l \approx 0.57$, as well as a domain of instability with $\pi R^2\rho_b \in [0.08, 0.43]$.

With the phase behavior of the uniform bulk system analyzed, we will now direct our attention toward microphase separation. As a first step, we shall determine those regions in the phase diagram where the uniform system becomes unstable to density fluctuations. In Eq. (2.151) we saw that $\rho_b k_B T \kappa_T = \tilde{S}(0)$, where $\tilde{S}$ is the static structure factor. Thus, $\tilde{S}(0) < 0$ means the system undergoes "macrophase" separation into an infinitely large gaseous and an infinitely large liquid phase. Similarly, it turns out that if $\tilde{S}(k_0) < 0$ for some $k_0 \neq 0$, the system will preferably form density modulations with a length scale on the order of $2\pi/k_0$. To prove this, consider the density distribution

$$\rho(\vec{r}) = \rho_b + \Delta\rho(\vec{r}), \tag{4.19}$$

where $\Delta\rho$ represents the deviation from the bulk density ρ_b. If $\Delta\rho$ is sufficiently small, we can calculate the intrinsic free energy $\mathcal{F}[\rho]$ via a functional Taylor expansion around ρ_b:

$$\begin{aligned}\mathcal{F}[\rho] &= \mathcal{F}[\rho_b] + \sum_{n=1}^{\infty} \frac{1}{n!} \int_V d^2\vec{r}_1 \cdots \int_V d^2\vec{r}_n \left.\frac{\delta^n \mathcal{F}[\rho]}{\delta\rho(\vec{r}_1)\cdots\delta\rho(\vec{r}_n)}\right|_{\rho=\rho_b} \Delta\rho(\vec{r}_1)\cdots\Delta\rho(\vec{r}_n) \\ &= \mathcal{F}[\rho_b] - k_B T \sum_{n=1}^{\infty} \frac{1}{n!} \int_V d^2\vec{r}_1 \cdots \int_V d^2\vec{r}_n\, C_n(\vec{r}_1, \ldots, \vec{r}_n)\, \Delta\rho(\vec{r}_1)\cdots\Delta\rho(\vec{r}_n)\end{aligned} \tag{4.20}$$

with

$$C_n(\vec{r}_1,\ldots,\vec{r}_n) \equiv -\beta \left.\frac{\delta^n \mathcal{F}[\rho]}{\delta\rho(\vec{r}_1)\cdots\delta\rho(\vec{r}_n)}\right|_{\rho=\rho_\mathrm{b}}. \tag{4.21}$$

Since the functional derivative of $\mathcal{F}$ in Eq. (4.21) is evaluated at the uniform bulk density ρ_b, C_n must be invariant under translation in that $C_n(\vec{r}_1-\Delta r,\ldots,\vec{r}_n-\Delta r) = C_n(\vec{r}_1,\ldots,\vec{r}_n)$ for any $\Delta\vec{r}\in\mathbb{R}^2$. Choosing $\Delta\vec{r}=\vec{r}_n$, we thus find that

$$C_n(\vec{r}_1,\ldots,\vec{r}_n) = C_n(\vec{r}_1-\vec{r}_n,\ldots,\vec{r}_{n-1}-\vec{r}_n,0) = C_n(\vec{r}_1-\vec{r}_n,\ldots,\vec{r}_{n-1}-\vec{r}_n), \tag{4.22}$$

where $C_n(\vec{r}_1,\ldots,\vec{r}_{n-1}) \equiv C_n(\vec{r}_1,\ldots,\vec{r}_{n-1},0)$ is the $(n-1)$-ary version of C_n with the same content of information. Inserting this into Eq. (4.20), the change $\Delta\mathcal{F}[\rho] \equiv \mathcal{F}[\rho]-\mathcal{F}[\rho_\mathrm{b}]$ in intrinsic free energy due to the presence of density fluctuations can be written as

$$\beta\Delta\mathcal{F}[\rho] = -\sum_{n=1}^{\infty}\frac{1}{n!}\int_V \mathrm{d}^2\vec{r}_1\cdots\int_V \mathrm{d}^2\vec{r}_n\, C_n(\vec{r}_1-\vec{r}_n,\ldots,\vec{r}_{n-1}-\vec{r}_n)\,\Delta\rho(\vec{r}_1)\cdots\Delta\rho(\vec{r}_n). \tag{4.23}$$

Now suppose that ρ is (L_x,L_y)-periodic so that $\rho(x+L_x,y+L_y)=\rho(x,y)$ for any $x,y\in\mathbb{R}$. We can then expand $\Delta\rho$ in a Fourier series as

$$\Delta\rho(\vec{r}) = \sum_{\vec{k}\in\mathbb{K}} \tilde{\rho}_{\vec{k}}\exp(\mathrm{i}\vec{k}\cdot\vec{r}) \tag{4.24}$$

with $\mathbb{K} \equiv \{(2\pi i/L_x, 2\pi j/L_y) : (i,j)\in\mathbb{Z}^2\setminus\{0\}\}$ and Fourier coefficients

$$\tilde{\rho}_{\vec{k}} \equiv \frac{1}{L_xL_y}\int_{[0,L_x]\times[0,L_y]}\mathrm{d}^2\vec{r}\,\rho(\vec{r})\exp(-\mathrm{i}\vec{k}\cdot\vec{r}). \tag{4.25}$$

Replacing $\Delta\rho$ in Eq. (4.23) with its Fourier expansion (4.24), have

$$\begin{aligned}
\frac{\beta\Delta\mathcal{F}[\rho]}{V} &= -\frac{1}{V}\sum_{n=1}^{\infty}\frac{1}{n!}\int_V \mathrm{d}^2\vec{r}_1\cdots\int_V \mathrm{d}^2\vec{r}_n\, C_n(\vec{r}_1-\vec{r}_n,\ldots,\vec{r}_{n-1}-\vec{r}_n)\\
&\quad\times\sum_{\vec{k}_1\in\mathbb{K}}\tilde{\rho}_{\vec{k}_1}\exp(\mathrm{i}\vec{k}_1\cdot\vec{r}_1)\cdots\sum_{\vec{k}_n\in\mathbb{K}}\tilde{\rho}_{\vec{k}_n}\exp(\mathrm{i}\vec{k}_n\cdot\vec{r}_n)\\
&= -\sum_{n=1}^{\infty}\frac{1}{n!}\sum_{\vec{k}_1\in\mathbb{K}}\cdots\sum_{\vec{k}_n\in\mathbb{K}}\tilde{\rho}_{\vec{k}_1}\cdots\tilde{\rho}_{\vec{k}_n}\,\frac{1}{V}\int_V \mathrm{d}^2\vec{r}_n\,\exp\left[\mathrm{i}\left(\vec{k}_1+\cdots+\vec{k}_n\right)\cdot\vec{r}_n\right]\\
&\quad\times\int_{V'}\mathrm{d}^2\vec{r}\,'_1\cdots\int_{V'}\mathrm{d}^2\vec{r}\,'_{n-1}\,C_n(\vec{r}\,'_1,\ldots,\vec{r}\,'_{n-1})\exp\left[\mathrm{i}\left(\vec{k}_1\cdot\vec{r}\,'_1+\cdots+\vec{k}_{n-1}\cdot\vec{r}\,'_{n-1}\right)\right],
\end{aligned} \tag{4.26}$$

where we rearranged some terms and used the substitution $\vec{r}_i \to \vec{r}\,'_i \equiv \vec{r}_i+\vec{r}_n$ for $i\in\{1,\ldots,n-1\}$

in the last step. Recognizing that

$$\lim_{V\to\infty}\left[\frac{1}{V}\int_V \mathrm{d}^2\vec{r}_n\,\exp\left\{\mathrm{i}\left(\vec{k}_1+\cdots+\vec{k}_n\right)\cdot\vec{r}_n\right\}\right]=\begin{cases}1 & \text{if } \vec{k}_1+\cdots+\vec{k}_n=0,\\ 0 & \text{otherwise,}\end{cases} \tag{4.27}$$

and

$$\begin{aligned}\lim_{V\to\infty}&\left[\int_{V'}\mathrm{d}^2\vec{r}\,'_1\cdots\int_{V'}\mathrm{d}^2\vec{r}\,'_{n-1}\,C_n(\vec{r}\,'_1,\ldots,\vec{r}\,'_{n-1})\exp\left\{\mathrm{i}\left(\vec{k}_1\cdot\vec{r}\,'_1+\cdots+\vec{k}_{n-1}\cdot\vec{r}\,'_{n-1}\right)\right\}\right]\\ &=\tilde{C}_n(-\vec{k}_1,\ldots,-\vec{k}_{n-1}),\end{aligned} \tag{4.28}$$

we arrive at

$$\lim_{V\to\infty}\frac{\beta\Delta\mathcal{F}[\rho]}{V}=-\sum_{n=1}^{\infty}\frac{1}{n!}\sum_{\vec{k}_1\in\mathbb{K}}^{\vec{k}_1+\cdots+\vec{k}_n=0}\cdots\sum_{\vec{k}_n\in\mathbb{K}}\tilde{\rho}_{\vec{k}_1}\cdots\tilde{\rho}_{\vec{k}_n}\,\tilde{C}_n(-\vec{k}_1,\ldots,-\vec{k}_{n-1}) \tag{4.29}$$

for the change in intrinsic free energy density in the limit $V\to\infty$. Note that the condition $\vec{k}_1=0$ cannot be fulfilled for $\vec{k}_1\in\mathbb{K}$ since $0\notin\mathbb{K}$ by definition of $\mathbb{K}$. Thus, the summand with $n=1$ always vanishes and the Taylor expansion up to the lowest non-trivial order is given by

$$\lim_{V\to\infty}\frac{\beta\Delta\mathcal{F}[\rho]}{V}=-\frac{1}{2}\sum_{\vec{k}\in\mathbb{K}}\tilde{\rho}_{\vec{k}}\tilde{\rho}_{-\vec{k}}\,\tilde{C}_2(-\vec{k})+O(\tilde{\rho}^3)=-\frac{1}{2}\sum_{\vec{k}\in\mathbb{K}}|\tilde{\rho}_{\vec{k}}|^2\,\tilde{C}_2(\vec{k})+O(\tilde{\rho}^3), \tag{4.30}$$

where we used that $-\vec{k}\in\mathbb{K}$ if $\vec{k}\in\mathbb{K}$, as well as $\tilde{\rho}_{-\vec{k}}=\tilde{\rho}^*_{\vec{k}}$ (with the star denoting complex conjugation) since ρ is a real function so that $\tilde{\rho}_{\vec{k}}\tilde{\rho}_{-\vec{k}}=\tilde{\rho}_{\vec{k}}\tilde{\rho}^*_{\vec{k}}=|\tilde{\rho}_{\vec{k}}|^2$. Let us now split $\mathcal{F}$ up into the ideal gas part $\mathcal{F}_{\mathrm{id}}$ and the excess part $\mathcal{F}_{\mathrm{ex}}$, $\mathcal{F}=\mathcal{F}_{\mathrm{id}}+\mathcal{F}_{\mathrm{ex}}$. For the former, we find that

$$\begin{aligned}\beta\frac{\delta^2\mathcal{F}_{\mathrm{id}}[\rho]}{\delta\rho(\vec{r}_1)\delta\rho(\vec{r}_2)}&=\frac{\delta^2}{\delta\rho(\vec{r}_2)\delta\rho(\vec{r}_1)}\int\mathrm{d}^2\vec{r}\,\phi_{\mathrm{id}}(\rho(\vec{r}))=\frac{\delta}{\delta\rho(\vec{r}_2)}\int\mathrm{d}^2\vec{r}\,\phi'_{\mathrm{id}}(\rho(\vec{r}))\underbrace{\frac{\delta\rho(\vec{r})}{\delta\rho(\vec{r}_1)}}_{=\delta(\vec{r}-\vec{r}_1)}\\ &=\frac{\delta\phi'_{\mathrm{id}}(\rho(\vec{r}_1))}{\delta\rho(\vec{r}_2)}=\phi''_{\mathrm{id}}(\rho(\vec{r}_1))\,\delta(\vec{r}_1-\vec{r}_2)=\frac{\delta(\vec{r}_1-\vec{r}_2)}{\rho(\vec{r}_1)}.\end{aligned} \tag{4.31}$$

Consequently, $C_2^{\mathrm{id}}(\vec{r})=-\delta(\vec{r})/\rho_{\mathrm{b}}$ and

$$\tilde{C}_2^{\mathrm{id}}(\vec{k})=\int\mathrm{d}^2\vec{r}\,C_2^{\mathrm{id}}(\vec{r})\exp(-\mathrm{i}\vec{k}\cdot\vec{r})=-\frac{1}{\rho_{\mathrm{b}}}\int\mathrm{d}^2\vec{r}\,\delta(\vec{r})\exp(-\mathrm{i}\vec{k}\cdot\vec{r})=-\frac{1}{\rho_{\mathrm{b}}}. \tag{4.32}$$

For the latter, we go back to Eq. (2.144) to see that

$$C_2^{\mathrm{ex}}(\vec{r}_1-\vec{r}_2)=C_2^{\mathrm{ex}}(\vec{r}_1,\vec{r}_2)=-\beta\left.\frac{\delta^2\mathcal{F}_{\mathrm{ex}}[\rho]}{\delta\rho(\vec{r}_1)\delta\rho(\vec{r}_2)}\right|_{\rho=\rho_{\mathrm{b}}}=c_2(|\vec{r}_1-\vec{r}_2|) \tag{4.33}$$

is just the direct two-point correlation function in the uniform bulk and hence $\tilde{C}_2^{\mathrm{ex}}(\vec{k})=\tilde{c}_2(|\vec{k}|)$.

Combining the ideal gas and excess contributions, and recalling the definition (2.149) of the static structure factor, we readily conclude that

$$\tilde{C}_2(\vec{k}) = \tilde{C}_2^{\mathrm{id}}(\vec{k}) + \tilde{C}_2^{\mathrm{ex}}(\vec{k}) = -\frac{1}{\rho_\mathrm{b}} + \tilde{c}_2(|\vec{k}|) = -\frac{1}{\rho_\mathrm{b}}\left[1 - \rho_\mathrm{b}\tilde{c}_2(|\vec{k}|)\right] = -\frac{1}{\rho_\mathrm{b}\tilde{S}(|\vec{k}|)}, \tag{4.34}$$

and therefore

$$\lim_{V\to\infty}\frac{\beta\Delta\mathcal{F}[\rho]}{V} = \frac{1}{2\rho_\mathrm{b}}\sum_{\vec{k}\in\mathbb{K}}\frac{|\tilde{\rho}_{\vec{k}}|^2}{\tilde{S}(|\vec{k}|)} + O(\tilde{\rho}^3). \tag{4.35}$$

The interpretation of this result is straightforward: if $\tilde{S}(k_0) < 0$ for some $k_0 > 0$, then there always exists a non-uniform density distribution $\rho \neq \rho_\mathrm{b}$ with a lower intrinsic free energy density than that of the uniform bulk; for instance, choosing an arbitrary $\vec{k}_0 \in \mathbb{R}^2$ with $|\vec{k}_0| = k_0$ and setting

$$\begin{aligned}\rho(\vec{r}) &= \rho_\mathrm{b} + \tilde{\rho}_{\vec{k}_0}\exp(\mathrm{i}\vec{k}_0\cdot\vec{r}) + \tilde{\rho}_{-\vec{k}_0}\exp(-\mathrm{i}\vec{k}_0\cdot\vec{r}) = \rho_\mathrm{b} + 2\,\mathrm{Re}\left[\tilde{\rho}_{\vec{k}_0}\exp(\mathrm{i}\vec{k}_0\cdot\vec{r})\right] \\ &= \rho_\mathrm{b} + 2\,\mathrm{Re}(\tilde{\rho}_{\vec{k}_0})\cos(\vec{k}_0\cdot\vec{r}) - 2\,\mathrm{Im}(\tilde{\rho}_{\vec{k}_0})\sin(\vec{k}_0\cdot\vec{r})\end{aligned} \tag{4.36}$$

for some $\tilde{\rho}_{\vec{k}_0} = \tilde{\rho}^*_{-\vec{k}_0} \in \mathbb{C}$, we have

$$\lim_{V\to\infty}\frac{\beta\Delta\mathcal{F}[\rho]}{V} = \frac{1}{2\rho_\mathrm{b}}\left[\frac{|\tilde{\rho}_{\vec{k}_0}|^2}{\tilde{S}(|\vec{k}_0|)} + \frac{|\tilde{\rho}_{-\vec{k}_0}|^2}{\tilde{S}(|-\vec{k}_0|)}\right] + O(\tilde{\rho}^3) = \frac{1}{\rho_\mathrm{b}}\frac{|\tilde{\rho}_{\vec{k}_0}|^2}{\tilde{S}(k_0)} + O(\tilde{\rho}^3) < 0 \tag{4.37}$$

if $|\tilde{\rho}_{\vec{k}_0}|$ is sufficiently small so that the higher-order terms are negligible.

It follows that microphase separation with an inhomogeneous density distribution is mandatory in those regions of a phase diagram where $\tilde{S}$ is *not* a positive function. As the border of this region is approached from the outside, $\tilde{S}$ must develop a singularity for some k_0 with $\tilde{S}(k) \to \infty$ as $k \to k_0$ so that the energy cost of a density modulation with wavenumber k_0 just vanishes. Right on said border, which has previously been termed the *λ-line* [75], the reciprocal static structure factor $\tilde{D} \equiv 1/\tilde{S}$ is zero at k_0 but otherwise strictly positive.

In Fig. 4.2(a), $\tilde{D}$ is shown for several *bulk packing fractions* $\eta_\mathrm{b} \equiv \pi R^2\rho_\mathrm{b}$ at fixed $B = 30\,\mu\mathrm{T}$ and $\Delta T = 0.10\,\mathrm{K}$. We can see that $\tilde{D} > 0$ for $0.5 \geq \eta_\mathrm{b} \gtrsim 0.458$; for $\eta_\mathrm{b} \approx 0.458$, we find that $\tilde{D} \geq 0$ and $\tilde{D}(k_\mathrm{min}) = 0$ precisely at the global minimum k_min of $\tilde{D}$, which means that the point $(\eta_\mathrm{b}, B, \Delta T) = (0.458, 30\,\mu\mathrm{T}, 0.10\,\mathrm{K})$ lies on the λ-line. Finally, for $0.458 \gtrsim \eta_\mathrm{b} \geq 0.4$, we have $\tilde{D}(k) < 0$ for all k within a small interval around k_min so that microphase separation must occur in this regime. In Fig. 4.2(b), we plot the global minimum k_min and $\tilde{D}(k_\mathrm{min})$ as a function of η_b. The graph for $\tilde{D}(k_\mathrm{min})$ tells us that in addition to the state with $\eta_\mathrm{b} \approx 0.458$, those with $\eta_\mathrm{b} \approx 0.097$ and $\eta_\mathrm{b} \approx 0.797$ also lie on the λ-line; for $0.097 \lesssim \eta_\mathrm{b} \lesssim 0.458$ and $\eta_\mathrm{b} \gtrsim 0.797$, the system favors inhomogeneous phases since $\tilde{D}(k_\mathrm{min}) < 0$. The value of $\lambda = 2\pi/k_\mathrm{min}$ can serve

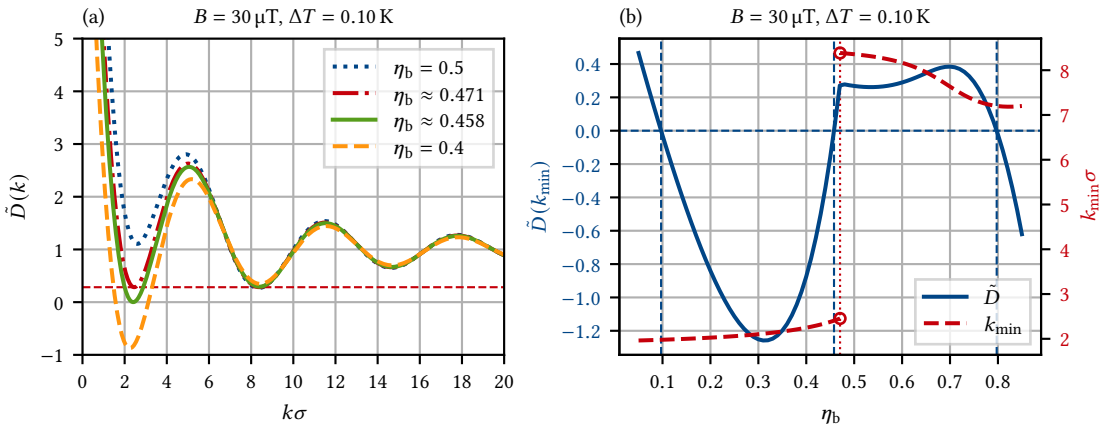

Figure 4.2.: (a) The reciprocal static structure factor $\tilde{D}(k) \equiv 1/\tilde{S}(k)$ as a function of k for $B = 30\,\mu\mathrm{T}$, $\Delta T = 0.10\,\mathrm{K}$ and several bulk packing fractions $\eta_b \equiv \pi R^2 \rho_b$. $\tilde{D}$ is strictly positive for $0.5 \gtrsim \eta_b \gtrsim 0.458$. For $0.458 \gtrsim \eta_b \gtrsim 0.4$, microphase separation must occur because $\tilde{D}(k)$ becomes negative for all k within a small interval around its global minimum $k_{\min}$. Since $\tilde{D}(k_{\min}) = 0$ for $\eta_b \approx 0.458$, the point $(\eta_b, B, \Delta T) = (0.458, 30\,\mu\mathrm{T}, 0.10\,\mathrm{K})$ lies on the λ-line. The dashed horizontal line marks the height of the first and second local minimum (both of which are simultaneously also the global minima) for $\eta_b \approx 0.471$. (b) The global minimum $k_{\min}$ and $\tilde{D}(k_{\min})$ as a function of η_b. The dashed vertical lines mark the bulk packing fractions for which $\tilde{D}(k_{\min}) = 0$, and that therefore lie on the λ-line. For $0.097 \lesssim \eta_b \lesssim 0.458$ and $\eta_b \gtrsim 0.797$, the system undergoes microphase separation since $\tilde{D}(k_{\min}) < 0$. At the bulk packing fraction marked by the dotted vertical line, $k_{\min}$ makes a discontinuous jump because the global minimum of $\tilde{D}$ shifts from the first to the second local minimum, as can be seen in (a).

as a rough estimate for the wavelength of the density oscillations of the equilibrium density distribution because the presence of a large frequency component $|\tilde{\rho}_{\vec{k}}|$ with $|\vec{k}| = k_{\min}$ would lead to a considerable reduction of the intrinsic free energy according to Eq. (4.37). At $\eta_b \approx 0.471$, there is a discontinuous jump from $k_{\min} \approx 2.45/\sigma$ to $k_{\min} \approx 8.38/\sigma$. The reason for this can be found in Fig. 4.2(a): the global minimum coincides with the first local mininum for $\eta_b \lesssim 0.471$, whereas it is located at the second local minimum for $\eta_b \gtrsim 0.471$. As a consequence, we can expect much longer density modulations with a wavelength on the order of $\lambda \approx (2\pi/2.1)\,\sigma \approx 3\sigma$ for $0.097 \lesssim \eta_b \lesssim 0.458$ than for $\eta_b \gtrsim 0.797$ where $\lambda \approx (2\pi/7.2)\sigma \approx 0.87\sigma$. A wavelength shorter than the hard disk diameter σ might appear dubious at first glance; however close-packed hard disks in a hexagonal arrangement correspond to a wavenumber of $k_{\mathrm{hcp}} = 4\pi/(\sqrt{3}\sigma) \approx 7.26/\sigma$ so that $k = 7.2/\sigma < k_{\mathrm{hcp}}$ is certainly possible and suggests crystallization. In fact, even $k > k_{\mathrm{hcp}}$ may be valid as long as the weighted density $w_\rho^2(\vec{r})$, which basically represents the "local" packing fraction at $\vec{r}$, is less then unity for all $\vec{r}$.

In Figs. 4.3, 4.4 and 4.5, numerous phase diagrams are displayed that feature the binodal, spinodal and λ-line, as well as the global minimum $k_{\min}$ of $\tilde{D}$ for those points that lie in the microphase regime (i. e., where $\tilde{D}(k_{\min}) < 0$). Since we have a three-dimensional phase space spanned by η_b, B, and ΔT, each of these figures show cross sections perpendicular to one of the three axes for

specific choices of the corresponding parameter.

In Fig. 4.3 we can see that the λ-line in the η_b–B plane changes in a rather complex manner compared to the binodal or the spinodal as ΔT increases. For $\Delta T = 0.08\,\mathrm{K}$, the microphase region is a single connected domain. While $k_{\min}$ appears to vary smoothly along the B axis, we notice a discontinous jump in the direction of η_b for $B \lesssim 40\,\mu\mathrm{T}$; the large values of $k_{\min}$ for higher packing fractions may again be indicative of a crystal-like structure. For $\Delta T = 0.0935\,\mathrm{K}$, the bridge between the low- and high-$k_{\min}$ regions only exists for very small magnetic fields; for $\Delta T \geq 0.10\,\mathrm{K}$, they are completely separated. The waist of the hourglass-shaped low-$k_{\min}$ region constricts upon further increase of ΔT until the low- and high-B domains are merely linked through a single point for $\Delta T \approx 0.1177\,\mathrm{K}$; afterwards, they break apart into a low- and an intermediate-$k_{\min}$ domain, respectively. The low-$k_{\min}$ domain then shrinks in size and eventually vanishes along with the binodal and spinodal. We note that the spinodal lies entirely within the low-B, low-$k_{\min}$ domain and approaches its border (which is just the λ-line if the low- and high-$k_{\min}$ regions are disconnected) as $B \to 0$. This makes perfectly sense: for $B = 0$, the competing interaction potential is purely attractive so that no micro-, but only regular macrophase separation with $k_{\min} = 0$ and $\tilde{D}(0) < 0$ should be possible. Thus, we can expect that $k_{\min} \to 0$ as $B \to 0$, which the phase diagrams indeed confirm; as a consequence, the defining equation of the λ-line, $\tilde{D}(k_{\min}) = 0$, becomes identical to the one of the spinodal, $\tilde{D}(0) = 0$.

In Fig. 4.4, the η_b–ΔT plane is displayed for various values of B. We see that for $B = 0$, the λ-line encloses a connected region that is split into a domain surrounded by the spinodal where $k_{\min} = 0$ and a domain where $k_{\min}$ is large. Apart from the border between these domains, the spinodal coincides precisely with the λ-line. Interpreting the high-$k_{\min}$ domain as a crystalline solid phase, we find that the phase diagram compares well with the one in Fig. 1.4(a) predicted for a system with no long-ranged repulsion (the fact that Fig. 4.4(a) – unlike Fig. 1.4(a) – does not show a fluid–solid coexistence region is simply because none was explicitly calculated). This agreement is not necessarily a given since the temperature plays a significantly different role in our model in that it directly alters the strength of the attraction between the particles rather than just determining their thermal energy (which barely changes since $\Delta T \equiv T_c - T \ll T_c$ so that $T \approx T_c$). At $B = 15\,\mu\mathrm{T}$, the former $k_{\min} = 0$ domain is replaced by one where $k_{\min}$ is non-zero but still small. The spinodal deviates noticeably from the λ-line for larger ΔT, but approaches it or the low-$k_{\min}$ boundary as $\Delta T \to 0$, where attraction dominates over repulsion and $k_{\min} \to 0$. For $B = 30\,\mu\mathrm{T}$, the binodal lies almost entirely within in the microphase regime, so that macroscopic gas–liquid coexistence is likely to be suppressed and supplanted by microphase separation as predicted in Fig. 1.4(b) for a moderate repulsion. As B increases, the critical point moves to ever lower values of ΔT until the binodal and spinodal are no longer visible. Furthermore, a second microphase region with intermediate $k_{\min}$ appears for higher ΔT and merges with the low-$k_{\min}$ domain at $B \approx 48.33\,\mu\mathrm{T}$ in a single spot before growing in width. In constrast to Fig. 1.4(c), there

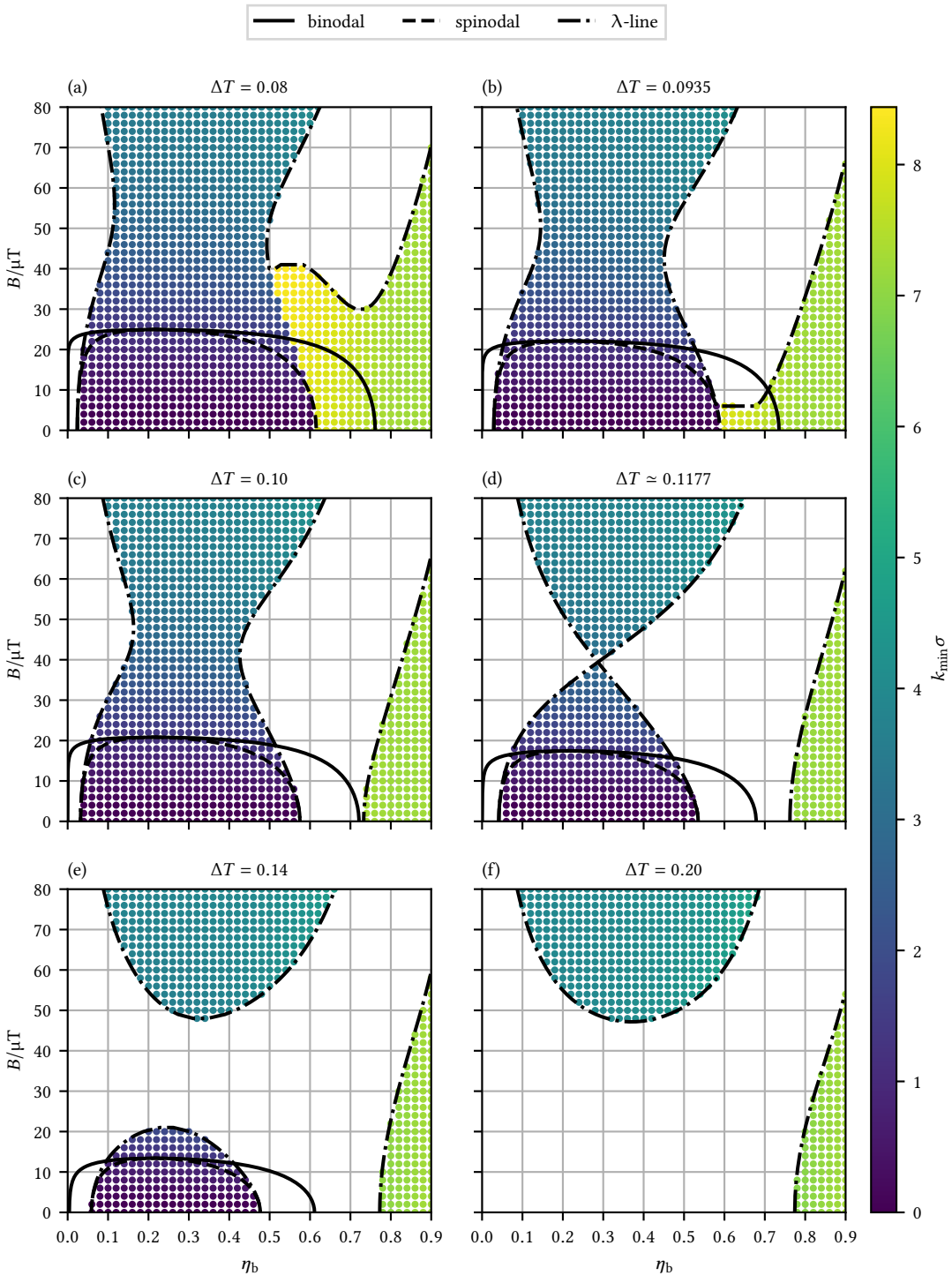

Figure 4.3.: Phase diagrams showing the binodal, spinodal and λ-line in the η_b–B plane for various values of ΔT. The symbols mark points where $\tilde{D}(k_{\min}) < 0$, i. e., where microphase separation must occur; their color encodes the global minimum $k_{\min}$ of $\tilde{D}$.

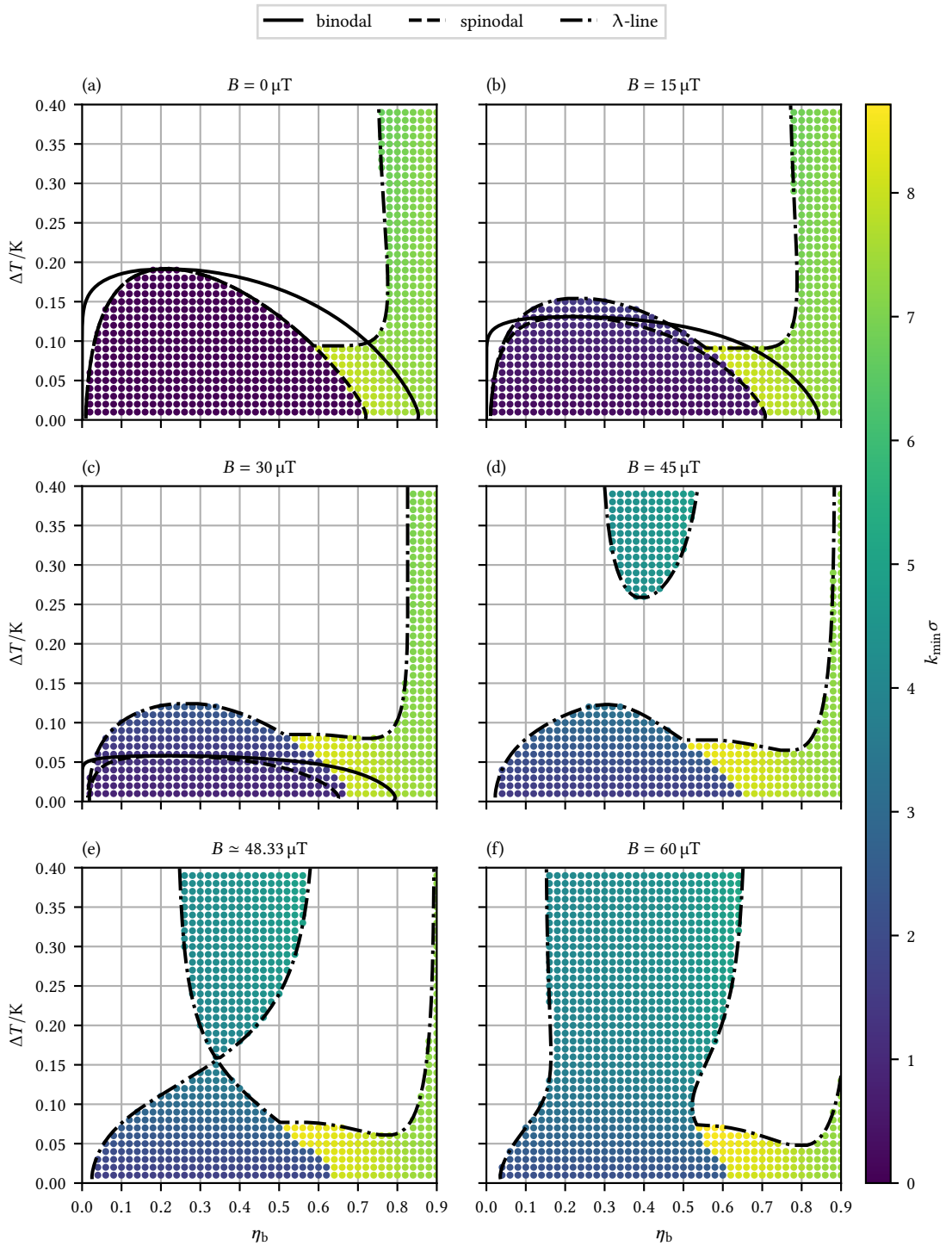

Figure 4.4.: Phase diagrams showing the binodal, spinodal and λ-line in the η_b–ΔT plane for various values of B. The symbols mark points where $\tilde{D}(k_{min}) < 0$, i. e., where microphase separation must occur; their color encodes the global minimum k_{min} of $\tilde{D}$.

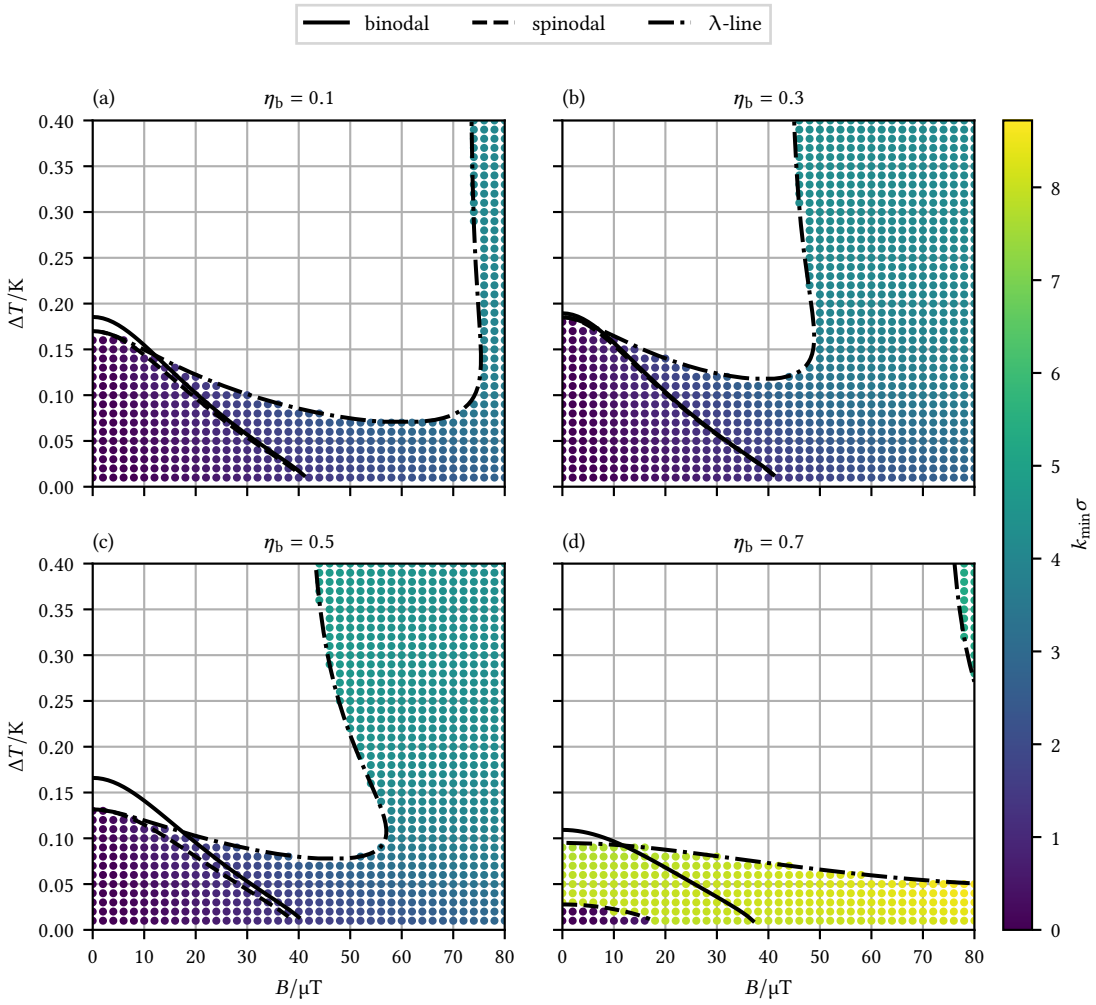

Figure 4.5.: Phase diagrams showing the binodal, spinodal and λ-line in the B–ΔT plane for various values of η_b. The symbols mark points where $\tilde{D}(k_{min}) < 0$, i. e., where microphase separation must occur; their color encodes the global minimum k_{min} of $\tilde{D}$.

are no indications that microphase separation gives way to disordered cluster or percolated fluid phases for strong repulsions.

Lastly, Fig. 4.5 shows the B–ΔT plane for different values of η_b. We see that microphase separation occurs for large B (strong repulsion) or small ΔT (strong attraction). For $\eta_b \leq 0.5$, there is no high-k_{min} region; intermediate k_{min} are found at large B and large ΔT, while small k_{min} are located at small B and small ΔT. For $\eta_b = 0.7$, a high-k_{min} region exists that contains a small low-k_{min} domain. The binodals and spinodals are the curves displayed in Fig. 4.1(b) for that value of α that corresponds to the respective η_b as given by Fig. 4.1(a).

In our three-dimensional phase space, it would arguably be more accurate to speak of a "λ-

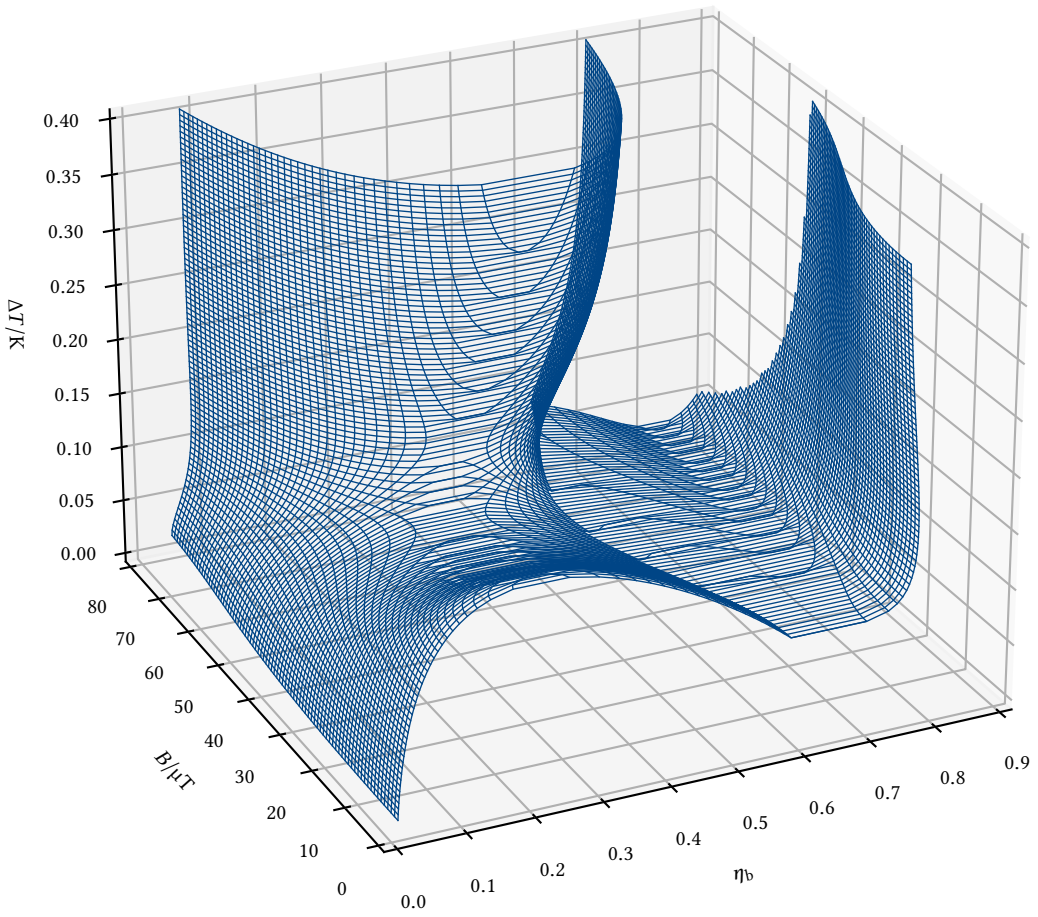

Figure 4.6.: Three-dimensional plot of the λ-surface in the phase space spanned by eta_b, B, and ΔT. At points that lie between the λ-surface and the coordinate planes in the background, the system undergoes microphase separation.

surface" rather than a λ-line. A visualization of this surface is presented in Fig. 4.6 (see also Figs. E.1 and E.2 in Appendix E for autostereograms of the same scene). At points that lie between the λ-surface and the coordinate planes in the background, the system undergoes microphase separation.

4.1.2. Landau-type theory

Now that we have ascertained where microphase separation must occur, let us continue with investigating which periodic density distributions will emerge in thermodynamic equilibrium. As already mentioned in the Introduction, Ciach et al. devised a general *Landau-type theory*

that predicts a universal sequence of microphases with increasing bulk densities [16, 17]; in two dimensions, a hexagonal droplet, a lamellar stripe and a hexagonal bubble phase were found to be stable [18–23]. To determine whether this is also true in our system, we shall now develop a Landau-type theory that is tailored to our model.

Shell expansion of the density distribution

To start with, we need to think about how to analytically express the density profiles under consideration. For our purposes, lamellar and hexagonal structures can be adequately described by functions of the form

$$\rho_{\mathrm{lam}}(\vec{r}) = \rho_0 + \sum_{i\in\mathbb{Z}} f(|x - iL_x|), \qquad \rho_{\mathrm{hex}}(\vec{r}) = \rho_0 + \sum_{i,j\in\mathbb{Z}} \sum_{n=1}^{2} f(|\vec{r} - (iL_x, jL_y) - \vec{R}_n|), \tag{4.38}$$

where $L_x/L_y = \sqrt{3}$, $\vec{R}_1 = 0$ and $\vec{R}_2 = (L_x/2, L_y/2)$ for the latter. It is clear that L_x and L_y represent the periodicity and the size of the unit cell in the x and y direction, respectively.

We can now rewrite ρ_{lam} as

$$\rho_{\mathrm{lam}}(\vec{r}) = \rho_0 + \int \mathrm{d}x'\, f(|x - x'|) \sum_{i\in\mathbb{Z}} \delta(x' - iL_x) = \rho_0 + \int \mathrm{d}x'\, f(|x - x'|)\, g_{\mathrm{lam}}(x'), \tag{4.39}$$

where the integral is the convolution $(f \otimes g_{\mathrm{lam}})(x)$ with the *Dirac comb*

$$g_{\mathrm{lam}}(x) = \sum_{i\in\mathbb{Z}} \delta(x - iL_x). \tag{4.40}$$

Since ρ_{lam} is L_x-periodic, we can use the convolution theorem and expand it in the Fourier series

$$\rho_{\mathrm{lam}}(\vec{r}) = \tilde{\rho}_0^{\mathrm{lam}} + \sum_{\vec{k}\in\mathbb{K}} \tilde{\rho}_{\vec{k}}^{\mathrm{lam}} \exp(\mathrm{i}\vec{k}\cdot\vec{r}) = \rho_{\mathrm{b}} + \sum_{\vec{k}\in\mathbb{K}} \tilde{f}(|\vec{k}|)\, \tilde{g}_{\vec{k}}^{\mathrm{lam}} \exp(\mathrm{i}\vec{k}\cdot\vec{r}) \tag{4.41}$$

with $\mathbb{K} \equiv \{(2\pi j/L_x, 0) : j \in \mathbb{Z}\setminus\{0\}\}$. The Fourier coefficients of g_{lam}, which itself is also L_x-periodic, are easily calculated as

$$\tilde{g}_{\vec{k}}^{\mathrm{lam}} \equiv \int_{-L_x/2}^{L_x/2} \mathrm{d}x\, g_{\mathrm{lam}}(x) \exp(-\mathrm{i}k_x x) = \int_{-L_x/2}^{L_x/2} \mathrm{d}x \sum_{i\in\mathbb{Z}} \delta(x - iL_x) \exp(-\mathrm{i}k_x x) = 1. \tag{4.42}$$

Let us now partition $\mathbb{K}$ into mutually disjoint *shells* $(\mathbb{K}_s)_{s\in\mathbb{N}}$ where all elements of $\mathbb{K}_s$ are of equal magnitude k_s that increases with each shell: $|\vec{k}| = k_s$ precisely if $\vec{k} \in \mathbb{K}_s$ and $k_s < k_{s+1}$ for all $s \in \mathbb{N}$; it is easy to see that $\mathbb{K}_s = \{(-2\pi s/L_x, 0), (2\pi s/L_x, 0)\}$ with $k_s = 2\pi s/L_x$. This allows us to

write the lamellar density distribution as

$$\rho_{\mathrm{lam}}(\vec{r}) = \rho_{\mathrm{b}} + \sum_{s=1}^{\infty} \tilde{f}(k_s) \sum_{\vec{k}\in\mathbb{K}_s} \tilde{g}_{\vec{k}}^{\mathrm{lam}} \exp(\mathrm{i}\vec{k}\cdot\vec{r}) = \rho_{\mathrm{b}} + \sum_{s=1}^{\infty} \Phi_s \, g_s^{\mathrm{lam}}(\vec{r}) \tag{4.43}$$

with the amplitudes $\Phi_s \equiv \tilde{f}(k_s)$ and

$$g_s^{\mathrm{lam}}(\vec{r}) \equiv \sum_{\vec{k}\in\mathbb{K}_s} g_{\vec{k}}^{\mathrm{lam}} \exp(\mathrm{i}\vec{k}\cdot\vec{r}) = \exp\left(-\mathrm{i}\frac{2\pi s}{L_x}x\right) + \exp\left(\mathrm{i}\frac{2\pi s}{L_x}x\right) = 2\cos\left(\frac{2\pi s}{L_x}x\right). \tag{4.44}$$

For the hexagonal structure, we similarly find that

$$\rho_{\mathrm{hex}}(\vec{r}) = \rho_0 + \int \mathrm{d}^2\vec{r}' \, f(|\vec{r}-\vec{r}'|)\, g_{\mathrm{hex}}(\vec{r}') = \rho_{\mathrm{b}} + \sum_{\vec{k}\in\mathbb{K}} \tilde{f}(|\vec{k}|)\, \tilde{g}_{\vec{k}}^{\mathrm{hex}} \exp(\mathrm{i}\vec{k}\cdot\vec{r}) \tag{4.45}$$

with

$$g_{\mathrm{hex}}(\vec{r}) = \sum_{i,j\in\mathbb{Z}} \sum_{n=1}^{2} \delta(\vec{r} - (iL_x, jL_y) - \vec{R}_n), \tag{4.46}$$

wave vectors $\mathbb{K} \equiv \{2\pi\,(i/L_x, j/L_y) : (i,j) \in \mathbb{Z}^2\backslash\{0\}\}$ and

$$\begin{aligned} \tilde{g}_{\vec{k}=2\pi\binom{i/L_x}{j/L_y}}^{\mathrm{hex}} &\equiv \int_{[0,L_x]\times[0,L_y]} \mathrm{d}^2\vec{r}\, g_{\mathrm{hex}}(\vec{r}) \exp(-\mathrm{i}\vec{k}\cdot\vec{r}) = 1 + \exp\left[-\mathrm{i}\left(\frac{2\pi i}{L_x}\frac{L_x}{2} + \frac{2\pi j}{L_y}\frac{L_y}{2}\right)\right] \\ &= 1 + \exp[-\mathrm{i}\pi(i+j)] = \begin{cases} 2 & \text{if } i+j \text{ is even,} \\ 0 & \text{otherwise.} \end{cases} \end{aligned} \tag{4.47}$$

Thus, actually only the wave vectors in $\mathbb{K} \equiv \{2\pi\,(i/L_x, j/L_y) : (i,j) \in \mathbb{Z}^2\backslash\{0\}, i+j \text{ is even}\}$ give a non-trivial contribution to ρ_{hex} and are therefore relevant. Splitting this reduced set into shells $(\mathbb{K}_s)_{s\in\mathbb{N}}$ of equal magnitudes $(k_s)_{s\in\mathbb{N}}$, we then have

$$\rho_{\mathrm{hex}}(\vec{r}) = \rho_{\mathrm{b}} + \sum_{s=1}^{\infty} \Phi_s \, g_s^{\mathrm{hex}}(\vec{r}) \tag{4.48}$$

with the amplitudes $\Phi_s \equiv \tilde{f}(k_s)$ and

$$g_s^{\mathrm{hex}}(\vec{r}) \equiv \sum_{\vec{k}\in\mathbb{K}_s} \tilde{g}_{\vec{k}}^{\mathrm{hex}} \exp(\mathrm{i}\vec{k}\cdot\vec{r}) \equiv \sum_{\vec{k}\in\mathbb{K}_s} 2\exp(\mathrm{i}\vec{k}\cdot\vec{r}) = 2\sum_{\vec{k}\in\mathbb{K}_s} \cos(\vec{k}\cdot\vec{r}). \tag{4.49}$$

The first shell, for instance, has magnitude $k_1 = 4\pi/L_x = 4\pi/(\sqrt{3}L_y)$ and is given by

$$\begin{aligned} \mathbb{K}_1 = \{ \quad & 2\pi(1/L_x, 1/L_y), \quad 2\pi(1/L_x, -1/L_y), \quad 2\pi(2/L_x, 0), \\ & -2\pi(1/L_x, 1/L_y), -2\pi(1/L_x, -1/L_y), -2\pi(2/L_x, 0)\}, \end{aligned} \tag{4.50}$$

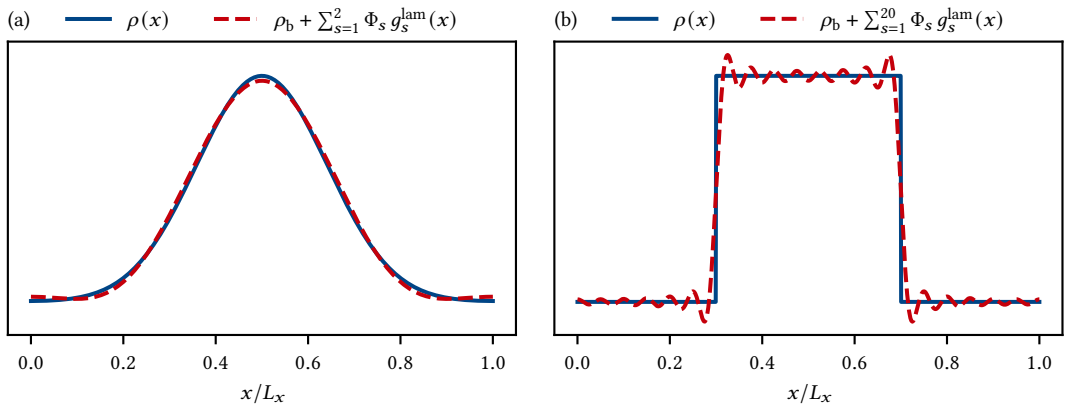

Figure 4.7.: (a) A hypothetical lamellar density profile $\rho(x)$ with a Gaussian peak (solid line) and its two-shell expansion $\rho_b + \sum_{s=1}^{2} \Phi_s g_s^{lam}(x)$ (dashed line) as a function of x; the agreement is already quite good. (b) A hypothetical lamellar density profile $\rho(x)$ with a rectangular peak (solid line) and its 20-shell expansion $\rho_b + \sum_{s=1}^{20} \Phi_s g_s^{lam}(x)$ (dashed line) as a function of x; the agreement is arguably worse than in (a), even though a lot more shells were incorporated.

so that

$$\begin{aligned} g_1^{hex}(\vec{r}) &= 4\left[\cos\left(\frac{2\pi x}{L_x} + \frac{2\pi y}{L_y}\right) + \cos\left(\frac{2\pi x}{L_x} - \frac{2\pi y}{L_y}\right) + \cos\left(\frac{4\pi x}{L_x}\right)\right] \\ &= 8\cos\left(\frac{2\pi x}{L_x}\right)\cos\left(\frac{2\pi y}{L_y}\right) + 4\cos\left(\frac{4\pi x}{L_x}\right). \end{aligned} \tag{4.51}$$

We see that both lamellar and hexagonal density distributions can be written as a "shell expansion" of the form

$$\rho(\vec{r}) = \rho_b + \sum_{s=1}^{\infty} \Phi_s\, g_s(\vec{r}) = \rho_b + \sum_{s=1}^{\infty} \Phi_s \sum_{\vec{k}\in\mathbb{K}_s} \tilde{g}_{\vec{k}} \exp(i\vec{k}\cdot\vec{r}), \tag{4.52}$$

where the functions g_s are universal for a given structure (lamellar or hexagonal) and the coefficients Φ_s determine the concrete shape of the fluctuations. The advantage of this representation is that lower shells are generally more significant than higher ones, so that many density profiles can be well approximated even if the summation in Eq. (4.52) is terminated after a few dozen (or even only a handful) of terms. In Fig. 4.7(a), a lamellar density distribution with a Gaussian peak as well as its two-shell expansion are plotted. The agreement is already quite good; if the third shell had also been included, the curves would be essentially indistinguishable. However, if the density profile changes abruptly such as in the case of the rectangular peak shown in Fig. 4.7(b), a lot more shells may be required for a sufficiently accurate description.

Free energy density of the $\hat{s}$-shell approximation

In the following, we shall assume density distributions in the $\hat{s}$-shell approximation, i. e.,

$$\rho(\vec{r}) = \rho_\mathrm{b} + \Delta\rho(\vec{r}) \;\text{ with }\; \Delta\rho(\vec{r}) = \sum_{s=1}^{\hat{s}} \Phi_s\, g_s(\vec{r}) = \sum_{s=1}^{\hat{s}} \Phi_s \sum_{\vec{k}\in\mathbb{K}_s} \tilde{g}_{\vec{k}} \exp(\mathrm{i}\vec{k}\cdot\vec{r}). \tag{4.53}$$

To calculate the intrinsic free energy $\mathcal{F}[\rho] = \mathcal{F}[\rho_\mathrm{b} + \Delta\rho]$ for such a density profile, we can now again perform a functional Taylor expansion of $\mathcal{F}$ around ρ_b as in Eq. (4.20) and find that

$$\lim_{V\to\infty} \frac{\beta\Delta\mathcal{F}[\rho]}{V} = -\sum_{n=1}^{\infty} \frac{1}{n!} \sum_{s_1,\ldots,s_n=1}^{\hat{s}} \Phi_{s_1}\cdots\Phi_{s_n} \sum_{\vec{k}_1\in\mathbb{K}_{s_1}}^{\vec{k}_1+\cdots+\vec{k}_n=0} \cdots \sum_{\vec{k}_n\in\mathbb{K}_{s_n}} \tilde{g}_{\vec{k}_1}\cdots\tilde{g}_{\vec{k}_n}\, \tilde{C}_n(-\vec{k}_1,\ldots,-\vec{k}_{n-1}) \tag{4.54}$$

for $\Delta\mathcal{F}[\rho] \equiv \mathcal{F}[\rho] - \mathcal{F}[\rho_\mathrm{b}]$ with only a slight variation of the derivation that led to Eq. (4.29). Next, we use that the terms to the right of the sum over the shells in Eq. (4.54) are identical for every permutation of $s_1,\ldots,s_n$. For example, consider the cases $(s_1,s_2,s_3) = (1,1,2)$ and $(s_1,s_2,s_3) = (1,2,1)$ for $n = 3$; then

$$\Phi_1\Phi_1\Phi_2 \sum_{\vec{k}_1\in\mathbb{K}_1,\,\vec{k}_2\in\mathbb{K}_1,\,\vec{k}_3\in\mathbb{K}_2}^{\vec{k}_1+\vec{k}_2+\vec{k}_3=0} \tilde{g}_{\vec{k}_1}\tilde{g}_{\vec{k}_2}\tilde{g}_{\vec{k}_3}\tilde{C}_3(-\vec{k}_1,-\vec{k}_2) = \Phi_1\Phi_2\Phi_1 \sum_{\vec{k}_1\in\mathbb{K}_1,\,\vec{k}_2\in\mathbb{K}_2,\,\vec{k}_3\in\mathbb{K}_1}^{\vec{k}_1+\vec{k}_2+\vec{k}_3=0} \tilde{g}_{\vec{k}_1}\tilde{g}_{\vec{k}_2}\tilde{g}_{\vec{k}_3}\tilde{C}_3(-\vec{k}_1,-\vec{k}_2). \tag{4.55}$$

This equality is actually not as obvious as it might seem at first glance because there is a subtle asymmetry: on the left hand side, the wave vector $\vec{k}_2$ that enters into $\tilde{C}_3$ is from the first shell, $\vec{k}_2 \in \mathbb{K}_1$, whereas on the right hand side, it is from the second shell, $\vec{k}_2 \in \mathbb{K}_2$. However, because $\vec{k}_1 + \vec{k}_2 + \vec{k}_3 = 0$, it turns out that we can exchange $\tilde{C}_3(-\vec{k}_1,-\vec{k}_2)$ for $\tilde{C}_3(-\vec{k}_1,-\vec{k}_3)$ on one side, so that the second argument to $\tilde{C}_3$ is from the same shell as on the other. This substitution is possible because $\tilde{C}_n(\vec{k}_1,\ldots,\vec{k}_{n-1})$ is invariant under replacement of any single argument with $\vec{k}_n \equiv -(\vec{k}_1+\cdots+\vec{k}_{n-1})$. Since the proof is easily generalized, we shall only show the special case $\tilde{C}_3(\vec{k}_1,\vec{k}_2) = \tilde{C}_3(\vec{k}_1,-\vec{k}_1-\vec{k}_2)$. Recall that $C_n(\vec{r}_1,\ldots,\vec{r}_{n-1}) = C_n(\vec{r}_1+\Delta\vec{r},\ldots,\vec{r}_{n-1}+\Delta\vec{r},\Delta\vec{r})$ for any $\Delta\vec{r}$ and note that the order of the arguments in $C_n(\vec{r}_1,\ldots,\vec{r}_n)$ is irrelevant due to its definition in terms of commuting functional derivatives. Thus, we have

$$\begin{aligned}
\tilde{C}_3(\vec{k}_1,-\vec{k}_1-\vec{k}_2) &= \int \mathrm{d}^2\vec{r}_1 \int \mathrm{d}^2\vec{r}_2\, C_3(\vec{r}_1,\vec{r}_2) \exp(-\mathrm{i}\vec{k}_1\cdot\vec{r}_1) \exp[\mathrm{i}(\vec{k}_1+\vec{k}_2)\cdot\vec{r}_2] \\
&= \int \mathrm{d}^2\vec{r}_2 \int \mathrm{d}^2\vec{r}_1 \underbrace{C_3(\vec{r}_1-\vec{r}_2,-\vec{r}_2)}_{=C_3(\vec{r}_1,0,\vec{r}_2)=C_3(\vec{r}_1,\vec{r}_2,0)=C_3(\vec{r}_1,\vec{r}_2)} \exp[-\mathrm{i}\vec{k}_1\cdot(\vec{r}_1-\vec{r}_2)] \exp[-\mathrm{i}(\vec{k}_1+\vec{k}_2)\cdot\vec{r}_2] \\
&= \int \mathrm{d}^2\vec{r}_1 \int \mathrm{d}^2\vec{r}_2\, C_3(\vec{r}_1,\vec{r}_2) \exp(-\mathrm{i}\vec{k}_1\cdot\vec{r}_1) \exp(-\mathrm{i}\vec{k}_2\cdot\vec{r}_2) = \tilde{C}_3(\vec{k}_1,\vec{k}_2).
\end{aligned} \tag{4.56}$$

This means that we can rewrite the sum over $s_1, \ldots, s_n$ in Eq. (4.54) by collecting those terms in which the first shell appears n_1 times, the second shell n_2 times, ... and the $\hat{s}$-th shell $n_{\hat{s}}$ times under the constraint that $n_1 + \cdots + n_{\hat{s}} = n$. Since there are $n!/(n_1! \cdots n_{\hat{s}}!)$ such terms, we find that

$$\begin{aligned}\lim_{V\to\infty} \frac{\beta\Delta\mathcal{F}[\rho]}{V} &= -\sum_{n=1}^{\infty} \frac{1}{n!} \sum_{n_1\in\mathbb{N}_0}^{n_1+\cdots+n_{\hat{s}}=n} \cdots \sum_{n_{\hat{s}}\in\mathbb{N}_0} \frac{n!}{n_1! \cdots n_{\hat{s}}!} \Phi_1^{n_1} \cdots \Phi_{\hat{s}}^{n_{\hat{s}}} \sum_{(\vec{k}_1,\ldots,\vec{k}_n)\in\mathbb{K}^{n_1,\ldots,n_{\hat{s}}}}^{\vec{k}_1+\cdots+\vec{k}_n=0} \tilde{g}_{\vec{k}_1} \cdots \tilde{g}_{\vec{k}_n} \tilde{C}_n(-\vec{k}_1, \ldots, -\vec{k}_{n-1}) \\ &= \sum_{n=1}^{\infty} \frac{1}{n!} \sum_{n_1\in\mathbb{N}_0}^{n_1+\cdots+n_{\hat{s}}=n} \cdots \sum_{n_{\hat{s}}\in\mathbb{N}_0} \Phi_1^{n_1} \cdots \Phi_{\hat{s}}^{n_{\hat{s}}} A_{n_1,\ldots,n_{\hat{s}}}, \end{aligned} \tag{4.57}$$

where the set $\mathbb{K}^{n_1,\ldots,n_{\hat{s}}} \equiv \mathbb{K}_1^{n_1} \times \cdots \times \mathbb{K}_{\hat{s}}^{n_{\hat{s}}}$ contains all n-tuples consisting of n_1 wave vectors from the first shell, followed by n_2 from the second, ... and finally $n_{\hat{s}}$ wave vectors from the $\hat{s}$-th shell, and where

$$A_{n_1,\ldots,n_{\hat{s}}} \equiv -\frac{n!}{n_1! \cdots n_{\hat{s}}!} \sum_{(\vec{k}_1,\ldots,\vec{k}_n)\in\mathbb{K}^{n_1,\ldots,n_{\hat{s}}}}^{\vec{k}_1+\cdots+\vec{k}_n=0} \tilde{g}_{\vec{k}_1} \cdots \tilde{g}_{\vec{k}_n} \tilde{C}_n(-\vec{k}_1, \ldots, -\vec{k}_{n-1}) \tag{4.58}$$

for $n = n_1 + \cdots + n_{\hat{s}}$. We can simplify this result by recognizing that there is again no contribution for $n = 1$ since $\vec{k}_1 \neq 0$; furthermore, for $n = 2$, the condition $\vec{k}_1 + \vec{k}_2 = 0$ cannot be satisfied if both vectors are from different shells. We therefore arrive at

$$\lim_{V\to\infty} \frac{\beta\Delta\mathcal{F}[\rho]}{V} = -\frac{1}{2} \sum_{s=1}^{\hat{s}} \Phi_s^2 \tilde{C}_2(k_s)\, \kappa_s + \sum_{n=3}^{\infty} \frac{1}{n!} \sum_{n_1\in\mathbb{N}_0}^{n_1+\cdots+n_{\hat{s}}=n} \cdots \sum_{n_{\hat{s}}\in\mathbb{N}_0} \Phi_1^{n_1} \cdots \Phi_{\hat{s}}^{n_{\hat{s}}} A_{n_1,\ldots,n_{\hat{s}}}, \tag{4.59}$$

where we used that $\tilde{C}_2(\vec{k}) = \tilde{C}_2(|\vec{k}|) = \tilde{C}_2(k_s)$ for $\vec{k} \in \mathbb{K}_s$ and defined

$$\kappa_s \equiv \sum_{\vec{k}_1,\vec{k}_2\in\mathbb{K}_s}^{\vec{k}_1+\vec{k}_2=0} \tilde{g}_{\vec{k}_1}\, \tilde{g}_{\vec{k}_2} = \sum_{\vec{k}\in\mathbb{K}_s} \tilde{g}_{\vec{k}}\, \tilde{g}_{-\vec{k}} = \sum_{\vec{k}\in\mathbb{K}_s} \tilde{g}_{\vec{k}}\, \tilde{g}_{\vec{k}}^{*} = \sum_{\vec{k}\in\mathbb{K}_s} |\tilde{g}_{\vec{k}}|^2. \tag{4.60}$$

In order to be able to evaluate Eq. (4.59) for our system, we now need to determine the correlation functions $\tilde{C}_n$ for $n \geq 2$. This is best accomplished by dealing with the contributions from $\mathcal{F}_{\text{id}}$, $\mathcal{F}_{\text{hd}}^{\text{ex}}$ and $\mathcal{F}_{\text{ci}}^{\text{ex}}$ separately.

Starting with the ideal gas, we find that

$$\beta \frac{\delta^n \mathcal{F}_{\text{id}}[\rho]}{\delta\rho(\vec{r}_1) \cdots \delta\rho(\vec{r}_n)} = \phi_{\text{id}}^{(n)}(\rho(\vec{r}_1))\, \delta(\vec{r}_1 - \vec{r}_n) \cdots \delta(\vec{r}_{n-1} - \vec{r}_n), \tag{4.61}$$

where

$$\phi_{\mathrm{id}}^{(n)}(\rho) \equiv \frac{\mathrm{d}^n}{\mathrm{d}\rho^n}\phi_{\mathrm{id}}(\rho) = \frac{\mathrm{d}^n}{\mathrm{d}\rho^n}\left[\rho\{\ln(\Lambda^2\rho)-1\}\right] = \begin{cases} \ln(\Lambda^2\rho) & \text{if } n=1, \\ -(n-2)!/(-\rho)^{n-1} & \text{if } n\geq 2. \end{cases} \tag{4.62}$$

Hence, $C_n^{\mathrm{id}}(\vec{r}_1,\ldots,\vec{r}_{n-1}) = -\phi_{\mathrm{id}}^{(n)}(\rho_\mathrm{b})\,\delta(\vec{r}_1)\cdots\delta(\vec{r}_{n-1})$ and

$$\tilde{C}_n^{\mathrm{id}}(\vec{k}_1,\ldots,\vec{k}_{n-1}) = -\phi_{\mathrm{id}}^{(n)}(\rho_\mathrm{b})\prod_{j=1}^{n-1}\Bigg[\underbrace{\int \mathrm{d}^2\vec{r}_j\,\delta(\vec{r}_j)\exp(-\mathrm{i}\vec{k}_j\cdot\vec{r}_j)}_{=1}\Bigg] = -\phi_{\mathrm{id}}^{(n)}(\rho_\mathrm{b}), \tag{4.63}$$

which leads to

$$\lim_{V\to\infty}\frac{\beta\Delta\mathcal{F}_{\mathrm{id}}[\rho]}{V} = \frac{1}{2}\sum_{s=1}^{\hat{s}}\Phi_s^2\frac{\kappa_s}{\rho_\mathrm{b}} + \sum_{n=3}^{\infty}\frac{1}{n!}\sum_{n_1\in\mathbb{N}_0}^{n_1+\cdots+n_{\hat{s}}=n}\cdots\sum_{n_{\hat{s}}\in\mathbb{N}_0}\Phi_1^{n_1}\cdots\Phi_{\hat{s}}^{n_{\hat{s}}}A^{\mathrm{id}}_{n_1,\ldots,n_{\hat{s}}} \tag{4.64}$$

with

$$A^{\mathrm{id}}_{n_1,\ldots,n_{\hat{s}}} = \frac{n!}{n_1!\cdots n_{\hat{s}}!}\phi_{\mathrm{id}}^{(n)}(\rho_\mathrm{b})\sum_{(\vec{k}_1,\ldots,\vec{k}_n)\in\mathbb{K}^{n_1,\ldots,n_{\hat{s}}}}^{\vec{k}_1+\cdots+\vec{k}_n=0}\tilde{g}_{\vec{k}_1}\cdots\tilde{g}_{\vec{k}_n} = -\frac{n!}{n_1!\cdots n_{\hat{s}}!}\frac{(n-2)!}{(-\rho_\mathrm{b})^{n-1}}\sum_{(\vec{k}_1,\ldots,\vec{k}_n)\in\mathbb{K}^{n_1,\ldots,n_{\hat{s}}}}^{\vec{k}_1+\cdots+\vec{k}_n=0}\tilde{g}_{\vec{k}_1}\cdots\tilde{g}_{\vec{k}_n}. \tag{4.65}$$

The n-th functional derivative of $\mathcal{F}_{\mathrm{hd}}^{\mathrm{ex}}$ is given by

$$\begin{aligned}\beta\frac{\delta^n\mathcal{F}_{\mathrm{hd}}^{\mathrm{ex}}[\rho]}{\delta\rho(\vec{r}_1)\cdots\delta\rho(\vec{r}_n)} &= \int\mathrm{d}^2\vec{r}\,\frac{\delta^n\phi_\rho^{\mathrm{hd}}(\vec{r})}{\delta\rho(\vec{r}_1)\cdots\delta\rho(\vec{r}_n)} = \int\mathrm{d}^2\vec{r}\sum_{w^1,\ldots,w^n}\frac{\delta^n\phi_\rho^{\mathrm{hd}}(\vec{r})}{\partial w_\rho^1\cdots\partial w_\rho^n}\frac{\delta w_\rho^1(\vec{r})}{\delta\rho(\vec{r}_1)}\cdots\frac{\delta w_\rho^n(\vec{r})}{\delta\rho(\vec{r}_n)} \\ &= \int\mathrm{d}^2\vec{r}\sum_{w^1,\ldots,w^n}\frac{\partial^n\phi_\rho^{\mathrm{hd}}(\vec{r})}{\partial w_\rho^1\cdots\partial w_\rho^n}\,\omega^1(\vec{r}-\vec{r}_1)\cdots\omega^n(\vec{r}-\vec{r}_n),\end{aligned} \tag{4.66}$$

where the sum runs over all nine scalar components of the weighted densities w^0, w^2, $\boldsymbol{w}^0$ (each with one component), $\boldsymbol{w}^1$ (with two components) and $\boldsymbol{w}^2$ (with four components), and ω^j denotes the weight function corresponding to the component w^j so that

$$\frac{\delta w_\rho^j(\vec{r})}{\delta\rho(\vec{r}_j)} = \frac{\delta}{\delta\rho(\vec{r}_j)}\int\mathrm{d}^2\vec{r}'\,\rho(\vec{r}')\,\omega^j(\vec{r}-\vec{r}') = \int\mathrm{d}^2\vec{r}'\,\underbrace{\frac{\delta\rho(\vec{r}')}{\delta\rho(\vec{r}_j)}}_{=\delta(\vec{r}'-\vec{r}_j)}\omega^j(\vec{r}-\vec{r}') = \omega^j(\vec{r}-\vec{r}_j). \tag{4.67}$$

For a uniform $\rho=\rho_\mathrm{b}$, the derivative of $\phi_\rho^{\mathrm{hd}}(\vec{r})$ becomes independent of $\vec{r}$ and we have

$$\tilde{C}_n^{\mathrm{hd}}(\vec{r}_1,\ldots,\vec{r}_{n-1}) = -\sum_{w^1,\ldots,w^n}\frac{\partial^n\phi_{\rho_\mathrm{b}}^{\mathrm{hd}}}{\partial w_{\rho_\mathrm{b}}^1\cdots\partial w_{\rho_\mathrm{b}}^n}\int\mathrm{d}^2\vec{r}\,\omega^1(\vec{r}-\vec{r}_1)\cdots\omega^{n-1}(\vec{r}-\vec{r}_{n-1})\,\omega^n(\vec{r}). \tag{4.68}$$

Calculating the Fourier transform, we find that

$$\begin{aligned}\tilde{C}_n^{\mathrm{hd}}(\vec{k}_1,\ldots,\vec{k}_{n-1}) &= -\sum_{w^1,\ldots,w^n} \frac{\partial^n \phi^{\mathrm{hd}}_{\rho_\mathrm{b}}}{\partial w^1_{\rho_\mathrm{b}} \cdots \partial w^n_{\rho_\mathrm{b}}} \int \mathrm{d}^2\vec{r} \prod_{j=1}^{n-1} \left[\int \mathrm{d}^2\vec{r}_j\, \omega^j(\vec{r}-\vec{r}_j) \exp(-\mathrm{i}\vec{k}_j\cdot\vec{r}_j) \right] \omega^n(\vec{r}) \\ &= -\sum_{w^1,\ldots,w^n} \frac{\partial^n \phi^{\mathrm{hd}}_{\rho_\mathrm{b}}}{\partial w^1_{\rho_\mathrm{b}} \cdots \partial w^n_{\rho_\mathrm{b}}} \int \mathrm{d}^2\vec{r} \prod_{j=1}^{n-1} \left[\int \mathrm{d}^2\vec{r}'_j\, \omega^j(\vec{r}'_j) \exp\{-\mathrm{i}\vec{k}_j\cdot(\vec{r}-\vec{r}'_j)\} \right] \omega^n(\vec{r}) \\ &= -\sum_{w^1,\ldots,w^n} \frac{\partial^n \phi^{\mathrm{hd}}_{\rho_\mathrm{b}}}{\partial w^1_{\rho_\mathrm{b}} \cdots \partial w^n_{\rho_\mathrm{b}}} \prod_{j=1}^{n-1} \left[\int \mathrm{d}^2\vec{r}'_j\, \omega^j(\vec{r}'_j) \exp[-\mathrm{i}(-\vec{k}_j)\cdot\vec{r}'_j] \right] \\ &\qquad\qquad \times \int \mathrm{d}^2\vec{r}\, \omega^n(\vec{r}) \exp[-\mathrm{i}(\vec{k}_1+\cdots+\vec{k}_{n-1})\cdot\vec{r}]\end{aligned}$$

by performing the substitution $\vec{r}_j \to \vec{r}'_j \equiv \vec{r}-\vec{r}_j$ and rearranging some terms. We identify the integrals as the Fourier transforms of the weight functions and arrive at

$$\tilde{C}_n^{\mathrm{hd}}(\vec{k}_1,\ldots,\vec{k}_{n-1}) = -\sum_{w^1,\ldots,w^n} \frac{\partial^n \phi^{\mathrm{hd}}_{\rho_\mathrm{b}}}{\partial w^1_{\rho_\mathrm{b}} \cdots \partial w^n_{\rho_\mathrm{b}}} \tilde{\omega}^1(-\vec{k}_1)\cdots\tilde{\omega}^{n-1}(-\vec{k}_{n-1})\, \tilde{\omega}^n(\vec{k}_1+\cdots+\vec{k}_{n-1}). \tag{4.69}$$

Noting that $\tilde{C}_2^{\mathrm{hd}}(\vec{k}) = \tilde{c}_2^{\mathrm{hd}}(|\vec{k}|)$, where $\tilde{c}_2^{\mathrm{hd}}$ is the Fourier transform of the hard disk direct two-point correlation function, we see that

$$\lim_{V\to\infty} \frac{\beta\Delta\mathcal{F}^{\mathrm{ex}}_{\mathrm{hd}}[\rho]}{V} = -\frac{1}{2}\sum_{s=1}^{\hat{s}} \Phi_s^2\, \tilde{c}_2^{\mathrm{hd}}(k_s)\,\kappa_s + \sum_{n=3}^{\infty} \frac{1}{n!} \sum_{n_1\in\mathbb{N}_0}^{n_1+\cdots+n_{\hat{s}}=n} \cdots \sum_{n_{\hat{s}}\in\mathbb{N}_0} \Phi_1^{n_1}\cdots\Phi_{\hat{s}}^{n_{\hat{s}}} A^{\mathrm{hd}}_{n_1,\ldots,n_{\hat{s}}} \tag{4.70}$$

with

$$\begin{aligned}A^{\mathrm{hd}}_{n_1,\ldots,n_{\hat{s}}} &\equiv \frac{n!}{n_1!\cdots n_{\hat{s}}!} \sum_{(\vec{k}_1,\ldots,\vec{k}_n)\in\mathbb{K}^{n_1,\ldots,n_{\hat{s}}}}^{\vec{k}_1+\cdots+\vec{k}_n=0} \tilde{g}_{\vec{k}_1}\cdots\tilde{g}_{\vec{k}_n} \sum_{w^1,\ldots,w^n} \frac{\partial^n \phi^{\mathrm{hd}}_{\rho_\mathrm{b}}}{\partial w^1_{\rho_\mathrm{b}} \cdots \partial w^n_{\rho_\mathrm{b}}} \tilde{\omega}^1(\vec{k}_1)\cdots\tilde{\omega}^{n-1}(\vec{k}_{n-1}) \\ &\qquad\qquad \times \tilde{\omega}^n(-\vec{k}_1-\cdots-\vec{k}_{n-1}) \qquad (4.71) \\ &= \frac{n!}{n_1!\cdots n_{\hat{s}}!} \sum_{w^1,\ldots,w^n} \frac{\partial^n \phi^{\mathrm{hd}}_{\rho_\mathrm{b}}}{\partial w^1_{\rho_\mathrm{b}} \cdots \partial w^n_{\rho_\mathrm{b}}} \sum_{(\vec{k}_1,\ldots,\vec{k}_n)\in\mathbb{K}^{n_1,\ldots,n_{\hat{s}}}}^{\vec{k}_1+\cdots+\vec{k}_n=0} \tilde{g}_{\vec{k}_1}\cdots\tilde{g}_{\vec{k}_n} \tilde{\omega}^1(\vec{k}_1)\cdots\tilde{\omega}^n(\vec{k}_n),\end{aligned}$$

where we used that $\vec{k}_n = -\vec{k}_1-\cdots-\vec{k}_{n-1}$ since the wave vectors sum to zero.

The competing interactions contribution is the least complicated of the three: because

$$\beta\frac{\delta^n\mathcal{F}^{\mathrm{ex}}_{\mathrm{ci}}[\rho]}{\delta\rho(\vec{r}_1)\cdots\delta\rho(\vec{r}_n)} = \begin{cases} \beta u_{\mathrm{ci}}(|\vec{r}_1-\vec{r}_2|) & \text{if } n=2, \\ 0 & \text{if } n\geq 3, \end{cases} \tag{4.72}$$

only the $n = 2$ term is relevant. With $C_2^{\mathrm{ci}}(\vec{r}) = -\beta u_{\mathrm{ci}}(|\vec{r}|)$ and $\tilde{C}_2^{\mathrm{ci}}(\vec{k}) = \tilde{c}_2^{\mathrm{ci}}(|\vec{k}|) = -\beta\tilde{u}_{\mathrm{ci}}(|\vec{k}|)$, we simply have

$$\lim_{V\to\infty}\frac{\beta\Delta\mathcal{F}_{\mathrm{ci}}^{\mathrm{ex}}[\rho]}{V} = \frac{1}{2}\sum_{s=1}^{\hat{s}}\Phi_s^2\,\beta\tilde{u}_{\mathrm{ci}}(k_s)\,\kappa_s. \tag{4.73}$$

Finally, exploiting that

$$\frac{1}{\rho_{\mathrm{b}}\tilde{S}(k)} = \frac{1-\rho_{\mathrm{b}}\tilde{c}_2(k)}{\rho_{\mathrm{b}}} = \frac{1}{\rho_{\mathrm{b}}} - \tilde{c}_2^{\mathrm{ci}}(k) - \tilde{c}_2^{\mathrm{hd}}(k) = \frac{1}{\rho_{\mathrm{b}}} + \beta\tilde{u}_{\mathrm{ci}}(k) - \tilde{c}_2^{\mathrm{hd}}(k) \tag{4.74}$$

and $A_{n_1,\ldots,n_{\hat{s}}} = A^{\mathrm{id}}_{n_1,\ldots,n_{\hat{s}}} + A^{\mathrm{hd}}_{n_1,\ldots,n_{\hat{s}}}$, we can add Eqs. (4.64), (4.70) and (4.73) to arrive at

$$\lim_{V\to\infty}\frac{\beta\Delta\mathcal{F}[\rho]}{V} = \frac{1}{2\rho_{\mathrm{b}}}\sum_{s=1}^{\hat{s}}\frac{\Phi_s^2\,\kappa_s}{\tilde{S}(k_s)} + \sum_{n=3}^{\infty}\frac{1}{n!}\sum_{n_1\in\mathbb{N}_0}^{n_1+\cdots+n_{\hat{s}}=n}\cdots\sum_{n_{\hat{s}}\in\mathbb{N}_0}\Phi_1^{n_1}\cdots\Phi_{\hat{s}}^{n_{\hat{s}}}A_{n_1,\ldots,n_{\hat{s}}}. \tag{4.75}$$

In practice, however, we need to truncate the infinite sum over n after the first $\hat{n}$ terms, resulting in the $\hat{n}$-th order approximation

$$\lim_{V\to\infty}\frac{\beta\Delta\mathcal{F}[\rho]}{V} \approx \frac{1}{2\rho_{\mathrm{b}}}\sum_{s=1}^{\hat{s}}\frac{\Phi_s^2\,\kappa_s}{\tilde{S}(k_s)} + \sum_{n=3}^{\hat{n}}\frac{1}{n!}\sum_{n_1\in\mathbb{N}_0}^{n_1+\cdots+n_{\hat{s}}=n}\cdots\sum_{n_{\hat{s}}\in\mathbb{N}_0}\Phi_1^{n_1}\cdots\Phi_{\hat{s}}^{n_{\hat{s}}}A_{n_1,\ldots,n_{\hat{s}}}. \tag{4.76}$$

Minimization of the free energy density

After deciding on a maximum shell $\hat{s}$ and order $\hat{n}$, we can use this expression to approximate the free energy of a lamellar or hexagonal density distribution in the $\hat{s}$-th shell expansion specified by the bulk density ρ_{b}, the amplitudes $\Phi_1,\ldots,\Phi_{\hat{s}}$ and, crucially, also the size of the unit cell determined by either $k_1^{\mathrm{lam}} = 2\pi/L_x$ or $k_1^{\mathrm{hex}} = 4\pi/L_x = 4\pi/(\sqrt{3}L_y)$. Since we are interested in the equilibrium density profile that is the minimum of $\mathcal{F}$ for a given fixed ρ_{b}, we simply minimize Eq. (4.76) numerically with respect to $\Phi_1,\ldots,\Phi_{\hat{s}}$ and k_1 using the Nelder–Mead method [76].

The choice of $\hat{s}$ and $\hat{n}$ is a matter of weighing up the accuracy against the expensiveness of the computation. The main problem is that the quantities $A_{n_1,\ldots,n_{\hat{s}}}$ become quite laborious to calculate for big $n = n_1 + \cdots + n_{\hat{s}}$ because the sum in Eq. (4.58) runs over a large number of wave vectors $\vec{k}_1,\ldots,\vec{k}_n$. Furthermore, there exist a total of $\mathcal{P}_{\hat{s}}(n) \equiv (n+\hat{s}-1)!/[n!\,(\hat{s}-1)!]$ different $A_{n_1,\ldots,n_{\hat{s}}}$ with $n_1 + \cdots + n_{\hat{s}} = n$, and that set grows rapidly with $\hat{s}$: for example, $\mathcal{P}_1(3) = 1$ (only A_3), $\mathcal{P}_2(3) = 4$ (namely $A_{3,0}$, $A_{2,1}$, $A_{1,2}$ and $A_{0,3}$), $\mathcal{P}_{10}(3) = 220$ and $\mathcal{P}_{20}(3) = 1540$. In practice, we are thus restricted to rather small values of $\hat{s}$ and $\hat{n}$, which means that one cannot expect too accurate predictions from the Landau-type theory. On the other hand, once the needed $A_{n_1,\ldots,n_{\hat{s}}}$ have been determined (note that it is possible to derive closed but potentially lengthy expression for these quantities that only depend on the wave number k_1 of a given structure; with enough patience, this can even be done by hand, but the use of a computer algebra system is strongly

recommended) the calculation and minimization of the free energy is relatively fast. The theory is therefore not entirely without merit if a high accuracy is not the primary objective.

Initially, we opted for $\hat{n} = 4$ (as for example in Ref. [77], where a similar Taylor expansion of $\mathcal{F}$ was performed) and $\hat{s} = 2$ (since determining $\mathcal{P}_2(3) + \mathcal{P}_2(4) = 4 + 5 = 9$ different $A_{n_1,\ldots,n_{\hat{s}}}$ for each type of structure – lamellar and hexagonal – was still deemed feasible). However, for the majority of states within the microphase region except those very close to the λ-line, the density profiles that were found to minimize the free energy turned out to be invalid, having had such excessive fluctuation amplitudes Φ_1 and Φ_2 that the density actually fell below zero at some points in space. The likely explanation for this is that the fourth-order expansion is simply too imprecise outside the vicinity of the λ-line where $\tilde{D} = 1/\tilde{S}$ is so negative that large Φ_1 and Φ_2 are strongly favored by the second-order, but only weakly (if at all) penalized in comparison by the third- and forth-order terms. Increasing $\hat{n}$ was not really an option because each additional order n would introduce $\mathcal{P}_2(n) = n+1$ more $A_{n_1,\ldots,n_{\hat{s}}}$. In the end, we decided to restrict the minimization procedure to non-negative density distributions by artificially assigning $\mathcal{F}[\rho] = \infty$ if $\min \rho < 0$. Unfortunately, for some constellations of Φ_1 and Φ_2, it can be surprisingly difficult to reliably ascertain $\min \rho$ analytically, especially for a hexagonal structure. However, this is trivial to do in the one-shell approximation, so that we settled on $\hat{s} = 1$ in the end.

In Fig. 4.8, several phase diagrams are shown that present the structure analysis based on our Landau-type theory. The symbols mark points where an inhomogeneous density profile was found to have a lower free energy density than the flat bulk; the shape of the symbols indicate whether a hexagonal droplet ("hex+", $\Phi_1 > 0$), a lamellar stripe ("lam", $|\Phi_1| > 0$), or a hexagonal bubble phase ("hex−", $\Phi_1 < 0$) attained the lowest free energy, whereas their color encodes the value of the principal wave number k_1 and thus the size of the corresponding unit cell.

The first thing to notice is that within the region enclosed by the λ-line, the Landau-type theory indeed predicts non-uniform microphases. This is also the case for some points outside that region, which means that the higher-than-second-order terms of

$$\lim_{V\to\infty} \frac{\beta\Delta\mathcal{F}[\rho]}{V} = \frac{\kappa_1}{2\rho_\mathrm{b}} \frac{\Phi_1^2}{\tilde{S}(k_1)} + O(\Phi_1^3) = \frac{\kappa_1}{2\rho_\mathrm{b}} \Phi_1^2 \tilde{D}(k_1) + O(\Phi_1^3) \tag{4.77}$$

must be sufficiently negative in sum there so as to overcompensate the positive contribution ($\tilde{S} > 0$) of the second-order term.

A comparison of k_1 with the minimum k_min of $\tilde{D}$ in Figs. 4.3(c, e), 4.4(d, f) and 4.5(b, c) reveals no significant differences, which means that unit cell size is still primarily determined by k_min; of course this is hardly unexpected given Eq. (4.77). Therefore, we likewise find a high-k_1 domain for larger bulk packing fractions η_b, and otherwise an intermediate- or low-k_1 domain when either the long-ranged repulsion or the short-ranged attraction, respectively, dominates.

Taking a closer look at the two latter domains in Figs. 4.8(a–d), we see that the sequence of mi-

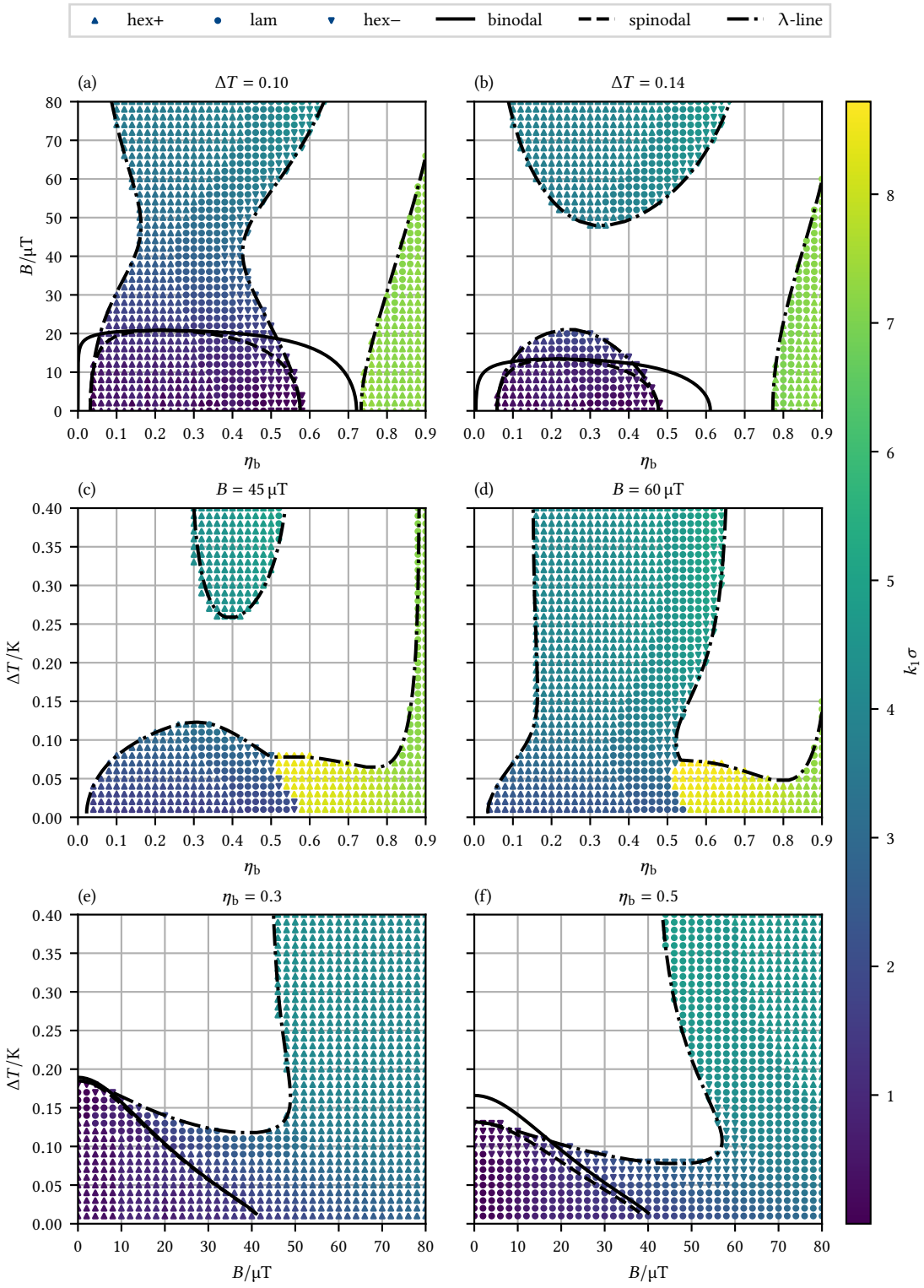

Figure 4.8.: Phase diagrams determined via the Landau-type theory. Symbols denote points where the hexagonal droplet (hex+), lamellar stripe (lam) or hexagonal bubble (hex−) phase has the lowest free energy; their color encodes the principal wavenumber k_1 and thus the size of the unit cell [$k_1^{\mathrm{lam}} = 2\pi/L_x$ and $k_1^{\mathrm{hex}\pm} = 4\pi/L_y = 4\pi/(\sqrt{3}L_x)$].

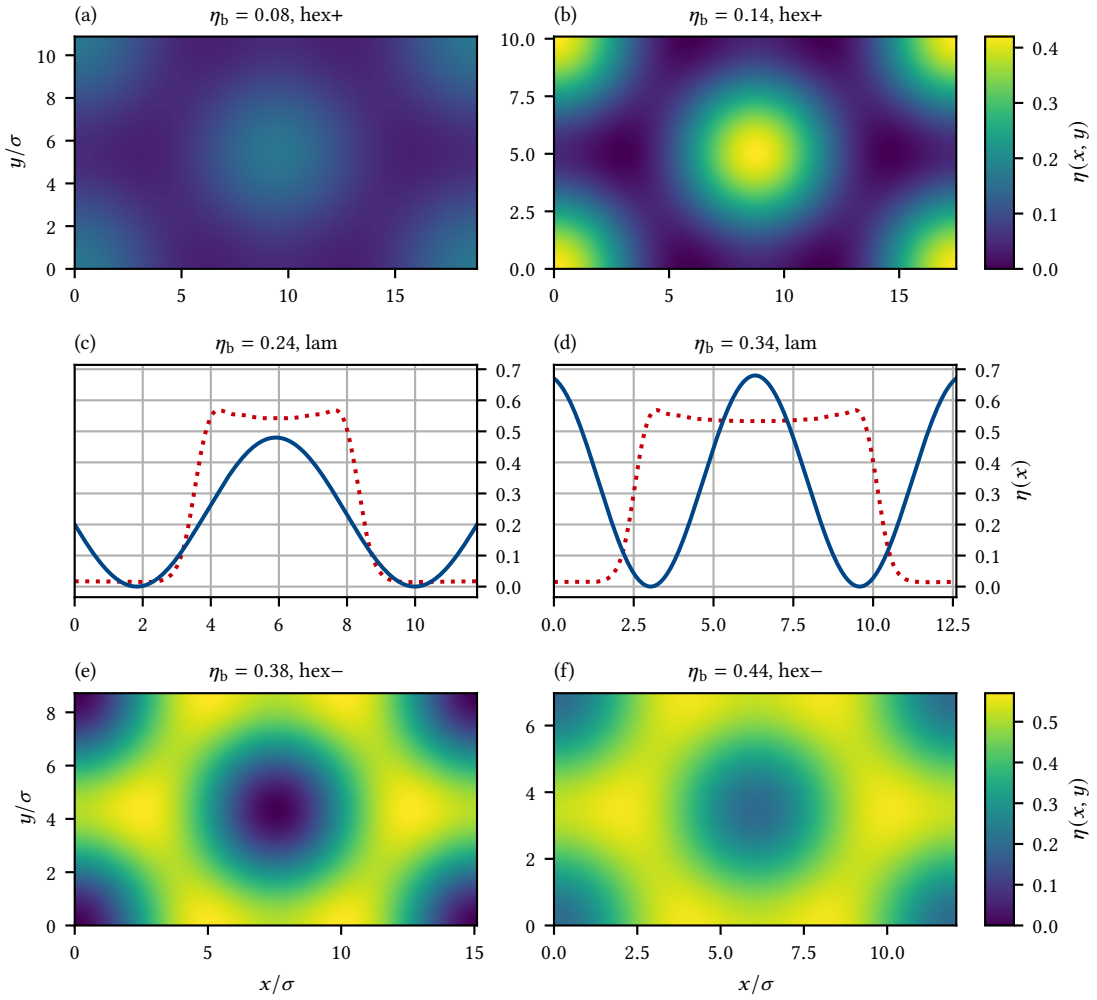

Figure 4.9.: Unit cells of the density profiles $\eta(\vec{r}) = \pi R^2 \rho(\vec{r})$ at various bulk packing fractions for $B = 10\,\mu\mathrm{T}$ and $\Delta T = 0.14\,\mathrm{K}$ resulting from the Landau-type theory. (a, b) Hexagonal droplet phase. (c, d) Lamellar stripe phase. (e, f) Hexagonal bubble phase.

crophases for increasing η_b is droplets → stripes → bubbles, in agreement with previous studies of microphase separation in two dimensions. The width of these phases differs considerably: for most combinations of B and ΔT, the droplet phase is by far the widest, while the bubble phase is so thin in some cases as to be barely noticeable. Curiously, the stripe phase appears to have an almost constant width that lies somewhere in between and forms a band that runs nearly parallel to either the intermediate-η_b branch of the λ-line or the low/high-k_1 domain border.

In the high-k_1 domain, the Landau-type theory predicts not only a hexagonal droplet/cluster phase (which we already anticipated for higher η_b), but also a lamellar stripe phase. However, the trustworthiness of these results is more than questionable since it is unlikely that the one-shell

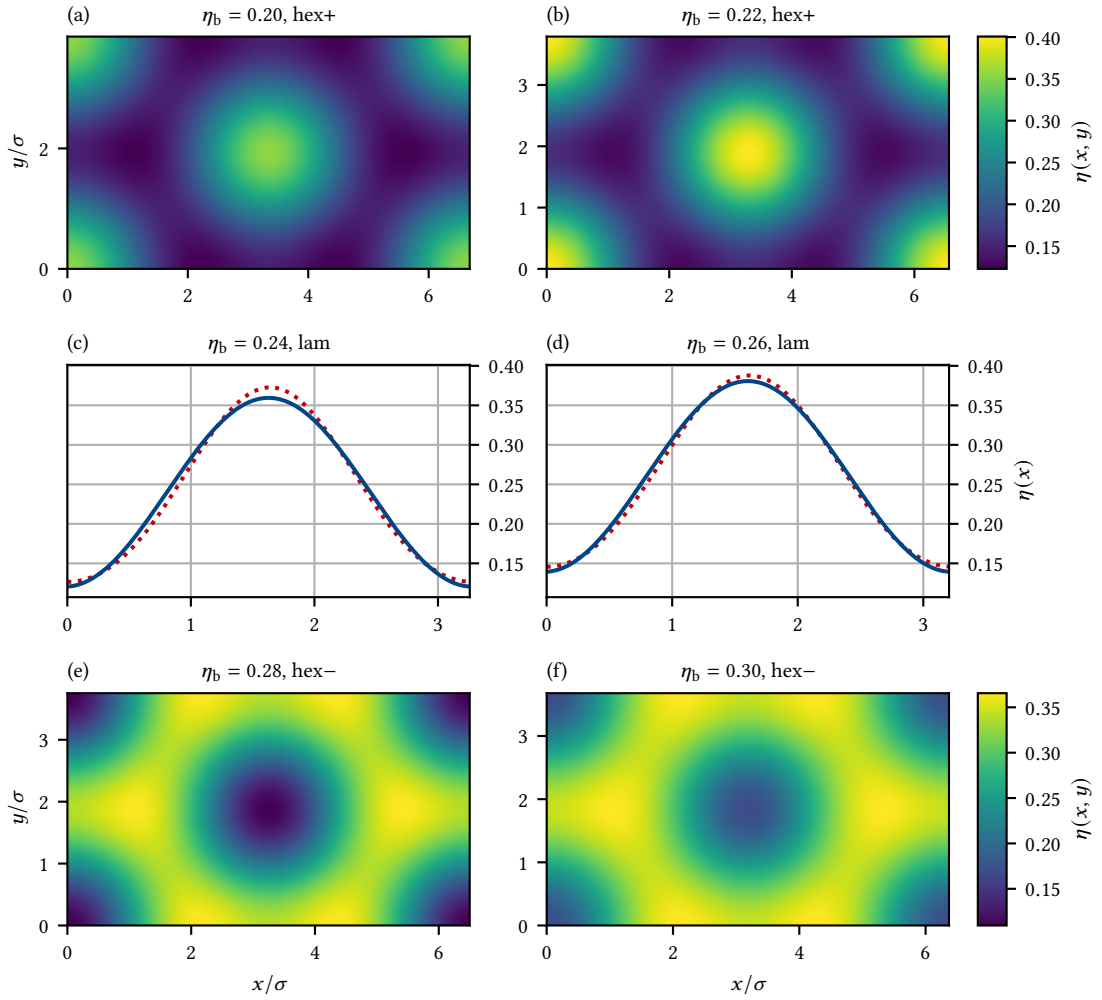

Figure 4.10.: Unit cells of the density profiles $\eta(\vec{r}) = \pi R^2 \rho(\vec{r})$ at various bulk packing fractions for $B = 20\,\mu\mathrm{T}$ and $\Delta T = 0.14\,\mathrm{K}$ resulting from the Landau-type theory. (a, b) Hexagonal droplet phase. (c, d) Lamellar stripe phase. (e, f) Hexagonal bubble phase.

approximation can faithfully represent the sharp density peaks one would expect in this regime.

In Figs. 4.8(e, f), the B–ΔT plane is shown for $\eta_b = 0.3$ and $\eta_b = 0.5$, respectively. At the lower packing fraction, the vast majority of states feature the droplet phase; there is only a thin band of lamellar states below the roughly horizontal part of the λ-line and a handful of bubble states located almost directly on the λ-line. Going to $\eta_b = 0.5$, we see that the microphase of many states has jumped to the next in the line of succession (droplets ⟶ stripes, stripes ⟶ bubbles), and that we can access all microphases through a suitable choice of B and ΔT.

In Fig. 4.9, the density profiles for various η_b at $B = 10\,\mu\mathrm{T}$ and $\Delta T = 0.14\,\mathrm{K}$ are plotted. We can see that for $\eta_b \in \{0.14\,\mathrm{K}, 0.24\,\mathrm{K}, 0.34\,\mathrm{K}, 0.38\,\mathrm{K}\}$, the density falls down to zero at some points;

since these lie deep within the microphase regime, the amplitude of the fluctuations become as large as possible without violating the (artificially enforced) condition that the density must not be negative. For $\eta_\mathrm{b} \in \{0.08\,\mathrm{K}, 0.44\,\mathrm{K}\}$ this is not the case, because these states are very close the λ-line. The density profiles shown in Fig. 4.10 are for states with $B = 20\,\mu\mathrm{T}$ and $\Delta T = 0.14\,\mathrm{K}$ that are located just below the tip of the low-k_1 domain [cf. Fig. 4.8(b)] and therefore also in the vicinity of the λ-line; consequently, the density is strictly positive for all packing fractions.

Conclusion

While the Landau-type theory allows us to quickly paint a rough picture of the (micro-)phase behavior in our system, it is unfortunately not suitable if predictions of high accuracy are desired. For this reason, we will have to develop another method that neither relies on a shell expansion of the density distribution, nor on a Taylor expansion of the intrinsic free energy functional.

4.1.3. Free minimization

The *free minimization* is an iterative scheme to determine the minimum ρ_eq of the grand potential functional

$$\Omega[\rho] = \mathcal{F}[\rho] + \int \mathrm{d}^2\vec{r}\,\rho(\vec{r})[\mathcal{V}^\mathrm{ext}(\vec{r}) - \mu] \tag{4.78}$$

by generating a sequence of density profiles $(\rho_i)_{i\in\mathbb{N}_0}$ that successively lower Ω and hence (ideally) approach the equilibrium density distribution so that $\rho_i \to \rho_\mathrm{eq}$ for $i \to \infty$. Even though the external potential vanishes in the bulk, we shall assume the general case of $\mathcal{V}^\mathrm{ext} \neq 0$ in the following.

Grand-canonical minimization

Let us first derive this scheme in a grand-canonical setting where we want to find the equilibrium density profile ρ_eq for a given chemical potential μ. Since ρ_eq minimizes Ω, the functional derivative of $\Omega[\rho]$ with respect to ρ evaluated at $\rho = \rho_\mathrm{eq}$ must vanish and we have that

$$\begin{aligned}
0 &= \beta \left.\frac{\delta\Omega[\rho]}{\delta\rho(\vec{r})}\right|_{\rho=\rho_\mathrm{eq}} = \beta \left.\frac{\delta\mathcal{F}[\rho]}{\delta\rho(\vec{r})}\right|_{\rho=\rho_\mathrm{eq}} + \beta\mathcal{V}^\mathrm{ext}(\vec{r}) - \beta\mu \\
&= \beta \left.\frac{\delta\mathcal{F}_\mathrm{id}[\rho]}{\delta\rho(\vec{r})}\right|_{\rho=\rho_\mathrm{eq}} + \beta \left.\frac{\delta\mathcal{F}_\mathrm{ex}[\rho]}{\delta\rho(\vec{r})}\right|_{\rho=\rho_\mathrm{eq}} + \beta\mathcal{V}^\mathrm{ext}(\vec{r}) - \beta[\mu_\mathrm{id}(\rho_\mathrm{eq}^\mathrm{b}) + \mu_\mathrm{ex}(\rho_\mathrm{eq}^\mathrm{b})] \\
&= \ln[\Lambda^2\rho_\mathrm{eq}(\vec{r})] - c_1(\rho_\mathrm{eq}, \vec{r}) + \beta\mathcal{V}^\mathrm{ext}(\vec{r}) - \ln(\Lambda^2\rho_\mathrm{eq}^\mathrm{b}) - \beta\mu_\mathrm{ex}(\rho_\mathrm{eq}^\mathrm{b}) \\
&= \ln\frac{\rho_\mathrm{eq}(\vec{r})}{\rho_\mathrm{eq}^\mathrm{b}} - c_1(\rho_\mathrm{eq}, \vec{r}) + \beta\mathcal{V}^\mathrm{ext}(\vec{r}) - \beta\mu_\mathrm{ex}(\rho_\mathrm{eq}^\mathrm{b}),
\end{aligned} \tag{4.79}$$

where

$$c_1(\rho, \vec{r}) \equiv -\beta \frac{\delta \mathcal{F}_{\mathrm{ex}}[\rho]}{\delta \rho(\vec{r})} \tag{4.80}$$

is the direct one-particle correlation function, $\mu_{\mathrm{id}}(\rho_\mathrm{b}) = k_\mathrm{B} T \ln(\Lambda^2 \rho_\mathrm{b})$ the chemical potential of the ideal gas and $\mu_{\mathrm{ex}}(\rho_\mathrm{b}) = \mu - \mu_{\mathrm{id}}(\rho_\mathrm{b})$ the excess chemical potential. Since the value of the thermal wavelength Λ is irrelevant for our purposes, we are free to choose $\Lambda^2 = \pi R^2$ for the sake of convenience. In our case, $c_1(\rho, \vec{r}) = c_1^{\mathrm{hd}}(\rho, \vec{r}) + c_1^{\mathrm{ci}}(\rho, \vec{r})$, where

$$c_1^{\mathrm{hd}}(\rho, \vec{r}) = -\beta \frac{\delta \mathcal{F}_{\mathrm{hd}}^{\mathrm{ex}}[\rho]}{\delta \rho(\vec{r})} = -\sum_{i=1}^{9} \int \mathrm{d}^2 \vec{r}\,' \, \frac{\partial \phi_\rho^{\mathrm{hd}}}{\partial w_\rho^i}(\vec{r}\,') \, \omega^i(\vec{r}\,' - \vec{r}) = -\sum_{i=1}^{9} \left(\frac{\partial \phi_\rho^{\mathrm{hd}}}{\partial w_\rho^i} \otimes \bar{\omega}^i \right)(\vec{r}), \tag{4.81}$$

with $\bar{\omega}(\vec{r}) = \omega(-\vec{r})$ and

$$c_1^{\mathrm{ci}}(\rho, \vec{r}) = -\beta \frac{\delta \mathcal{F}_{\mathrm{ci}}^{\mathrm{ex}}[\rho]}{\delta \rho(\vec{r})} = -\int \mathrm{d}^2 \vec{r}\,' \rho(\vec{r}\,') \, \beta u_{\mathrm{ci}}(|\vec{r} - \vec{r}\,'|) = -(\rho \otimes \beta u_{\mathrm{ci}})(\vec{r}). \tag{4.82}$$

If we "solve" Eq. (4.79) for $\rho_{\mathrm{eq}}(\vec{r})$, we find that the equilibrium density distribution satisfies the self-consistency relation

$$\rho_{\mathrm{eq}}(\vec{r}) = \rho_{\mathrm{eq}}^{\mathrm{b}} \exp[c_1(\rho_{\mathrm{eq}}, \vec{r}) - \beta \mathcal{V}^{\mathrm{ext}}(\vec{r}) + \beta \mu_{\mathrm{ex}}(\rho_{\mathrm{eq}}^{\mathrm{b}})]. \tag{4.83}$$

Note that this *cannot* be used to directly calculate $\rho_{\mathrm{eq}}(\vec{r})$ because the right-hand side depends itself on ρ_{eq}. We can, however, perform a so-called *Picard iteration* by evaluating both sides of Eq. (4.83) for some (non-equilibrium) density profile ρ_i instead of ρ_{eq}, and then mixing them with a sufficiently small mixing parameter $\alpha_i \in (0, 1)$ to obtain the successor

$$\rho_{i+1}(\vec{r}) = \alpha_i \, \rho_i^{\mathrm{b}} \exp[c_1(\rho_i, \vec{r}) - \beta \mathcal{V}^{\mathrm{ext}}(\vec{r}) + \beta \mu_{\mathrm{ex}}(\rho_i^{\mathrm{b}})] + (1 - \alpha_i) \, \rho_i(\vec{r}) \tag{4.84}$$

such that $\Omega[\rho_{i+1}] < \Omega[\rho_i]$. The iteration is stopped after $\hat{\imath}$ steps if

$$\max_{\vec{r}} \left| \frac{\rho_{\hat{\imath}}(\vec{r})}{\rho_{\hat{\imath}}^{\mathrm{b}}} - \exp[c_1(\rho_{\hat{\imath}}, \vec{r}) - \beta \mathcal{V}^{\mathrm{ext}}(\vec{r}) + \beta \mu_{\mathrm{ex}}(\rho_{\hat{\imath}}^{\mathrm{b}})] \right| < \epsilon \tag{4.85}$$

for some small $\epsilon > 0$, i. e., once the self-consistency equation is sufficiently well satisfied.

Be aware that Eq. (4.79), which served as starting point of the derivation, also holds if ρ_{eq} is only a local minimum of Ω; the Picard iteration may therefore just as well reach a metastable state. Where it ends up depends to a large part on where it started, i. e., on the initial density distribution ρ_0. Since we have good reason to believe that, in our system, the thermodynamically stable states are either uniform or offer a droplet, stripe or bubble pattern, it can be wise to perform the minimization four times with different ρ_0, each representing one of the possible structures (for example by choosing $\rho_0 = \rho_\mathrm{b}$, $\rho_0 = \rho_\mathrm{b} + \Phi_1 \, g_1^{\mathrm{hex}}$, $\rho_0 = \rho_\mathrm{b} + \Phi_1 \, g_1^{\mathrm{lam}}$ or $\rho_0 = \rho_\mathrm{b} - \Phi_1 \, g_1^{\mathrm{hex}}$

for some ρ_b and $\Phi_1 > 0$), and then to compare which run resulted in the lowest grand potential.

The grand-canonical minimization is especially useful for determining phase boundaries: if, for a given chemical potential μ_coex, there are two different minima $\rho_\mathrm{A} \neq \rho_\mathrm{B}$ with the same pressure $P = -\Omega/V$, these states can coexist and lie on the border between phases "A" and "B". Then, assuming that $\rho_\mathrm{A}^\mathrm{b} < \rho_\mathrm{B}^\mathrm{b}$, phase "A" is favored for $\mu < \mu_\mathrm{coex}$ or $\rho_\mathrm{b} < \rho_\mathrm{A}^\mathrm{b}$, phase "B" for $\mu > \mu_\mathrm{coex}$ or $\rho_\mathrm{b} > \rho_\mathrm{B}^\mathrm{b}$, and potentially a mixed phase for $\rho_\mathrm{A}^\mathrm{b} < \rho_\mathrm{b} < \rho_\mathrm{B}^\mathrm{b}$.

Quasi-canonical minimization

Since the concrete value of the chemical potential is seldom of interest to us, it may be more illuminating to replace μ with its conjugate thermodynamic quantity, namely the total particle number or, equivalently, the bulk density ρ_b. Minimizing Ω "quasi-canonically" for a given fixed ρ_b requires only a slight modification of the grand-canonical iteration scheme. Integrating Eq. (4.83) to determine the equilibrium bulk density, we find that

$$\rho_\mathrm{eq}^\mathrm{b} = \frac{1}{V}\int_V \mathrm{d}^2\vec{r}\,'\rho_\mathrm{eq}(\vec{r}\,') = \rho_\mathrm{eq}^\mathrm{b}\exp[\beta\mu_\mathrm{ex}(\rho_\mathrm{eq}^\mathrm{b})]\,\frac{1}{V}\int_V \mathrm{d}^2\vec{r}\,'\exp\left[c_1(\rho_\mathrm{eq},\vec{r}\,') - \beta\mathcal{V}^\mathrm{ext}(\vec{r}\,')\right], \quad (4.86)$$

which can be recast into

$$\beta\mu_\mathrm{ex}(\rho_\mathrm{eq}^\mathrm{b}) = -\ln\left[\frac{1}{V}\int_V \mathrm{d}^2\vec{r}\,'\exp\{c_1(\rho_\mathrm{eq},\vec{r}\,') - \beta\mathcal{V}^\mathrm{ext}(\vec{r}\,')\}\right]. \quad (4.87)$$

We can now plug this into Eq. (4.83) to eliminate the excess chemical potential $\mu_\mathrm{ex}(\rho_\mathrm{eq}^\mathrm{b})$ and arrive at the quasi-canonical self-consistency equation

$$\rho_\mathrm{eq}(\vec{r}) = \rho_\mathrm{eq}^\mathrm{b}\frac{\exp[c_1(\rho_\mathrm{eq},\vec{r}) - \beta\mathcal{V}^\mathrm{ext}(\vec{r})]}{\frac{1}{V}\int_V \mathrm{d}^2\vec{r}\,'\exp[c_1(\rho_\mathrm{eq},\vec{r}\,') - \beta\mathcal{V}^\mathrm{ext}(\vec{r}\,')]} \quad (4.88)$$

for the equilibrium density profile. In analogy to Eq. (4.84), this ostensibly suggests a Picard iteration with the recurrence relation

$$\rho_{i+1}(\vec{r}) = \alpha_i\,\rho_i^\mathrm{b}\frac{\exp[c_1(\rho_i,\vec{r}) - \beta\mathcal{V}^\mathrm{ext}(\vec{r})]}{\frac{1}{V}\int_V \mathrm{d}^2\vec{r}\,'\exp[c_1(\rho_i,\vec{r}\,') - \beta\mathcal{V}^\mathrm{ext}(\vec{r}\,')]} + (1-\alpha_i)\,\rho_i(\vec{r}), \quad (4.89)$$

which, however, has the deficiency that $\rho_{i+1}^\mathrm{b} = \rho_i^\mathrm{b}$ and hence $\rho_i^\mathrm{b} \neq \rho_\mathrm{b}$ unless already $\rho_0^\mathrm{b} = \rho_\mathrm{b}$; but even if ρ_0 were to satisfy this condition, minor numerical inaccuracies tend to build up over the course of the iteration to the effect that, in practice, $|\rho_i^\mathrm{b} - \rho_0^\mathrm{b}|$ grows with i. A simple remedy for these shortcomings is to use

$$\rho_{i+1}(\vec{r}) = \alpha_i\,\rho_\mathrm{b}\frac{\exp[c_1(\rho_i,\vec{r}) - \beta\mathcal{V}^\mathrm{ext}(\vec{r})]}{\frac{1}{V}\int_V \mathrm{d}^2\vec{r}\,'\exp[c_1(\rho_i,\vec{r}\,') - \beta\mathcal{V}^\mathrm{ext}(\vec{r}\,')]} + (1-\alpha_i)\,\rho_\mathrm{b}\frac{\rho_i(\vec{r})}{\frac{1}{V}\int_V \mathrm{d}^2\vec{r}\,'\rho_i(\vec{r}\,')}, \quad (4.90)$$

instead, which has the desirable property that $\rho^{\mathrm{b}}_{i+1} = \rho_{\mathrm{b}}$ regardless of ρ^{b}_i and, by extension, ρ^{b}_0. The mixing parameters $\alpha_i \in (0,1)$ are chosen such that $\mathcal{A}[\rho_{i+1}] < \mathcal{A}[\rho_i]$, where the Helmholtz free energy functional $\mathcal{A}$ given by

$$\mathcal{A}[\rho] = \Omega[\rho] - \mu\frac{\partial\Omega[\rho]}{\partial\mu} = \Omega[\rho] + \mu\int \mathrm{d}^2\vec{r}\,\rho(\vec{r}) = \mathcal{F}[\rho] + \int \mathrm{d}^2\vec{r}\,\rho(\vec{r})\,\mathcal{V}^{\mathrm{ext}}(\vec{r}) \tag{4.91}$$

is the Legendre transform of Ω with respect to μ (the grand potential Ω itself is an inappropriate measure in this context as is explicitly depends on μ, which is allowed to vary during the quasi-canonical minimization), and the Picard iteration is stopped as soon as

$$\max_{\vec{r}}\left|\frac{\rho_{\hat{\imath}}(\vec{r})}{\rho^{\mathrm{b}}_{\hat{\imath}}} - \frac{\exp[c_1(\rho_{\hat{\imath}},\vec{r}) - \beta\mathcal{V}^{\mathrm{ext}}(\vec{r})]}{\frac{1}{V}\int_V \mathrm{d}^2\vec{r}\,'\exp[c_1(\rho_{\hat{\imath}},\vec{r}\,') - \beta\mathcal{V}^{\mathrm{ext}}(\vec{r}\,')]}\right| < \epsilon \tag{4.92}$$

for some $\epsilon > 0$. Note that, once we have determined the equilibrium density distribution ρ_{eq}, Eq. (4.87) allows us to calculate the associated chemical potential via

$$\beta\mu = \beta\mu_{\mathrm{id}}(\rho^{\mathrm{b}}_{\mathrm{eq}}) + \beta\mu_{\mathrm{ex}}(\rho^{\mathrm{b}}_{\mathrm{eq}}) = \ln(\Lambda^2\rho^{\mathrm{b}}_{\mathrm{eq}}) - \ln\left[\frac{1}{V}\int_V \mathrm{d}^2\vec{r}\,'\exp\{c_1(\rho_{\mathrm{eq}},\vec{r}\,') - \beta\mathcal{V}^{\mathrm{ext}}(\vec{r}\,')\}\right]. \tag{4.93}$$

Implementation

We perform the Picard iteration on a workstation by discretizing the density profiles on a regular grid of $M_x \times M_y$ lattice points located at $\vec{r}_{ij} = (i\,\Delta x, j\,\Delta y)$ with $\Delta x \equiv L_x/M_x$ and $\Delta y \equiv L_y/M_y$ for $i \in \{0,\ldots,M_x-1\}$ and $j \in \{0,\ldots,M_y-1\}$, where $L_x \times L_y$ is either the size of the system, or the size of the unit cell of a periodic structure if the system itself is infinitely large. We choose a minimum resolution of $\min\{M_x/L_x, M_y/L_y\} \geq 10/\sigma$.

The integrals involved in calculating $\mathcal{F}_{\mathrm{id}}[\rho]$, $\mathcal{F}^{\mathrm{ex}}_{\mathrm{ci}}[\rho]$ $\mathcal{F}^{\mathrm{ex}}_{\mathrm{hd}}[\rho]$, $\Omega[\rho]$ and $\mathcal{A}[\rho]$ can be simply approximated as sums, so that

$$\frac{\beta\mathcal{F}_{\mathrm{id}}[\rho]}{V} \approx \frac{1}{M_x}\sum_{i=0}^{M_x-1}\frac{1}{M_y}\sum_{j=0}^{M_y-1}\rho(\vec{r}_{ij})\,[\ln\{\Lambda^2\rho(\vec{r}_{ij})\} - 1], \tag{4.94}$$

$$\frac{\beta\mathcal{F}^{\mathrm{hd}}_{\mathrm{ex}}[\rho]}{V} \approx \frac{1}{M_x}\sum_{i=0}^{M_x-1}\frac{1}{M_y}\sum_{j=0}^{M_y-1}\phi_{\mathrm{hd}}\Big(w^0_\rho(\vec{r}_{ij}), w^2_\rho(\vec{r}_{ij}), \boldsymbol{w}^0_\rho(\vec{r}_{ij}), \boldsymbol{w}^1_\rho(\vec{r}_{ij}), \boldsymbol{w}^2_\rho(\vec{r}_{ij})\Big). \tag{4.95}$$

$$\frac{\beta\mathcal{F}^{\mathrm{ex}}_{\mathrm{ci}}[\rho]}{V} \approx -\frac{1}{2}\frac{1}{M_x}\sum_{i=0}^{M_x-1}\frac{1}{M_y}\sum_{j=0}^{M_y-1}\rho(\vec{r}_{ij})\,c^{\mathrm{ci}}_1(\rho,\vec{r}_{ij}) \tag{4.96}$$

$$\frac{\Omega[\rho]}{V} \approx \frac{\mathcal{F}[\rho]}{V} + \frac{1}{M_x}\sum_{i=0}^{M_x-1}\frac{1}{M_y}\sum_{j=0}^{M_y-1}\rho(\vec{r}_{ij})[\mathcal{V}^{\mathrm{ext}}(\vec{r}_{ij}) - \mu], \tag{4.97}$$

$$\frac{\mathcal{A}[\rho]}{V} \approx \frac{\mathcal{F}[\rho]}{V} + \frac{1}{M_x}\sum_{i=0}^{M_x-1}\frac{1}{M_y}\sum_{j=0}^{M_y-1}\rho(\vec{r}_{ij})\,\mathcal{V}^{\text{ext}}(\vec{r}_{ij}), \tag{4.98}$$

and the recurrence relations for the grand- and quasi-canonical minimization become

$$\rho_{l+1}(\vec{r}_{ij}) = \alpha_l\,\rho_l^{\text{b}}\exp[c_1(\rho_l,\vec{r}_{ij}) - \beta\mathcal{V}^{\text{ext}}(\vec{r}_{ij}) + \beta\mu_{\text{ex}}(\rho_l^{\text{b}})] + (1-\alpha_l)\,\rho_l(\vec{r}_{ij}) \tag{4.99}$$

and

$$\begin{aligned}\rho_{l+1}(\vec{r}_{ij}) = {}& \frac{\alpha_l\,\rho_{\text{b}}\,\exp[c_1(\rho_l,\vec{r}_{ij}) - \beta\mathcal{V}^{\text{ext}}(\vec{r}_{ij})]}{\frac{1}{M_x}\sum_{m=0}^{M_x-1}\frac{1}{M_y}\sum_{n=0}^{M_y-1}\exp[c_1(\rho_l,\vec{r}_{mn}) - \beta\mathcal{V}^{\text{ext}}(\vec{r}_{mn})]} \\ & + \frac{(1-\alpha_l)\,\rho_{\text{b}}\,\rho_l(\vec{r}_{ij})}{\frac{1}{M_x}\sum_{m=0}^{M_x-1}\frac{1}{M_x}\sum_{n=0}^{M_y-1}\rho_l(\vec{r}_{mn})},\end{aligned} \tag{4.100}$$

respectively.

The case is more complicated for the weighted densities w_ρ^0, w_ρ^2, $\boldsymbol{w}_\rho^0$, $\boldsymbol{w}_\rho^1$ and $\boldsymbol{w}_\rho^2$, as well as the direct one-particle correlation functions c_1^{hd} and c_1^{ci}, which are defined in terms of convolutions of the form

$$f_\rho(\vec{r}) = (g_\rho \otimes h)(\vec{r}) = \int_{\mathbb{R}^2}\mathrm{d}^2\vec{r}\,'\,g_\rho(\vec{r}\,')\,h(\vec{r}-\vec{r}\,') = \int_{\mathbb{R}^2}\mathrm{d}^2\vec{r}\,'\,g_\rho(\vec{r}-\vec{r}\,')\,h(\vec{r}\,'), \tag{4.101}$$

where either $g_\rho = \rho$ or $g_\rho = \partial\phi_\rho^{\text{hd}}/\partial w_\rho^l$ for some scalar component w_ρ^l of the weighted densities. Computing these convolutions on the grid directly via

$$f_\rho(\vec{r}_{ij}) \approx \sum_{m\in\mathbb{Z}}\Delta x\sum_{n\in\mathbb{Z}}\Delta y\,g_\rho(\vec{r}_{mn})\,h(\vec{r}_{ij}-\vec{r}_{mn}) = \sum_{m\in\mathbb{Z}}\Delta x\sum_{n\in\mathbb{Z}}\Delta y\,g_\rho(\vec{r}_{ij}-\vec{r}_{mn})\,h(\vec{r}_{mn}) \tag{4.102}$$

is problematic because (i) this would have to be done for all $M_x \times M_y$ points of the grid, which is extremely expensive, and (ii) the sums in Eq. (4.102) have to extend over all of $\mathbb{Z}$ since the integral in Eq. (4.101) in general encompasses the entire $\mathbb{R}^2$ unless the system is finite. However, if ρ is (L_x, L_y)-periodic, then both g_ρ and f_ρ are, too, and we can express the latter as the discrete Fourier series

$$f_\rho(\vec{r}_{ij}) = \sum_{m=0}^{M_x-1}\sum_{n=0}^{M_y-1}\hat{f}_\rho(\vec{k}_{mn})\exp(\mathrm{i}\vec{k}_{mn}\cdot\vec{r}_{ij}) \tag{4.103}$$

with the wave vector $\vec{k}_{mn} \equiv 2\pi[(m-\lceil M_x/2\rceil+1)/L_x, (n-\lceil M_y/2\rceil+1)/L_y]$, the ceiling function $\lceil x\rceil \equiv \min\{n\in\mathbb{Z} : n \geq x\}$ and the *discrete Fourier transform* of f_ρ

$$\hat{f}_\rho(\vec{k}_{mn}) \equiv \frac{1}{M_x}\sum_{i=0}^{M_x-1}\frac{1}{M_y}\sum_{j=0}^{M_y-1}f_\rho(\vec{r}_{ij})\exp(-\mathrm{i}\vec{k}_{mn}\cdot\vec{r}_{ij}). \tag{4.104}$$

Inserting Eq. (4.102), we find the discrete analog of the convolution theorem which states that

$$\begin{aligned}
\hat{f}_\rho(\vec{k}_{mn}) &\approx \frac{\Delta x}{M_x}\sum_{i=0}^{M_x-1}\frac{\Delta y}{M_y}\sum_{j=0}^{M_y-1}\sum_{u,v\in\mathbb{Z}} g_\rho(\vec{r}_{ij}-\vec{r}_{uv})\,h(\vec{r}_{uv})\exp(-\mathrm{i}\vec{k}_{mn}\cdot\vec{r}_{ij}) \\
&= \frac{1}{M_x}\sum_{i=0}^{M_x-1}\frac{1}{M_y}\sum_{j=0}^{M_y-1} g_\rho(\vec{r}_{ij})\exp(-\mathrm{i}\vec{k}_{mn}\cdot\vec{r}_{ij})\sum_{u,v\in\mathbb{Z}}\Delta x\Delta y\,h(\vec{r}_{uv})\exp(-\mathrm{i}\vec{k}_{mn}\cdot\vec{r}_{uv}) \\
&\approx \frac{1}{M_x}\sum_{i=0}^{M_x-1}\frac{1}{M_y}\sum_{j=0}^{M_y-1} g_\rho(\vec{r}_{ij})\exp(-\mathrm{i}\vec{k}_{mn}\cdot\vec{r}_{ij})\int \mathrm{d}^2\vec{r}\,h(\vec{r})\exp(-\mathrm{i}\vec{k}_{mn}\cdot\vec{r}), \\
&= \hat{g}_\rho(\vec{k}_{mn})\,\tilde{h}(\vec{k}_{mn})
\end{aligned} \tag{4.105}$$

with the *discrete* Fourier transform of $\hat{g}_\rho$,

$$\hat{g}_\rho(\vec{k}_{mn}) \equiv \frac{1}{M_x}\sum_{i=0}^{M_x-1}\frac{1}{M_y}\sum_{j=0}^{M_y-1} g_\rho(\vec{r}_{ij})\exp(-\mathrm{i}\vec{k}_{mn}\cdot\vec{r}_{ij}), \tag{4.106}$$

and the *continuous* Fourier transform of h,

$$\tilde{h}(\vec{k}) \equiv \int \mathrm{d}^2\vec{r}\,h(\vec{r})\exp(-\mathrm{i}\vec{k}\cdot\vec{r}). \tag{4.107}$$

This gives us a considerable advantage because there exist so-called *fast Fourier transform* algorithms such as "FFTW" [78, 79] that can compute the discrete Fourier transform (4.106) from g_ρ to $\hat{g}_\rho$ as well as the inverse transform (4.103) from $\hat{f}_\rho$ back to f_ρ very efficiently for all $M_x \times M_y$ grid points simultaneously. The continuous Fourier transform $\tilde{h}$ can often be calculated analytically or at least approximated numerically; as $\tilde{h}$ does not change over the course of the Picard iteration, it is sufficient to do this only once at the beginning for all grid points, provided that the results are stored. Since we can indeed expect a periodic density distribution in the infinite bulk, we thus have

$$w_\rho^l(\vec{r}_{ij}) \approx \sum_{m=0}^{M_x-1}\sum_{n=0}^{M_y-1}\hat{\rho}(\vec{k}_{mn})\,\tilde{\omega}^l(\vec{k}_{mn})\exp(\mathrm{i}\vec{k}_{mn}\cdot\vec{r}_{ij}), \tag{4.108}$$

$$c_1^{\mathrm{hd}}(\rho,\vec{r}_{ij}) \approx -\sum_{m=0}^{M_x-1}\sum_{n=0}^{M_y-1}\sum_{l=1}^{9}\widehat{\frac{\partial\phi_\rho^{\mathrm{hd}}}{\partial w_\rho^l}}(\vec{k}_{mn})\,\tilde{\omega}^l(-\vec{k}_{mn})\exp(\mathrm{i}\vec{k}_{mn}\cdot\vec{r}_{ij}), \tag{4.109}$$

$$c_1^{\mathrm{ci}}(\rho,\vec{r}_{ij}) \approx -\sum_{m=0}^{M_x-1}\sum_{n=0}^{M_y-1}\hat{\rho}(\vec{k}_{mn})\,\beta\tilde{u}_{\mathrm{ci}}(|\vec{k}_{mn}|)\exp(\mathrm{i}\vec{k}_{mn}\cdot\vec{r}_{ij}). \tag{4.110}$$

Note that, within this implementation, the Picard algorithm can minimize Ω or $\mathcal{A}$ only for a fixed unit cell size $L_x \times L_y$. The period of the equilibrium density profile is, however, not known *a priori*, and it is therefore imperative to perform the minimization also with respect to L_x and

L_y. Since L_y is irrelevant for a lamellar structure and $L_y = L_x/\sqrt{3}$ for a hexagonal one, we use a *golden section search* [80] to numerically minimize either $\Omega[\rho_{L_x}]$ or $\mathcal{A}[\rho_{L_x}]$ as a function of L_x, where ρ_{L_x} denotes the result of the Picard iteration for a given L_x.

The general-purpose programming capabilities of modern graphics processing units (GPU) allow us to accelerate the computations considerably [81]. Many calculations are of the type "single instruction, multiple data" (SIMD) in the sense that a quantity must be calculated for each point on the grid by applying one and the same function to one or more other quantities at the same grid point, i. e., $Q(\vec{r}_{ij}) \leftarrow f(q_1(\vec{r}_{ij}), q_2(\vec{r}_{ij}), \dots)$ or $\hat{Q}(\vec{k}_{ij}) \leftarrow f(\hat{q}_1(\vec{k}_{ij}), \hat{q}_2(\vec{k}_{ij}), \dots)$ for all $i \in \{0, \dots, M_x - 1\}$ and $j \in \{0, \dots, M_y - 1\}$. On a regular central processing unit (CPU), such operations typically have to be carried out sequentially by looping over all grid points and dealing with one after the other. A GPU, on the other hand, is specifically optimized for SIMD-type problems and able to execute the function (called a *kernel*) for thousands of grid points in parallel, resulting in a significantly increased performance compared to a CPU. The FFT algorithm can also be adapted to take advantage of this kind of parallelization [82], as well as reductions like the summation over all grid points relevant for Eqs. (4.94) to (4.98) [83].

Phase diagrams

Putting this free minimization technique into practice, we calculated diagrams in the η_b–B plane by employing the following procedure:

(i) We divide the η_b–B plane into an evenly-spaced grid with $(M_\eta + 1) \times (M_B + 1)$ points given by $(\eta_i^\mathrm{b}, B_j) \equiv (\eta_0^\mathrm{b} + i\Delta\eta_\mathrm{b}, B_0 + j\Delta B)$ for $i \in \{0, \dots, M_\eta\}$, $j \in \{0, \dots, M_B\}$ and suitable choices of η_0^b, $\Delta\eta_\mathrm{b}$, B_0 and ΔB.

(ii) We select $j_0 \in \{1, \dots, M_B - 1\}$ and perform a quasi-canonical minimization at $(\eta_i^\mathrm{b}, B_{j_0})$ for all $i \in \{0, \dots, M_\eta\}$. We do this separately for each microphase, beginning with some $\eta_{i_0}^\mathrm{b}$ where the microphase is predicted by the Landau-type theory to be stable (which implies $i_0^{\mathrm{hex}+} < i_0^\mathrm{lam} < i_0^{\mathrm{hex}-}$) and initializing the Picard iteration with the corresponding equilibrium density distribution from the Landau-type theory. We then continue with $\eta_{i_0-1}^\mathrm{b}$ and $\eta_{i_0+1}^\mathrm{b}$, but now using the equilibrium density profiles found previously by free minimization for η_{i_0} to set up the Picard iteration. The equilibrium density distributions for $\eta_{i_0-1}^\mathrm{b}$ and $\eta_{i_0+1}^\mathrm{b}$ then serve as starting points for $\eta_{i_0-2}^\mathrm{b}$ and $\eta_{i_0+2}^\mathrm{b}$, respectively, and so on, until we have reached η_0^b and $\eta_{M_\eta}^\mathrm{b}$.

(iii) We calculate the chemical potential $\mu(\eta_i^\mathrm{b}, B_{j_0})$ as well as the pressure $P(\eta_i^\mathrm{b}, B_{j_0})$ for every $i \in \{0, \dots, M_\eta\}$ and for each microphase. By plotting P versus μ, we can we can estimate the coexistence chemical potential $\mu_{\mathrm{hex}+}^\mathrm{lam}(B_{j_0})$ where the curves of the droplet and the stripe phase cross, as well as $\mu_\mathrm{lam}^{\mathrm{hex}-}(B_{j_0})$ where the stripe and the bubble phase have equal pressure.

(iv) We then determine $\mu^{\text{lam}}_{\text{hex+}}(B_{j_0})$ and $\mu^{\text{hex}-}_{\text{lam}}(B_{j_0})$ to a high degree of accuracy by using Brent's method [84] to numerically search for the root of $\Delta P^{\text{lam}}_{\text{hex+}}(\mu) \equiv P^{\text{lam}}_{B_{j_0}}(\mu) - P^{\text{hex+}}_{B_{j_0}}(\mu)$ and $\Delta P^{\text{hex}-}_{\text{lam}}(\mu) \equiv P^{\text{hex}-}_{B_{j_0}}(\mu) - P^{\text{lam}}_{B_{j_0}}(\mu)$ in the vicinity of our estimates for $\mu^{\text{lam}}_{\text{hex+}}(B_{j_0})$ and $\mu^{\text{hex}-}_{\text{lam}}(B_{j_0})$, respectively. The pressures for a given chemical potential are computed via grand-canonical minimization.

(v) We repeat steps (ii)–(iv) for $j_0 - 1$ and $j_0 + 1$ instead of j_0 so that we have knowledge of the coexistence chemical potentials $\mu^{\text{lam}}_{\text{hex+}}(B_j)$ and $\mu^{\text{hex}-}_{\text{lam}}(B_j)$ for all $j \in \{j_0 - 1, j_0, j_0 + 1\}$. We can now approximate $\mu^{\text{lam}}_{\text{hex+}}$ and $\mu^{\text{hex}-}_{\text{lam}}$ with a spline, allowing us to extrapolate a guess for $\mu^{\text{lam}}_{\text{hex+}}(B_{j_0-2})$, $\mu^{\text{lam}}_{\text{hex+}}(B_{j_0+2})$ and $\mu^{\text{hex}-}_{\text{lam}}(B_{j_0-2})$, $\mu^{\text{hex}-}_{\text{lam}}(B_{j_0+2})$ without the need of steps (ii) and (iii). We then perform step (iv) for $j_0 - 2$ and $j_0 + 2$ instead of j_0 to refine our estimates. Using these new points to extend the splines, we then determine $\mu^{\text{lam}}_{\text{hex+}}(B_{j_0-3})$, $\mu^{\text{lam}}_{\text{hex+}}(B_{j_0+3})$ and $\mu^{\text{hex}-}_{\text{lam}}(B_{j_0-3})$, $\mu^{\text{hex}-}_{\text{lam}}(B_{j_0+3})$, and so on, until we know $\mu^{\text{hex}-}_{\text{lam}}(B_j)$ and $\mu^{\text{hex}-}_{\text{lam}}(B_j)$ for all $j \in \{0, \ldots, M_B\}$.

(vi) As a by-product of calculating the coexistence chemical potentials, we also obtain the density profiles and bulk packing fractions $\eta^{\text{B}}_{\text{A}}(B)$ of phase "A" in coexistance with phase "B" for a magnetic field B. We then have $\eta^{\text{lam}}_{\text{hex+}}(B) < \eta^{\text{hex+}}_{\text{lam}}(B) < \eta^{\text{hex}-}_{\text{lam}}(B) < \eta^{\text{lam}}_{\text{hex}-}(B)$ with stable droplets for $\eta_{\text{b}} < \eta^{\text{lam}}_{\text{hex+}}(B)$, stripes for $\eta^{\text{hex+}}_{\text{lam}}(B) < \eta_{\text{b}} < \eta^{\text{hex}-}_{\text{lam}}(B)$ and bubbles for $\eta_{\text{b}} > \eta^{\text{lam}}_{\text{hex}-}(B)$. We perform a quasi-canonical minimization for all grid points (η^{b}_i, B_j) that lie in one of these regions where a pure microphase is stable, i. e., not in coexistence with another microphase. We begin with those points closest to the coexistence bulk packing fractions for a given B_j by initializing the Picard iteration with the corresponding coexistence density distributions. We then use the resulting density profiles to start off the minimization for the points one $\Delta\eta_{\text{b}}$-step further away from the phase boundary, and so on, successively working ourselves across each region.

(vii) Last, we filter out those points where the non-uniform density profile ρ does not have a lower Helmholtz free energy $\mathcal{A}$ than the uniform bulk at the corresponding bulk density ρ_{b}, i. e., when $\mathcal{A}[\rho] \geq \mathcal{A}[\rho_{\text{b}}]$. We mark the remaining points in an η_{b}–B phase diagram, with the shape of the symbols indicating the stable microphase and their color specifying the principal wave number k_1 [$k_1^{\text{lam}} = 2\pi/L_x$ and $k_1^{\text{hex}\pm} = 4\pi/L_x = 4\pi/(\sqrt{3}L_y)$] of the structure.

Since this takes a lot of time, we have only calculated two phase diagrams: one for $\Delta T = 0.10\,\text{K}$ and one for $\Delta T = 0.14\,\text{K}$, as can be seen in Fig. 4.11. We show the low-to-intermediate-k_1 domain for the former, and only the low-k_1 domain for the latter case. Unfortunately, we were not able to conclusively ascertain the phase behavior in the intermediate-k_1 domain for $\Delta T = 0.14\,\text{K}$ because for some B, the droplet and bubble phases were so unstable in the stripe regime (even for μ only

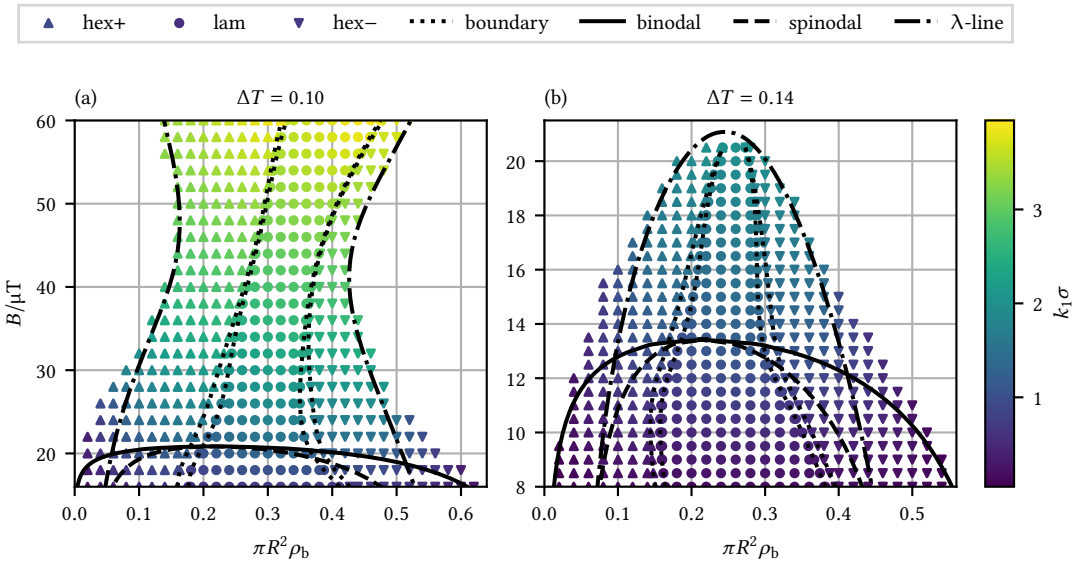

Figure 4.11.: Phase diagrams in the η_b–B plane for (a) $\Delta T = 0.10\,\mathrm{K}$ and (b) $\Delta T = 0.14\,\mathrm{K}$ determined via free minimization. Symbols denote points where the hexagonal droplet (hex+), lamellar stripe (lam) or hexagonal bubble (hex–) phase has the lowest free energy; their color encodes the principal wavenumber k_1 and thus the size of the unit cell [$k_1^{\mathrm{lam}} = 2\pi/L_x$ and $k_1^{\mathrm{hex}\pm} = 4\pi/L_y = 4\pi/(\sqrt{3}L_x)$]. Dottes lines mark the phase boundaries and connect the states capable of coexisting with a counterpart in the neighboring phase.

slightly above $\mu_{\mathrm{hex+}}^{\mathrm{lam}}(B)$ or below $\mu_{\mathrm{lam}}^{\mathrm{hex-}}(B)$) that the grand-canonical minimization would always lead to a lamellar density distribution (even when initialized with a hexagonal one), thus making it difficult to accurately determine the pressure curves of the individual phases and by extension the coexistence chemical potentials themselves. For both temperatures, the high-k_1 domain was also inaccessible because the one-particle direct correlation function c_1 became so large over the course of the Picard iteration that $\exp[c_1(\rho_i, \vec{r})]$ (as required by Eqs. (4.84) and (4.90)) could no longer be represented as a double-precision floating-point number.

Comparing Figs. 4.11(a) and 4.11(b) with their Landau-type theory counterparts Figs. 4.8(a) and 4.8(b), respectively, we see that the subdivision of the low-k_1 domain has changed noticeably, becoming a lot more symmetric: The droplet phase is no longer as dominant, whereas the bubble phase has grown significantly; the stripe phase now lies quite centrally within and widens alongside with the entire microphase region as B decreases, instead of forming a band of near-constant width close and parallel to the intermediate-η_b λ-line. The free minimization also predicts stable non-uniform density profiles well past the λ-line; in the limit of very small B, the microphase regime appears to extend up to the binodal. We were unable to determine the phase behavior for lower magnetic fields than shown in Fig. 4.11 because the unit cells would become so large that the hexagonal structures did not fit into the available computer memory any more.

The intermediate-k_1 domains of Figs. 4.11(a) and 4.8(a) at larger B, on the other hand, are

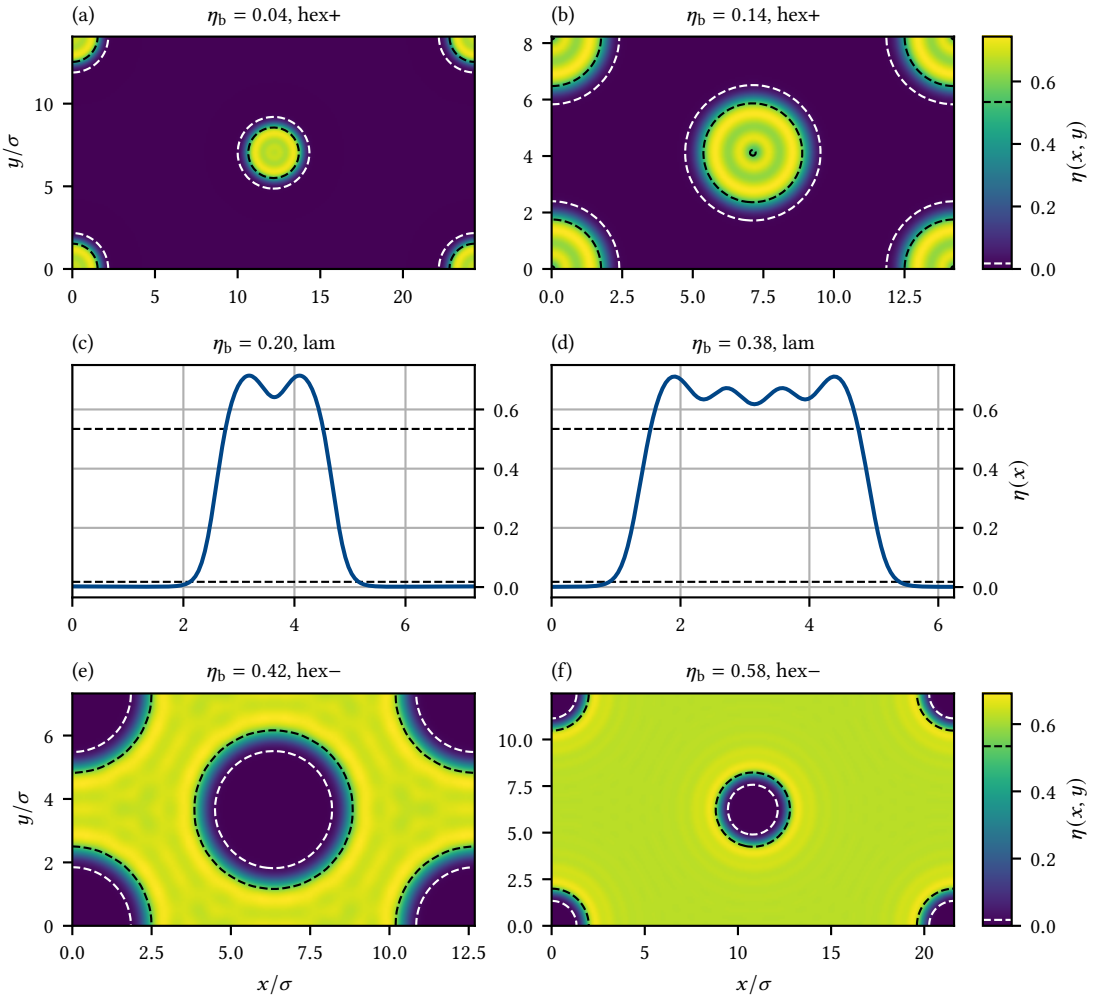

Figure 4.12.: Unit cells of the equilibrium density profiles $\eta(\vec{r}) = \pi R^2 \rho(\vec{r})$ at various bulk packing fractions for $\Delta T = 0.10\,\mathrm{K}$ and $B = 18\,\mu\mathrm{T}$ resulting from free minimization. Dashed lines mark the bulk packing fractions of the uniform gas and liquid at coexistence ($\eta_g \approx 0.014$ and $\eta_l \approx 0.548$, respectively). (a, b) Hexagonal droplet phase. (c, d) Lamellar stripe phase. (e, f) Hexagonal bubble phase.

actually in fairly good qualitative agreement: the droplet phase is relatively wide, the bubble phase rather thin, and the stripe phase bends markedly toward higher packing fractions as B increases.

Equilibrium density distributions

Let us continue by taking a more detailed look at the structure of the system. In Fig. 4.12, we show the equilibrium density profiles for $\Delta T = 0.10\,\mathrm{K}$, $B = 18\,\mu\mathrm{T}$ (near the lower end of the range of magnetic fields that were still accessible to free minimization for that temperature) and various

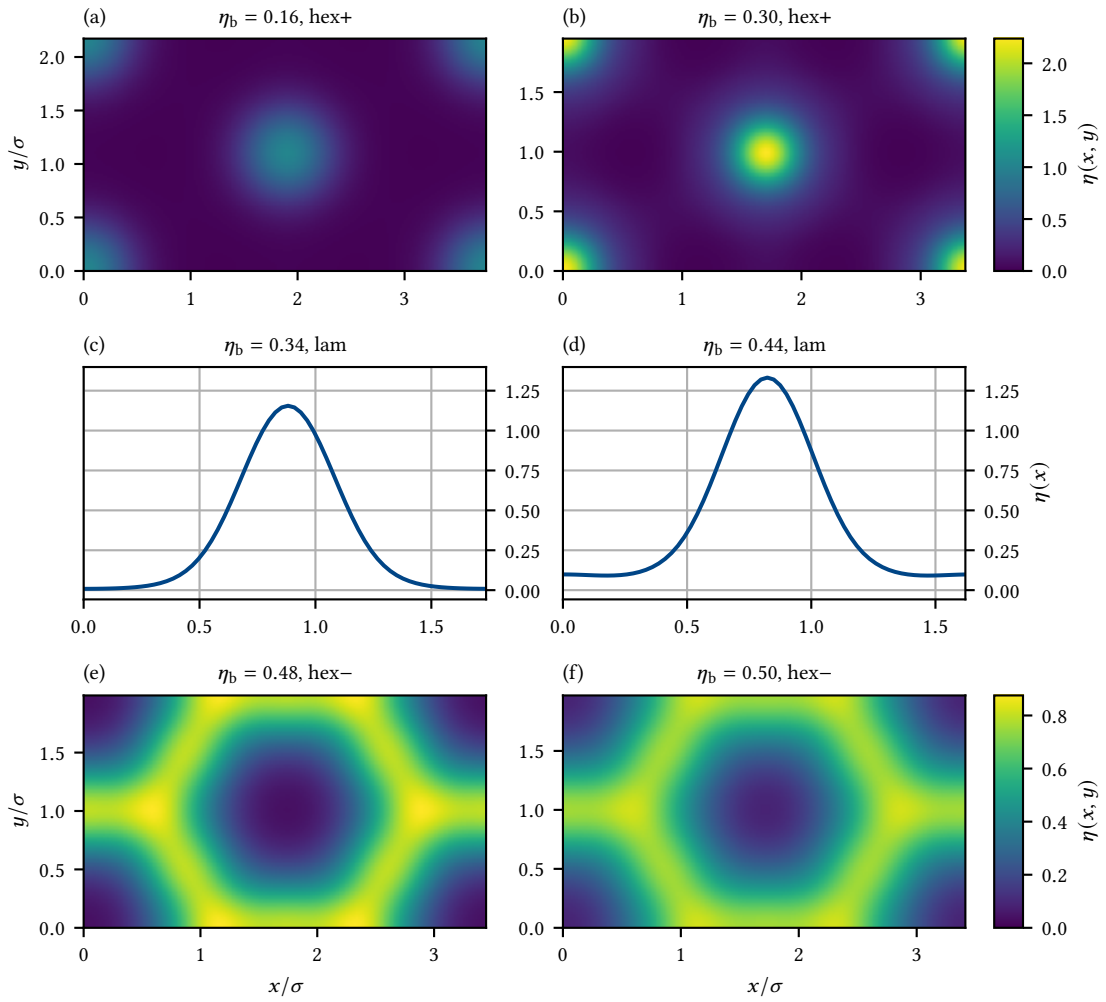

Figure 4.13.: Unit cells of the equilibrium density profiles $\eta(\vec{r}) = \pi R^2 \rho(\vec{r})$ at various bulk packing fractions for $\Delta T = 0.10\,\mathrm{K}$ and $B = 58\,\mu\mathrm{T}$ resulting from free minimization. (a, b) Hexagonal droplet phase. (c, d) Lamellar stripe phase. (e, f) Hexagonal bubble phase.

increasing values of η_b. We see that the sparse and the dense regions are quite distinct, separated only by a thin transition zone. Whereas the density is practically zero in the former, it oscillates around $\eta \approx 0.65$ in the latter; these oscillations are likely a consequence of packing effects that are well-known to occur in hard core systems at higher packing fractions. Interestingly, this appears to be the case for all packing fractions. One might have also imagined that, at least within the same microphase, the density would just increase globally upon going to higher η_b in the sense that $\eta'(\vec{r}) \approx \eta(\vec{r}) + \Delta\eta_b$ at $\eta_b' = \eta_b + \Delta\eta_b$. However, the system actually accommodates for changes of η_b in a different way: it essentially alters the relative size of the sparse and dense regions, with the former occupying the majority of the volume at low, and the latter at high η_b.

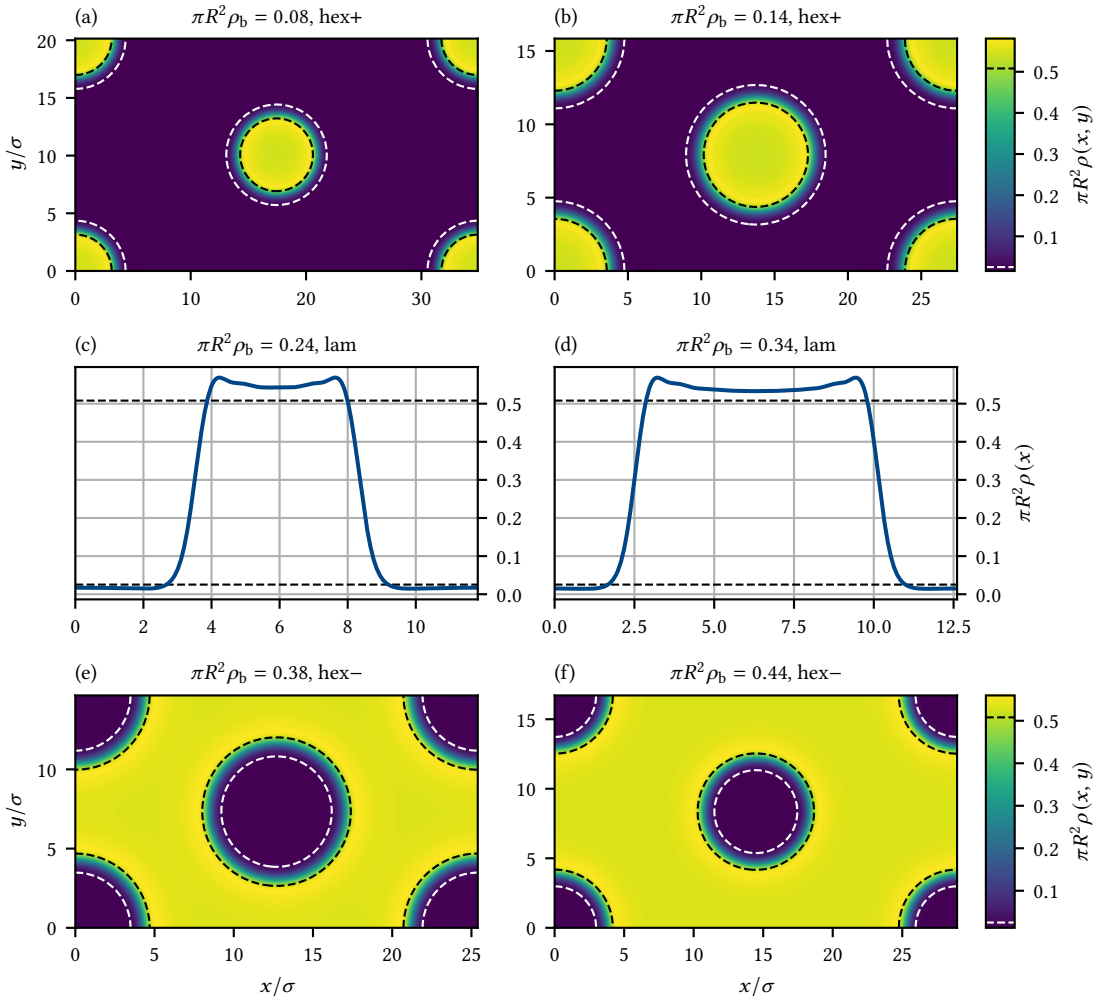

Figure 4.14.: Unit cells of the equilibrium density profiles $\eta(\vec{r}) = \pi R^2\rho(\vec{r})$ at various bulk packing fractions η_b for $\Delta T = 0.14\,\mathrm{K}$ and $B = 10\,\mu\mathrm{T}$ resulting from free minimization. Dashed lines mark the bulk packing fractions of the uniform gas and liquid at coexistence ($\eta_g \approx 0.025$ and $\eta_l \approx 0.508$, respectively). (a, b) Hexagonal droplet phase. (c, d) Lamellar stripe phase. (e, f) Hexagonal bubble phase.

Curiously, the diameter of the droplets and bubbles seems to remain more or less constant at roughly 5σ. Decreasing η_b within the droplet phase is therefore accompanied by a growth of the sparse region, while increasing η_b within the bubble phase results in a larger dense region; in either cases, the unit cell has to expand as well in order to "make room." In the stripe phase, on the other hand, the absolute size of both the dense and sparse region varies; the length of the unit cell also changes, but to a much lesser extent.

In Fig. 4.13, we can see that for the same temperature $\Delta T = 0.10\,\mathrm{K}$ but a much higher magnetic field of $B = 58\,\mu\mathrm{T}$, the equilibrium density distributions are considerably different. First of all, the

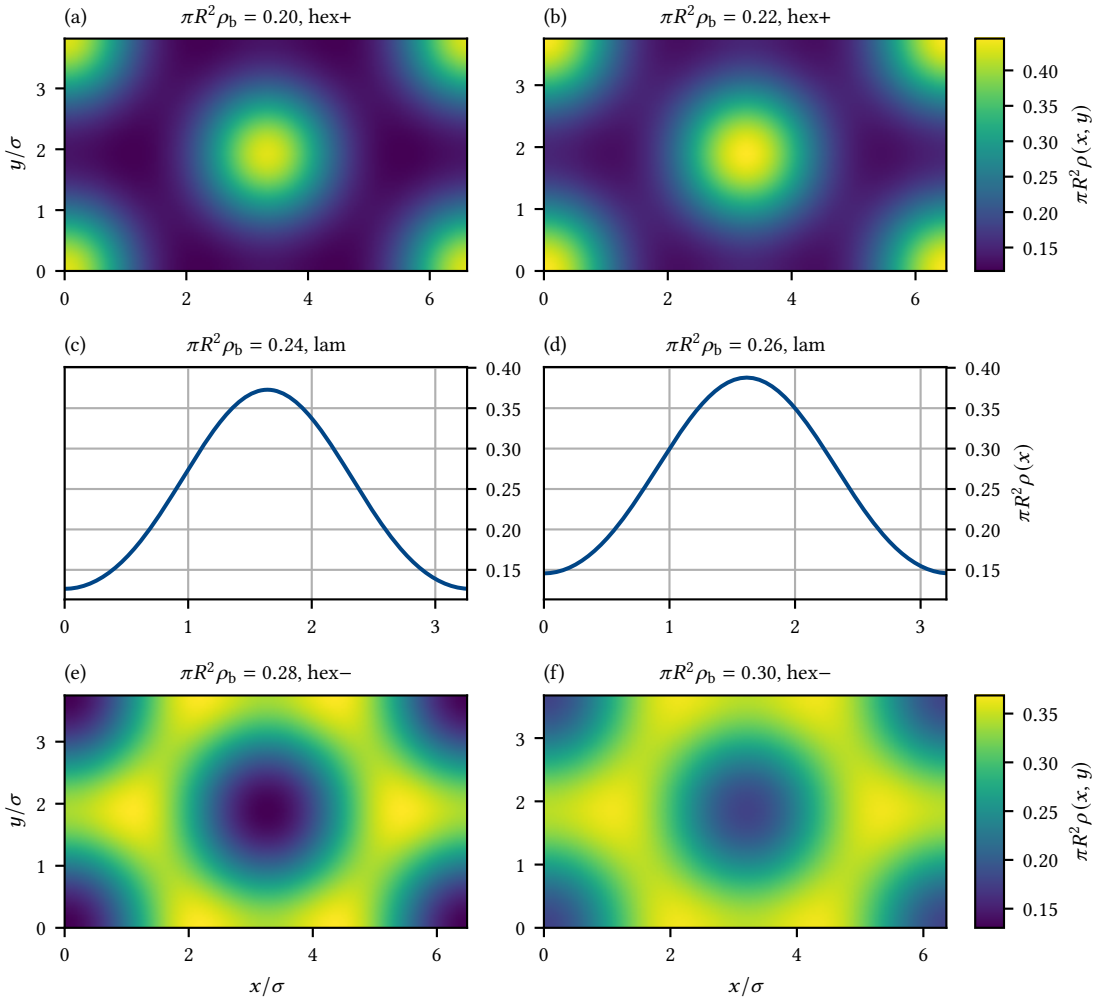

Figure 4.15.: Unit cells of the equilibrium density profiles $\eta(\vec{r}) = \pi R^2\rho(\vec{r})$ at various bulk packing fractions for $\Delta T = 0.14\,\mathrm{K}$ and $B = 20\,\mu\mathrm{T}$ resulting from free minimization. (a, b) Hexagonal droplet phase. (c, d) Lamellar stripe phase. (e, f) Hexagonal bubble phase.

dense regions no longer have the character of a plateau but rather that of a peak or a ridge, which makes it difficult to define a meaningful border between them and the sparse regions. Second, an increase in η_b leads to significantly taller peaks in the droplet phase; to higher ridges and also denser sparse regions in the stripe phase; or to actually lower ridges but denser sparse regions in the bubble phase. Third, the unit cells are a lot smaller and exhibit only slight variations in size. Last, the sparse regions of the bubble phase are not radially symmetric but have a hexagonal shape, giving rise to a honeycomb pattern.

At $\Delta T = 0.14\,\mathrm{K}$ and $B = 10\,\mu\mathrm{T}$ (which is again near the lower end of the range accessible to free minimization), we find the equilibrium density profiles displayed in Fig. 4.14. We can

make the same general observations that we already did for Fig. 4.12 with only a few minor differences: the density of the sparse region is not as close to zero and that of the dense region falls down to around $\eta \approx 0.55$, which is not high enough to cause oscillations due to packing effects; furthermore, the size of the droplets and bubbles is about twice as large with a diameter of roughly 10σ, but still relatively constant. Crucially, though, the mechanism with which the systems adepts to higher bulk densities is identical. We can directly compare Fig. 4.14 with the corresponding results from the Landau-type theory shown in Fig. 4.9 and fail to detect any resemblance whatsoever, confirming the inaccuracy of the Landau-type theory in this regime.

Finally, Fig. 4.15 shows the equilibrium density profiles at $\Delta T = 0.14\,\mathrm{K}$ and the moderate magnetic field $B = 20\,\mu\mathrm{T}$ (near the top of the low-k_1 domain). As in Fig. 4.13, the dense regions are again peak- or ridge-like, but broader and less sharp; the density distribution of the lamellar phase is almost sinusoidal in shape. In the droplet and stripe phase, an increase in η_b indeed appears to result in a global increase of the density in that $\eta'(\vec{r}) \approx \eta(\vec{r}) + \Delta\eta_\mathrm{b}$ for $\eta'_\mathrm{b} = \eta_\mathrm{b} + \Delta\eta_\mathrm{b}$; in the bubble phase, on the other hand, mainly the sparse region becomes denser. Comparing Fig. 4.15 with the results from the Landau-type theory in Fig. 4.10, we actually see a rather good agreement both in regard to the form of the density profiles as well as the size of the unit cells. This seems to speak in favor of our suspicion that the results of the Landau-type theory might be relatively accurate in this case due to the vicinity of the states to the λ-line.

Free minimization vs. Landau-type theory

In Fig. 4.16, we can see a direct comparison of the density distributions from the free minimization and the Landau-type theory for $\Delta T = 0.14\,\mathrm{K}$ and $B \in \{10\,\mu\mathrm{T}, 20\,\mu\mathrm{T}\}$. At $B = 10\,\mu\mathrm{T}$ [Figs. 4.16(a–c)], the discrepancy between the two approaches is enormous. One important reason for this is that the "true" (according to free minimization) density profiles at lower magnetic fields feature almost rectangular peaks or ridges alike to the one shown in Fig. 4.7(b) and therefore require dozens of shells to be adequately represented as opposed to the one-shell approximation we used for the Landau-type theory. Thus, even for state points near the λ-line such as $\eta_\mathrm{b} = 0.08$ [Fig. 4.16(a)], the prediction of the Landau-type theory can be very far off. A similar problem is to be expected at high B where the peaks and ridges appear to become relatively sharp. At moderate magnetic fields such as $B = 20\,\mu\mathrm{T}$ [Figs. 4.16(d–f)], on the other hand, it may happen that the equilibrium density distributions vary so slowly that the first shell gives a sufficiently good description.

Weak repulsion limit

Let us end our discussion of the free minimization by taking a closer look at the limit of a weak long-ranged repulsion, i. e., at the limit of small magnetic fields B. We have already made the

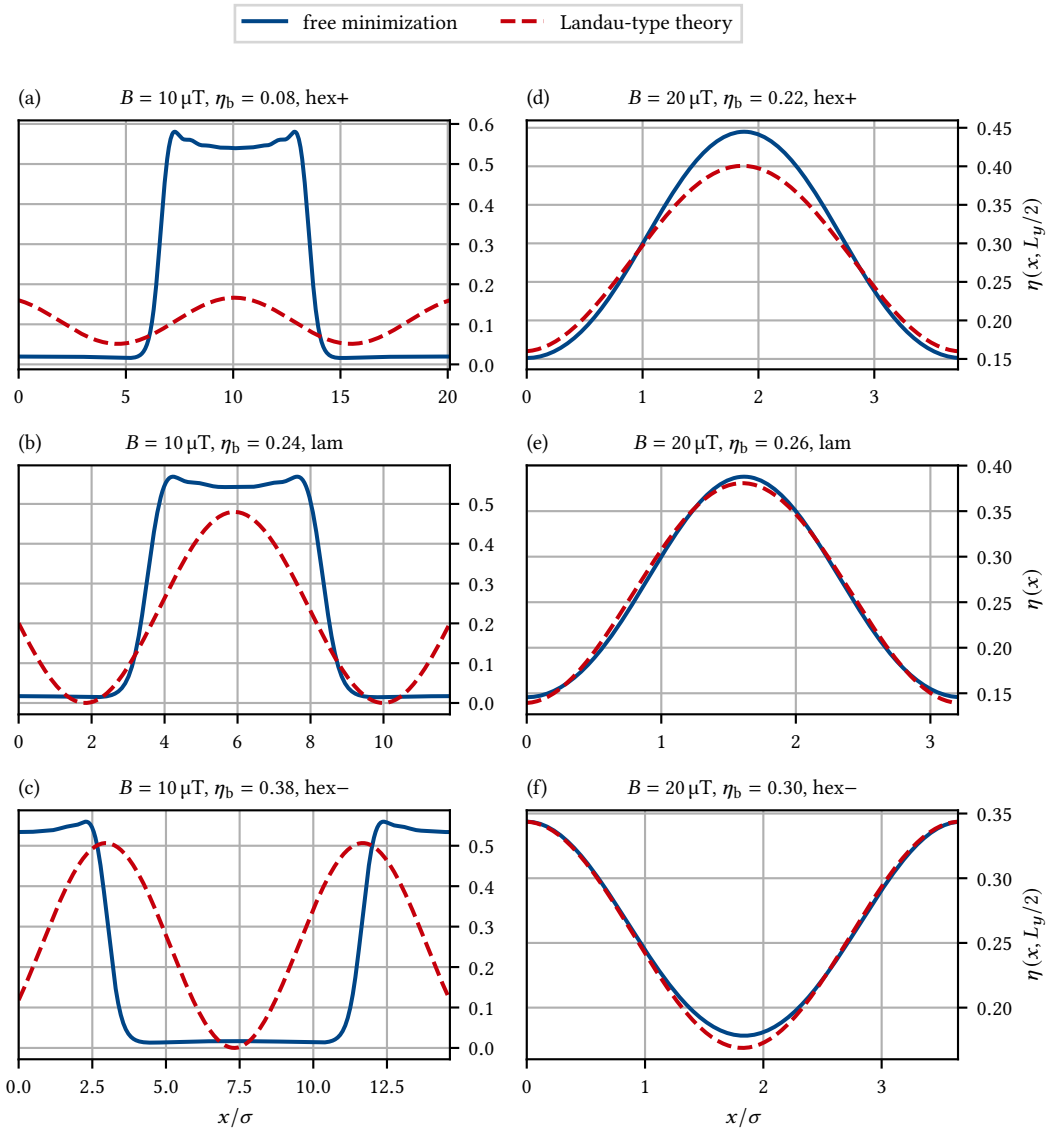

Figure 4.16.: Comparison of the density profiles obtained via free minimization (solid lines) and the Landau-type theory (dashed lines) for $\Delta T = 0.14\,\mathrm{K}$, $B \in \{10\,\mu\mathrm{T}, 20\,\mu\mathrm{T}\}$ and various bulk packing fractions η_b. For the hexagonal droplet (a, d) and bubble (c, f) structures, $\eta(x, y) = \pi R^2 \rho(x, y)$ is shown as a function of x for $y = L_y/2$.

interesting observations that, as B decreases,

(i) the λ-line converges toward the spinodal when there is a gap between the low- and high-k_1 domains in the η_b–B plane;

(ii) the principal wave vector k_1 in the low-k_1 domain goes to zero, which means that the wavelength of the density fluctuations and the size of the unit cells diverge;

(iii) the region where non-uniform microphases are theromodynamically stable (or at least

preferred to the homogeneous bulk) extends past the λ-line and up to the binodal;

(iv) the system develops dense and sparse plateaus with an almost constant density and separated by a relatively thin transition zone;

(v) changes of the bulk density primarily affect the relative size of these plateaus and not their average density.

Now, recall that for $B = 0$, we have a purely attractive hard core system that undergoes a macroscopic separation (i. e., $k_1 = 0$) into a gaseous and a liquid phase at state points enclosed by the binodal. The (average) densities ρ_g and ρ_l of the two phases are just the bulk densities of the uniform states lying on the binodal and the same for all $\rho_\mathrm{b} \in [\rho_\mathrm{g}, \rho_\mathrm{l}]$; as a consequence, the volume ratio of the phases is determined by

$$\frac{V_\mathrm{g}}{V_\mathrm{l}} = \frac{\rho_\mathrm{l} - \rho_\mathrm{b}}{\rho_\mathrm{b} - \rho_\mathrm{g}} \tag{4.111}$$

and varies with ρ_b.

Thus, the mechanisms of microphase separation at low magnetic fields are essentially identical to those of macrophase separation at $B = 0$. This suggests the hypothesis that in the presence of a weak long-ranged repulsion, gas–liquid coexistence manifests itself in the form of periodic density profiles exhibiting gaseous and liquid domains with the (average) densities ρ_g and ρ_l dictated by the binodal, and the volume ratio given by Eq. (4.111).

To test this conjecture, let us go back to Fig. 4.12, which showed the equilibrium density distributions for $\Delta T = 0.10\,\mathrm{K}$ and $B = 18\,\mu\mathrm{T}$. In the plots, we have also marked the bulk packing fractions of the gas and the liquid at coexistence which, according to the binodal in Fig. 4.11(a), are $\eta_\mathrm{g} \approx 0.014$ and $\eta_\mathrm{l} \approx 0.548$ for these states. We can see that the average packing fraction of the sparse region is close to η_g, but that of the dense region is considerably higher than η_l. This poor agreement is of course not very convincing, but not too surprising either because $B = 18\,\mu\mathrm{T}$ is only marginally below the critical magnetic field $B_\mathrm{c} \approx 20.8\,\mu\mathrm{T}$ at the top of the binodal for $\Delta T = 0.10\,\mathrm{K}$, and therefore still relatively strong; another indication for this is that λ-line can still be clearly distinguished from the spinodal.

We should expect a better agreement for $\Delta T = 0.14\,\mathrm{K}$ and $B = 10\,\mu\mathrm{T}$, which lies slightly further away from the critical magnetic field of $B_\mathrm{c} \approx 13.4\,\mu\mathrm{T}$, as can be seen in Fig. 4.11(b). Here, the coexistence packing fractions are $\eta_\mathrm{g} \approx 0.025$ and $\eta_\mathrm{l} \approx 0.508$, and a look at Fig. 4.14 reveals that they are indeed much closer to the average packing fractions in the sparse and dense regions, respectively.

As already mentioned before, going to even lower magnetic fields proved to be problematic because the unit cells would become so large that the hexagonal structures did not fit into the available computer memory anymore. Lamellar density profiles, however, require much less memory since they are constant in the y direction, which allows us to simply choose a grid with $M_y = 1$.

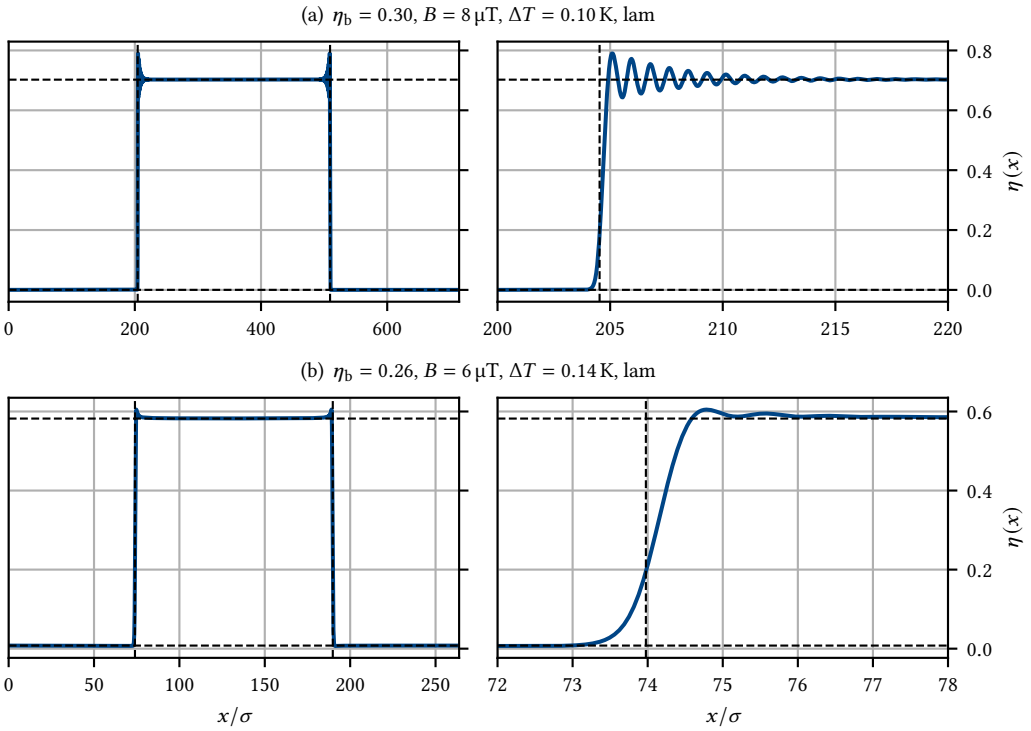

Figure 4.17.: Lamellar density profiles at (a) $\eta_b = 0.30$, $B = 8\,\mu T$, $\Delta T = 0.10\,K$ and (b) $\eta_b = 0.26$, $B = 6\,\mu T$, $\Delta T = 0.14\,K$. The panels on the left show the whole unit cell, those on the right a close-up of the transition zone between the sparse and the dense region. Horizontal dashed lines mark the bulk packing fractions of the uniform gas and liquid at coexistence [$\eta_g \approx 0.116 \times 10^{-3}$ and $\eta_l \approx 0.702$ for (a), $\eta_g \approx 7.79 \times 10^{-3}$ and $\eta_l \approx 0.582$ for (b)]. Vertical dashed lines mark the estimated locations of the transition zones according to Eq. (4.111).

Hence, we were able to determine the lamellar equilibrium density distributions at $\eta_b = 0.30$, $B = 8\,\mu T$, $\Delta T = 0.10\,K$ and $\eta_b = 0.26$, $B = 6\,\mu T$, $\Delta T = 0.14\,K$ as shown in Fig. 4.17. We can see that for such small B, the wavelength of the fluctuations has grown to hundreds of σ and the density profiles have acquired an effectively rectangular shape, transitioning from a sparse to a dense region over the length of only a few σ. The average packing fractions of these regions coincide perfectly with those of the gas and liquid phases at coexistence [$\eta_g \approx 0.116 \times 10^{-3}$ and $\eta_l \approx 0.702$ for Fig. 4.17(a), $\eta_g \approx 7.79 \times 10^{-3}$ and $\eta_l \approx 0.582$ for Fig. 4.17(b)], and the volume ratio is precisely predicted by Eq. (4.111). Thus, we can justifiably say that genuine gaseous and liquid domains of finite size (or at least with a finite extent in one direction in the case of stripes) and with distinct average densities coexist in a periodic arrangement.

At first glance, one might be tempted to think that by knowing only the binodal, we can already guess the equilibrium density distributions at low magnetic fields and a given bulk density. This is a fallacy, however, because even though we can estimate the densities and the *relative* size of the sparse and dense regions, we do not know the other two required pieces of information: the

thermodynamically stable structure and the *absolute* size of the unit cell. It would be an potential topic for further research to investigate whether there exists a less expensive way of determining this missing information than free minimization.

Conclusion

Free minimization does not come without its downsides: it is complicated to implement and computationally expensive, it had difficulties to determine the phase boundaries under certain circumstances, and it outright failed at high packing fractions and very low magnetic fields due to divergences and memory constraints, respectively. But when it *did* work, it delivered very interesting results that proved to be a lot more trustworthy than those of the Landau-type theory.

For large B, we found that the equilibrium density profiles have quite small unit cells and feature very sharp and tall peaks or ridges. By decreasing B, these structures would spread out and become much broader – with the effect that, at moderate B, the density fluctuations became so smooth that they were well described by the one-shell approximation, leading to a surprisingly good agreement with the Landau-type theory. Going to even smaller B, this agreement worsened significantly as the peaks and ridges turned into more or less flat plateaus with a relatively clear-cut edge beyond which a sparse plain followed. At B well below the critical magnetic field B_c of the binodal, the average density of the sparse and dense regions is identical to the bulk density of the corresponding gaseous and liquid states at coexistence; we interpret this as gas–liquid phase separation occurring in the form of periodic density distributions.

4.2. Confined system

Up to this point, we have only concerned ourselves with the fictitious case of a system with an infinite volume and no external potential. Although this bulk limit can be approached in experiments by confining the particles to a sufficiently large cell, it can never be fully realized in the end. Thus, to allow for a more meaningful comparison of experimental results with theoretical predictions, we shall now investigate whether – and if so, how – microphase separation manifests itself when the volume of the system is finite and relatively small. Another important reason to do so is that, as we will come to see, our method of studying the dynamics is not applicable in the bulk.

4.2.1. Methodology

To determine the equilibrium states in a finite system, we directly use the Picard iteration to freely minimize $\Omega[\rho]$ or $\mathcal{A}[\rho]$ with respect to the density profile ρ. Employing the Landau-type theory beforehand to obtain a first approximation is not expedient anymore because the

one-shell expansion is certainly no longer appropriate.

In principle, restricting the particles to a certain region $\mathbb{V} \subseteq [0, l_x] \times [0, l_y]$ with volume $V = |\mathbb{V}| \leq l_x \times l_y$ is only a matter of setting the external potential to $\mathcal{V}^{\text{ext}}(\vec{r}) = \infty$ if $\vec{r} \notin \mathbb{V}$. However, the problem is that our implementation of the free minimization algorithm for the bulk relied on the density distribution being periodic in order to speed up the calculations by taking advantage of the convolution theorem. To be able to make use of this optimization also in the case of a confined system, we have to transform a finite density profile into a periodic one in such a way that the particles in the unit cell under consideration cannot interact with their virtual mirror images in the other cells.

If all particles are in $\mathbb{V} \subseteq [0, l_x] \times [0, l_y]$, then the separation between any two of them is no larger than $r_{\text{max}} \equiv (l_x^2 + l_y^2)^{1/2}$, which means that we can artificially truncate u_{ci} at r_{max}, i. e.,

$$u_{\text{ci}}(r) = \begin{cases} u_{\text{cas}}(\sigma) + u_{\text{mag}}(\sigma) & \text{if } r \leq \sigma, \\ u_{\text{cas}}(r) + u_{\text{mag}}(r) & \text{if } \sigma < r \leq r_{\text{max}}, \\ 0 & \text{otherwise,} \end{cases} \tag{4.112}$$

without altering the interactions within $\mathbb{V}$ (keep in mind that truncating u_{ci} also affects its Fourier transform $\tilde{u}_{\text{ci}}$). This has the consequence that two colloids of diameter σ do not interact with each other if they are more than a distance $W \equiv \max\{\sigma, r_{\text{max}}\}$ apart. As external potential, we now choose

$$\mathcal{V}^{\text{ext}}(\vec{r}) \equiv \sum_{i,j \in \mathbb{Z}} \mathcal{V}_{\mathbb{V}}^{\text{ext}}(x + iL_x, y + jL_y) \tag{4.113}$$

with $L_x \equiv l_x + W$, $L_y \equiv l_y + W$ and

$$\mathcal{V}_{\mathbb{V}}^{\text{ext}}(\vec{r}) \equiv \begin{cases} \infty & \text{if } \vec{r} \notin \mathbb{V}, \\ 0 & \text{otherwise.} \end{cases} \tag{4.114}$$

Since $\mathcal{V}^{\text{ext}}$ is (L_x, L_y)-periodic by construction, symmetry dictates that the equilibrium density distribution must be, too. Within each unit cell of size $L_x \times L_y$, only a subregion with volume V can actually contain any particles – and because the separation between the mirror images of that subregion is at least W, they cannot influence one another. The particles in $\mathbb{V}$ are therefore completely isolated from their environment. Through an appropriate choice of the unit cell and the external potential, we are thus able to apply our existing free minimization procedure also to a confined system.

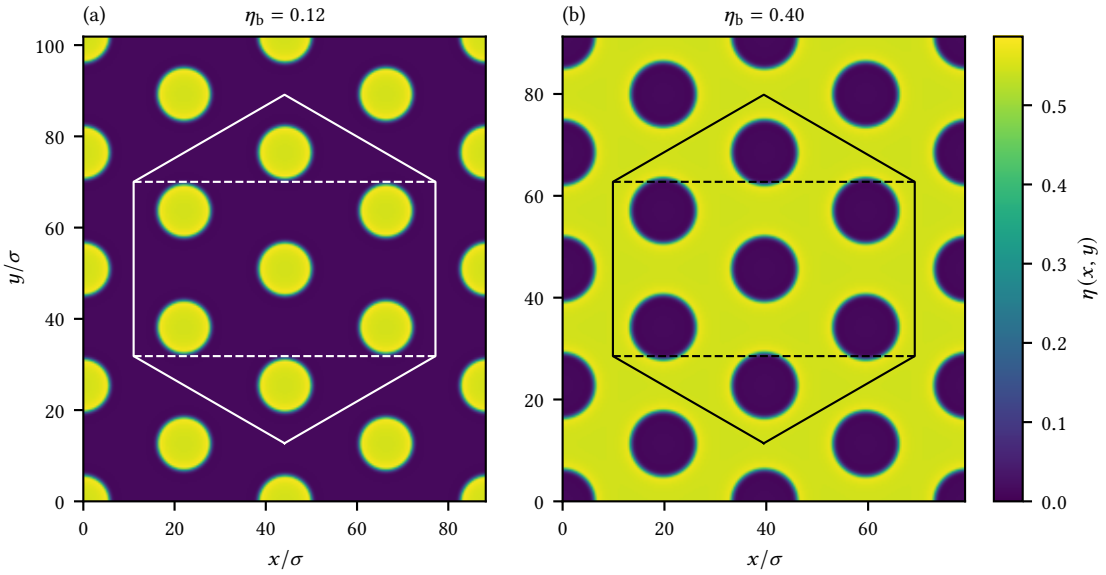

Figure 4.18.: Equilibrium density profiles for $B = 9\,\mu\mathrm{T}$ and $\Delta T = 0.14\,\mathrm{K}$ in the bulk. The solid hexagon and dashed rectangle indicate possible cells for a confined system that are compatible with the bulk structure. (a) Hexagonal droplet phase at $\eta_b = 0.12$. (b) Hexagonal bubble phase at $\eta_b = 0.40$.

4.2.2. Hexagonal and rectangular cells

If the system is finite, it is on us to decide how the cell containing the particles should look like. Since we are interested in observing clear signs of microphase separation, the question arises as to which sizes and shapes of $\mathbb{V}$ are conducive to achieving this goal. In the absence of any other guidance, it would certainly make sense to use our knowledge about the bulk for orientation. While the lamellar phase is problematic due to the infinite length of the stripes, it seems at least plausible that the droplet and bubble phases might also prevail in the confined system if we "cut out" a suitable portion of the equilibrium density profile in the bulk.

Consider for example the droplet ($\eta_b = 0.12$) and bubble ($\eta_b = 0.40$) states for an infinite system ($\Delta T = 0.14$, $B = 9\,\mu\mathrm{T}$) shown in Fig. 4.18. One possibility, as indicated by the solid outline, is to use a hexagonal cell that has a side length of $\sqrt{27}\pi/(2k_1^{\mathrm{hex}})$ and is able to fit one central droplet or bubble as well as its six nearest neighbors. This indeed works quite well as the equilibrium density distributions of the confined system shown in Figs. 4.19(a,c) demonstrate: although the size, shape and/or the position of the droplets and bubbles changed slightly (note that the outer droplets moved toward to wall of the cell whereas the bubbles moved toward the center), all seven of them still exist. We were curious to know what would happen if we used this hexagonal cell at an intermediate bulk packing fraction ($\eta_b = 0.24$) where the stripe phase would be stable in the infinite system; since the lamellar density profile does not suggest a "natural" choice for the

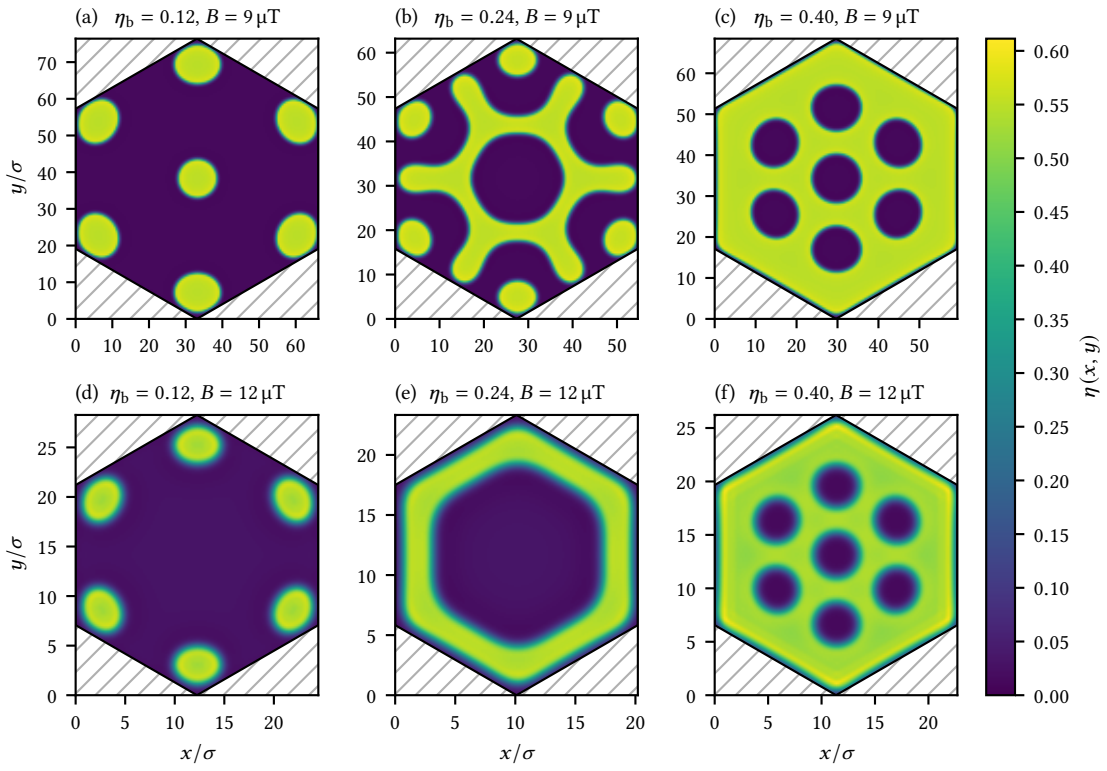

Figure 4.19.: Equilibrium density profiles at $\Delta T = 0.14\,\mathrm{K}$ for a hexagonal cell with side length $\sqrt{27}\pi/(2k_1)$, where k_1 denotes the principal wavenumber of the corresponding equilibrium structures in the bulk.

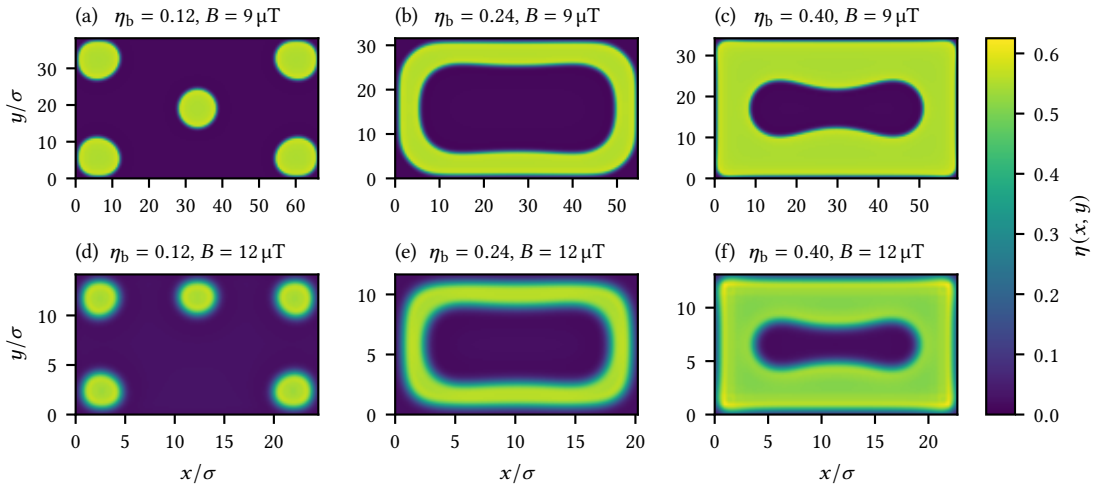

Figure 4.20.: Equilibrium density profiles at $\Delta T = 0.14\,\mathrm{K}$ for a rectangular cell with side lengths $L_x = \sqrt{3}L_y = 6\pi/k_1$, where k_1 denotes the principal wavenumber of the corresponding equilibrium structures in the bulk.

size of the hexagon, we used a side length of $\sqrt{27}\pi/(2k_1^{\mathrm{lam}})$. The outcome is shown in Fig. 4.19(b) and resembles a ship's wheel with six handles, each perpendicular to one side of the hexagon, and a large bubble in the center; in addition, there is one smaller droplet in every corner of the cell. In a sense, it is a really fascinating density distribution that blends droplet, bubble and elongated structures together. While these results are certainly encouraging, the equilibrium density profiles that this approach produces are unfortunately not as consistent as one would hope. For example, if we repeat the same process at a higher magnetic field ($B = 12\,\mu\mathrm{T}$), we can see in Figs. 4.19(d–f) that the central droplet has vanished and that the ship's wheel at $\eta_{\mathrm{b}} = 0.24$ has turned into a hexagonal ring that runs alongside the wall of the cell. Only the bubble phase retained its original characteristics.

We also tried a rectangular cell with $L_x = \sqrt{3}L_y = 6\pi/k_1$, as suggested by the dashed outline in Fig. 4.18, hoping to stabilize a central droplet/bubble and four of its nearest neighbors. For $B = 9\,\mu\mathrm{T}$, we can see in Figs. 4.20(a–c) that this only succeeded at $\eta_{\mathrm{b}} = 0.12$ with the droplets, whereas the bubbles at $\eta_{\mathrm{b}} = 0.40$ merged into a single dumbbell-shaped cavity surrounded by a thick ring of higher density. We find the same structure also at $\eta_{\mathrm{b}} = 0.24$, albeit with a ring that is much thinner. As shown in Figs. 4.20(d–f), this ring phase even survives if we increase the magnetic field to $B = 12\,\mu\mathrm{T}$, but the central droplet surprisingly moves toward one of the long sides of the cell (and we have not been able to identify another configuration with a lower free energy).

We can definitely assert that, if the system undergoes microphase separation in the infinite bulk at a particular state point, than there is a good chance that this also happens if the particles are confined to a finite cell whose size is on the same order as the wavelength of the density fluctuations in the bulk. Unfortunately, there is not a one-to-one correspondence between the structures that are stable in the bulk and those that emerge under confinement. What really complicates the phase behavior, though, is that certain structures appear to come in multiple variants. At least for the hexagonal and rectangular cells that we investigated, this could potentially make the calculation of a phase diagram rather difficult.

4.2.3. Square cells

It turns out, however, that square cells exhibit a fairly simple and consistent phase behavior: between almost uniform gas and liquid phases at very low and very high bulk densities, respectively, we have only observed a phase with four droplets (one in each corner of the cell) at lower, as well as one with a ring of variable width at higher bulk densities. In Fig. 4.21, we plot several density distributions for a cell with $L \equiv L_x = L_y = 2\sqrt{3}\pi/k_1$, where k_1 again denotes the principal wavenumber of the stable bulk structure. For $\Delta T = 0.14\,\mathrm{K}$ and all $B \in \{9\,\mu\mathrm{T}, 12\,\mu\mathrm{T}\}$, we find a droplet phase at $\eta_{\mathrm{b}} = 0.12$ and a ring phase at $\eta_{\mathrm{b}} = 0.40$. At $\eta_{\mathrm{b}} = 0.24$, where the stripe phase is stable in the bulk, it depends on B whether the confined system preferably forms a ring

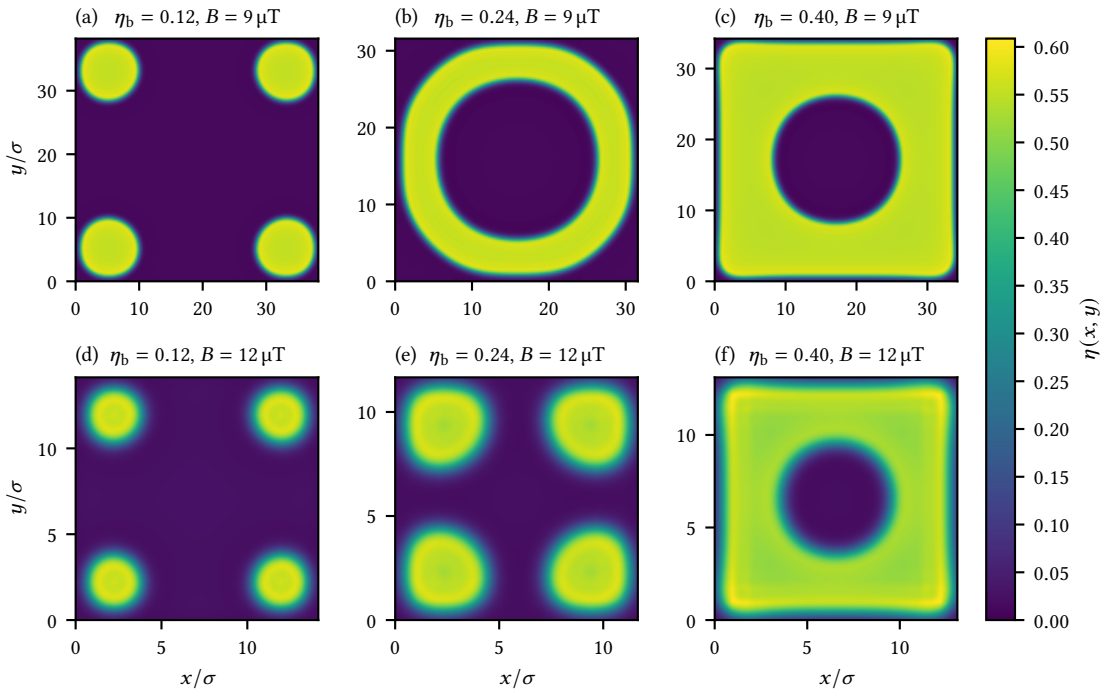

Figure 4.21.: Equilibrium density profiles at $\Delta T = 0.14\,\mathrm{K}$ for a square cell with side length $L = L_x = L_y = 2\sqrt{3}\pi/k_1$, where k_1 denotes the principal wavenumber of the corresponding equilibrium structures in the bulk.

($B = 9\,\mu\mathrm{T}$) or droplets ($B = 12\,\mu\mathrm{T}$).

Note that we have so far always selected the size of the cell according to the bulk structure which varies with η_b, B and ΔT. In experiments, replacing the cell every time that the external parameters are altered would be highly impractical, of course. Luckily, the phase behavior in a square cell does not depend *that* sensitively on the cell's size, so that if we just stick to some reasonable choice for L, we find that, at least for a certain range of magnetic fields and temperatures, the system still follows the phase sequence of gas → droplets → ring → liquid as the bulk density increases.

In the end, we decided to go with a side length of $L \in \{20\sigma, 30\sigma\}$ and found a good-natured phase behavior at a temperature of $\Delta T = 0.16\,\mathrm{K}$ and for magnetic fields within a few percent of $B = 8\,\mu\mathrm{T}$ (which is slightly below $B_c \approx 9.79\,\mu\mathrm{T}$). For both cell sizes, we calculated a phase diagram in the η_b–B plane by determining the coexistence states lying on the phase borders in the same way that we did for the bulk system. In Fig. 4.22, we can see that the two phase diagrams look quite similar; they feature a droplet phase that is much narrower compared to the ring phase and "sandwiched" between rather wide regions of coexistence, particularly at lower B. This is in contrast to the phase diagrams for the infinite system in Fig. 4.11, where the droplet, stripe and bubble phases are almost equal in width and separated by relatively slim gaps. It could be that the

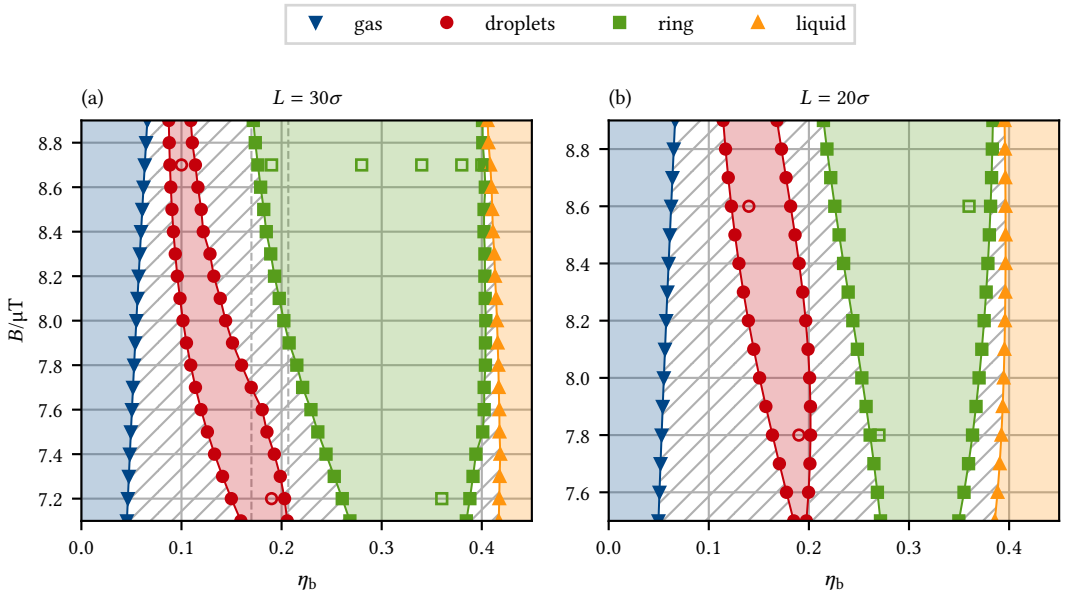

Figure 4.22.: Phase diagrams in the η_b–B plane for $\Delta T = 0.16\,\mathrm{K}$ and a system confined to a square cell with side length (a) $L = 30\sigma$ or (b) $L = 20\sigma$. Filled symbols show the coexistence states of the gas, droplet, ring and liquid phases; the regions of coexistence are hatched. Unfilled symbols mark the state points of the density profiles shown in Figs. 4.23 and 4.24. The dashed vertical lines in (a) indicate a range of bulk packing fractions where, depending on B, either the droplet or the ring phase can be stable.

stripe and bubble phases effectively coalesce into a single, broad ring phase upon confinement, which would explain why the droplet phase is considerable thinner.

A closer inspection of the phase diagram for $L = 30\sigma$ reveals an interesting trait that it does not share with the one for $L = 20\sigma$, namely that the droplet and ring phases overlap to some extent in the sense that, depending on the magnetic field, either of the two can be stable for a small range of bulk packing fractions ($0.17 \lesssim \eta_b \lesssim 0.207$). This means that is should be possible to transition from one phase to the other solely by varying B, which is something that we will come back to when we study the dynamics of the system.

In Figs. 4.23 and 4.24, we show the equilibrium density profiles for those states marked by the unfilled symbols in Figs. 4.22(a) and 4.22(b), respectively. While the majority of them do not stand out and are very similar to those in Fig. 4.21, we find that the central bubble of the ring phase can take on a remarkable variety shapes for $L = 30\sigma$ and higher magnetic fields: if $B = 8.7\,\mu\mathrm{T}$, for example, the region enclosed by the ring is almost square at $\eta_b = 0.19$, resembles a four-leaf clover at $\eta_b = 0.28$, looks like a horseshoe at $\eta_b = 0.34$, becomes a slit at $\eta_b = 0.38$ and ends up as a small disk at $\eta_b = 0.40$.

The effects of confinement in systems with microphase separation have already been the target of several studies. Serna et al. investigated a three-dimensional colloidal system with competing

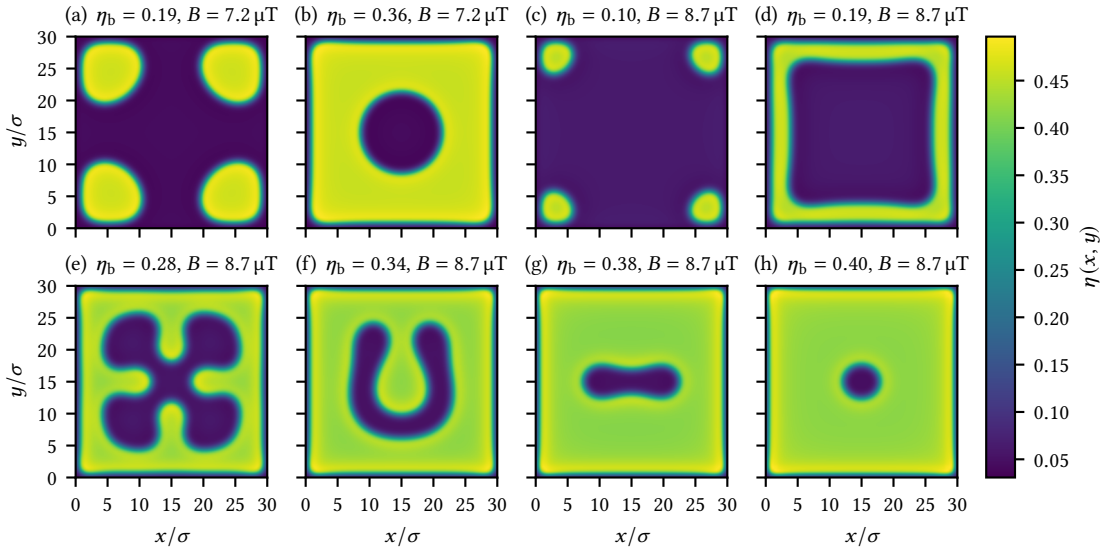

Figure 4.23.: Equilibrium density profiles at $\Delta T = 0.16\,\mathrm{K}$ and $B = 7.2\,\mu\mathrm{T}$ (a, b) or $B = 8.7\,\mu\mathrm{T}$ (c–h) for a square cell with side length $L = 30\sigma$. (a, c) Droplet phase. (b, d–h) Ring phase in a variety of different shapes.

interactions and focused on the hexagonal cylindrical phase [85], which is similar to the two-dimensional hexagonal droplet phase extended in the perpendicular direction. They found that this phase can also be stable when confined to channels with hard walls and a triangular or hexagonal cross section, i. e., a shape compatible with the equilibrium pattern in the bulk. For square cross sections, the cylinders form in some cases a square lattice comparable to the droplet phase we observed in a square cell; however, whereas we never encountered a stable phase with more than four droplets, the number of cylinders does not seem to be limited. Interestingly, for larger chemical potentials (and thus bulk densities), Serna et al. also found analogs of the ring phase in the form of (possibly multiple concentric) tubes parallel to the channels. Pękalski et al.

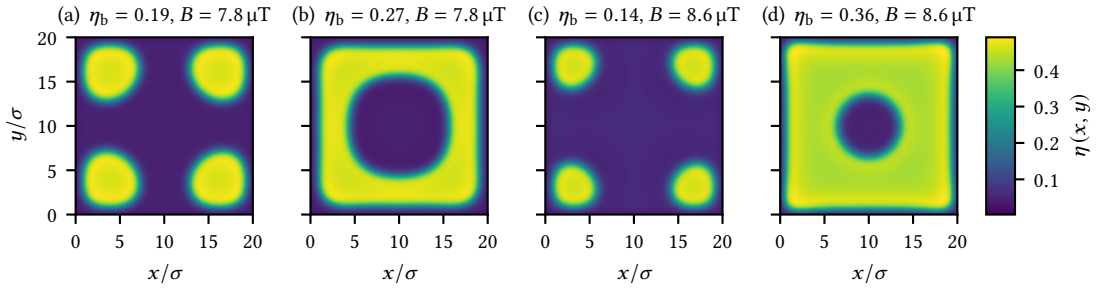

Figure 4.24.: Equilibrium density profiles at $\Delta T = 0.16\,\mathrm{K}$ and $B = 7.8\,\mu\mathrm{T}$ (a, b) or $B = 8.6\,\mu\mathrm{T}$ (c, d) for a square cell with side length $L = 20\sigma$. (a, c) Droplet phase. (b, d) Ring phase.

likewise observed concentric rings in their study of a two-dimensional triangular lattice model with competing interactions in hexagonal confinement [86]. In a two-dimensional system with a short-ranged Yukawa attraction, long-ranged Coulomb repulsion and a circular logarithmic trap, Xu et al. found droplet and ring structures along with other more exotic ones [87]; similar patterns also emerged in a two-dimensional system studied by Liu et al., featuring a short-ranged exponential attraction, long-ranged Yukawa repulsion and circular quadratic trap [88].

Now that we have a good understanding of the phase behavior of our model system when it is confined to a square cell, we can turn our attention to investigating the dynamics of microphase separation.

5. Dynamics

In the previous chapter, we saw that our model system with competing attractive critical Casimir and repulsive magnetic dipole interactions can exhibit stable microphases with inhomogeneous density distributions for suitable combinations of the temperature T, the magnetic field B and the bulk packing fraction η_b. If one were to conduct experiments in order to test our theoretical predictions, one would need to take into consideration that the structure of the system must evolve dynamically over time until it eventually converges on a state of equilibrium. It is not guaranteed, however, that this state corresponds to the one with the lowest Helmholtz free energy: the dynamics might also draw to a halt if the system becomes stuck in a local minimum. For this reason, we shall first study the dynamical evolution of the density profiles theoretically. It should be interesting to see just how easily the system is trapped by local minima, and whether we can take advantage of the ability to change T and B *in situ* to navigate the free energy landscape and arrive at the global minimum.

5.1. Brownian motion and the Langevin equation

During microscopy studies in 1827, Robert Brown observed that pollen grains immersed in water would perform an essentially random walk through space [7]. This so-called *Brownian motion* arises because the pollen are being constantly "bombarded" from all directions with water molecules, each collision transferring a tiny amount of momentum from one participant to the other. Since colloids are similar in size to pollen grains – and typically even smaller – they behave in the same way.

Let us follow Langevin [89, 90] to derive the equation that determines the trajectory q of a single colloidal particle with mass m submerged in a solvent. If the colloid only interacts with the molecules of the solvent, we can write Newton's second law as

$$m\frac{\mathrm{d}^2\vec{q}(t)}{\mathrm{d}t^2} = -\gamma\frac{\mathrm{d}\vec{q}(t)}{\mathrm{d}t} + \vec{\zeta}(t), \tag{5.1}$$

where the first term on the right hand side represents Stokes' drag with the friction coefficient γ, and $\vec{\zeta}$ is a force that accounts for the random collisions of the solvent's molecules with the colloid. Since it is hopeless to describe $\vec{\zeta}$ on a molecular level, we take $\vec{\zeta}(t)$ to be a random variable. By extension, $\vec{q}(t)$ also becomes a random variable and Eq. (5.1) then turns into a stochastic differential equation. Instead of calculating the true trajectory of the colloid, we will therefore

have to content ourselves with making purely probabilistic predictions. Because we can expect $\vec{\zeta}(t)$ and $\vec{q}(t)$ to be normally distributed, it is sufficient to determine their mean and variance to fully specify the statistical picture.

It is reasonable to assume that the molecules will hit the colloid from all directions with equal probability so that

$$\langle\vec{\zeta}(t)\rangle = 0. \tag{5.2}$$

Taking the mean of both sides of Eq. (5.1), we arrive at the ordinary differential equation

$$m\frac{\mathrm{d}^2\langle\vec{q}(t)\rangle}{\mathrm{d}t^2} = -\gamma\frac{\mathrm{d}\langle\vec{q}(t)\rangle}{\mathrm{d}t} + \langle\vec{\zeta}(t)\rangle = -\gamma\frac{\mathrm{d}\langle\vec{q}(t)\rangle}{\mathrm{d}t} \tag{5.3}$$

for $\langle\vec{q}(t)\rangle$, which is solved by

$$\langle\vec{q}(t)\rangle = \langle\vec{q}(t_0)\rangle + \frac{m}{\gamma}\left.\frac{\mathrm{d}\langle\vec{q}(t)\rangle}{\mathrm{d}t}\right|_{t=t_0}\left[1 - \exp\left\{-\frac{\gamma}{m}(t-t_0)\right\}\right]. \tag{5.4}$$

If the colloid is brought into contact with the solvent at $t = 0$, it follows for $t_0 \gg m/\gamma$ that

$$\left.\frac{\mathrm{d}\langle\vec{q}(t)\rangle}{\mathrm{d}t}\right|_{t=t_0} = \left.\frac{\mathrm{d}\langle\vec{q}(t)\rangle}{\mathrm{d}t}\right|_{t=0}\exp\left(-\frac{\gamma}{m}t_0\right) \approx 0, \tag{5.5}$$

in which case Eq. (5.4) simplifies to

$$\langle\vec{q}(t)\rangle \approx \langle\vec{q}(t_0)\rangle. \tag{5.6}$$

Thus, the average position of the colloid does not change over time.

Let us now continue by calculating the variance of $\vec{q}(t)$,

$$\langle\Delta\vec{q}(t)^2\rangle = \langle[\vec{q}(t) - \langle\vec{q}(t)\rangle]^2\rangle = \langle\vec{q}(t)^2\rangle - \langle\vec{q}(t)\rangle^2 \tag{5.7}$$

with $\Delta\vec{q}(t) \equiv \vec{q}(t) - \langle\vec{q}(t)\rangle$. Using that

$$\frac{\mathrm{d}\vec{q}(t)^2}{\mathrm{d}t} = 2\vec{q}(t)\frac{\mathrm{d}\vec{q}(t)}{\mathrm{d}t}, \qquad \frac{\mathrm{d}^2\vec{q}(t)^2}{\mathrm{d}t^2} = 2\left(\frac{\mathrm{d}\vec{q}(t)}{\mathrm{d}t}\right)^2 + 2\vec{q}(t)\frac{\mathrm{d}^2\vec{q}(t)}{\mathrm{d}t^2} \tag{5.8}$$

and multiplying Eq. (5.1) with $2\vec{q}(t)$, we find that

$$2\vec{q}(t)\vec{\zeta}(t) = 2m\vec{q}(t)\frac{\mathrm{d}^2\vec{q}(t)}{\mathrm{d}t^2} + 2\gamma\vec{q}(t)\frac{\mathrm{d}\vec{q}(t)}{\mathrm{d}t} = m\frac{\mathrm{d}^2\vec{q}(t)^2}{\mathrm{d}t^2} - 2m\left(\frac{\mathrm{d}\vec{q}(t)}{\mathrm{d}t}\right)^2 + \gamma\frac{\mathrm{d}\vec{q}(t)^2}{\mathrm{d}t}, \tag{5.9}$$

which, after taking the mean, leads to

$$m\frac{\mathrm{d}^2\langle\vec{q}(t)^2\rangle}{\mathrm{d}t^2} - \frac{2}{m}\langle\vec{p}(t)^2\rangle + \gamma\frac{\mathrm{d}\langle\vec{q}(t)^2\rangle}{\mathrm{d}t} = 2\langle\vec{q}(t)\rangle\langle\vec{\zeta}(t)\rangle = 0 \tag{5.10}$$

with the momentum $\vec{p}(t) = m[\mathrm{d}\vec{q}(t)/\mathrm{d}t]$ of the colloid. In thermodynamic equilibrium, we can calculate $\langle\vec{p}^2\rangle$ as an ensemble average to be

$$\langle\vec{p}^2\rangle = \frac{1}{\mathcal{Z}_{\mathrm{can}}h^d}\int \mathrm{d}^d\vec{q}\int \mathrm{d}^d\vec{p}\,\vec{p}^2\exp\left[-\beta\left\{\frac{\vec{p}^2}{2m}+\mathcal{V}(\vec{q})\right\}\right] = d\frac{m}{\beta} = dmk_{\mathrm{B}}T, \tag{5.11}$$

so that Eq. (5.10) becomes

$$m\frac{\mathrm{d}^2\langle\vec{q}(t)^2\rangle}{\mathrm{d}t^2}+\gamma\frac{\mathrm{d}\langle\vec{q}(t)^2\rangle}{\mathrm{d}t}-2dk_{\mathrm{B}}T = 0. \tag{5.12}$$

The solution to this differential equation for $\langle\vec{q}(t)^2\rangle$ is given by

$$\langle\vec{q}(t)^2\rangle = \langle\vec{q}(t_0)^2\rangle + 2d\frac{k_{\mathrm{B}}T}{\gamma}(t-t_0)+\frac{m}{\gamma}\left[\left.\frac{\mathrm{d}\langle\vec{q}(t)^2\rangle}{\mathrm{d}t}\right|_{t=t_0}-2d\frac{k_{\mathrm{B}}T}{\gamma}\right]\left[1-\exp\left\{-\frac{\gamma}{m}(t-t_0)\right\}\right]. \tag{5.13}$$

For $t_0 \gg m/\gamma$, this means that

$$\left.\frac{\mathrm{d}\langle\vec{q}(t)^2\rangle}{\mathrm{d}t}\right|_{t=t_0} = 2d\frac{k_{\mathrm{B}}T}{\gamma}+\left[\left.\frac{\mathrm{d}\langle\vec{q}(t)^2\rangle}{\mathrm{d}t}\right|_{t=0}-2d\frac{k_{\mathrm{B}}T}{\gamma}\right]\exp\left(-\frac{\gamma}{m}t_0\right)\approx 2d\frac{k_{\mathrm{B}}T}{\gamma} \tag{5.14}$$

and hence

$$\langle\vec{q}(t)^2\rangle \approx \langle\vec{q}(t_0)^2\rangle + 2d\frac{k_BT}{\gamma}(t-t_0). \tag{5.15}$$

For the variance of $\vec{q}(t)$, we therefore find

$$\begin{aligned}\langle\Delta\vec{q}(t)^2\rangle &= \langle\vec{q}(t)^2\rangle-\langle\vec{q}(t)\rangle^2 \approx \langle\vec{q}(t_0)^2\rangle+2d\frac{k_BT}{\gamma}(t-t_0)-\langle\vec{q}(t_0)\rangle^2\\ &= \langle\Delta\vec{q}(t_0)^2\rangle+2d\frac{k_BT}{\gamma}(t-t_0)\end{aligned} \tag{5.16}$$

It turns out that we can directly arrive at Eqs. (5.6) and (5.16) if we neglect the inertial term on the left hand side of Eq. (5.1),

$$\gamma\frac{\mathrm{d}\vec{q}(t)}{\mathrm{d}t} = \vec{\zeta}(t), \tag{5.17}$$

and demand that the covariance of the individual components of $\vec{\zeta}(t)$ is given by

$$\langle\zeta_k(t)\,\zeta_l(t')\rangle = 2\gamma k_{\mathrm{B}}T\delta_{kl}\delta(t-t'). \tag{5.18}$$

We can formally solve Eq. (5.17) for $\vec{q}(t)$ in the sense that

$$\vec{q}(t) = \vec{q}(t_0)+\int_{t_0}^{t}\mathrm{d}t'\,\frac{\mathrm{d}\vec{q}(t')}{\mathrm{d}t'} = \vec{q}(t_0)+\frac{1}{\gamma}\int_{t_0}^{t}\mathrm{d}t'\,\vec{\zeta}(t'), \tag{5.19}$$

from which

$$\langle \vec{q}(t) \rangle = \langle \vec{q}(t_0) \rangle + \frac{1}{\gamma} \int_{t_0}^{t} \mathrm{d}t' \underbrace{\langle \vec{\zeta}(t') \rangle}_{=0} = \langle \vec{q}(t_0) \rangle \tag{5.20}$$

immediately follows. Furthermore, we find that

$$\begin{aligned} \langle \vec{q}(t)^2 \rangle &= \left\langle \left[\vec{q}(t_0) + \frac{1}{\gamma} \int_{t_0}^{t} \mathrm{d}t' \, \vec{\zeta}(t') \right] \left[\vec{q}(t_0) + \frac{1}{\gamma} \int_{t_0}^{t} \mathrm{d}t'' \, \vec{\zeta}(t'') \right] \right\rangle \\ &= \langle \vec{q}(t_0)^2 \rangle + \frac{2}{\gamma} \langle \vec{q}(t_0) \rangle \cdot \int_{t_0}^{t} \mathrm{d}t' \underbrace{\langle \vec{\zeta}(t') \rangle}_{=0} + \frac{1}{\gamma^2} \int_{t_0}^{t} \mathrm{d}t' \int_{t_0}^{t} \mathrm{d}t'' \underbrace{\langle \vec{\zeta}(t') \cdot \vec{\zeta}(t'') \rangle}_{=2d\gamma k_\mathrm{B} T \delta(t'-t'')} \\ &= \langle \vec{q}(t_0)^2 \rangle + 2d \frac{k_\mathrm{B} T}{\gamma} (t - t_0) \end{aligned} \tag{5.21}$$

and thus

$$\begin{aligned} \langle \Delta \vec{q}(t)^2 \rangle &= \langle \vec{q}(t)^2 \rangle - \langle \vec{q}(t) \rangle^2 = \langle \vec{q}(t_0)^2 \rangle + 2d \frac{k_\mathrm{B} T}{\gamma} (t - t_0) - \langle \vec{q}(t_0) \rangle^2 \\ &= \langle \Delta \vec{q}(t_0)^2 \rangle + 2d \frac{k_\mathrm{B} T}{\gamma} (t - t_0). \end{aligned} \tag{5.22}$$

The so-called Langevin equation (5.17) in combination with (5.18) is therefore statistically equivalent to (5.1) at time scales much larger than m/γ.

If the system consists of a collection of N colloids that additionally interact with each other through the pair potential u and are subject to the external potential $\mathcal{V}_\mathrm{ext}$, the Langevin equation is naturally generalized to a coupled set of N differential equations for the trajectories $(\vec{q}_1, \ldots, \vec{q}_N)$ in that

$$\gamma \frac{\mathrm{d}\vec{q}_i(t)}{\mathrm{d}t} = \vec{K}_i(\vec{q}_i(t), t) + \vec{\zeta}_i(t) \tag{5.23}$$

with the deterministic force

$$\vec{K}_i(\vec{r}, t) = -\sum_{j=1\,(j\neq i)}^{N} \vec{\nabla} u(\vec{r} - \vec{q}_j(t)) - \vec{\nabla} \mathcal{V}^\mathrm{ext}(\vec{r}) \tag{5.24}$$

and $\langle \zeta_{ik}(t) \, \zeta_{jl}(t') \rangle = 2\gamma k_\mathrm{B} T \delta_{ij} \delta_{kl} \delta(t - t')$.

In Brownian dynamics simulations, the Langevin equation is integrated numerically [91] in small time steps of Δt via, for example,

$$\vec{q}_i(t + \Delta t) = \int_{t}^{t+\Delta t} \mathrm{d}t' \, \frac{\mathrm{d}\vec{q}_i(t')}{\mathrm{d}t'} \approx \frac{\vec{K}_i(\vec{q}_i(t), t) + \vec{Z}_i(t)}{\gamma} \Delta t, \tag{5.25}$$

where $Z_{ik}(t)$ is randomly picked according to a normal distribution with zero mean and a variance of $2\gamma k_\mathrm{B} T / \Delta t$.

5.2. Dynamic density functional theory

Instead of calculating the individual trajectories of a large collection of colloids, dynamical density functional theory (DDFT) [92] specifies how the density profile of the system evolves when the motion of the particles is dictated by the Langevin equation (5.23). This is especially useful in our case because it allows us to leverage many facilities already developed for the static DFT and to directly compare the equilibrium states predicted by the two methods.

5.2.1. Derivation

To derive the fundamental equation of DDFT, we will follow Marconi and Tarazona [93, 94]. Given some function f and a stochastic differential equation of the form

$$\frac{\mathrm{d}\vec{r}(t)}{\mathrm{d}t} = \vec{a}(\vec{r}(t), t) + b(\vec{r}(t), t)\,\vec{\zeta}(t) \tag{5.26}$$

with $\langle \zeta_k(t)\,\zeta_l(t')\rangle = c^2\delta_{kl}\delta(t-t')$, Itô's lemma of stochastic calculus [95] states that

$$\begin{aligned}\frac{\mathrm{d}f(\vec{r}(t))}{\mathrm{d}t} &= \frac{\mathrm{d}\vec{r}(t)}{\mathrm{d}t}\cdot\vec{\nabla}f(\vec{r}(t)) + \frac{1}{2}[cb(\vec{r},t)]^2\,\vec{\nabla}^2 f(\vec{r}(t)) \\ &= \left[\vec{a}(\vec{r}(t),t) + b(\vec{r}(t),t)\,\vec{\zeta}(t)\right]\cdot\vec{\nabla}f(\vec{r}(t)) + \frac{1}{2}[cb(\vec{r},t)]^2\,\vec{\nabla}^2 f(\vec{r}(t)).\end{aligned} \tag{5.27}$$

If we compare Eq. (5.26) with the Langevin equation (5.23), we can identify

$$\vec{r}(t) \mathrel{\hat{=}} \vec{q}_i(t), \qquad \vec{a}(\vec{r}(t),t) \mathrel{\hat{=}} \frac{\vec{K}_i(\vec{q}_i(t),t)}{\gamma}, \qquad b(\vec{r}(t),t) \mathrel{\hat{=}} \frac{1}{\gamma}, \qquad c \mathrel{\hat{=}} \sqrt{2\gamma k_\mathrm{B}T}, \tag{5.28}$$

and therefore see that

$$\begin{aligned}\gamma\frac{\mathrm{d}f(\vec{q}_i(t))}{\mathrm{d}t} &= \left[\vec{K}_i(\vec{q}_i(t),t) + \vec{\zeta}_i(t)\right]\cdot\vec{\nabla}f(\vec{q}_i(t)) + k_\mathrm{B}T\,\vec{\nabla}^2 f(\vec{q}_i(t)) \\ &= \vec{K}_i(\vec{q}_i(t),t)\cdot\vec{\nabla}f(\vec{q}_i(t)) + \vec{\zeta}_i(t)\cdot\vec{\nabla}f(\vec{q}_i(t)) + k_\mathrm{B}T\,\vec{\nabla}^2 f(\vec{q}_i(t)).\end{aligned} \tag{5.29}$$

The next step is to express every occurrence of $\vec{q}_i(t)$ in Eq. (5.29) in terms of the instantaneous density operator for the i-th particle,

$$\hat{\rho}_i(\vec{r},t) \equiv \delta(\vec{r} - \vec{q}_i(t)). \tag{5.30}$$

On the left hand side, we trivially have

$$\gamma\frac{\mathrm{d}f(\vec{q}_i(t))}{\mathrm{d}t} = \gamma\frac{\mathrm{d}}{\mathrm{d}t}\int_{\mathbb{V}}\mathrm{d}^d\vec{r}\,\hat{\rho}_i(\vec{r},t)\,f(\vec{r}) = \gamma\int_{\mathbb{V}}\mathrm{d}^d\vec{r}\,\frac{\mathrm{d}\hat{\rho}_i(\vec{r},t)}{\mathrm{d}t}\,f(\vec{r}),$$

assuming that the particles are confined to a finite volume $\mathbb{V}$. On the right hand side, we make use of integration by parts and the fact that the surface contributions vanish because $\hat{\rho}_i(\vec{r},t) = 0$

if $\vec{r} \in \partial\mathbb{V}$. Dealing with each of the three terms individually, we thus find that

$$\begin{aligned}
\vec{K}_i(\vec{q}_i(t),t)\cdot\vec{\nabla}f(\vec{q}_i(t)) &= \int_{\mathbb{V}} \mathrm{d}^d\vec{r}\,\hat{\rho}_i(\vec{r},t)\,\vec{K}_i(\vec{r},t)\cdot\vec{\nabla}f(\vec{r}) = -\int_{\mathbb{V}} \mathrm{d}^d\vec{r}\,\vec{\nabla}_{\vec{r}}\cdot[\hat{\rho}_i(\vec{r},t)\,\vec{K}_i(\vec{r},t)]\,f(\vec{r}),\\
\vec{\zeta}_i(t)\cdot\vec{\nabla}f(\vec{q}_i(t)) &= \int_{\mathbb{V}} \mathrm{d}^d\vec{r}\,\vec{\zeta}_i(t)\cdot\hat{\rho}_i(\vec{r},t)\,\vec{\nabla}f(\vec{r}) = -\int_{\mathbb{V}} \mathrm{d}^d\vec{r}\,\vec{\zeta}_i(t)\cdot\vec{\nabla}_{\vec{r}}\hat{\rho}_i(\vec{r},t)\,f(\vec{r}),\\
\vec{\nabla}^2 f(\vec{q}_i(t)) &= \int_{\mathbb{V}} \mathrm{d}^d\vec{r}\,\hat{\rho}_i(\vec{r},t)\,\vec{\nabla}^2 f(\vec{r}) = \int_{\mathbb{V}} \mathrm{d}^d\vec{r}\,\vec{\nabla}^2_{\vec{r}}\hat{\rho}_i(\vec{r},t)\,f(\vec{r}).
\end{aligned}$$

This means that we are able rewrite Eq. (5.29) as

$$\begin{aligned}
&\int_{\mathbb{V}} \mathrm{d}^d\vec{r}\,\left[\gamma\frac{\mathrm{d}\hat{\rho}_i(\vec{r},t)}{\mathrm{d}t}\right] f(\vec{r})\\
&\qquad = \int_{\mathbb{V}} \mathrm{d}^d\vec{r}\,\left[-\vec{\nabla}_{\vec{r}}\cdot\{\hat{\rho}_i(\vec{r},t)\,\vec{K}_i(\vec{r},t)\} - \vec{\zeta}_i(t)\cdot\vec{\nabla}_{\vec{r}}\hat{\rho}_i(\vec{r},t) + k_{\mathrm{B}}T\,\vec{\nabla}^2_{\vec{r}}\hat{\rho}_i(\vec{r},t)\right] f(\vec{r}),
\end{aligned} \tag{5.31}$$

and since this holds for *any* function f, we can conclude that

$$\begin{aligned}
\gamma\frac{\mathrm{d}\hat{\rho}_i(\vec{r},t)}{\mathrm{d}t} &= -\vec{\nabla}_{\vec{r}}\cdot[\hat{\rho}_i(\vec{r},t)\,\vec{K}_i(\vec{r},t)] - \vec{\zeta}_i(t)\cdot\vec{\nabla}_{\vec{r}}\hat{\rho}_i(\vec{r},t) + k_{\mathrm{B}}T\,\vec{\nabla}^2_{\vec{r}}\hat{\rho}_i(\vec{r},t)\\
&= \vec{\nabla}_{\vec{r}}\cdot[k_{\mathrm{B}}T\,\vec{\nabla}_{\vec{r}}\hat{\rho}_i(\vec{r},t) - \hat{\rho}_i(\vec{r},t)\,\vec{K}_i(\vec{r},t)] - \vec{\zeta}_i(t)\cdot\vec{\nabla}_{\vec{r}}\hat{\rho}_i(\vec{r},t).
\end{aligned} \tag{5.32}$$

Summing Eq. (5.32) now over all particles $i \in \{1,\ldots,N\}$ results in

$$\begin{aligned}
\gamma\frac{\mathrm{d}\hat{\rho}(\vec{r},t)}{\mathrm{d}t} = \vec{\nabla}_{\vec{r}}\cdot\Bigg[k_{\mathrm{B}}T\,\vec{\nabla}_{\vec{r}}\hat{\rho}(\vec{r},t) + \int_{\mathbb{V}} \mathrm{d}^d\vec{r}'\,\hat{\rho}^{(2)}(\vec{r},\vec{r}',t)\,\vec{\nabla}u(\vec{r}-\vec{r}') + \hat{\rho}(\vec{r},t)\,\vec{\nabla}\mathcal{V}^{\mathrm{ext}}(\vec{r})\Bigg]\\
- \sum_{i=1}^{N}\vec{\zeta}_i(t)\cdot\vec{\nabla}_{\vec{r}}\hat{\rho}_i(\vec{r},t),
\end{aligned} \tag{5.33}$$

where we defined the (total) instantaneous density operator as

$$\hat{\rho}(\vec{r},t) \equiv \sum_{i=1}^{N}\hat{\rho}_i(\vec{r},t) = \sum_{i=1}^{N}\delta(\vec{r}-\vec{q}_i(t)), \tag{5.34}$$

and used the explicit form (5.24) for $\vec{K}_i(\vec{r},t)$ so that

$$\begin{aligned}
\sum_{i=1}^{N}\hat{\rho}_i(\vec{r},t)\,\vec{K}_i(\vec{r},t) &= -\sum_{i=1}^{N}\hat{\rho}_i(\vec{r},t)\sum_{j=1(j\neq i)}^{N}\vec{\nabla}u(\vec{r}-\vec{q}_j(t)) - \sum_{i=1}^{N}\hat{\rho}_i(\vec{r},t)\,\vec{\nabla}\mathcal{V}^{\mathrm{ext}}(\vec{r})\\
&= -\int_{\mathbb{V}}\mathrm{d}^d\vec{r}'\,\hat{\rho}^{(2)}(\vec{r},\vec{r}',t)\,\vec{\nabla}u(\vec{r}-\vec{r}') - \hat{\rho}(\vec{r},t)\,\vec{\nabla}\mathcal{V}^{\mathrm{ext}}(\vec{r})
\end{aligned} \tag{5.35}$$

with the two-point instantaneous density operator

$$\hat{\rho}^{(2)}(\vec{r},\vec{r}',t) \equiv \sum_{i=1}^{N}\hat{\rho}_i(\vec{r},t)\sum_{j=1(j\neq i)}^{N}\delta(\vec{r}'-\vec{q}_j(t)) \equiv \sum_{i=1}^{N}\sum_{j=1(j\neq i)}^{N}\delta(\vec{r}-\vec{q}_i(t))\,\delta(\vec{r}'-\vec{q}_j(t)). \tag{5.36}$$

Finally, taking the mean of Eq. (5.33) and exploiting that $\langle\vec{\zeta}_i(t)\rangle = 0$, we arrive at

$$\gamma\frac{\mathrm{d}\rho_t(\vec{r})}{\mathrm{d}t} = \vec{\nabla}_{\vec{r}}\cdot\left[k_\mathrm{B}T\,\vec{\nabla}\rho_t(\vec{r}) + \int_{\mathbb{V}}\mathrm{d}^d\vec{r}'\,\rho_t^{(2)}(\vec{r},\vec{r}')\,\vec{\nabla}u(\vec{r}-\vec{r}') + \rho_t(\vec{r})\,\vec{\nabla}\mathcal{V}^\mathrm{ext}(\vec{r})\right], \tag{5.37}$$

where $\rho_t(\vec{r}) \equiv \langle\hat{\rho}(\vec{r},t)\rangle$ and $\rho_t^{(2)}(\vec{r},\vec{r}') \equiv \langle\hat{\rho}^{(2)}(\vec{r},\vec{r}',t)\rangle$. While Eq. (5.37) actually determines the time evolution of the density distribution ρ_t exactly, it is unfortunately only of little use in practice because we typically have no knowledge of $\rho_t^{(2)}$. We are therefore required to find a suitable approximation.

Since the equilibrium density profile ρ_eq is stationary, we have that

$$0 = \gamma\frac{\mathrm{d}\rho_\mathrm{eq}(\vec{r})}{\mathrm{d}t} = \vec{\nabla}_{\vec{r}}\cdot\left[k_\mathrm{B}T\,\vec{\nabla}\rho_\mathrm{eq}(\vec{r}) + \int_{\mathbb{V}}\mathrm{d}^d\vec{r}'\,\rho_\mathrm{eq}^{(2)}(\vec{r},\vec{r}')\,\vec{\nabla}u(\vec{r}-\vec{r}') + \rho_\mathrm{eq}(\vec{r})\,\vec{\nabla}\mathcal{V}^\mathrm{ext}(\vec{r})\right], \tag{5.38}$$

which means that the bracketed term on the right hand side must be spatially constant; and since $\rho_\mathrm{eq}(\vec{r}) = 0 = \rho_\mathrm{eq}^{(2)}(\vec{r},\vec{r}')$ for all $\vec{r}\in\partial\mathbb{V}$, it must in fact be zero for all $\vec{r}\in\mathbb{V}$,

$$0 = k_\mathrm{B}T\,\vec{\nabla}\rho_\mathrm{eq}(\vec{r}) + \int_{\mathbb{V}}\mathrm{d}^d\vec{r}'\,\rho_\mathrm{eq}^{(2)}(\vec{r},\vec{r}')\,\vec{\nabla}u(\vec{r}-\vec{r}') + \rho_\mathrm{eq}(\vec{r})\,\vec{\nabla}\mathcal{V}^\mathrm{ext}(\vec{r}). \tag{5.39}$$

Because ρ_eq minimizes the grand potential functional, we also know that

$$\begin{aligned} 0 &= \frac{\delta\Omega[\rho_\mathrm{eq}]}{\delta\rho_\mathrm{eq}(\vec{r})} = \frac{\delta\mathcal{F}[\rho_\mathrm{eq}]}{\delta\rho_\mathrm{eq}(\vec{r})} + \mathcal{V}^\mathrm{ext}(\vec{r}) - \mu = \frac{\delta\mathcal{F}_\mathrm{id}[\rho_\mathrm{eq}]}{\delta\rho_\mathrm{eq}(\vec{r})} + \frac{\delta\mathcal{F}_\mathrm{ex}[\rho_\mathrm{eq}]}{\delta\rho_\mathrm{eq}(\vec{r})} + \mathcal{V}^\mathrm{ext}(\vec{r}) - \mu \\ &= k_\mathrm{B}T\ln[\Lambda^d\rho_\mathrm{eq}(\vec{r})] - k_\mathrm{B}T\,c_1(\rho_\mathrm{eq},\vec{r}) + \mathcal{V}^\mathrm{ext}(\vec{r}) - \mu, \end{aligned} \tag{5.40}$$

from which

$$0 = \rho_\mathrm{eq}(\vec{r})\vec{\nabla}_{\vec{r}}\frac{\delta\Omega[\rho_\mathrm{eq}]}{\delta\rho_\mathrm{eq}(\vec{r})} = k_\mathrm{B}T\,\vec{\nabla}\rho_\mathrm{eq}(\vec{r}) - k_\mathrm{B}T\,\rho_\mathrm{eq}(\vec{r})\,\vec{\nabla}_{\vec{r}}\,c_1(\rho_\mathrm{eq},\vec{r}) + \rho_\mathrm{eq}(\vec{r})\vec{\nabla}\mathcal{V}^\mathrm{ext}(\vec{r}) \tag{5.41}$$

directly follows. Comparing Eqs. (5.39) and (5.41) we immediately see that

$$\int_{\mathbb{V}}\mathrm{d}^d\vec{r}'\rho_\mathrm{eq}^{(2)}(\vec{r},\vec{r}')\,\vec{\nabla}u(\vec{r}-\vec{r}') = -k_\mathrm{B}T\,\rho_\mathrm{eq}(\vec{r})\,\vec{\nabla}_{\vec{r}}\,c_1(\rho_\mathrm{eq},\vec{r}). \tag{5.42}$$

If we assume that this relation approximately holds also out of equilibrium,

$$\int_{\mathbb{V}}\mathrm{d}^d\vec{r}'\rho_t^{(2)}(\vec{r},\vec{r}')\,\vec{\nabla}u(\vec{r}-\vec{r}') \approx -k_\mathrm{B}T\,\rho_t(\vec{r})\,\vec{\nabla}_{\vec{r}}\,c_1(\rho_t,\vec{r}), \tag{5.43}$$

we can actually close Eq. (5.37) with respect to ρ_t as

$$\begin{aligned} \gamma\frac{\mathrm{d}\rho_t(\vec{r})}{\mathrm{d}t} &\approx \vec{\nabla}_{\vec{r}}\cdot\left[k_\mathrm{B}T\,\vec{\nabla}\rho_t(\vec{r}) - k_\mathrm{B}T\,\rho_t(\vec{r})\,\vec{\nabla}_{\vec{r}}\,c_1(\rho_t,\vec{r}) + \rho_t(\vec{r})\,\vec{\nabla}\mathcal{V}^\mathrm{ext}(\vec{r})\right] \\ &= k_\mathrm{B}T\,\vec{\nabla}_{\vec{r}}\cdot\left[\vec{\nabla}\rho_t(\vec{r}) + \rho_t(\vec{r})\,\vec{\nabla}_{\vec{r}}\{\beta\mathcal{V}^\mathrm{ext}(\vec{r}) - c_1(\rho_t,\vec{r})\}\right]. \end{aligned} \tag{5.44}$$

This is the central result of DDFT, allowing us to compute ρ_t by (numerically) integrating Eq. (5.44). It can also be cast into the continuity equation

$$\frac{\mathrm{d}\rho_t(\vec{r})}{\mathrm{d}t} = -\vec{\nabla}\cdot\vec{j}_t(\vec{r}) \tag{5.45}$$

with the particle current

$$\vec{j}_t(\vec{r}) = -\frac{k_\mathrm{B}T}{\gamma}\left[\vec{\nabla}\rho_t(\vec{r}) + \rho_t(\vec{r})\,\vec{\nabla}_{\vec{r}}\{\beta\mathcal{V}^\mathrm{ext}(\vec{r}) - c_1(\rho_t,\vec{r})\}\right] = -\frac{\rho_t(\vec{r})}{\gamma}\vec{\nabla}_{\vec{r}}\frac{\delta\mathcal{A}[\rho_t]}{\delta\rho_t(\vec{r})}. \tag{5.46}$$

Note that the dynamics correctly preserve the number of particles in the system since $\vec{j}_t(\vec{r}) = 0$ for all $\vec{r}\in\partial\mathbb{V}$ and therefore

$$\frac{\mathrm{d}\mathcal{N}[\rho_t]}{\mathrm{d}t} = \int_\mathbb{V}\mathrm{d}^d\vec{r}\,\frac{\mathrm{d}\rho_t(\vec{r})}{\mathrm{d}t} = -\int_\mathbb{V}\mathrm{d}^d\vec{r}\,\vec{\nabla}\cdot\vec{j}_t(\vec{r}) = -\int_{\partial\mathbb{V}}\mathrm{d}^d\vec{r}\,\vec{n}(\vec{r})\cdot\vec{j}_t(\vec{r}) = 0. \tag{5.47}$$

Furthermore, the Helmholtz free energy always decreases over time or remains constant because

$$\frac{\mathrm{d}\mathcal{A}[\rho_t]}{\mathrm{d}t} = \int_\mathbb{V}\mathrm{d}^d\vec{r}\,\frac{\delta\mathcal{A}[\rho_t]}{\delta\rho_t(\vec{r})}\,\frac{\mathrm{d}\rho_t(\vec{r})}{\mathrm{d}t} = -\int_\mathbb{V}\mathrm{d}^d\vec{r}\,\frac{\delta\mathcal{A}[\rho_t]}{\delta\rho_t(\vec{r})}\,\vec{\nabla}\cdot\vec{j}_t(\vec{r}) \tag{5.48}$$

$$= \int_\mathbb{V}\mathrm{d}^d\vec{r}\,\vec{\nabla}_{\vec{r}}\frac{\delta\mathcal{A}[\rho_t]}{\delta\rho_t(\vec{r})}\cdot\vec{j}_t(\vec{r}) = -\int_\mathbb{V}\mathrm{d}^d\vec{r}\,\frac{\rho_t(\vec{r})}{\gamma}\left[\vec{\nabla}_{\vec{r}}\frac{\delta\mathcal{A}[\rho_t]}{\delta\rho_t(\vec{r})}\right]^2 \leq 0. \tag{5.49}$$

5.2.2. Integration

Just like static DFT benefits from performing certain calculations in Fourier space, so does DDFT. In addition to any convolutions that may be required to compute $c_1(\rho_t,\vec{r})$, this also applies to the divergence and the gradients that appear on the right hand side of Eq. (5.44). Let $\vec{g}(\vec{r}) \equiv \vec{\nabla}f(\vec{r})$ and $\psi(\vec{r}) \equiv \vec{\nabla}\cdot\vec{\varphi}(\vec{r})$, then

$$\begin{aligned}\int\mathrm{d}^d\vec{k}\,\tilde{\vec{g}}(\vec{k})\exp(\mathrm{i}\vec{k}\cdot\vec{r}) = (2\pi)^d g(\vec{r}) = (2\pi)^d\vec{\nabla}f(\vec{r}) = \vec{\nabla}_{\vec{r}}\cdot\int\mathrm{d}^d\vec{k}\,\tilde{f}(\vec{k})\exp(\mathrm{i}\vec{k}\cdot\vec{r})\\ = \int\mathrm{d}^d\vec{k}\,[\mathrm{i}\vec{k}\tilde{f}(\vec{k})]\exp(\mathrm{i}\vec{k}\cdot\vec{r})\end{aligned} \tag{5.50}$$

and similarly

$$\begin{aligned}\int\mathrm{d}^d\vec{k}\,\tilde{\psi}(\vec{k})\exp(\mathrm{i}\vec{k}\cdot\vec{r}) = (2\pi)^d\psi(\vec{r}) = (2\pi)^d\vec{\nabla}_{\vec{r}}\cdot\vec{\varphi}(\vec{r}) = \vec{\nabla}_{\vec{r}}\cdot\int\mathrm{d}^d\vec{k}\,\tilde{\vec{\varphi}}(\vec{k})\exp(\mathrm{i}\vec{k}\cdot\vec{r})\\ = \int\mathrm{d}^d\vec{k}\,[\mathrm{i}\vec{k}\cdot\tilde{\vec{\varphi}}(\vec{k})]\exp(\mathrm{i}\vec{k}\cdot\vec{r}),\end{aligned} \tag{5.51}$$

so that $\tilde{\vec{g}}(\vec{k}) = \mathrm{i}\vec{k}\tilde{f}(\vec{k})$ and $\tilde{\psi}(\vec{k}) = \mathrm{i}\vec{k}\cdot\tilde{\vec{\varphi}}(\vec{k})$. A corollary of this is that if $\vec{\varphi}(\vec{r}) = \vec{\nabla}f(\vec{r})$ and thus $\psi(\vec{r}) = \vec{\nabla}^2 f(\vec{r})$, then $\tilde{\psi}(\vec{k}) = \mathrm{i}\vec{k}\cdot\mathrm{i}\vec{k}\tilde{f}(\vec{k}) = -\vec{k}^2\tilde{f}(\vec{k})$. Derivatives in real space therefore reduce to a trivial multiplication in Fourier space.

In principle we could integrate Eq. (5.44) in small time steps of Δt using Euler's method,

$$\begin{aligned}\rho_{t+\Delta t}(\vec{r}) &= \rho_t(\vec{r}) + \int_t^{t+\Delta t} \mathrm{d}t' \frac{\mathrm{d}\rho_{t'}(\vec{r})}{\mathrm{d}t'} \approx \rho_t(\vec{r}) + \frac{\mathrm{d}\rho_t(\vec{r})}{\mathrm{d}t}\Delta t \\ &= \rho_t(\vec{r}) + \frac{k_\mathrm{B}T}{\gamma}\vec{\nabla}_{\vec{r}} \cdot \left[\vec{\nabla}\rho_t(\vec{r}) + \rho_t(\vec{r})\,\vec{\nabla}_{\vec{r}}\{\beta\mathcal{V}^{\mathrm{ext}}(\vec{r}) - c_1(\rho_t,\vec{r})\}\right]\Delta t.\end{aligned} \tag{5.52}$$

Unfortunately, this integrator demands an extremely small Δt and hence many steps in order to be reasonably accurate; otherwise, the errors accumulate very quickly. A better approach for DDFT is to use a technique called *exponential time differencing* [96, 97]. Writing Eq. (5.44) as

$$\beta\gamma\frac{\mathrm{d}\rho_t(\vec{r})}{\mathrm{d}t} = \vec{\nabla}^2\rho_t(\vec{r}) + \vec{\nabla}_{\vec{r}} \cdot \left[\rho_t(\vec{r})\,\vec{\nabla}_{\vec{r}}\{\beta\mathcal{V}^{\mathrm{ext}}(\vec{r}) - c_1(\rho_t,\vec{r})\}\right] = \vec{\nabla}^2\rho_t(\vec{r}) + \varsigma(\rho_t,\vec{r}) \tag{5.53}$$

with

$$\varsigma(\rho_t,\vec{r}) \equiv \vec{\nabla}_{\vec{r}} \cdot \left[\rho_t(\vec{r})\,\vec{\nabla}_{\vec{r}}\{\beta\mathcal{V}^{\mathrm{ext}}(\vec{r}) - c_1(\rho_t,\vec{r})\}\right], \tag{5.54}$$

we see that its Fourier transform is simply

$$\beta\gamma\frac{\mathrm{d}\tilde{\rho}_t(\vec{k})}{\mathrm{d}t} = -\vec{k}^2\tilde{\rho}_t(\vec{k}) + \tilde{\varsigma}(\tilde{\rho}_t,\vec{k}). \tag{5.55}$$

It is not difficult to verify that Eq. (5.55) is solved by

$$\tilde{\rho}_t(\vec{k}) = \tilde{\rho}_{t_0}(\vec{k})\exp\left(-\vec{k}^2\frac{t-t_0}{\beta\gamma}\right) + \frac{1}{\beta\gamma}\int_{t_0}^{t}\mathrm{d}t'\,\tilde{\varsigma}(\tilde{\rho}_{t'},\vec{k})\exp\left(-\vec{k}^2\frac{t-t'}{\beta\gamma}\right). \tag{5.56}$$

In the special case of non-interacting colloids [$c_1(\rho_t,\vec{r}) = 0$] and a vanishing external potential [$\mathcal{V}^{\mathrm{ext}}(\vec{r}) = 0$], we have $\varsigma(\rho_t,\vec{r}) = 0 = \tilde{\varsigma}(\tilde{\rho}_t,\vec{k})$, so that $\tilde{\rho}_t(\vec{k}) = \tilde{\rho}_{t_0}(\vec{k})\exp[-\vec{k}^2(t-t_0)/(\beta\gamma)]$ becomes the exact closed solution to the diffusion equation $\beta\gamma[\mathrm{d}\tilde{\rho}_t(\vec{k})/\mathrm{d}t] = -\vec{k}^2\tilde{\rho}_t(\vec{k})$. In contrast, the whole solution (5.56) for the general case is *not* closed because the second term on the right hand side requires knowledge of $\tilde{\varsigma}(\tilde{\rho}_{t'},\vec{r})$ for all $t' \in [t_0,t]$. If the interval $|t-t_0|$ is sufficiently small, however, we may assume that $\tilde{\varsigma}(\tilde{\rho}_{t'},\vec{r}) \approx \tilde{\varsigma}(\tilde{\rho}_{t_0},\vec{r})$, and therefore

$$\begin{aligned}\tilde{\rho}_t(\vec{k}) &\approx \tilde{\rho}_{t_0}(\vec{k})\exp\left(-\vec{k}^2\frac{t-t_0}{\beta\gamma}\right) + \frac{\tilde{\varsigma}(\tilde{\rho}_{t_0},\vec{k})}{\beta\gamma}\int_{t_0}^{t}\mathrm{d}t'\exp\left(-\vec{k}^2\frac{t-t'}{\beta\gamma}\right) \\ &= \begin{cases}\tilde{\rho}_{t_0}(0) + \tilde{\varsigma}(\tilde{\rho}_{t_0},0)\dfrac{t-t_0}{\beta\gamma} & \text{if } \vec{k} = 0, \\ \tilde{\rho}_{t_0}(\vec{k})\exp\left(-\vec{k}^2\dfrac{t-t_0}{\beta\gamma}\right) + \dfrac{\tilde{\varsigma}(\tilde{\rho}_{t_0},\vec{k})}{\vec{k}^2}\left[1-\exp\left(-\vec{k}^2\dfrac{t-t_0}{\beta\gamma}\right)\right] & \text{otherwise.}\end{cases}\end{aligned} \tag{5.57}$$

In order to avoid the need for choosing a concrete drag coefficient γ (which depends on the size of the colloids and the viscosity of the solvent), it is convenient to specify the dynamics in terms

of the dimensionless *Brownian time*

$$\tau \equiv \frac{t}{\beta\gamma\sigma^2}. \tag{5.58}$$

This finally allows us to evolve the density distribution in small steps of $\Delta\tau$ via

$$\tilde{\rho}_{\tau+\Delta\tau}(\vec{k}) \approx \begin{cases} \tilde{\rho}_\tau(0) + \tilde{\varsigma}(\tilde{\rho}_\tau, 0)\,\sigma^2\Delta\tau & \text{if } \vec{k} = 0, \\ \tilde{\rho}_\tau(\vec{k})\exp(-\sigma^2\vec{k}^2\Delta\tau) + \tilde{\varsigma}(\tilde{\rho}_\tau, \vec{k})\,\dfrac{1-\exp(-\sigma^2\vec{k}^2\Delta\tau)}{\vec{k}^2} & \text{otherwise.} \end{cases} \tag{5.59}$$

5.2.3. Implementation

In our derivation of DDFT, we assumed that the system is contained inside a finite volume $\mathbb{V}$ and that the density profile vanishes at the surface, i. e., $\rho_t(\vec{r}) = 0$ for all $\vec{r} \in \partial\mathbb{V}$. Alternatively, we could have also allowed an infinitely large volume $\mathbb{V} = \mathbb{R}^d$ and demanded that $\rho_t(\vec{r}) \to 0$ for $|\vec{r}| \to \infty$. Obviously, this condition is not satisfied in the bulk where we have found either uniform or periodic density distributions to be stable that do not decay asymptotically. And even if it were not for this technicality, there is another – more practical – problem. Only the periodicity of the density profiles makes it possible to study the infinite bulk with DFT in the first place because we can limit the calculations to a finite unit cell. We saw, however, that the size and shape of this cell in equilibrium depends on the concrete values of certain parameters such as the packing fraction, the magnetic field, and the temperature. This means that if we wanted to investigate how a system in equilibrium at some initial state point $(B, T) = (B_\mathrm{i}, T_\mathrm{i})$ responds after a change of the parameters to their final values $(B, T) = (B_\mathrm{f}, T_\mathrm{f})$, we would somehow have to dynamically adjust the unit cell over time in order to properly describe the evolution of the density distribution. Unfortunately, it is not at all clear how to do this correctly – actually, it is may be that the intermediate, non-equilibrium states are not even periodic. In the end, though, it is really an academic issue since the infinite bulk is a purely fictitious construct and thus inaccessible to experiments. For these reasons, we shall only concern ourselves with the dynamics of a confined system.

As in the static case, we do this by suitably extending the density profile of a system confined to the volume $\mathbb{V} \subseteq [0, l_x] \times [0, l_y]$ into a (L_x, L_y)-periodic one and discretizing the corresponding unit cell on a regular grid with $M_x \times M_y$ lattice points (we double the minimum resolution to $\min\{M_x/L_x, M_y/L_y\} \geq 20/\sigma$ because the dynamics depend rather sensitively on it). This again allows us to make use of discrete Fourier transforms so that Eq. (5.59) becomes

$$\hat{\rho}_{\tau+\Delta\tau}(\vec{k}_{mn}) \approx \begin{cases} \hat{\rho}_\tau(0) + \hat{\varsigma}(\hat{\rho}_\tau, 0)\,\sigma^2\Delta\tau & \text{if } \vec{k}_{mn} = 0, \\ \hat{\rho}_\tau(\vec{k}_{mn})\exp(-\sigma^2\vec{k}_{mn}^2\Delta\tau) + \hat{\varsigma}(\hat{\rho}_\tau, \vec{k}_{mn})\,\dfrac{1-\exp(-\sigma^2\vec{k}_{mn}^2\Delta\tau)}{\vec{k}_{mn}^2} & \text{otherwise} \end{cases} \tag{5.60}$$

for $\vec{k}_{mn} \equiv 2\pi[(m - \lceil M_x/2\rceil + 1)/L_x, (n - \lceil M_y/2\rceil + 1)/L_y]$, where the divergence and gradient in Eq. (5.54) can be computed in Fourier space via $\hat{\vec{g}}(\vec{k}_{mn}) \approx \mathrm{i}\vec{k}_{mn}\hat{f}(\vec{k}_{mn})$ for $\vec{g}(\vec{r}_{ij}) \equiv \vec{\nabla} f(\vec{r}_{ij})$ and $\hat{\psi}(\vec{k}_{mn}) \approx \mathrm{i}\vec{k}_{mn} \cdot \hat{\vec{\varphi}}(\vec{k}_{mn})$ for $\psi(\vec{r}_{ij}) \equiv \vec{\nabla} \cdot \vec{\varphi}(\vec{r}_{ij})$; other quantities such as $c_1 = c_1^{\mathrm{hd}} + c_1^{\mathrm{ci}}$ or $\mathcal{A}$ are calculated as described in Section 4.1.3. We choose a time step of $\Delta\tau \equiv 5 \times 10^{-4}$, which is a good compromise with regard to accuracy and computational costs.

The periodic extension of the density distribution works similarly to the method shown in Section 4.2.1, with the exception that we cannot use a discontinuous external potential (which jumps from zero to infinity) in DDFT since that would lead to problems with the spatial derivatives in Eq. (5.54). Instead, we construct an external potential that goes smoothly from zero to some sufficiently large value $\mathcal{V}_{\max}^{\mathrm{ext}} < \infty$ within a transition zone of width w. We artificially limit the range of the competing interaction potential u_{ci} to $r_{\max} \equiv [(l_x + 2w)^2 + (l_y + 2w)^2]^{1/2}$; the maximum interaction range of two colloids is therefore $W \equiv \max\{\sigma, r_{\max}\}$. Furthermore, let

$$\Delta_{\mathbb{V}}(\vec{r}) \equiv \begin{cases} -\min\{|\vec{r} - \vec{r}_{\mathrm{s}}| : \vec{r}_{\mathrm{s}} \in \partial\mathbb{V}\} & \text{if } \vec{r} \in \mathbb{V}, \\ \min\{|\vec{r} - \vec{r}_{\mathrm{s}}| : \vec{r}_{\mathrm{s}} \in \partial\mathbb{V}\} & \text{otherwise} \end{cases} \tag{5.61}$$

denote the signed distance between some point $\vec{r}$ and the surface of $\mathbb{V}$, and

$$\mathrm{S}_3(x) \equiv \begin{cases} 0 & \text{if } x < 0, \\ -20\,x^7 + 70\,x^6 - 84\,x^5 + 35\,x^4 & \text{if } 0 \le x < 1, \\ 1 & \text{otherwise} \end{cases} \tag{5.62}$$

the third smoothstep function (which is thrice continuously differentiable). We then assign

$$\mathcal{V}^{\mathrm{ext}}(\vec{r}) \equiv \sum_{i,j\in\mathbb{Z}} \mathcal{V}_{\mathbb{V}}^{\mathrm{ext}}(x + iL_x, y + jL_y) \tag{5.63}$$

with $L_x \equiv l_x + 2w + W$, $L_y \equiv l_y + 2w + W$ and

$$\mathcal{V}_{\mathbb{V}}^{\mathrm{ext}}(\vec{r}) \equiv \begin{cases} \mathcal{V}_{\max}^{\mathrm{ext}}\,\mathrm{S}_3(\Delta_{\mathbb{V}}(\vec{r})/w + b) & \text{if } \vec{r} \in [-w, L_x - w] \times [-w, L_y - w] \\ 0 & \text{otherwise.} \end{cases} \tag{5.64}$$

We shall choose $w = \sigma$, $\mathcal{V}_{\max}^{\mathrm{ext}} = 50\,k_{\mathrm{B}}T$ and $b \approx 0.156$; the corresponding potential is shown in Fig. 5.1(a). In the case of an ideal gas, for which $\rho(\vec{r})/\rho(\vec{r}') = \exp[-\beta\{\mathcal{V}^{\mathrm{ext}}(\vec{r}) - \mathcal{V}^{\mathrm{ext}}(\vec{r}')\}]$, this means that $\rho(\vec{r}_{\mathrm{o}})/\rho(\vec{r}_{\mathrm{i}}) = \exp(-\beta\mathcal{V}_{\max}^{\mathrm{ext}}) \approx 0$ and $\rho(\vec{r}_{\mathrm{s}})/\rho(\vec{r}_{\mathrm{i}}) = \exp[-\beta\mathcal{V}_{\max}^{\mathrm{ext}}\,S_3(b)] \approx 0.5$ if $\Delta_{\mathbb{V}}(\vec{r}_{\mathrm{i}}) \le -wb$, $\Delta_{\mathbb{V}}(\vec{r}_{\mathrm{s}}) = 0$ and $\Delta_{\mathbb{V}}(\vec{r}_{\mathrm{o}}) \ge w(1-b)$, as can be seen in Fig. 5.1(b). It turns out that this "soft" external potential leads to well-behaved dynamics while giving rise to equilibrium density profiles which are practically indistinguishable from those that result from a "hard" potential.

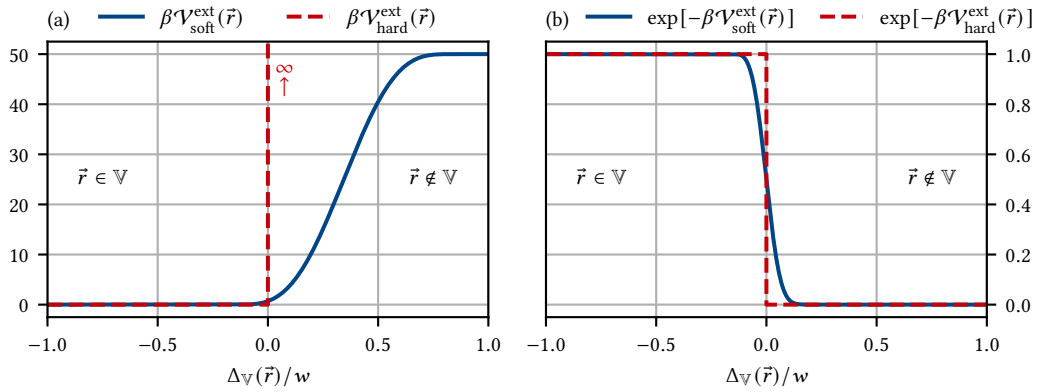

Figure 5.1.: Comparison of the "soft" external potential $\mathcal{V}^{\text{ext}}_{\text{soft}}$ from Eq. (5.63) with the "hard" $\mathcal{V}^{\text{ext}}_{\text{hard}}$ from Eq. (4.113).

5.3. Dynamics of microphase separation

Let us now use our DDFT framework to investigate the dynamics of a closed system confined to a square cell with side length L, where the bulk packing fraction η_{b} is held constant but the magnetic field B and temperature T are allowed to change over time. In particular, we wish to emulate the following procedure that an experiment designed to study microphase separation might adhere to: at first, (B, T) are set to some initial $(B_{\text{i}}, T_{\text{i}})$ *outside* the microphase regime where the thermodynamically stable state is an almost uniform fluid that the system is certain to arrive at after a reasonable period of equilibration. Once equilibrium has been reached at, say, time $\tau = 0$, we begin to vary (B, T) and stop after some transition time τ_{t} so as to end up at a final $(B_{\text{f}}, T_{\text{f}})$ which lies *inside* the microphase regime where either a droplet or a ring configuration is stable. The questions that we are interested in answering are:

(i) Will the system eventually self-assemble into the stable configuration as $\tau \to \infty$, or will it rather become stuck in a metastable state with a higher Helmholtz free energy?

(ii) How does the way in which (B, T) is altered for $\tau \in [0, \tau_{\text{t}}]$ – i. e., the path taken through parameter space to go from $(B_{\text{i}}, T_{\text{i}})$ to $(B_{\text{f}}, T_{\text{f}})$ – affect the outcome of the time evolution?

(iii) Which implications with regard to experimental studies of microphase separation might be inferred from the results?

For $L = 30\sigma$, $\eta_{\text{b}} = 0.19$ and $\Delta T_{\text{f}} = 0.16\,\text{K}$, we shall target the droplet state at $B_{\text{f}} = 7.2\,\mu\text{T}$ [Fig. 4.23(a)] and the ring state at $B_{\text{f}} = 8.7\,\mu\text{T}$ [Fig. 4.23(d)], whereas for $L = 20\sigma$, $B_{\text{f}} = 7.8\,\mu\text{T}$ and $\Delta T_{\text{f}} = 0.16\,\text{K}$, we aim for the droplet state at $\eta_{\text{b}} = 0.19$ [Fig. 4.24(a)] and the ring state at $\eta_{\text{b}} = 0.27$ [Fig. 4.24(b)]. For the initial fluid configurations with $\eta_{\text{b}} \in \{0.19, 0.27\}$, we turn the magnetic field completely off, $B_{\text{i}} = 0$, so that there is no long-ranged repulsion (and hence no competing interactions) and select a temperature that results in only a weak attraction between the colloids:

$\Delta T_\mathrm{i} = 0.195\,\mathrm{K}$ for $L = 30\sigma$ and $\Delta T_\mathrm{i} = 0.2\,\mathrm{K}$ for $L = 20\sigma$; the reason for choosing these slightly different ΔT_i depending on L is that the initial equilibrium density distributions for $L = 30\sigma$ and $L = 20\sigma$ are then very similar for identical bulk packing fractions, as shown in Fig. 5.2.

The most direct way of transitioning from $(B_\mathrm{i}, T_\mathrm{i})$ to $(B_\mathrm{f}, T_\mathrm{f})$ is via an instantaneous ($\tau_\mathrm{t} = 0$), discontinuous jump at $\tau = 0$, i. e.,

$$(B_\tau, T_\tau) = \begin{cases} (B_\mathrm{i}, T_\mathrm{i}) & \text{if } \tau < 0, \\ (B_\mathrm{f}, T_\mathrm{f}) & \text{otherwise.} \end{cases} \tag{5.65}$$

Unfortunately, this method failed in all attempts to guide the particles from a fluid to a stable droplet or ring configuration, with the system always falling into a local minimum of the Helmholtz free energy instead. In Fig. 5.3, we can see what happens when we try to go to the droplet state for $L = 30\sigma$. Already after a short period of time, the colloids aggregate into a multitude of smaller droplets and thin stripes ($\tau = 10$) due to the sudden increase of the attractive critical Casimir forces that comes from raising the temperature closer toward T_c. The structures in the center then coalesce into two concentric rings, while the stripes closest to the wall contract and withdraw from the droplets in the corners of the cell ($\tau = 30$). Eventually, the two rings merge into one larger central droplet and the outer stripes assume a roughly elliptical shape, resulting in a total of nine droplets of different sizes ($\tau = 900$) kept apart by the magnetic repulsion. The same general behavior can also be seen for the other target states.

We consistently observe that, after abruptly imposing competing interactions onto the system, the particles first tend to clump into many smaller agglomerations because of the strong short-ranged attraction which then combine into bigger structures until the weak long-ranged

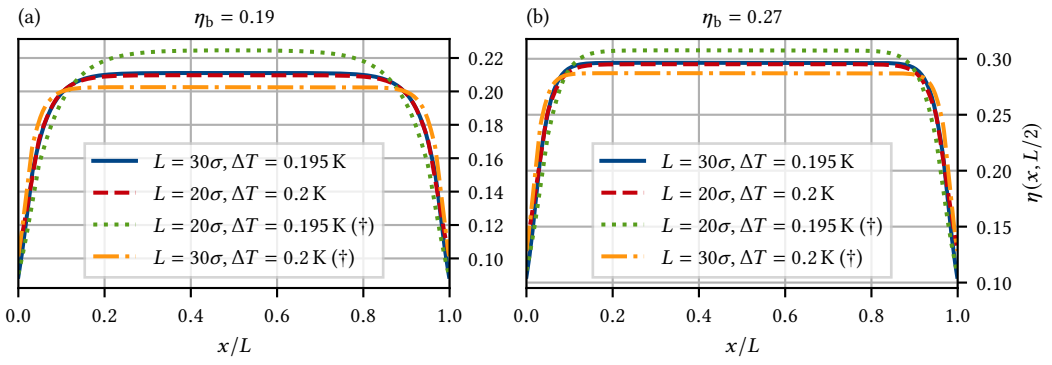

Figure 5.2.: Comparison of the initial fluid states with $B_\mathrm{i} = 0$ and $\eta_\mathrm{b} = 0.19$ (a) or $\eta_\mathrm{b} = 0.27$ (b) used as the starting configurations of the dynamics. Choosing slightly different temperatures depending on the cell size, $\Delta T_\mathrm{i} = 0.195\,\mathrm{K}$ for $L = 30\sigma$ and $\Delta T_\mathrm{i} = 0.2\,\mathrm{K}$ for $L = 20\sigma$, results in very similar density distributions at equal bulk packing fractions. The other states, marked with (†), are shown to demonstrate the discrepancies at identical temperatures.

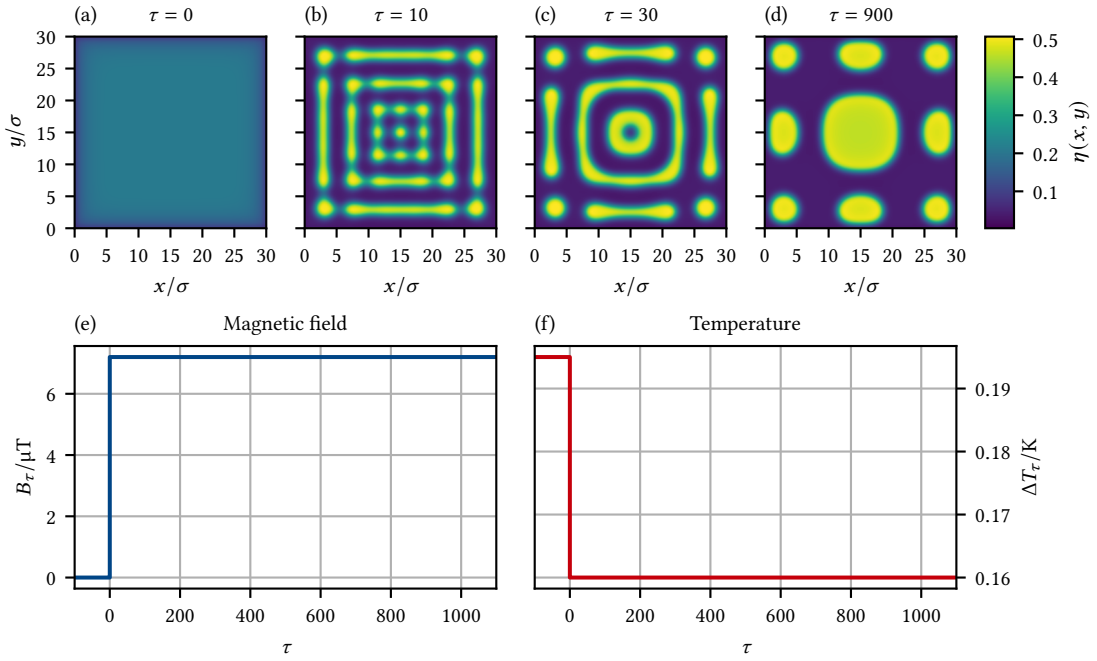

Figure 5.3.: Dynamic evolution of the density distribution of a system with $L = 30\sigma$ and $\eta_\mathrm{b} = 0.19$ after equilibrating into the fluid state at $B_\mathrm{i} = 0$ and $\Delta T_\mathrm{i} = 0.195\,\mathrm{K}$ (a) and then abruptly jumping to $B_\mathrm{f} = 7.2\,\mu\mathrm{T}$ and $\Delta T_\mathrm{f} = 0.16\,\mathrm{K}$ at $\tau = 0$. Eventually, the colloids assemble into a metastable configuration with nine droplets (d) instead of the stable one with only four [Fig. 4.23(a)]. Panels (e) and (f) show, respectively, the magnetic field and the temperature as a function of time τ. See the supplemental material [98] for an animation.

repulsion gains the upper hand and prevents further merging. This makes it difficult for the colloids to assemble into the stable equilibrium configurations which feature fewer but larger structures (either four droplets or a single ring). Another problem is that a droplet is very likely to emerge at the center of the cell that has no incentive to dissolve, but is not present in stable equilibrium.

It would not be surprising to encounter similar issues also in actual experiments. Matters may arguably even be worse in practice since the instantaneous state of the system is never as perfectly symmetrical as the density profile (which represents the *average* distribution of the particles) in DDFT might suggest: at the moment when the competing interactions are turned on, there can, for example, be slightly more colloids in one quadrant of the cell than in the other three, which then potentially leads to a haphazard growth of rather irregular structures. In fact, this conjecture appears to agree with the findings of an experimental study of phospholipid monolayers conducted by Helm and Möhwald [39], who discovered that a fast transition into the microphase regime would cause a much broader variety of differently-sized clusters than a slower one.

5.3.1. Fluid → ring

Since the results of Helm and Möhwald suggest that it may be advantageous to go from the initial to the final parameters at a more leisurely pace, it seems reasonable to try a gradual transition over the course of some non-zero but finite time $\tau_\mathrm{t} > 0$ next. Probably the first choice that comes to mind is a simple linear interpolation between $(B_\mathrm{i}, T_\mathrm{i})$ and $(B_\mathrm{f}, T_\mathrm{f})$,

$$(B_\tau, T_\tau) = \begin{cases} (B_\mathrm{i}, T_\mathrm{i}) & \text{if } \tau < 0, \\ (B_\mathrm{i}, T_\mathrm{i}) + (B_\mathrm{f} - B_\mathrm{i}, T_\mathrm{f} - T_\mathrm{i}) \frac{\tau}{\tau_\mathrm{t}} & \text{if } 0 \leq \tau < \tau_\mathrm{t}, \\ (B_\mathrm{f}, T_\mathrm{f}) & \text{otherwise.} \end{cases} \tag{5.66}$$

However, this would require a recalculation of $\tilde{u}_\mathrm{ci}$ after every DDFT step $\Delta\tau \equiv 5 \times 10^{-4} \ll \tau_\mathrm{t}$ for as long as $\tau \in [0, \tau_\mathrm{t}]$, which can become quite expensive and increase the computation time considerably. Because of this inefficiency, we instead use a staircase function with step length of $\tau_\mathrm{s} \equiv 5 \ll \tau_\mathrm{t}$ for the interpolation,

$$(B_\tau, T_\tau) = \begin{cases} (B_\mathrm{i}, T_\mathrm{i}) & \text{if } \tau < 0, \\ (B_\mathrm{i}, T_\mathrm{i}) + (B_\mathrm{f} - B_\mathrm{i}, T_\mathrm{f} - T_\mathrm{i}) \frac{\lceil \tau/\tau_\mathrm{s} \rceil}{\tau_\mathrm{t}/\tau_\mathrm{s}} & \text{if } 0 \leq \tau < \tau_\mathrm{t}, \\ (B_\mathrm{f}, T_\mathrm{f}) & \text{otherwise,} \end{cases} \tag{5.67}$$

which reduces the frequency of updating $\tilde{u}_\mathrm{ci}$ by a factor of $\tau_\mathrm{s}/\Delta\tau = 10\,000$.

As can be seen in Fig. 5.4, this method indeed proves successful in producing the stable ring structure for $L = 30\sigma$ if a transition time of $\tau_\mathrm{t} = 1000$ (which appears to be near the lower end of the range of viable values) is chosen. Initially, the intensifying attraction draws the colloids toward the center of the cell where they begin to form a slight bump surrounded by a squarish ring with pronounced corners ($\tau = 250$). After a while, the central bump disappears ($\tau = 500$), the ring becomes more clearly defined ($\tau = 750$) and its thickness almost uniform by the time that the magnetic field and temperature reach their final values ($\tau = 1000 = \tau_\mathrm{t}$). The ring then enters a phase of expansion during the long-ranged repulsion causes the particles at opposite points of the structure to be pushed away from each other, thereby leading to a growth of the ring's diameter ($\tau = 1250$) until it is stopped by the wall of the cell ($\tau = 1500$). Eventually, the system arrives at the stable equilibrium state [cf. Figs. 5.4(h) and 4.23(d)].

We observe that the success of this method depends quite sensitively on the choice of the initial conditions. For instance, if we set out with a marginally weaker attraction ($\Delta T_\mathrm{i} = 0.20\,\mathrm{K}$), then the density is too evenly distributed at the beginning [Fig. 5.5(a)] and a small droplet develops inside the ring [Figs. 5.5(b–d)]. If the attraction is slightly stronger ($\Delta T_\mathrm{i} = 0.19\,\mathrm{K}$) at the start, then the colloids are so concentrated around the center of the cell [Fig. 5.5(e)] that they form a large droplet rather than a ring [Figs. 5.5(f–h)].

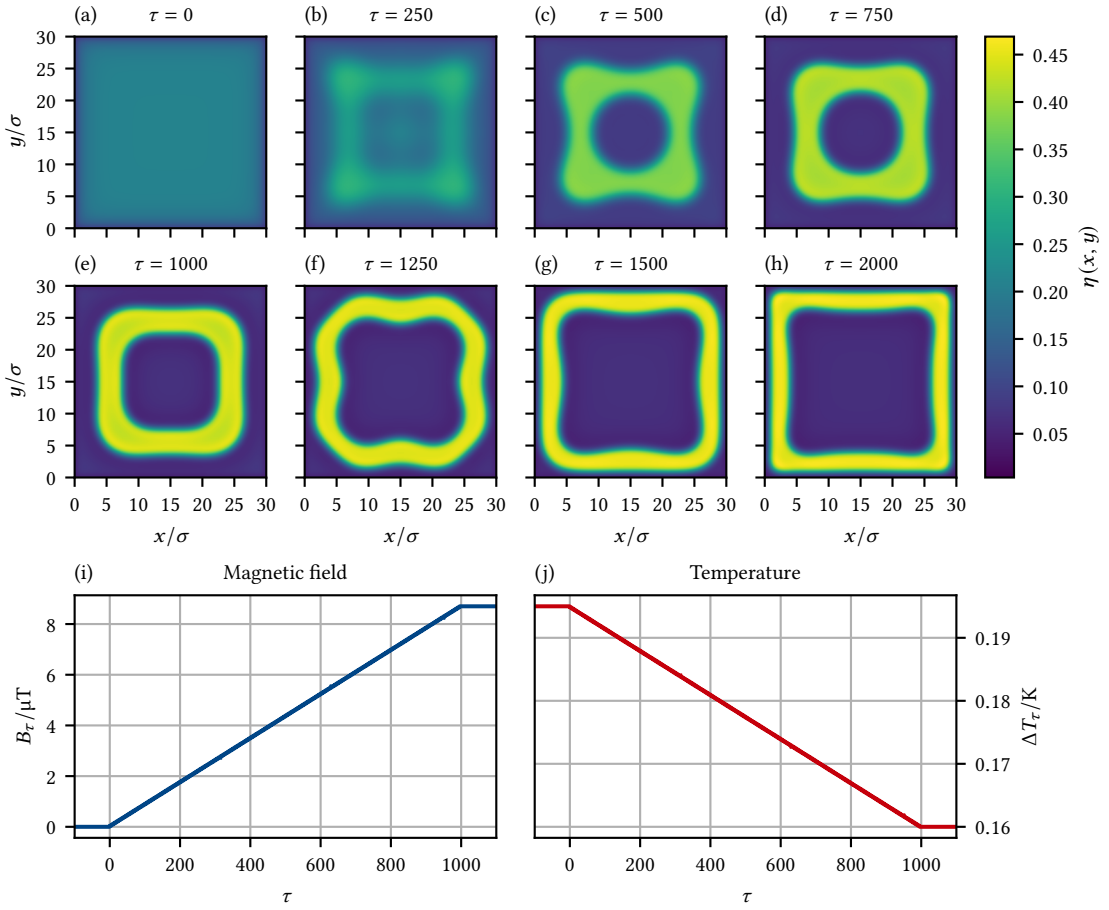

Figure 5.4.: Dynamic evolution of the density distribution of a system with $L = 30\sigma$ and $\eta_\mathrm{b} = 0.19$ after equilibrating into the fluid state at $B_\mathrm{i} = 0$ and $\Delta T_\mathrm{i} = 0.195\,\mathrm{K}$ (a) and then going quasi-linearly (with a step length of $\tau_\mathrm{s} = 5$) to $B_\mathrm{f} = 8.7\,\mu\mathrm{T}$ and $\Delta T_\mathrm{f} = 0.16\,\mathrm{K}$ until $\tau = 1000 = \tau_\mathrm{t}$ as per Eq. (5.67). Eventually, the system arrives at the stable ring configuration [cf. (h) and Fig. 4.23(d)]. Panels (i) and (j) show the magnetic field and the temperature, respectively, as a function of time τ. See the supplemental material [98] for an animation.

We can see in Fig. 5.6 that a (quasi-)linear interpolation between the initial and final parameters also manages to recover the ring configuration in the smaller cell with side length $L = 20\sigma$ [cf. Figs. 5.6(d) and 4.24(b)] – provided that we use a *much* shorter transition time of $\tau_\mathrm{t} = 100$. It turns out that a transition can in fact also progress *too* slowly: if we pick $\tau_\mathrm{t} = 1000$ instead (as we did for $L = 30\sigma$), then the particles condense once again into a single droplet.

Unfortunately, taking a (quasi-)linear path through parameter space does not seem to be a universal solution that is guaranteed to end up at the stable state if only the right initial temperature and transition time are chosen. For example, going (quasi-)linearly from $(B_\mathrm{i}, \Delta T_\mathrm{i}) = (0, 0.195\,\mathrm{K})$ to $(B_\mathrm{f}, \Delta T_\mathrm{f}) = (7.2\,\mu\mathrm{T}, 0.16\,\mathrm{K})$ over $\tau_\mathrm{t} = 1000$ for $L = 30\sigma$ and $\eta_\mathrm{b} = 0.19$ produces a metastable ring and not the stable droplet configuration. This is actually not that surprising: since the evolu-

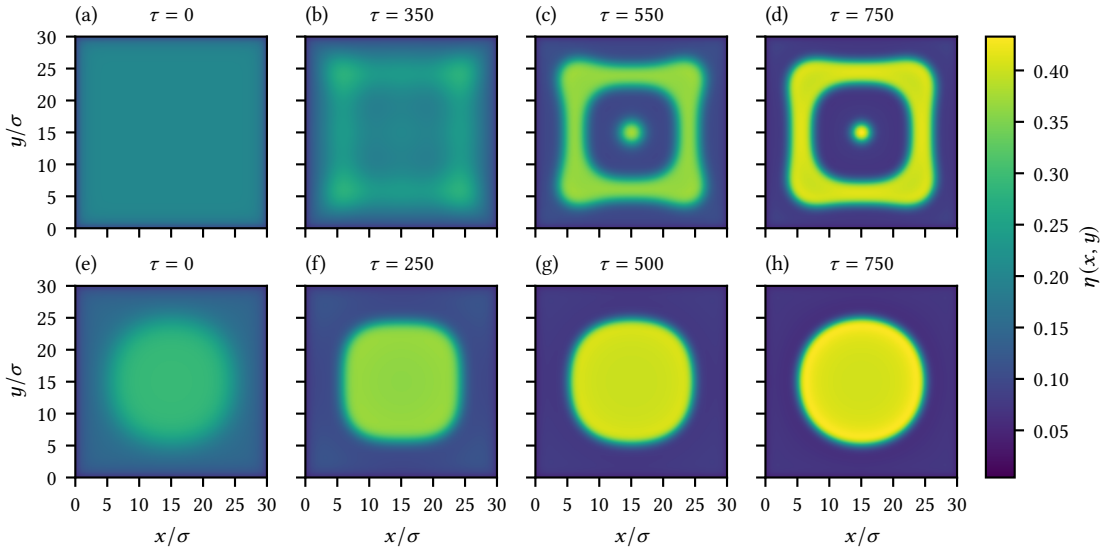

Figure 5.5.: Dynamic evolution of the density distribution of a system with $L = 30\sigma$ and $\eta_b = 0.19$. After equilibrating into the fluid state at $B_i = 0$ and $\Delta T_i = 0.2\,\mathrm{K}$ (a) and then going quasi-linearly (with a step length of $\tau_s = 5$) to $B_f = 8.7\,\mu\mathrm{T}$ and $\Delta T_f = 0.16\,\mathrm{K}$ until $\tau = 1000 = \tau_t$ as per Eq. (5.67), a metastable ring with a central droplet eventually develops (d). Starting out with the fluid configuration for $\Delta T_i = 0.19\,\mathrm{K}$ instead (e), a single cluster forms (h).

tion of the system at the beginning is first and foremost dictated by the temperature-dependent attraction, we can expect the dynamics to be very similar at early times if the final states have only slightly different magnetic fields ($B_f = 7.2\,\mu\mathrm{T}$ vs. $B_f = 8.7\,\mu\mathrm{T}$) and equal temperature – a ring therefore forms during this stage also for $B_f = 7.2\,\mu\mathrm{T}$ and does not break apart into four droplets as the repulsion becomes stronger but simply grows in diameter.

5.3.2. Fluid → droplets

While it turned out to be relatively straightforward to force the assembly of a ring, it proved to be all the more challenging to devise a procedure that would result in the formation of four droplets. After dozens of failed attempts during which either a ring, a central droplet or some other undesirable feature emerged, we were in fact almost ready to admit defeat. Luckily, not long before giving up hope completely, we stumbled upon a strategy that appeared to succeed reliably and required only a minor modification. The magnetic field is now given by

$$B_\tau = \begin{cases} B_i & \text{if } \tau < \tau_m, \\ B_m + (B_f - B_m)\frac{\lceil(\tau-\tau_m)/\tau_s\rceil}{(\tau_t-\tau_m)/\tau_s} & \text{if } \tau_m \le \tau < \tau_t, \\ B_f & \text{otherwise.} \end{cases} \tag{5.68}$$

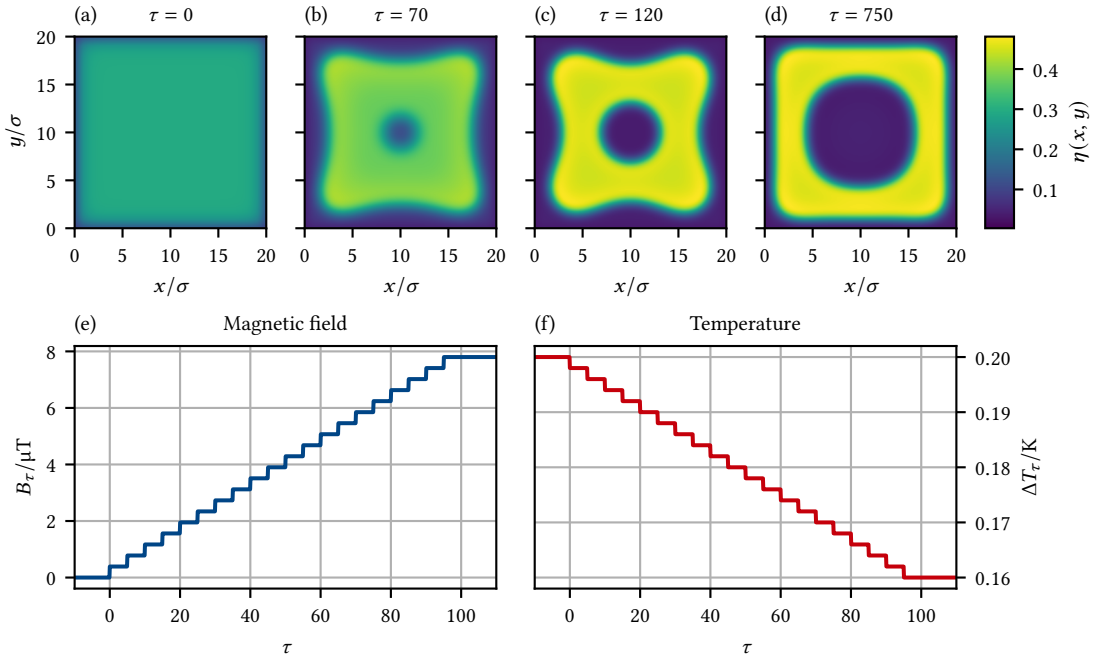

Figure 5.6.: Dynamic evolution of the density distribution of a system with $L = 20\sigma$ and $\eta_\mathrm{b} = 0.19$ after equilibrating into the fluid state at $B_\mathrm{i} = 0$ and $\Delta T_\mathrm{i} = 0.2\,\mathrm{K}$ (a) and then going quasi-linearly (with a step length of $\tau_\mathrm{s} = 5$) to $B_\mathrm{f} = 7.8\,\mu\mathrm{T}$ and $\Delta T_\mathrm{f} = 0.16\,\mathrm{K}$ until $\tau = 100 \equiv \tau_\mathrm{t}$ as per Eq. (5.67). Eventually, the system arrives at the stable ring configuration [cf. (d) and Fig. 4.24(b)]. Panels (e) and (f) show the magnetic field and the temperature, respectively, as a function of time τ. See the supplemental material [98] for an animation.

It initially remains constant at $B_\mathrm{i} = 0$, then jumps instantaneously to some intermediate value $B_\mathrm{m} \in (B_\mathrm{i}, B_\mathrm{f})$ at a time $\tau = \tau_\mathrm{m} > 0$ and after that continues quasi-linearly to B_f until $\tau = \tau_\mathrm{t} > \tau_\mathrm{m}$. The temperature, on the other hand, simply goes in a quasi-linear fashion from T_i to T_f over τ_t,

$$T_\tau = \begin{cases} T_\mathrm{i} & \text{if } \tau < 0, \\ T_\mathrm{i} + (T_\mathrm{f} - T_\mathrm{i}) \frac{\lceil \tau/\tau_\mathrm{s} \rceil}{\tau_\mathrm{t}/\tau_\mathrm{s}} & \text{if } 0 \leq \tau < \tau_\mathrm{t}, \\ T_\mathrm{f} & \text{otherwise,} \end{cases} \tag{5.69}$$

just as before. Making the right choices for T_i, τ_t, τ_m, B_m and τ_t is again crucial for success, but actually involves less amount of guesswork than one might suspect at first glance.

Let us take a look at Fig. 5.7 in order to understand how this method manages to produce the stable droplet state for $L = 30\sigma$. The temperature $T_\mathrm{i} \equiv 0.195\,\mathrm{K}$ is selected such that the system initially forms a ring without a central cluster. The transition time $\tau_\mathrm{t} \equiv 1500$ is then chosen so as to satisfy the criterion that the ring assumes a particular shape at some point, namely that it develops four very pronounced corners connected by rather delicate bridges. We find that these bridges are the thinnest, and thus most fragile, at $\tau = 350 \equiv \tau_\mathrm{m}$ [Fig. 5.7(b)]. It is precisely at this

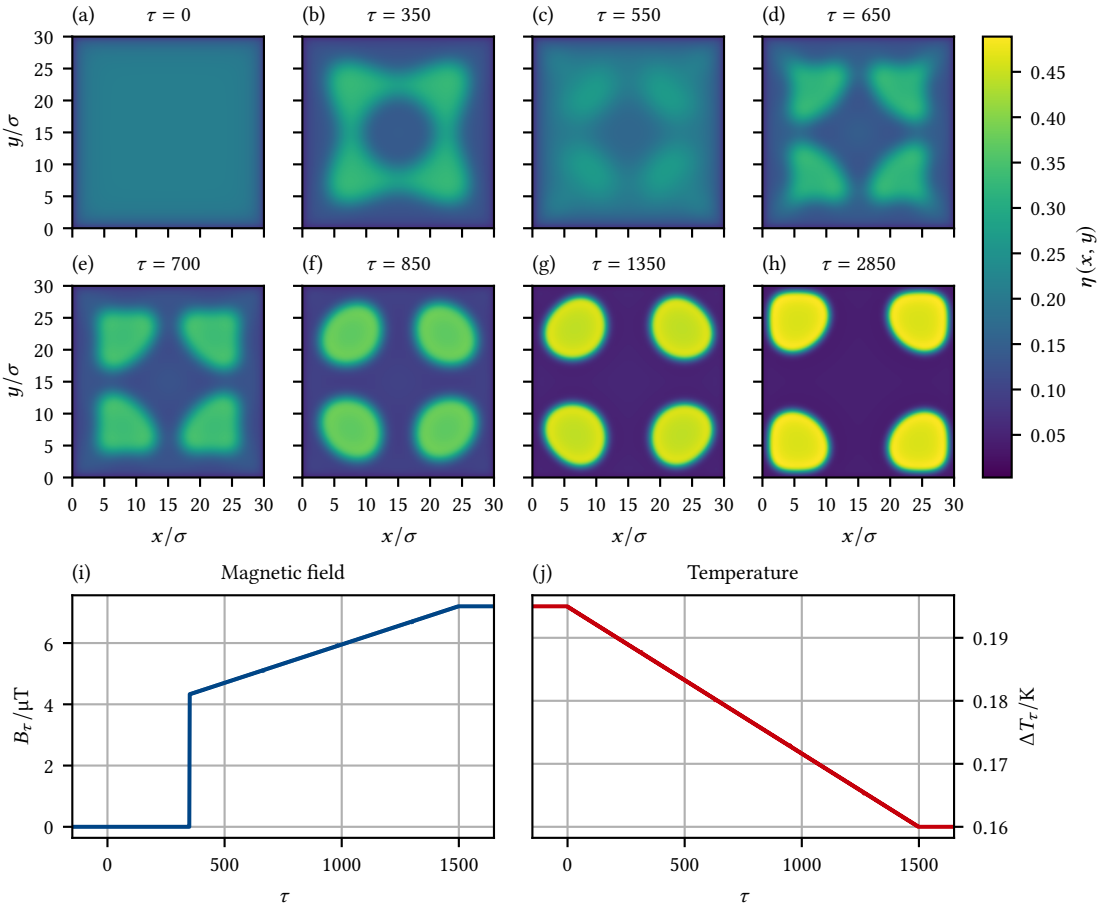

Figure 5.7.: Dynamic evolution of the density distribution of a system with $L = 30\sigma$ and $\eta_b = 0.19$ after equilibrating into the fluid state at $B_i = 0$ and $\Delta T_i = 0.195\,\mathrm{K}$ (a), and then going to $B_f = 7.2\,\mu\mathrm{T}$ and $\Delta T_f = 0.16\,\mathrm{K}$ according to Eqs. (5.68) and (5.69) as shown in panels (i) and (j). Eventually, the system arrives at the stable droplet configuration [cf. (h) and Fig. 4.23(a)]. See the supplemental material [98] for an animation.

moment that we suddenly turn on the magnetic field to $B_m = 0.6\,B_f = 4.32\,\mu\mathrm{T}$, which causes the corners to be blown apart and the links between them to be severed. With growing attraction, the scattered remains of the ring subsequently gather into four distinct droplets; at the same time, the repulsion between the droplets becomes stronger and pushes them away from each other and into the corners of the cell. Eventually, the system reaches the stable equilibrium configuration [cf. Figs. 5.7(h) and 4.23(a)].

As we can see in Fig. 5.8, we are also able to make the colloids assemble into the stable droplet state for $L = 20\sigma$ by means of this procedure [cf. Figs. 5.8(d) and 4.24(a)]. In this case, we used $\Delta T_i = 0.2\,\mathrm{K}$, $\tau_t = 150$, $\tau_m = 70$, and $B_m = 0.9\,B_f = 7.02\,\mu\mathrm{T}$. Note that the smaller system again requires a much shorter transition time than the larger one.

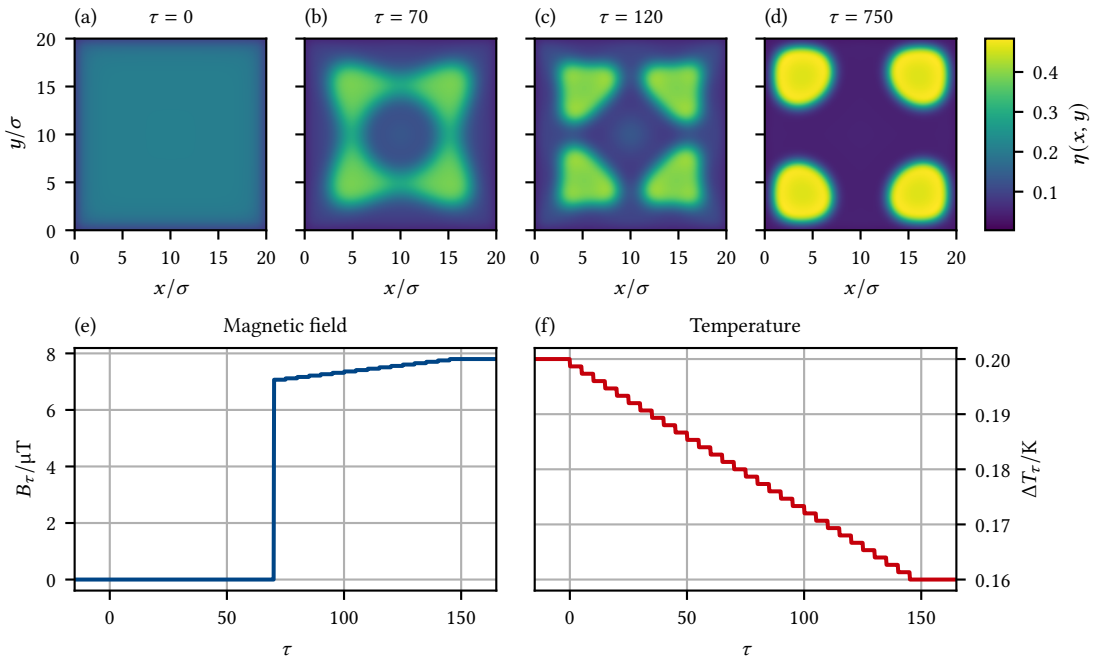

Figure 5.8.: Dynamic evolution of the density distribution of a system with $L = 20\sigma$ and $\eta_\mathrm{b} = 0.19$ after equilibrating into the fluid state at $B_\mathrm{i} = 0$ and $\Delta T_\mathrm{i} = 0.2\,\mathrm{K}$ (a) and then going to $B_\mathrm{f} = 7.8\,\mu\mathrm{T}$ and $\Delta T_\mathrm{f} = 0.16\,\mathrm{K}$ according to Eqs. (5.68) and (5.69) as shown in panels (e) and (f). Eventually, the system arrives at the stable droplet configuration [cf. (d) and Fig. 4.24(a)]. See the supplemental material [98] for an animation.

5.3.3. Droplets ⇄ ring

So far, our efforts have focused on realizing the rather intricate evolution from a fluid to a droplet or ring configuration. Unsurprisingly, going the opposite way is quite trivial in comparison: an instantaneous jump in parameter space out of the microphase regime would always lead to the dissolution of droplet and ring structures and eventually result in the stable fluid state. A corollary of this is that in most circumstances it should be possible to transition between the droplet and ring phases via a detour into the fluid phase: droplets ⇄ fluid ⇄ ring.

Recall that we found the droplet and ring phases to overlap in the phase diagram for $L = 30\sigma$ and $\Delta T = 0.16\,\mathrm{K}$ [Fig. 4.22(a)] such that at certain packing fractions ($0.17 \lesssim \eta_\mathrm{b} \lesssim 0.207$), there exist stable droplet configurations at lower and stable ring configurations at higher magnetic fields. Examples for this are the previously targeted droplet ($B = 7.2\,\mu\mathrm{T}$) and ring ($B = 8.7\,\mu\mathrm{T}$) states at $\eta_\mathrm{b} = 0.19$. This poses the question: can we go from one to the other without a stopover in the fluid state, by only varying the magnetic field while keeping the temperature constant?

Simply taking B directly from B_i to B_f, whether abruptly or (quasi-)linearly, proved unsuccessful: increasing the magnetic field from $B_\mathrm{i} = 7.2\,\mu\mathrm{T}$ to $B_\mathrm{f} = 8.7\,\mu\mathrm{T}$ just causes the droplets to be driven further into the corners of the cell, whereas decreasing B from $B_\mathrm{i} = 8.7\,\mu\mathrm{T}$ to $B_\mathrm{f} = 7.2\,\mu\mathrm{T}$

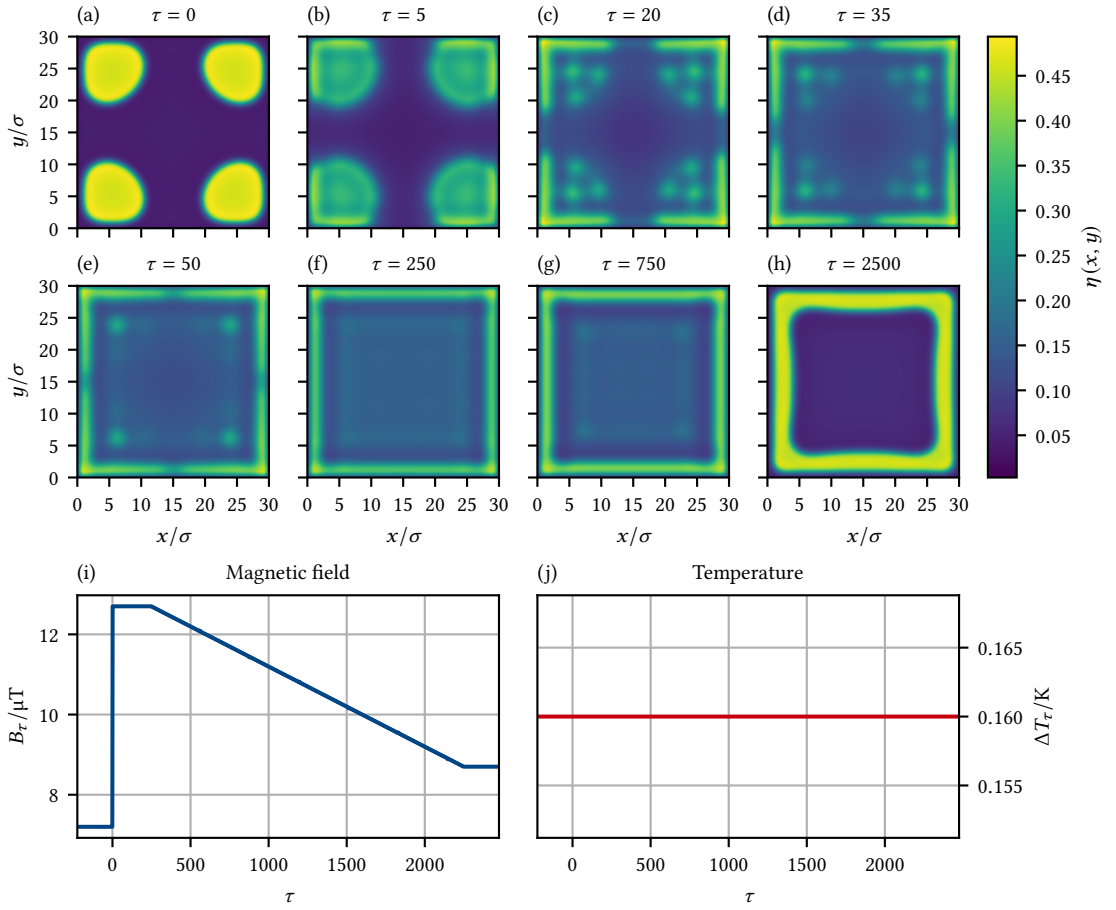

Figure 5.9.: Dynamic evolution of the density distribution of a system with $L = 30\sigma$ and $\eta_\mathrm{b} = 0.19$ after equilibrating into the droplet state at $B_\mathrm{i} = 7.2\,\mu\mathrm{T}$ and $\Delta T_\mathrm{i} = 0.16\,\mathrm{K}$ [cf. (a) and Fig. 4.23(a)] and then going to $B_\mathrm{f} = 8.7\,\mu\mathrm{T}$ according to Eq. (5.70) while keeping the temperature constant as shown in panels (i) and (j). Eventually, the system arrives at the stable ring configuration [cf. (h) and Fig. 4.23(d)]. See the supplemental material [98] for an animation.

forces the ring to contract. In both cases, no phase transition occurs – the system retains its original topology and ends up in a metastable state.

As shown in Fig. 5.9, we were, however, able to induce a transition from the droplet to the ring phase using a slightly more complicated strategy given by

$$B_\tau = \begin{cases} B_\mathrm{i} & \text{if } \tau < 0, \\ B_\mathrm{m} & \text{if } 0 \leq \tau < \tau_\mathrm{m}, \\ B_\mathrm{m} + (B_\mathrm{f} - B_\mathrm{m}) \frac{\lceil (\tau - \tau_\mathrm{m})/\tau_\mathrm{s} \rceil}{(\tau_\mathrm{t} - \tau_\mathrm{m})/\tau_\mathrm{s}} & \text{if } \tau_\mathrm{m} \leq \tau < \tau_\mathrm{t}, \\ B_\mathrm{f} & \text{if } \tau \geq \tau_\mathrm{t}. \end{cases} \tag{5.70}$$

The trick is to instantaneously increase the magnetic field at $\tau = 0$ from $\mathrm{B_i} \equiv 7.2\,\mu\mathrm{T}$ to a value

$B_\mathrm{m} \equiv 12.7\,\mu\mathrm{T}$ above $B_\mathrm{f} \equiv 8.7\,\mu\mathrm{T}$. Provided that B_m is sufficiently large, the droplets are immediately blown apart and the particles are pushed against the wall of the cell where they eventually form a thin ring. Once the system has effectively settled into an intermediate state of equilibrium at $\tau = 250 \equiv \tau_\mathrm{m}$, we dial the magnetic field *very* slowly (lest small droplets develop inside the ring) down in a quasi-linear manner so as to finally reach B_f at $\tau = 2250 \equiv \tau_\mathrm{t}$. The stable ring configuration then emerges after a short while [cf. Figs. 5.9(h) and 4.23(d)].

Using a variation of this method where we take the magnetic field from $B_\mathrm{i} = 8.7\,\mu\mathrm{T}$ abruptly down to some $\mathrm{B_m}$ *smaller* than $B_\mathrm{f} = 7.2\,\mu\mathrm{T}$ and then gradually back up to B_f unfortunately does not result in a transition from the ring to the droplet phase. If B is decreased below B_f, the ring simply contracts and potentially even turns into a large droplet. We have also not been able to come up with an alternative strategy that worked without allowing the temperature to change, and it may very well be that there actually is none. In the end, the problem lies in the difficulty of disassembling a solid ring.

Summary

We have studied the dynamics of our model system – confined to a square cell – by means of DDFT in order to ascertain how it responds to changes of the competing interactions by varying the magnetic field and the temperature. At first, we attempted to emulate an experiment where the system is initially at equilibrium in a fluid state with no repulsion ($B_\mathrm{i} = 0$) and only weak attraction ($T_\mathrm{i} \ll T_\mathrm{c}$), and then brought to a point (B_f, T_f) inside microphase regime where either a droplet or ring phase is thermodynamically stable. We found that it is all but certain that the system actually reaches the stable configuration, and more likely than not to become stuck in a metastable state. For example, jumping instantaneously from (B_i, T_i) to (B_f, T_f) tends to result in a larger number of differently-sized droplets because the sudden increase of the attraction to full strength leads to the local development of many smaller agglomerations that then coalesce until they grow large enough to repel each other. In fact, it appears that the starting point (B_i, T_i) and the concrete path taken through parameter space are more relevant for the ensuing structure than the destination (B_f, T_f) itself.

This suggests that each stable microphase can only be reached with a unique and specific strategy. We saw that a (quasi-)linear interpolation from (B_i, T_i) to (B_f, T_f) is able to generate a ring if the initial state and the transition time are suitably chosen. We also managed to produce a configuration of four droplets by using a minor modification whereby the magnetic field remains disabled at the beginning for a certain duration before it is abruptly turned on to some intermediate value and then increased (quasi-)linearly to B_f. In both cases, the larger system ($L = 30\sigma$) required a transition time an order of magnitude longer than the smaller one ($L = 20\sigma$). At those packing fractions and temperatures where, depending on the strength of the magnetic field, either the droplet or the ring phase is stable, we found a way to transition from the former to the

latter while keeping T constant that involves an instantaneous increase of B above B_f, followed by a slow (quasi-)linear decrease down to B_f. However, we failed to discover a path in the opposite direction which leads from a ring directly to a droplet configuration without having to make a detour to the fluid phase en route.

If our results are any indication, it turns out to be rather non-trivial to produce a specific structure in the presence of competing interactions, even if it is thermodynamically stable and represents the global minimum of the free energy landscape. Carefully plotting a path through parameter space into and inside the microphase regime seems to be crucial to safely navigate this landscape and prevent the system from getting trapped in the metastable state of a local free energy minimum. We suspect that this problem is often underestimated (or even disregarded) in experimental studies, which may contribute to the difficulty of observing the stable periodic density profiles predicted by theory. Considering that conditions are never ideal in reality, it stands to reason that even small asymmetries at the beginning can potentially amplify over time after the competing interactions are turned on, giving rise to highly irregular configurations in the end. It is unclear at this point whether the methods that we found to make the transition between the stable states within DDFT possible work equally well in experiments, or whether more invasive measures need to be taken. Further experimental research to elicit how the way in which the system is brought into the microphase regime affects the outcome is therefore most certainly warranted.

6. Conclusion

Let us recapitulate what we have done and come to learn. In an effort to gain deeper insights into the mechanics of microphase separation due to competing interactions, we have proposed an effectively two-dimensional model system that is theoretically accessible and presumed to be experimentally realizable, featuring spherical silica colloids subject to short-ranged attractive and long-ranged repulsive forces which can be tuned easily and independently from each other. The colloids are equipped with a paramagnetic core and submerged in a mixture of water and 2,6-Lutidine. Under the force of gravity, they sediment toward the bottom of a confining cell and form a flat monolayer. The cell is placed inside a homogeneous external magnetic field perpendicular to the monolayer. Upon approaching the lower critical demixing temperature T_c of the water–2,6-Lutidine mixture from below, the increasing correlation length of the solvent in combination with the colloids' preference for adsorbing water rather than 2,6-Lutidine leads to a critical Casimir attraction between the colloids whose strength and reach can be adjusted via minute changes of the temperature T. Within the paramagnetic core of each colloid, a magnetic dipole moment is induced that is proportional and parallel to the external magnetic field. Because the magnetic dipoles are all normal to the monolayer, they give rise to a repulsion in the lateral direction that can be controlled by varying the strength B of the magnetic field. We saw that, by choosing suitable values for B and $\Delta T \equiv T_c - T$, we are able to construct interaction potentials that offer the typical SALR characteristics in that the colloids are attracted to one another at smaller separations, and repelled from each other at larger ones.

We went on to study the static phase behavior of this system by means of density functional theory (DFT) – at first with a focus on the infinite bulk. By calculating the binodal and spinodal, we unsurprisingly found that a macroscopic separation into a sparse gaseous and a dense liquid phase is preferred to a single uniform fluid phase with some intermediate density if the attraction is strong and the repulsion weak enough. Next, we set out to investigate whether modulated microphases are thermodynamically stable and favored over homogeneous ones under certain circumstances. We showed that a sufficient condition for this is that the global minimum $\tilde{D}(k_{\min})$ of the reciprocal Fourier transform of the static structure factor is negative: a density profile that fluctuates with the corresponding wavelength $\lambda = 2\pi/k_{\min}$ has a lower energy compared to a flat one with the same bulk packing fraction η_b. We found that there indeed exists a region in the phase diagram spanned by η_b, B and ΔT where this is the case, and where microphase separation therefore occurs. For small and intermediate η_b, we identified a low-$k_{\min}$ domain at smaller B

or ΔT, as well as an intermediate-$k_{\min}$ domain at larger B or ΔT. For large η_b, we observed a high-$k_{\min}$ domain that suggests crystallization. If we look at different cross sections of the phase diagram that lie perpendicular to the B or ΔT axis, these domains vary in size and shape, some of them might not be present at all, and they may be disconnected or joined together. If they are joined, $k_{\min}$ increases smoothly from the lower to the intermediate values, but jumps abruptly to the higher ones; the reason for this is that the global minimum of $\tilde{D}$ shifts from the first to the second local minimum. In the limit of vanishing repulsion, $B \to 0$, we continuously recover a purely attractive system that only offers macrophase separation: the high-$k_{\min}$ domain vanishes and the wavelength of the density fluctuations in the low-$k_{\min}$ one diverges since $k_{\min} \to 0$; at $B = 0$, the spinodal coincides with the border of the zero-$k_{\min}$ domain.

To determine the structure of the microphases, we then developed a Landau-type theory by Taylor-expanding the intrinsic free energy functional $\mathcal{F}$ around the bulk density ρ_b up to $\hat{n}$-th order, and restricting ourselves to density distributions that can be represented within the $\hat{s}$-shell expansion. Choosing $\hat{n} = 4$ and $\hat{s} = 1$, this enabled us to quickly approximate $\mathcal{F}[\rho]$ for a density profile $\rho(\vec{r}) \equiv \Phi_1 g_1(\vec{r})$ with a certain structure g_1 as a function of the principal wavenumber k_1 and the fluctuation amplitude Φ_1 of the first shell. By numerically minimizing the intrinsic free energy with respect to k_1 and Φ_1 for different g_1, we could estimate which microphase is favored at a given point $(\eta_b, B, \Delta T)$ in parameter space. We considered the hexagonal droplet, lamellar stripe and hexagonal bubble structures that were observed in prior theoretical studies of two-dimensional systems with competing interactions to emerge in that precise order with increasing bulk density, and were able to confirm that our model features exactly the same sequence of stable microphases. While our Landau-type theory gave us a relatively fast and inexpensive means of computing a phase diagram, its accuracy turned out to be rather questionable because the restriction to the first shell implied that only slowly-varying density distributions could be faithfully represented, and because the minimization of the fourth-order Taylor expansion of $\mathcal{F}$ would often result in invalid density profiles with $\rho(\vec{r}) < 0$ for some $\vec{r}$ unless the requirement that ρ be non-negative was artificially enforced.

To improve the quality of our predictions, we implemented the Picard algorithm on a workstation, allowing us to freely minimize either the grand potential $\Omega[\rho]$ (in a grand-canonical setting with fixed chemical potential μ) or the Helmholtz free energy $\mathcal{A}[\rho]$ (in a quasi-canonical setting with fixed bulk density ρ_b) with respect to a density distribution ρ which has been discretized on a regular grid. While we found the same stable microphases as we did with the Landau-type theory (droplets → stripes → bubbles), their location in parameter space and their borders changed noticeably. Especially at lower magnetic fields, the differences were quite significant. We attributed this to the fact that the equilibrium density profiles are not slowly-varying in the case of a weak repulsion, but exhibit distinct sparse and dense domains separated by a very thin transition zone. We saw that the density distribution *within* these domains is almost flat, and

that, as $B \to 0$, the average density therein approaches either that of the gaseous or that of the liquid bulk coexistence state lying on the binodal. To accommodate for different bulk densities, the system therefore has to adjust the relative size of the domains. We furthermore discovered that the microphase regime can grow beyond the λ-line/surface surrounding the region with $\tilde{D}(k_{\min}) < 0$ and extend up the binodal. We interpret these observations for the weak repulsion limit as a mesoscopic gas–liquid phase separation with periodic density profiles.

We ended our analysis of the statics by investigating the phase behavior of a system that is confined to a finite cell. Initially we attempted to recover analogs of the droplet and bubble patterns the were stable in the bulk by choosing hexagonal or rectangular cells that were compatible in size. It turned out, however, that this does not work reliably and that these cell shapes permit a confusingly large number of different structures. In the end, we decided to focus on square cells, for which we only detected two microphases (in addition to the almost uniform gaseous or liquid states at very low and very high bulk packing fractions, respectively): one at lower η_b that comprises four droplets, and another one at intermediate and higher η_b that features a single ring. We proceeded by calculating a phase diagram at a fixed temperature for a larger cell with side length $L = 30\sigma$ and for a smaller one with $L = 20\sigma$. In both cases, we found the ring to be stable for a much wider range of bulk packing fractions than the droplets; an explanation for this could be that the stripe and the bubble phase of the bulk effectively combine into a single ring phase upon confinement. We noticed that the droplet and ring phases overlap to some extent in the phase diagram for the larger cell in the sense that for some η_b, the former is stable at lower B and the latter at higher B; in this, we saw the possibility of inducing a phase transition at constant temperature by solely varying the magnetic field.

Lastly, we employed dynamic density functional theory (DDFT) to study the dynamics of microphase separation in this confined system. We wanted to ascertain how the density distribution evolves if the external parameters – the magnetic field B and the temperature T – are changed over time, and whether the specific path taken through parameter space from an initial $(B_\mathrm{i}, T_\mathrm{i})$ to some final $(B_\mathrm{f}, T_\mathrm{f})$ has an influence on the structure of the equilibrium state that eventually emerges. We saw that if the end point lies inside the microphase regime, the system can quite easily become trapped in a local (as opposed to *the* global) minimum of the rather complicated free energy landscape unless that path is carefully chosen. It actually seems that this path may have a larger impact on the outcome of the dynamic evolution of the density profile than $(B_\mathrm{f}, T_\mathrm{f})$ itself. In particular, an instantaneous jump into the microphase regime always resulted in an metastable configuration. We managed to devise different strategies that would reliably lead from an almost uniform fluid at the beginning to either a stable droplet or to a stable ring state in the end. We also found a way to transition from a droplet to a ring configuration in the aforementioned overlap region by keeping the temperature fixed and altering only the magnetic field; however, we failed to discover a *direct* path in the opposite direction.

We come to the conclusion that the system presented in this thesis promises to be a very valuable model to further our understanding of microphase separation induced by competing interactions. The simplicity of the setup and the triviality of imaging colloidal monolayers via microscopy call for experimental studies against which our (or future) theoretical findings can be compared. The ability of tuning the attraction and repulsion between the particles *in situ* by adjusting the temperature and the magnetic field, respectively, opens up intriguing possibilities. We saw that the composition of these two contributions, and hence the shape of the interaction potential, greatly affect the character of the equilibrium density distribution. Especially the coexistence of periodically arranged, mesoscopically sized and clearly defined gaseous and liquid domains at weaker repulsive forces appears to be quite interesting. We found that, in the presence of competing interactions, the free energy landscape is fraught with local minima in which the dynamics are prone to getting stuck. This could be one of the factors why, in contrast to theoretical predictions, periodic configurations with a high degree of symmetry are rarely observed in experiments. However, we showed that the system can – at least in theory – be guided to the stable thermodynamic equilibrium state by suitably varying the temperature and the magnetic field over time.

In the end, the hope is that this study can convince other statistical physicists – both theoreticians and experimentalists alike – that our two-dimensional colloidal system with competing attractive critical Casimir and repulsive magnetic dipole interactions is compelling enough to warrant further research of which the present thesis only marks the beginning.

Acknowledgments

If someone had foretold me at the start of my physics studies at the University of Tübingen that I would wind up at this point almost ten years later, I would have seriously questioned that person's mental health. Writing a doctoral thesis already appeared unlikely enough, but doing so in the field of *thermodynamics*? Utterly preposterous! What had piqued my interest in physics at an early age were astronomy and space travel, and what had convinced me to study physics were electromagnetism and the double slit experiment. I wanted to learn about the theory of relativity and black holes. I wanted to find out whether Schrödinger's cat was dead or alive. Or both. Or neither. In comparison, phase transitions and heat engines just seemed rather mundane. Boring, even. I had not really grown fond of thermodynamics in school, and I cannot say that the Physics 101 lectures at university did much to change that.

I was therefore not exactly bursting with enthusiasm when I was faced with an entire mandatory course on thermodynamics and statistical physics, held by Prof. Dr. Roland Roth. However, to his merit and to my lasting surprise, he somehow managed to slowly turn my aversion to this topic into a fascination for it I would not have thought possible. So much so, in fact, that I visited his follow-up course on advanced statistical physics, completed an internship in his group, and wrote my bachelor's, master's and finally also my doctoral thesis under his supervision and guidance. I am indebted to him for providing me with these opportunities and shaping my academic career so profoundly.

I would like to give a shout-out to all my other colleagues in the Roth group whom I had the privilege of working and becoming acquainted with. Especially Nikolas Ditz, Florian Gußmann, Hendrik Hansen-Goos, Matthias Scholtyszeck, Daniel Stopper, and Michael Zimmermann cannot be left unmentioned in this regard. I must also thank Prof. Dr. Martin Oettel for agreeing to be the second supervisor for my doctoral thesis and for co-organizing the insightful and illuminating *Density Functional Days*.

It am honored to have met and become friends with some truly remarkable people during my time in Tübingen. I raise a glass to Sebastian Völkel for all our hiking, skiing and biking trips which awakened the adventurer within me; to Martin Bohnert and Jonas Leister for the sometimes more, sometimes less enlightening, but never uncontroversial discussions over lunch; and to Pit Burgbacher, Lucas Jordan, Daniel Mieg, Manuel Nonnenmacher, Timo Schössler, Timo Storzer and Philip Wolf for the jovial dinners and merry wine tastings. I wish them all the best for the path that lies ahead.

In the end, however, it is my family that deserves my deepest of gratitude. I thank my kind and loving parents for their unconditional and unwavering support. I thank my brother, his magnanimous wife and their wonderful children for making me not only feel always welcome in their home, but also a very proud uncle. Lastly, I thank Elisabeth for stealing my heart and holding on to it, for encouraging me to keep on going when my motivation dwindled, and for each and every second spent together – may there be many more of those yet to come.

Appendix

A. Decomposition of the Mayer f-function for hard disks

To prove that the Mayer f-function for hard disks,

$$f_{ab}(\vec{r}) = \begin{cases} -1 & \text{if } |\vec{r}| < R_a + R_b, \\ 0 & \text{otherwise,} \end{cases} \tag{A.1}$$

can indeed be decomposed into

$$-f_{ab} = \omega_a^2 \star \omega_b^0 + \omega_a^0 \star \omega_b^2 + \frac{1}{2\pi} \sum_{m=0}^{\infty} C_m \, \boldsymbol{\omega}_a^m \star \boldsymbol{\omega}_b^m \tag{A.2}$$

as claimed in Section 2.3.2, let us simply calculate the individual terms. To evaluate the first one, we use polar coordinates and find

$$\begin{aligned} (\omega_a^2 \star \omega_b^0)(\vec{r}) &= \int \mathrm{d}^2\vec{r}' \, \omega_a^2(\vec{r}' - \vec{r}) \, \omega_b^0(\vec{r}') = \int \mathrm{d}^2\vec{r}' \, \Theta(R_a - |\vec{r}' - \vec{r}|) \, \frac{\delta(R_b - |\vec{r}'|)}{2\pi R_b} \\ &= \int_0^\infty \mathrm{d}r' \int_{-\pi}^{\pi} \mathrm{d}\varphi' \, r' \, \Theta\!\left(R_a - \sqrt{(r')^2 + |\vec{r}|^2 - 2|\vec{r}|r'\cos\varphi'}\right) \frac{\delta(R_b - r')}{2\pi R_b} \\ &= \frac{1}{2\pi} \int_{-\pi}^{\pi} \mathrm{d}\varphi' \, \Theta\!\left(R_a - \sqrt{R_b^2 + |\vec{r}|^2 - 2|\vec{r}|R_b\cos\varphi'}\right) \\ &= \begin{cases} \Theta(R_a - R_b) & \text{if } |\vec{r}| \le |R_a - R_b|, \\ \varphi_b(\vec{r})/\pi & \text{if } |R_a - R_b| < |\vec{r}| < R_a + R_b, \\ 0 & \text{otherwise,} \end{cases} \end{aligned} \tag{A.3}$$

with the angle

$$\varphi_b(\vec{r}) \equiv \arccos \frac{|\vec{r}|^2 + R_b^2 - R_a^2}{2|\vec{r}|R_b}. \tag{A.4}$$

Now consider the case of two partially overlapping disks with radii R_a and R_b and centers separated by a vector $\vec{r}$ with $|R_a - R_b| < |\vec{r}| < R_a + R_b$ as depicted in Fig. A.1. If we look at the triangle formed by the disks' centers, A and B, and one of the two intersection points of the disks' surfaces, C, then it is clear from the law of cosines that $\varphi_b(\vec{r})$ can be identified as the angle at the

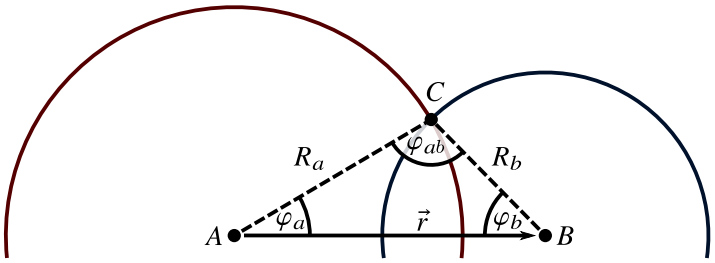

Figure A.1.: Two partially overlapping disks with radii R_a and R_b whose centers A and B are separated by a vector $\vec{r}$ with $|R_a - R_b| < |\vec{r}| < R_a + R_b$. One of the two intersection points of the disks' surfaces is marked as C. The points A, B and C define a triangle with interior angles φ_a, φ_b and φ_{ab} at the respective vertices.

vertex B. Analogously, we have that

$$(\omega_a^0 \star \omega_b^2)(\vec{r}), = \begin{cases} \Theta(R_b - R_a) & \text{if } |\vec{r}| \leq |R_a - R_b| \\ \varphi_a(\vec{r})/\pi & \text{if } |R_a - R_b| < |\vec{r}| < R_a + R_b, \\ 0 & \text{otherwise,} \end{cases} \tag{A.5}$$

where

$$\varphi_a(\vec{r}) \equiv \arccos \frac{|\vec{r}|^2 + R_a^2 - R_b^2}{2|\vec{r}|R_a} \tag{A.6}$$

is the angle at the vertex A. Determining $\boldsymbol{\omega}_a^m \star \boldsymbol{\omega}_b^m$ is slightly more complicated. We begin with

$$\begin{aligned}
(\boldsymbol{\omega}_a^m \star \boldsymbol{\omega}_b^m)(\vec{r}) &= \int \mathrm{d}^2\vec{r}' \sum_{i_1=1}^{2} \cdots \sum_{i_m=1}^{2} [\boldsymbol{\omega}_a^m(\vec{r}' - \vec{r})]_{i_1,\ldots,i_m} [\boldsymbol{\omega}_b^m(\vec{r}')]_{i_1,\ldots,i_m} \\
&= \int \mathrm{d}^2\vec{r}' \sum_{i_1=1}^{2} \cdots \sum_{i_m=1}^{2} \frac{(x'_{i_1} - x_{i_1}) \cdots (x'_{i_m} - x_{i_m})}{|\vec{r}' - \vec{r}|^m} \frac{x'_{i_1} \cdots x'_{i_m}}{|\vec{r}'|^m} \, \delta(R_a - |\vec{r}' - \vec{r}|) \, \delta(R_b - |\vec{r}'|) \\
&= \int \mathrm{d}^2\vec{r}' \left[\frac{\vec{r}' \cdot (\vec{r}' - \vec{r})}{|\vec{r}'| \, |\vec{r}' - \vec{r}|} \right]^m \delta(R_a - |\vec{r}' - \vec{r}|) \, \delta(R_b - |\vec{r}'|) \\
&= \int_0^\infty \mathrm{d}r' \int_{-\pi}^{\pi} \mathrm{d}\varphi' \, r' \left[\frac{(r')^2 - r'|\vec{r}| \cos\varphi'}{r'\sqrt{(r')^2 + |\vec{r}|^2 - 2r'|\vec{r}| \cos\varphi'}} \right]^m \delta(R_b - r') \\
&\qquad \times \delta\left(R_a - \sqrt{(r')^2 + |\vec{r}|^2 - 2r'|\vec{r}| \cos\varphi'} \right) \\
&= \int_{-\pi}^{\pi} \mathrm{d}\varphi' \, R_b \left[\frac{R_b^2 - |\vec{r}|R_b \cos\varphi'}{R_b\sqrt{R_b^2 + |\vec{r}|^2 - 2R_b|\vec{r}| \cos\varphi'}} \right]^m \delta\left(R_a - \sqrt{R_b^2 + |\vec{r}|^2 - 2R_b|\vec{r}| \cos\varphi'} \right).
\end{aligned} \tag{A.7}$$

To continue, we use that, for some function f with only simple roots Z_f,

$$\delta(f(\varphi)) = \sum_{\varphi_0 \in Z_f} \frac{\delta(\varphi - \varphi_0)}{|f'(\varphi_0)|}, \tag{A.8}$$

where f' denotes the derivative of f. For

$$f(\varphi) \equiv R_a - \sqrt{R_b^2 + |\vec{r}|^2 - 2R_b|\vec{r}|\cos\varphi} \tag{A.9}$$

we have

$$Z_f = \begin{cases} \{-\varphi_b(\vec{r}), \varphi_b(\vec{r})\} & \text{if } |R_a < R_b| < |\vec{r}| < R_a + R_b, \\ \varnothing & \text{otherwise} \end{cases} \tag{A.10}$$

and

$$|f'(\pm\varphi_b(\vec{r}))| = \frac{R_b}{R_a}|\vec{r}|\sin\varphi_b(\vec{r}), \tag{A.11}$$

which leads to

$$\begin{aligned} (\boldsymbol{\omega}_a^m \star \boldsymbol{\omega}_b^m)(\vec{r}) &= \begin{cases} 2\frac{R_a}{|\vec{r}|\sin\varphi_b(\vec{r})}\left[\frac{R_b^2 - |\vec{r}|R_b\cos\varphi_b(\vec{r})}{R_b\sqrt{R_b^2+|\vec{r}|^2-2R_b|\vec{r}|\cos\varphi_b(\vec{r})}}\right]^m & \text{if } |R_a - R_b| < |\vec{r}| < R_a + R_b, \\ 0 & \text{otherwise,} \end{cases} \\ &= \begin{cases} 2\frac{R_a\cos^m\varphi_{ab}(\vec{r})}{|\vec{r}|\sin\varphi_b(\vec{r})} & \text{if } |R_a - R_b| < |\vec{r}| < R_a + R_b, \\ 0 & \text{otherwise,} \end{cases} \end{aligned} \tag{A.12}$$

where

$$\varphi_{ab}(\vec{r}) \equiv \arccos\frac{R_a^2 + R_b^2 - |\vec{r}|^2}{2R_aR_b} \tag{A.13}$$

is the angle at the vertex C. Since $|\vec{r}|\sin\varphi_b(\vec{r}) = R_a\sin\varphi_{ab}(\vec{r})$ according to the law of sines, we arrive at

$$(\boldsymbol{\omega}_a^m \star \boldsymbol{\omega}_b^m)(\vec{r}) = \begin{cases} 2\frac{\cos^m\varphi_{ab}(\vec{r})}{\sin\varphi_{ab}(\vec{r})} & \text{if } |R_a - R_b| < |\vec{r}| < R_a + R_b, \\ 0 & \text{otherwise.} \end{cases} \tag{A.14}$$

Noting that

$$\sum_{m=0}^{\infty} C_m \frac{\cos^m\varphi}{\sin\varphi} = \varphi \tag{A.15}$$

for $\varphi \in (0, \pi)$ and the coefficients given in Eq. (2.91), we see that

$$\frac{1}{2\pi}\sum_{m=1}^{\infty} C_m(\boldsymbol{\omega}_a^m \star \boldsymbol{\omega}_b^m)(\vec{r}) = \begin{cases} \varphi_{ab}(\vec{r})/\pi & \text{if } |R_a - R_b| < |\vec{r}| < R_a + R_b, \\ 0 & \text{otherwise.} \end{cases} \tag{A.16}$$

Finally, combining Eqs. (A.3), (A.5) and (A.16) gives us

$$\begin{aligned} &(\omega_a^2 \star \omega_b^0)(\vec{r}) + (\omega_a^0 \star \omega_b^2)(\vec{r}) + \frac{1}{2\pi}\sum_{m=0}^{\infty} C_m\,(\boldsymbol{\omega}_a^m \star \boldsymbol{\omega}_b^m)(\vec{r}) \\ &\quad= \begin{cases} \Theta(R_a - R_b) + \Theta(R_b - R_a) & \text{if } |\vec{r}| \le |R_a - R_b|, \\ [\varphi_a(\vec{r}) + \varphi_b(\vec{r}) + \varphi_{ab}(\vec{r})]/\pi & \text{if } |R_a - R_b| < |\vec{r}| < R_a + R_b, \\ 0 & \text{otherwise,} \end{cases} \\ &\quad= \begin{cases} 1 & \text{if } |\vec{r}| \le R_a + R_b, \\ 0 & \text{otherwise,} \end{cases} \\ &\quad= -f_{ab}(\vec{r}), \end{aligned} \tag{A.17}$$

where we used that $\Theta(x) + \Theta(-x) = 1$ and that the sum of angles $\varphi_a(\vec{r}) + \varphi_b(\vec{r}) + \varphi_{ab}(\vec{r})$ of the triangle ABC is equal to π.

B. A relationship between chemical potential and pressure

In the bulk, we can write the grand potential as $\beta\Omega[\rho_\mathrm{b}] = V\phi_{\rho_\mathrm{b}} - V\rho_\mathrm{b}\beta\mu$. In equilibrium,

$$\begin{aligned} 0 = \beta\frac{\delta\Omega[\rho_\mathrm{b}]}{\delta\rho_\mathrm{b}} = V\,\frac{\mathrm{d}\phi_{\rho_\mathrm{b}}}{\mathrm{d}\rho_\mathrm{b}} - V\beta\mu \quad &\rightsquigarrow \quad \beta\mu = \frac{\mathrm{d}\phi_{\rho_\mathrm{b}}}{\mathrm{d}\rho_\mathrm{b}} \quad \rightsquigarrow \quad \beta\frac{\partial\mu}{\partial\rho_\mathrm{b}} = \frac{\mathrm{d}^2\phi_{\rho_\mathrm{b}}}{\mathrm{d}\rho_\mathrm{b}^2}, \\ \beta P = -\beta\frac{\partial\Omega[\rho_\mathrm{b}]}{\partial V} = \rho_\mathrm{b}\beta\mu - \phi_{\rho_\mathrm{b}} = \rho_\mathrm{b}\frac{\mathrm{d}\phi_{\rho_\mathrm{b}}}{\mathrm{d}\rho_\mathrm{b}} - \phi_{\rho_\mathrm{b}} \quad &\rightsquigarrow \quad \beta\frac{\partial P}{\partial\rho_\mathrm{b}} = \rho_\mathrm{b}\frac{\mathrm{d}^2\phi_{\rho_\mathrm{b}}}{\mathrm{d}\rho_\mathrm{b}^2}, \end{aligned} \tag{B.1}$$

and therefore

$$\frac{\partial P}{\partial\rho_\mathrm{b}} = \rho_\mathrm{b}\frac{\partial\mu}{\partial\rho_\mathrm{b}}. \tag{B.2}$$

C. Derivation of the Ornstein–Zernike relation

Writing the grand canonical partition sum as

$$\mathcal{Z}_\mathrm{gc} = \sum_{n=0}^{\infty}\frac{1}{h^{dn}n!}\int \mathrm{d}^{dn}\boldsymbol{q}\int \mathrm{d}^{dn}\boldsymbol{p}\,\exp[-\beta\{\mathcal{H}_\mathrm{int}(n,\boldsymbol{q},\boldsymbol{p}) - \int \mathrm{d}^d\vec{r}\,\hat{\rho}_{\vec{r}}(n,\boldsymbol{q},\boldsymbol{p})\,\mu_\mathrm{int}(\vec{r})\}], \tag{C.1}$$

we find that

$$\frac{\delta\Omega}{\delta\mu_{\mathrm{int}}(\vec{r})} = -k_{\mathrm{B}}T\frac{\delta \ln \mathcal{Z}_{\mathrm{gc}}}{\delta\mu_{\mathrm{int}}(\vec{r})} = -\frac{k_{\mathrm{B}}T}{\mathcal{Z}_{\mathrm{gc}}}\frac{\delta\mathcal{Z}_{\mathrm{gc}}}{\delta\mu_{\mathrm{int}}(\vec{r})} = -\langle\hat{\rho}_{\vec{r}}\rangle = -\rho(\vec{r}) \tag{C.2}$$

and

$$\begin{aligned} k_{\mathrm{B}}T\frac{\delta\rho(\vec{r})}{\delta\mu_{\mathrm{int}}(\vec{r}')} &= -\frac{1}{\beta}\frac{\delta^2\Omega}{\delta\mu_{\mathrm{int}}(\vec{r}')\,\delta\mu_{\mathrm{int}}(\vec{r})} = \frac{1}{\beta^2}\frac{\delta^2 \ln \mathcal{Z}_{\mathrm{gc}}}{\delta\mu_{\mathrm{int}}(\vec{r}')\,\delta\mu_{\mathrm{int}}(\vec{r})} \\ &= \frac{1}{\beta^2}\left[\frac{1}{\mathcal{Z}_{\mathrm{gc}}}\frac{\delta^2\mathcal{Z}_{\mathrm{gc}}}{\delta\mu_{\mathrm{int}}(\vec{r}')\,\delta\mu_{\mathrm{int}}(\vec{r})} - \frac{1}{\mathcal{Z}_{\mathrm{gc}}}\frac{\delta\mathcal{Z}_{\mathrm{gc}}}{\delta\mu_{\mathrm{int}}(\vec{r}')}\cdot\frac{1}{\mathcal{Z}_{\mathrm{gc}}}\frac{\delta\mathcal{Z}_{\mathrm{gc}}}{\delta\mu_{\mathrm{int}}(\vec{r})}\right] \\ &= \langle\hat{\rho}_{\vec{r}}\,\hat{\rho}_{\vec{r}'}\rangle - \langle\hat{\rho}_{\vec{r}}\rangle\langle\hat{\rho}_{\vec{r}'}\rangle = \langle\hat{\rho}_{\vec{r}}\rangle\langle\hat{\rho}_{\vec{r}'}\rangle h_2(\vec{r},\vec{r}') + \langle\hat{\rho}_{\vec{r}}\rangle\,\delta(\vec{r}-\vec{r}') \\ &= \rho(\vec{r})\rho(\vec{r}')\,h_2(\vec{r},\vec{r}') + \rho(\vec{r})\,\delta(\vec{r}-\vec{r}') \end{aligned} \tag{C.3}$$

with the two-point total correlation function h_2 from Eq. (2.142). Using Eq. (C.2), we see that

$$\mathcal{F}[\rho] = \Omega[\rho] + \int \mathrm{d}^d\vec{r}\,\rho(\vec{r})\,\mu_{\mathrm{int}}(\vec{r}) = \Omega[\rho] - \int \mathrm{d}^d\vec{r}\,\frac{\delta\Omega[\rho]}{\delta\mu_{\mathrm{int}}(\vec{r})}\,\mu_{\mathrm{int}}(\vec{r}), \tag{C.4}$$

and that $\mathcal{F}$ is therefore the Legendre transformation of Ω with respect to μ_{int}. Thus,

$$\frac{\delta\mathcal{F}[\rho]}{\delta\rho(\vec{r})} = \mu_{\mathrm{int}}(\vec{r}). \tag{C.5}$$

Defining the one-body direct correlation function as

$$c_1(\vec{r}) \equiv -\beta\frac{\delta\mathcal{F}_{\mathrm{ex}}[\rho]}{\delta\rho(\vec{r})} = \beta\frac{\delta\mathcal{F}_{\mathrm{id}}[\rho]}{\delta\rho(\vec{r})} - \beta\frac{\delta\mathcal{F}[\rho]}{\delta\rho(\vec{r})} = \ln[\Lambda^d\rho(\vec{r})] - \beta\mu_{\mathrm{int}}(\vec{r}), \tag{C.6}$$

we have that

$$\beta\frac{\delta\mu_{\mathrm{int}}(\vec{r})}{\delta\rho(\vec{r}')} = \frac{\delta\ln[\Lambda^d\rho(\vec{r})]}{\delta\rho(\vec{r}')} - \frac{\delta c_1(\vec{r})}{\delta\rho(\vec{r}')} = \frac{\delta(\vec{r}-\vec{r}')}{\rho(\vec{r})} - c_2(\vec{r},\vec{r}'), \tag{C.7}$$

where c_2 is the two-point direct correlation function defined in Eq. (2.144). Finally, with

$$\begin{aligned} \delta(\vec{r}-\vec{r}') &= \frac{\delta\mu_{\mathrm{int}}(\vec{r})}{\delta\mu_{\mathrm{int}}(\vec{r}')} = \int \mathrm{d}^d\vec{r}''\,\frac{\delta\mu_{\mathrm{int}}(\vec{r})}{\delta\rho(\vec{r}'')}\frac{\delta\rho(\vec{r}'')}{\delta\mu_{\mathrm{int}}(\vec{r}')} \\ &= \int \mathrm{d}^d\vec{r}''\left[\frac{\delta(\vec{r}-\vec{r}'')}{\rho(\vec{r})} - c_2(\vec{r},\vec{r}'')\right]\left[\rho(\vec{r}'')\rho(\vec{r}')h_2(\vec{r}'',\vec{r}') + \rho(\vec{r}'')\delta(\vec{r}''-\vec{r}')\right] \\ &= \rho(\vec{r}')\left[h_2(\vec{r},\vec{r}') - \int \mathrm{d}^d\vec{r}''\,c_2(\vec{r},\vec{r}'')\rho(\vec{r}'')h_2(\vec{r}'',\vec{r}') - c_2(\vec{r},\vec{r}')\right] + \delta(\vec{r}-\vec{r}'), \end{aligned} \tag{C.8}$$

the Ornstein–Zernike relation

$$h_2(\vec{r},\vec{r}') = c_2(\vec{r},\vec{r}') + \int \mathrm{d}^d\vec{r}''\,c_2(\vec{r},\vec{r}'')\rho(\vec{r}'')h_2(\vec{r}'',\vec{r}') \tag{C.9}$$

immediately follows.

D. Fourier transforms in two dimensions

The Fourier transform $\tilde{f} : \mathbb{R}^2 \to \mathbb{C}$ of some function $f : \mathbb{R}^2 \to \mathbb{C}$ is defined as

$$\tilde{f}(\vec{k}) \equiv \int \mathrm{d}^2\vec{r}\, f(\vec{r}) \exp(-\mathrm{i}\vec{k}\cdot\vec{r}). \tag{D.1}$$

If f is radially symmetric, $f(\vec{r}) = f(|\vec{r}|)$, then also $\tilde{f}(\vec{k}) = \tilde{f}(|\vec{k}|)$ with

$$\begin{aligned}\tilde{f}(\vec{k}) &= \int \mathrm{d}^2\vec{r}\, f(|\vec{r}|) \exp(-\mathrm{i}\vec{k}\cdot\vec{r}) = \int_0^\infty \mathrm{d}r \int_0^{2\pi} \mathrm{d}\varphi\, r f(r) \exp(-\mathrm{i}|\vec{k}|r\cos\varphi) \\ &= \int_0^\infty \mathrm{d}r\, r f(r) \underbrace{\int_0^{2\pi} \mathrm{d}\varphi \exp(-\mathrm{i}|\vec{k}|r\cos\varphi)}_{=2\pi J_0(|\vec{k}|r)} = 2\pi \int_0^\infty \mathrm{d}r\, r f(r) J_0(|\vec{k}|r),\end{aligned} \tag{D.2}$$

where J_0 denotes the zeroth Bessel function of the first kind.

The Fourier transforms of those quantities that enter into the theoretical description of our model system – namely the hard disk weight functions ω^0, ω^2, $\boldsymbol{\omega}^0$, $\boldsymbol{\omega}^1$ and $\boldsymbol{\omega}^2$, as well as the competing interaction potential u_{ci} – can be expressed in terms of Bessel and Struve functions, for which we shall now derive some useful identities.

D.1. Bessel and Struve functions

The n-th Bessel function of the first kind is defined as

$$J_n(x) \equiv \frac{1}{2\pi} \int_{\varphi_0}^{\varphi_0+2\pi} \mathrm{d}\varphi \exp[\mathrm{i}(x\sin\varphi - n\varphi)], \tag{D.3}$$

where the choice of φ_0 is arbitrary since the integrand $\exp[\mathrm{i}(x\sin\varphi - n\varphi)]$ is 2π-periodic in φ. We can therefore also perform the substitution $\varphi \to \varphi - \pi/2$ without adjusting the limits of integration to find the representation

$$\begin{aligned}J_n(x) &= \frac{1}{2\pi} \int_{\varphi_0}^{\varphi_0+2\pi} \mathrm{d}\varphi \exp[\mathrm{i}\,\{x\sin(\varphi-\pi/2) - n(\varphi-\pi/2)\}] \\ &= \frac{\exp(\mathrm{i}n\pi/2)}{2\pi} \int_{\varphi_0}^{\varphi_0+2\pi} \mathrm{d}\varphi \exp(-\mathrm{i}x\cos\varphi)\exp(-\mathrm{i}n\varphi) \\ &= \frac{\exp(\mathrm{i}\pi/2)^n}{2\pi} \int_{\varphi_0}^{\varphi_0+2\pi} \mathrm{d}\varphi \exp(-\mathrm{i}x\cos\varphi)\exp(-\mathrm{i}\varphi)^n \\ &= \frac{\mathrm{i}^n}{2\pi} \int_{\varphi_0}^{\varphi_0+2\pi} \mathrm{d}\varphi \exp(-\mathrm{i}x\cos\varphi)\,(\cos\varphi - \mathrm{i}\sin\varphi)^n.\end{aligned} \tag{D.4}$$

Using that

$$\int_{\varphi_0}^{\varphi_0+2\pi} \mathrm{d}\varphi \exp(-\mathrm{i}x\cos\varphi)\cos^k\varphi\sin^{2l+1}\varphi = \int_{-\pi}^{\pi} \mathrm{d}\varphi \exp(-\mathrm{i}x\cos\varphi)\cos^k\varphi\sin^{2l+1}\varphi = 0 \tag{D.5}$$

for all $k, l \in \mathbb{N}_0$ because the integrand is an uneven function of φ, it follows from Eq. (D.4) that

$$J_0(x) = \frac{1}{2\pi}\int_{\varphi_0}^{\varphi_0+2\pi} \mathrm{d}\varphi \exp(-\mathrm{i}x\cos\varphi), \tag{D.6}$$

that

$$\begin{aligned} J_1(x) &= \frac{\mathrm{i}}{2\pi}\int_{\varphi_0}^{\varphi_0+2\pi} \mathrm{d}\varphi \exp(-\mathrm{i}x\cos\varphi)\,(\cos\varphi - \mathrm{i}\sin\varphi) \\ &= -\frac{1}{\mathrm{i}2\pi}\int_{\varphi_0}^{\varphi_0+2\pi} \mathrm{d}\varphi \exp(-\mathrm{i}x\cos\varphi)\cos\varphi, \end{aligned} \tag{D.7}$$

and that

$$\begin{aligned} J_2(x) &= \frac{\mathrm{i}^2}{2\pi}\int_{\varphi_0}^{\varphi_0+2\pi} \mathrm{d}\varphi \exp(-\mathrm{i}x\cos\varphi)\,(\cos\varphi - \mathrm{i}\sin\varphi)^2 \\ &= -\frac{1}{2\pi}\int_{\varphi_0}^{\varphi_0+2\pi} \mathrm{d}\varphi \exp(-\mathrm{i}x\cos\varphi)\,(\cos^2\varphi - \sin^2\varphi - \mathrm{i}2\cos\varphi\sin\varphi) \\ &= \frac{1}{2\pi}\int_{\varphi_0}^{\varphi_0+2\pi} \mathrm{d}\varphi \exp(-\mathrm{i}x\cos\varphi)\,(\sin^2\varphi - \cos^2\varphi). \end{aligned} \tag{D.8}$$

Substituting either $\sin^2\varphi - \cos^2\varphi = 1 - 2\cos^2$ or $\sin^2\varphi - \cos^2\varphi = 2\sin^2\varphi - 1$ in Eq. (D.8) and employing Eq. (D.6), we see that

$$J_2(x) = J_0(x) - \frac{1}{\pi}\int_{\varphi_0}^{\varphi_0+2\pi} \mathrm{d}\varphi \exp(-\mathrm{i}x\cos\varphi)\cos^2\varphi \tag{D.9}$$

and

$$J_2(x) = \frac{1}{\pi}\int_{\varphi_0}^{\varphi_0+2\pi} \mathrm{d}\varphi \exp(-\mathrm{i}x\cos\varphi)\sin^2\varphi - J_0(x). \tag{D.10}$$

We can summarize these results as

$$\int_{\varphi_0}^{\varphi_0+2\pi} \mathrm{d}\varphi \exp(-\mathrm{i}x\cos\varphi) \begin{pmatrix} \cos^k\varphi\sin^{2l+1}\varphi \\ 1 \\ \cos\varphi \\ \cos^2\varphi \\ \sin^2\varphi \end{pmatrix} = \begin{pmatrix} 0 \\ 2\pi J_0(x) \\ -\mathrm{i}2\pi J_1(x) \\ \pi[J_0(x) - J_2(x)] \\ \pi[J_0(x) + J_2(x)] \end{pmatrix} \tag{D.11}$$

for all $k, l \in \mathbb{N}_0$. Also note that

$$\begin{aligned} J_{-1}(x) &= \frac{\exp(-\mathrm{i}\pi/2)}{2\pi} \int_{\varphi_0}^{\varphi_0+2\pi} \mathrm{d}\varphi \exp(-\mathrm{i}x\cos\varphi)\exp(\mathrm{i}\varphi) \\ &= -\frac{\mathrm{i}}{2\pi} \int_{\varphi_0}^{\varphi_0+2\pi} \mathrm{d}\varphi \exp(-\mathrm{i}x\cos\varphi)\,(\cos\varphi + \mathrm{i}\sin\varphi) \\ &= \frac{1}{\mathrm{i}2\pi} \int_{\varphi_0}^{\varphi_0+2\pi} \mathrm{d}\varphi \exp(-\mathrm{i}x\cos\varphi)\cos\varphi = -J_1(x). \end{aligned} \tag{D.12}$$

The derivative of J_n is given by

$$\begin{aligned} \frac{\mathrm{d}J_n(x)}{\mathrm{d}x} &= \frac{1}{2\pi}\frac{\mathrm{d}}{\mathrm{d}x}\int_{\varphi_0}^{\varphi_0+2\pi}\mathrm{d}\varphi\exp[\mathrm{i}(x\sin\varphi - n\varphi)] = \frac{1}{2\pi}\int_{\varphi_0}^{\varphi_0+2\pi}\mathrm{d}\varphi\exp[\mathrm{i}(x\sin\varphi - n\varphi)]\underbrace{\mathrm{i}\sin\varphi}_{=\exp(\mathrm{i}\varphi)-\cos\varphi} \\ &= \frac{1}{2\pi}\int_{\varphi_0}^{\varphi_0+2\pi}\mathrm{d}\varphi\exp[\mathrm{i}\{x\sin\varphi - (n-1)\varphi\}] - \frac{1}{2\pi}\int_{\varphi_0}^{\varphi_0+2\pi}\mathrm{d}\varphi\,\exp[\mathrm{i}(x\sin\varphi - n\varphi)]\cos\varphi \\ &= J_{n-1}(x) - \frac{1}{2\pi}\int_{\varphi_0}^{\varphi_0+2\pi}\mathrm{d}\varphi\underbrace{\exp[\mathrm{i}(x\sin\varphi - n\varphi)]}_{\equiv f(\varphi)}\left[\frac{n}{x} + \frac{\mathrm{i}(x\cos\varphi - n)}{\mathrm{i}x}\right] \\ &= J_{n-1}(x) - \frac{n}{x}\frac{1}{2\pi}\int_{\varphi_0}^{\varphi_0+2\pi}\mathrm{d}\varphi\,\exp[\mathrm{i}(x\sin\varphi - n\varphi)] - \frac{1}{\mathrm{i}2\pi x}\int_{\varphi_0}^{\varphi_0+2\pi}\mathrm{d}\varphi\underbrace{f(\varphi)\,\mathrm{i}(x\cos\varphi - n)}_{=f'(\varphi)} \\ &= J_{n-1}(x) - n\frac{J_n(x)}{x} - \frac{1}{\mathrm{i}2\pi x}\int_{\varphi_0}^{\varphi_0+2\pi}\mathrm{d}\varphi\,f'(\varphi) = J_{n-1}(x) - n\frac{J_n(x)}{x} - \frac{f(\varphi_0+2\pi)-f(\varphi_0)}{\mathrm{i}2\pi x} \\ &= J_{n-1}(x) - n\frac{J_n(x)}{x}, \end{aligned} \tag{D.13}$$

where we made use of the fact that $f(\varphi_0 + 2\pi) = f(\varphi_0)$ for $f(\varphi) \equiv \exp[\mathrm{i}(x\sin\varphi - n\varphi)]$. A direct consequence of this is that

$$x^n J_{n-1}(x) = x^n\left[n\frac{J_n(x)}{x} + \frac{\mathrm{d}J_n(x)}{\mathrm{d}x}\right] = nx^{n-1}J_n(x) + x^n\frac{\mathrm{d}J_n(x)}{\mathrm{d}x} = \frac{\mathrm{d}}{\mathrm{d}x}[x^n J_n(x)]. \tag{D.14}$$

Another identity for the derivative of J_n is

$$\frac{\mathrm{d}J_n(x)}{\mathrm{d}x} = \frac{1}{2\pi}\int_{\varphi_0}^{\varphi_0+2\pi}\mathrm{d}\varphi\exp[\mathrm{i}(x\sin\varphi - n\varphi)]\underbrace{\mathrm{i}\sin\varphi}_{=[\exp(\mathrm{i}\varphi)-\exp(-\mathrm{i}\varphi)]/2} = \frac{J_{n-1}(x) - J_{n+1}(x)}{2}. \tag{D.15}$$

Comparing Eqs. (D.13) and (D.15), we have that

$$J_{n+1}(x) = 2n\frac{J_n(x)}{x} - J_{n-1}(x). \tag{D.16}$$

The n-th Struve function is defined as

$$\boldsymbol{H}_n(x) \equiv \sum_{m=0}^{\infty} \frac{(-1)^m}{\Gamma\left(m+\frac{3}{2}\right)\Gamma\left(m+n+\frac{3}{2}\right)} \left(\frac{x}{2}\right)^{2m+n+1}, \tag{D.17}$$

where

$$\Gamma(x) \equiv \int_0^{\infty} \mathrm{d}t\, t^{x-1} \exp(-t) \tag{D.18}$$

is the Gamma function with the properties that $x\Gamma(x) = \Gamma(x+1)$ for all $x > 0$, $\Gamma(1) = 1$ and $\Gamma\left(\frac{1}{2}\right) = \sqrt{\pi}$. We find that

$$\begin{aligned} \boldsymbol{H}_{-1}(x) &= \sum_{m=0}^{\infty} \frac{(-1)^m}{\Gamma\left(m+\frac{3}{2}\right)\Gamma\left(m+\frac{1}{2}\right)} \left(\frac{x}{2}\right)^{2m} = \sum_{m=-1}^{\infty} \frac{(-1)^{m+1}}{\Gamma\left(m+\frac{5}{2}\right)\Gamma\left(m+\frac{3}{2}\right)} \left(\frac{x}{2}\right)^{2(m+1)} \\ &= \frac{1}{\Gamma\left(\frac{3}{2}\right)\Gamma\left(\frac{1}{2}\right)} - \sum_{m=0}^{\infty} \frac{(-1)^m}{\Gamma\left(m+\frac{3}{2}\right)\Gamma\left(m+\frac{5}{2}\right)} \left(\frac{x}{2}\right)^{2m+2} = \frac{2}{\pi} - \boldsymbol{H}_1(x), \end{aligned} \tag{D.19}$$

and that

$$\begin{aligned} \frac{\mathrm{d}\boldsymbol{H}_n(x)}{\mathrm{d}x} &= \sum_{m=0}^{\infty} \frac{(-1)^m(2m+n+1)}{\Gamma\left(m+\frac{3}{2}\right)\Gamma\left(m+n+\frac{3}{2}\right)x} \left(\frac{x}{2}\right)^{2m+n+1} = \sum_{m=0}^{\infty} \frac{(-1)^m\left(m+\frac{n}{2}+\frac{1}{2}\right)}{\Gamma\left(m+\frac{3}{2}\right)\Gamma\left(m+n+\frac{3}{2}\right)} \left(\frac{x}{2}\right)^{2m+n} \\ &= \sum_{m=0}^{\infty} \frac{(-1)^m\left(m+n+\frac{1}{2}\right)}{\Gamma\left(m+\frac{3}{2}\right)\Gamma\left(m+n+\frac{3}{2}\right)} \left(\frac{x}{2}\right)^{2m+n} - \frac{n}{2} \sum_{m=0}^{\infty} \frac{(-1)^m}{\Gamma\left(m+\frac{3}{2}\right)\Gamma\left(m+n+\frac{3}{2}\right)} \left(\frac{x}{2}\right)^{2m+n} \\ &= \sum_{m=0}^{\infty} \frac{(-1)^m}{\Gamma\left(m+\frac{3}{2}\right)\Gamma\left(m+n+\frac{1}{2}\right)} \left(\frac{x}{2}\right)^{2m+n} - \frac{n}{x} \sum_{m=0}^{\infty} \frac{(-1)^m}{\Gamma\left(m+\frac{3}{2}\right)\Gamma\left(m+n+\frac{3}{2}\right)} \left(\frac{x}{2}\right)^{2m+n+1} \\ &= \boldsymbol{H}_{n-1}(x) - \frac{n}{x}\boldsymbol{H}_n(x). \end{aligned} \tag{D.20}$$

It follows from Eqs. (D.12) and (D.13) that

$$\frac{\mathrm{d}J_0(x)}{\mathrm{d}x} = J_{-1}(x) = -J_1(x), \qquad \frac{\mathrm{d}J_1(x)}{\mathrm{d}x} = J_0(x) - \frac{J_1(x)}{x}, \tag{D.21}$$

and from Eqs. (D.19) and (D.20) that

$$\frac{\mathrm{d}\boldsymbol{H}_0(x)}{\mathrm{d}x} = \boldsymbol{H}_{-1}(x) = \frac{2}{\pi} - \boldsymbol{H}_1(x), \qquad \frac{\mathrm{d}\boldsymbol{H}_1(x)}{\mathrm{d}x} = \boldsymbol{H}_0(x) - \frac{\boldsymbol{H}_1(x)}{x}. \tag{D.22}$$

Using this, a trivial calculation shows that the derivative of

$$\Psi(x) \equiv \frac{\pi x}{2}\left[J_1(x)\boldsymbol{H}_0(x) - J_0(x)\boldsymbol{H}_1(x)\right] \tag{D.23}$$

is given by

$$\frac{\mathrm{d}\Psi(x)}{\mathrm{d}x} = xJ_1(x), \tag{D.24}$$

and that the derivative of

$$G(x) \equiv 1 + J_1(x) - \left(x + \frac{1}{x}\right) J_0(x) - \Psi(x) \tag{D.25}$$

is therefore

$$\frac{\mathrm{d}G(x)}{\mathrm{d}x} = J_0(x) - \frac{J_1(x)}{x} - \left(1 - \frac{1}{x^2}\right) J_0(x) + \left(x + \frac{1}{x}\right) J_1(x) - xJ_1(x) = \frac{J_0(x)}{x^2}. \tag{D.26}$$

D.2. Hard disk weight functions

Since $\omega^0(\vec{r}) = \delta(R - |\vec{r}|)/(2\pi R)$ is radially symmetric, we can use Eq. (D.2) to find that

$$\tilde{\omega}^0(\vec{k}) = 2\pi \int_0^\infty \mathrm{d}r\, r \frac{\delta(R-r)}{2\pi R} J_0(|\vec{k}|r) = J_0(|\vec{k}|R) \xrightarrow{\vec{k}\to 0} 1. \tag{D.27}$$

For $\omega^2(\vec{r}) = \Theta(R - |\vec{r}|)$, we additionally exploit Eq. (D.14) to arrive at

$$\begin{aligned} \tilde{\omega}^2(\vec{k}) &= 2\pi \int_0^\infty \mathrm{d}r\, r\, \Theta(R-r) J_0(|\vec{k}|r) = \frac{2\pi}{|\vec{k}|^2} \int_0^{|\vec{k}|R} \mathrm{d}x\, x J_0(x) \\ &= \frac{2\pi R}{|\vec{k}|} J_1(|\vec{k}|R) \xrightarrow{\vec{k}\to 0} \pi R^2. \end{aligned} \tag{D.28}$$

Since $\boldsymbol{\omega}^0(\vec{r}) = \delta(R - |\vec{r}|) = 2\pi R\, \omega^0(\vec{r})$, it is clear that

$$\tilde{\boldsymbol{\omega}}^0(\vec{k}) = 2\pi R\, \tilde{\omega}^0(\vec{k}) = 2\pi R\, J_0(|\vec{k}|R) \xrightarrow{\vec{k}\to 0} 2\pi R. \tag{D.29}$$

Matters are more complicated for $\boldsymbol{\omega}^1(\vec{r}) = (\vec{r}/|\vec{r}|)\, \delta(R - |\vec{r}|)$, which is lacking radial symmetry. To evaluate Eq. (D.1), we express the integral with respect to $\vec{r}$ in polar coordinates (r, φ), where r denotes the norm of $\vec{r}$, and φ the angle between $\vec{r}$ and $\vec{k}$. The vector $\vec{r}$ can then be written as

$$\vec{r} = r \begin{pmatrix} \cos\varphi & -\sin\varphi \\ \sin\varphi & \cos\varphi \end{pmatrix} \frac{\vec{k}}{|\vec{k}|} = \frac{r}{|\vec{k}|} \begin{pmatrix} k_x \cos\varphi - k_y \sin\varphi \\ k_x \sin\varphi + k_y \cos\varphi \end{pmatrix}, \tag{D.30}$$

so that $\vec{k} \cdot \vec{r} = |\vec{k}| r \cos\varphi$. In conjunction with Eq. (D.11), this gives us

$$\begin{aligned} \tilde{\boldsymbol{\omega}}^1(\vec{k}) &= \int \mathrm{d}^2\vec{r}\, \boldsymbol{\omega}^1(\vec{r}) \exp(-\mathrm{i}\vec{k}\cdot\vec{r}) = \int \mathrm{d}^2\vec{r}\, \frac{\vec{r}}{|\vec{r}|}\, \delta(R - |\vec{r}|) \exp(-\mathrm{i}\vec{k}\cdot\vec{r}) \\ &= \frac{R}{|\vec{k}|} \int_0^{2\pi} \mathrm{d}\varphi\, \exp(-\mathrm{i}|\vec{k}|R\cos\varphi) \begin{pmatrix} k_x\cos\varphi - k_y\sin\varphi \\ k_x\sin\varphi + k_y\cos\varphi \end{pmatrix} \\ &= \frac{R}{|\vec{k}|} \begin{pmatrix} -\mathrm{i}2\pi J_1(|\vec{k}|R) k_x \\ -\mathrm{i}2\pi J_1(|\vec{k}|R) k_y \end{pmatrix} = -\mathrm{i}2\pi R J_1(|\vec{k}|R) \frac{\vec{k}}{|\vec{k}|} \xrightarrow{\vec{k}\to 0} 0. \end{aligned} \tag{D.31}$$

For $\boldsymbol{\omega}^2(\vec{r}) = \left(\begin{smallmatrix} x^2 & xy \\ xy & y^2 \end{smallmatrix}\right) \frac{\delta(R-|\vec{r}|)}{|\vec{r}|^2}$, we use the same approach. Substituting Eq. (D.30) for $\vec{r}$, we have

$$\boldsymbol{\omega}^2(\vec{r}) = \begin{pmatrix} k_x^2 \mathrm{c}_\varphi^2 + k_y^2 \mathrm{s}_\varphi^2 - 2k_x k_y \mathrm{c}_\varphi \mathrm{s}_\varphi & k_x k_y (\mathrm{c}_\varphi^2 - \mathrm{s}_\varphi^2) + (k_x^2 - k_y^2)\mathrm{c}_\varphi \mathrm{s}_\varphi \\ k_x k_y (\mathrm{c}_\varphi^2 - \mathrm{s}_\varphi^2) + (k_x^2 - k_y^2)\mathrm{c}_\varphi \mathrm{s}_\varphi & k_x^2 \mathrm{s}_\varphi^2 + k_y^2 \mathrm{c}_\varphi^2 + 2k_x k_y \mathrm{c}_\varphi \mathrm{s}_\varphi \end{pmatrix} \frac{\delta(R-r)}{|\vec{k}|^2} \tag{D.32}$$

with the abbreviations $\mathrm{c}_\varphi \equiv \cos\varphi$ and $\mathrm{s}_\varphi \equiv \sin\varphi$. The terms proportional to $\mathrm{c}_\varphi \mathrm{s}_\varphi = \cos\varphi \sin\varphi$ can be omitted in the Fourier integral since their contribution vanishes according to Eq. (D.5). We then find that

$$\begin{aligned}
\tilde{\boldsymbol{\omega}}^2(\vec{k}) &= \int \mathrm{d}^2\vec{r}\, \boldsymbol{\omega}^2(\vec{r}) \exp(-\mathrm{i}\vec{k}\cdot\vec{r}) = \int \mathrm{d}^2\vec{r} \begin{pmatrix} x^2 & xy \\ yx & y^2 \end{pmatrix} \frac{\delta(R-|\vec{r}|)}{|\vec{r}|^2} \exp(-\mathrm{i}\vec{k}\cdot\vec{r}) \\
&= \frac{R}{|\vec{k}|^2} \int_0^{2\pi} \mathrm{d}\varphi\, \exp(-\mathrm{i}|\vec{k}|R\cos\varphi) \begin{pmatrix} k_x^2 \mathrm{c}_\varphi^2 + k_y^2 \mathrm{s}_\varphi^2 & k_x k_y (\mathrm{c}_\varphi^2 - \mathrm{s}_\varphi^2) \\ k_x k_y (\mathrm{c}_\varphi^2 - \mathrm{s}_\varphi^2) & k_x^2 \mathrm{s}_\varphi^2 + k_y^2 \mathrm{c}_\varphi^2 \end{pmatrix} \\
&= \frac{\pi R}{|\vec{k}|^2} \begin{pmatrix} k_x^2 + k_y^2 & 0 \\ 0 & k_x^2 + k_y^2 \end{pmatrix} J_0(|\vec{k}|R) - \frac{\pi R}{|\vec{k}|^2} \begin{pmatrix} k_x^2 - k_y^2 & 2k_x k_y \\ 2k_x k_y & k_y^2 - k_x^2 \end{pmatrix} J_2(|\vec{k}|R) \\
&= \pi R J_0(|\vec{k}|R)\mathbf{1}_2 - \frac{\pi R}{|\vec{k}|^2} J_2(|\vec{k}|R) \begin{pmatrix} k_x^2 - k_y^2 & 2k_x k_y \\ 2k_x k_y & k_y^2 - k_x^2 \end{pmatrix} \xrightarrow{\vec{k}\to 0} \pi R\, \mathbf{1}_2 .
\end{aligned} \tag{D.33}$$

Consequently, a rather tedious but straightforward calculation shows that the hard disk direct two-point correlation function in the bulk is given by

$$\begin{aligned}
\tilde{C}_2^{\mathrm{hd}}(\vec{k}) &= -\sum_{i,j=1}^{9} \frac{\partial^2 \phi_{\rho_\mathrm{b}}^{\mathrm{hd}}}{\partial w_{\rho_\mathrm{b}}^i \partial w_{\rho_\mathrm{b}}^j} \tilde{\omega}^i(-\vec{k})\, \tilde{\omega}^j(\vec{k}) \\
&= \frac{7\pi R^2}{6(1-\eta_\mathrm{b})} J_2(|\vec{k}|R)^2 + \left[\frac{5\pi R^2}{6(1-\eta_\mathrm{b})} - \frac{4\pi\eta_\mathrm{b}(1+\eta_\mathrm{b})}{|\vec{k}|^2(1-\eta_\mathrm{b})^3} \right] J_1(|\vec{k}|R)^2 \\
&\qquad - \frac{4\pi R(1+\eta_\mathrm{b})}{|\vec{k}|(1-\eta_\mathrm{b})^2} J_1(|\vec{k}|R) J_0(|\vec{k}|R) - \frac{2\pi R^2}{1-\eta_\mathrm{b}} J_0(|\vec{k}|R)^2 \\
&= \frac{5\pi R^2}{6(1-\eta_\mathrm{b})} \left[J_1(|\vec{k}|R)^2 - J_0(|\vec{k}|R)^2 \right] + \frac{2\eta_\mathrm{b}^2 - 40\eta_\mathrm{b} + 14}{3|\vec{k}|^2(1-\eta_\mathrm{b})^3} \pi J_1(|\vec{k}|R)^2 \\
&\qquad + \frac{2\eta_\mathrm{b} - 26}{3|\vec{k}|(1-\eta_\mathrm{b})^2} \pi R J_0(|\vec{k}|R) J_1(|\vec{k}|R) \\
&\xrightarrow{\vec{k}\to 0} -\frac{\eta_\mathrm{b}^2 - 3\eta_\mathrm{b} + 4}{(1-\eta_\mathrm{b})^3} \pi R^2,
\end{aligned} \tag{D.34}$$

where we used that $J_2(x) = 2J_1(x)/x - J_0(x)$ according to Eq. (D.16).

D.3. Competing interaction potential

For the truncated competing interaction potential

$$u_{\mathrm{ci}}(r) = \begin{cases} u_{\mathrm{cas}}(\sigma) + u_{\mathrm{mag}}(\sigma) & \text{if } r \leq \sigma, \\ u_{\mathrm{cas}}(r) + u_{\mathrm{mag}}(r) & \text{if } \sigma < r \leq r_{\mathrm{max}}, \\ 0 & \text{otherwise,} \end{cases} \tag{D.35}$$

we can split the Fourier transform

$$\tilde{u}_{\mathrm{ci}}(\vec{k}) = 2\pi \int_0^{r_{\mathrm{max}}} \mathrm{d}r\, r u_{\mathrm{ci}}(r) J_0(|\vec{k}|r) = \tilde{u}_{\mathrm{ci}}^{\mathrm{core}}(\vec{k}) + \tilde{u}_{\mathrm{ci}}^{\mathrm{mag}}(\vec{k}) + \tilde{u}_{\mathrm{ci}}^{\mathrm{cas}}(\vec{k}) \tag{D.36}$$

into a core, a magnetic dipole and a critical Casimir contribution. With Eq. (D.14), the core contribution becomes

$$\begin{aligned} \tilde{u}_{\mathrm{ci}}^{\mathrm{core}}(\vec{k}) &\equiv 2\pi \int_0^{\sigma} \mathrm{d}r\, r u_{\mathrm{ci}}(\sigma) J_0(|\vec{k}|r) = \frac{2\pi}{|\vec{k}|^2} u_{\mathrm{ci}}(\sigma) \int_0^{|\vec{k}|\sigma} \mathrm{d}x\, x J_0(x) \\ &= \frac{2\pi\sigma}{|\vec{k}|} [u_{\mathrm{mag}}(\sigma) + u_{\mathrm{cas}}(\sigma)]\, J_1(|\vec{k}|\sigma) \xrightarrow{\vec{k}\to 0} \pi\sigma^2 [u_{\mathrm{mag}}(\sigma) + u_{\mathrm{cas}}(\sigma)]. \end{aligned} \tag{D.37}$$

Using Eq. (D.26), the magnetic dipole contribution can be written as

$$\begin{aligned} \tilde{u}_{\mathrm{ci}}^{\mathrm{mag}}(\vec{k}) &\equiv 2\pi \int_{\sigma}^{r_{\mathrm{max}}} \mathrm{d}r\, r u_{\mathrm{mag}}(r) J_0(|\vec{k}|r) = 2\pi \int_{\sigma}^{r_{\mathrm{max}}} \mathrm{d}r\, r \frac{\mu_0}{4\pi} \frac{\chi^2 B^2}{r^3} J_0(|\vec{k}|r) \\ &= \frac{\mu_0}{2} \chi^2 B^2 \int_{\sigma}^{r_{\mathrm{max}}} \mathrm{d}r\, \frac{J_0(|\vec{k}|r)}{r^2} = \frac{\mu_0}{2} \chi^2 B^2 |\vec{k}| \int_{|\vec{k}|\sigma}^{|\vec{k}|r_{\mathrm{max}}} \mathrm{d}x\, \frac{J_0(x)}{x^2} \\ &= \frac{\mu_0}{2} \chi^2 B^2 |\vec{k}| [G(|\vec{k}|r_{\mathrm{max}}) - G(|\vec{k}|\sigma)] \xrightarrow{\vec{k}\to 0} \frac{\mu_0}{2} \chi^2 B^2 \left(\frac{1}{\sigma} - \frac{1}{r_{\mathrm{max}}} \right). \end{aligned} \tag{D.38}$$

In the limit $r_{\mathrm{max}} \to \infty$, one finds that

$$\tilde{u}_{\mathrm{ci}}^{\mathrm{mag}}(\vec{k}) = -\frac{\mu_0}{2} \chi^2 B^2 |\vec{k}| G(|\vec{k}|\sigma) \xrightarrow{\vec{k}\to 0} \frac{\mu_0}{2\sigma} \chi^2 B^2. \tag{D.39}$$

Because the scaling function $\Theta_{|\bigcirc}^{\pm\pm}$ is not known analytically, the critical Casimir contribution

$$\tilde{u}_{\mathrm{ci}}^{\mathrm{cas}}(\vec{k}) \equiv 2\pi \int_{\sigma}^{r_{\mathrm{max}}} \mathrm{d}r\, r u_{\mathrm{cas}}(r) J_0(|\vec{k}|r) = \frac{\pi k_{\mathrm{B}} T}{2} \int_{\sigma}^{r_{\mathrm{max}}} \mathrm{d}r\, \frac{ra}{r-a} \Theta_{|\bigcirc}^{\pm\pm}\left(\frac{r-a}{\xi(T)} \right) J_0(|\vec{k}|r) \tag{D.40}$$

has to be determined numerically. We compute the integral with the adaptive *QAGS* routine which is part the *GNU Scientific Library* [99, 100]. As this method requires finite bounds of integration, we approximate the limit $r_{\mathrm{max}} \to \infty$ by choosing $r_{\mathrm{max}} \equiv \sigma + 120\xi(T)$ since the integrand is negligibly small for $r > \sigma + 120\xi(T)$.

E. Autostereograms of the λ-surface

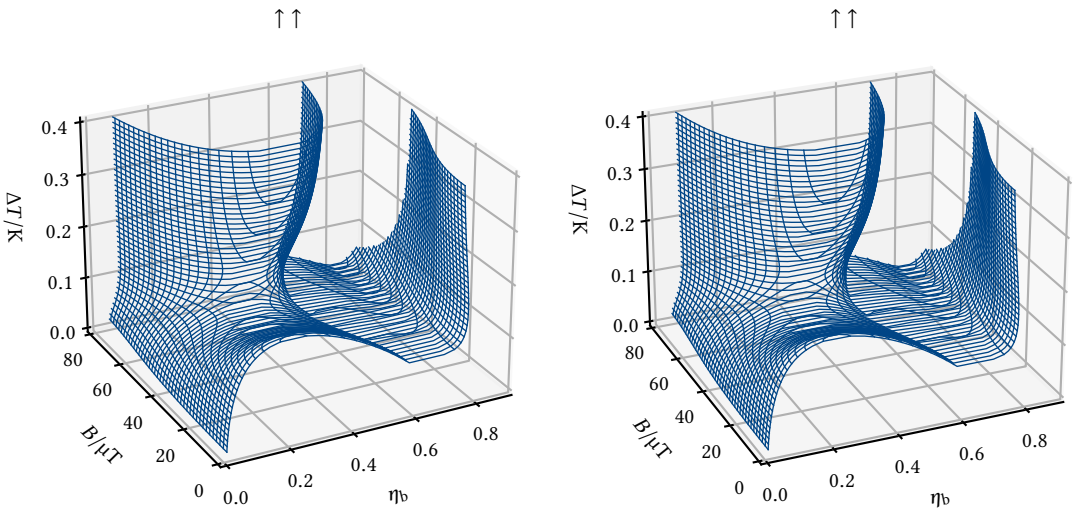

Figure E.1.: Autostereogram of the λ-surface for the "wall-eyed" viewing technique: train your eyes on a point *behind* the page so that your left eye is looking at the left image and your right eye at the right image (↑ ↑). Use the arrows at the top as a guide to aid you in getting the two images to coalesce into a single one at the center of the page. If you succeed, the central image should give you the illusion of depth. See Fig. E.2 for a version with the two images swapped to allow for "cross-eyed" viewing.

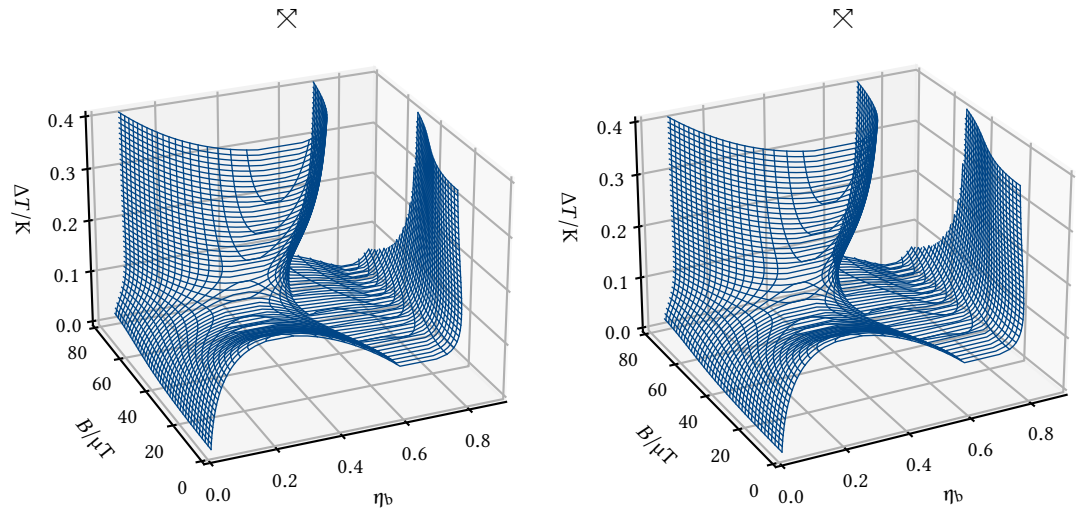

Figure E.2.: Autostereogram of the λ-surface for the "cross-eyed" viewing technique: train your eyes on a point *in front of* the page (it may help to focus on the tip of a pen) so that your left eye is looking at the *right* image and your right eye at the *left* image (⤫). Use the arrows at the top as a guide to aid you in getting the two images to coalesce into a single one at the center of the page. If you succeed, the central image should give you the illusion of depth. See Fig. E.1 for a version with the two images swapped to allow for "wall-eyed" viewing.

References

[1] M. Seul and D. Andelman, "Domain Shapes and Patterns: The Phenomenology of Modulated Phases," Science **267**, 476 (1995).

[2] F. S. Bates and G. H. Fredrickson, "Block Copolymer Thermodynamics: Theory and Experiment," Annual Review of Physical Chemistry **41**, PMID: 20462355, 525 (1990).

[3] A. K. Khandpur, S. Foerster, F. S. Bates, I. W. Hamley, A. J. Ryan, W. Bras, K. Almdal, and K. Mortensen, "Polyisoprene-Polystyrene Diblock Copolymer Phase Diagram near the Order-Disorder Transition," Macromolecules **28**, 8796 (1995).

[4] H.-C. Kim, S.-M. Park, and W. D. Hinsberg, "Block Copolymer Based Nanostructures: Materials, Processes, and Applications to Electronics," Chemical Reviews **110**, PMID: 19950962, 146 (2010).

[5] M. Seul and M. J. Sammon, "Competing interactions and domain-shape instabilities in a monomolecular film at an air-water interface," Phys. Rev. Lett. **64**, 1903 (1990).

[6] H. Möhwald, "Phospholipid and Phospholipid-Protein Monolayers at the Air/Water Interface," Annual Review of Physical Chemistry **41**, PMID: 2257038, 441 (1990).

[7] R. Brown, "XXVII. A brief account of microscopical observations made in the months of June, July and August 1827, on the particles contained in the pollen of plants; and on the general existence of active molecules in organic and inorganic bodies," The Philosophical Magazine **4**, 161 (1828).

[8] A. Einstein, "Über die von der molekularkinetischen Theorie der Wärme geforderte Bewegung von in ruhenden Flüssigkeiten suspendierten Teilchen," Annalen der Physik **322**, 549 (1905).

[9] A. D. Dinsmore, E. R. Weeks, V. Prasad, A. C. Levitt, and D. A. Weitz, "Three-dimensional confocal microscopy of colloids," Appl. Opt. **40**, 4152 (2001).

[10] J. Turkevich and J. Hillier, "Electron Microscopy of Colloidal Systems," Analytical Chemistry **21**, 475 (1949).

[11] A. J. Archer and N. B. Wilding, "Phase behavior of a fluid with competing attractive and repulsive interactions," Phys. Rev. E **76**, 031501 (2007).

[12] M. Edelmann and R. Roth, "Gyroid phase of fluids with spherically symmetric competing interactions," Phys. Rev. E **93**, 062146 (2016).

[13] D. Pini and A. Parola, "Pattern formation and self-assembly driven by competing interactions," Soft Matter **13**, 9259 (2017).

[14] Y. Zhuang and P. Charbonneau, "Equilibrium Phase Behavior of the Square-Well Linear Microphase-Forming Model," The Journal of Physical Chemistry B **120**, PMID: 27117230, 6178 (2016).

[15] Y. Zhuang, K. Zhang, and P. Charbonneau, "Equilibrium Phase Behavior of a Continuous-Space Microphase Former," Phys. Rev. Lett. **116**, 098301 (2016).

[16] A. Ciach, J. Pękalski, and W. T. Góźdź, "Origin of similarity of phase diagrams in amphiphilic and colloidal systems with competing interactions," Soft Matter **9**, 6301 (2013).

[17] A. Ciach, "Universal sequence of ordered structures obtained from mesoscopic description of self-assembly," Phys. Rev. E **78**, 061505 (2008).

[18] A. Imperio and L. Reatto, "A bidimensional fluid system with competing interactions: spontaneous and induced pattern formation," Journal of Physics: Condensed Matter **16**, S3769 (2004).

[19] A. Imperio and L. Reatto, "Microphase separation in two-dimensional systems with competing interactions," The Journal of Chemical Physics **124**, 164712 (2006).

[20] A. Imperio and L. Reatto, "Microphase morphology in two-dimensional fluids under lateral confinement," Phys. Rev. E **76**, 040402 (2007).

[21] A. Imperio, D. Pini, and L. Reatto, "Fluctuations and pattern formation in fluids with competing interactions," in *Collective Phenomena in Macroscopic Systems* (2007), pp. 117–126.

[22] A. Imperio, L. Reatto, and S. Zapperi, "Rheology of colloidal microphases in a model with competing interactions," Phys. Rev. E **78**, 021402 (2008).

[23] A. J. Archer, "Two-dimensional fluid with competing interactions exhibiting microphase separation: Theory for bulk and interfacial properties," Phys. Rev. E **78**, 031402 (2008).

[24] F. Ghezzi and J. C. Earnshaw, "Formation of meso-structures in colloidal monolayers," Journal of Physics: Condensed Matter **9**, L517 (1997).

[25] F. Ghezzi, J. Earnshaw, M. Finnis, and M. McCluney, "Pattern Formation in Colloidal Monolayers at the Air–Water Interface," Journal of Colloid and Interface Science **238**, 433 (2001).

[26] J. Ruiz-García, R. Gámez-Corrales, and B. I. Ivlev, "Foam and cluster structure formation by latex particles at the air/water interface," Physica A: Statistical Mechanics and its Applications **236**, Proceedings of the Workshop on Current Problems in Complex Fluids, 97 (1997).

[27] J. Ruiz-García, R. Gámez-Corrales, and B. I. Ivlev, "Formation of two-dimensional colloidal voids, soap froths, and clusters," Phys. Rev. E **58**, 660 (1998).

[28] J. Ruiz-García and B. I. Ivlev, "Formation of colloidal clusters and chains at the air/water interface," Molecular Physics **95**, 371 (1998).

[29] R. P. Sear, S.-W. Chung, G. Markovich, W. M. Gelbart, and J. R. Heath, "Spontaneous patterning of quantum dots at the air-water interface," Phys. Rev. E **59**, R6255 (1999).

[30] A. Stradner, H. Sedgwick, F. Cardinaux, W. C. K. Poon, S. U. Egelhaaf, and P. Schurtenberger, "Equilibrium cluster formation in concentrated protein solutions and colloids," Nature **432**, 492 (2004).

[31] A. I. Campbell, V. J. Anderson, J. S. van Duijneveldt, and P. Bartlett, "Dynamical Arrest in Attractive Colloids: The Effect of Long-Range Repulsion," Phys. Rev. Lett. **94**, 208301 (2005).

[32] C. L. Klix, C. P. Royall, and H. Tanaka, "Structural and Dynamical Features of Multiple Metastable Glassy States in a Colloidal System with Competing Interactions," Phys. Rev. Lett. **104**, 165702 (2010).

[33] Y. Zhuang and P. Charbonneau, "Recent Advances in the Theory and Simulation of Model Colloidal Microphase Formers," The Journal of Physical Chemistry B **120**, PMID: 27466702, 7775 (2016).

[34] C. P. Royall, "Hunting mermaids in real space: known knowns, known unknowns and unknown unknowns," Soft Matter **14**, 4020 (2018).

[35] C. L. Klix, K. Murata, H. Tanaka, S. R. Williams, A. Malins, and C. P. Royall, "Novel kinetic trapping in charged colloidal clusters due to self-induced surface charge organization," Scientific Reports **3**, 2072 (2013).

[36] A. de Candia, E. Del Gado, A. Fierro, N. Sator, M. Tarzia, and A. Coniglio, "Columnar and lamellar phases in attractive colloidal systems," Phys. Rev. E **74**, 010403 (2006).

[37] Y. Zhuang and P. Charbonneau, "Communication: Microphase equilibrium and assembly dynamics," The Journal of Chemical Physics **147**, 091102 (2017).

[38] M. Tarzia and A. Coniglio, "Lamellar order, microphase structures, and glassy phase in a field theoretic model for charged colloids," Phys. Rev. E **75**, 011410 (2007).

[39] C. A. Helm and H. Möhwald, "Equilibrium and nonequilibrium features determining superlattices in phospholipid monolayers," The Journal of Physical Chemistry **92**, 1262 (1988).

[40] K. Zahn, J. M. Méndez-Alcaraz, and G. Maret, "Hydrodynamic Interactions May Enhance the Self-Diffusion of Colloidal Particles," Phys. Rev. Lett. **79**, 175 (1997).

[41] R. Bubeck, C. Bechinger, S. Neser, and P. Leiderer, "Melting and Reentrant Freezing of Two-Dimensional Colloidal Crystals in Confined Geometry," Phys. Rev. Lett. **82**, 3364 (1999).

[42] O. Zvyagolskaya, A. J. Archer, and C. Bechinger, "Criticality and phase separation in a two-dimensional binary colloidal fluid induced by the solvent critical behavior," EPL (Europhysics Letters) **96**, 28005 (2011).

[43] C. E. Shannon, "A mathematical theory of communication," The Bell System Technical Journal **27**, 379 (1948).

[44] E. T. Jaynes, "Information Theory and Statistical Mechanics," Phys. Rev. **106**, 620 (1957).

[45] R. Evans, "The nature of the liquid-vapour interface and other topics in the statistical mechanics of non-uniform, classical fluids," Advances in Physics **28**, 143 (1979).

[46] J. K. Percus, "Equlibrium state of a classical fluid of hard rods in an external field," Journal of Statistical Physics **15**, 505 (1976).

[47] T. K. Vanderlick, H. T. Davis, and J. K. Percus, "The statistical mechanics of inhomogeneous hard rod mixtures," The Journal of Chemical Physics **91**, 7136 (1989).

[48] Y. Rosenfeld, "Free-energy model for the inhomogeneous hard-sphere fluid mixture and density-functional theory of freezing," Phys. Rev. Lett. **63**, 980 (1989).

[49] R. Roth, K. Mecke, and M. Oettel, "Communication: Fundamental measure theory for hard disks: Fluid and solid," The Journal of Chemical Physics **136**, 081101 (2012).

[50] E. Helfand, H. L. Frisch, and J. L. Lebowitz, "Theory of the Two- and One-Dimensional Rigid Sphere Fluids," The Journal of Chemical Physics **34**, 1037 (1961).

[51] J.-P. Hansen and I. R. McDonald, *Theory of Simple Liquids*, 4th ed. (Academic Press, Oxford, 2013).

[52] E. S. R. Gopal, "Critical opalescence," Resonance **5**, 37 (2000).

[53] B. Widom, "Surface Tension and Molecular Correlations near the Critical Point," The Journal of Chemical Physics **43**, 3892 (1965).

[54] L. P. Kadanoff, "Scaling laws for ising models near T_c," Physics Physique Fizika **2**, 263 (1966).

[55] K. G. Wilson and J. Kogut, "The renormalization group and the *epsilon* expansion," Physics Reports **12**, 75 (1974).

[56] H. B. Casimir, "On the attraction between two perfectly conducting plates," Proc. Kon. Ned. Akad. Wet. **51**, 793 (1948).

[57] S. K. Lamoreaux, "Demonstration of the Casimir Force in the 0.6 to 6 μm Range," Phys. Rev. Lett. **78**, 5 (1997).

[58] M. Krech and D. P. Landau, "Casimir effect in critical systems: A Monte Carlo simulation," Phys. Rev. E **53**, 4414 (1996).

[59] M. E. Fisher and P. de Gennes, "Wall phenomena in a critical binary mixture," C. R. Seances Acad. Sci, Ser. B **287**, 207 (1978).

[60] M. Krech, "Fluctuation-induced forces in critical fluids," Journal of Physics: Condensed Matter **11**, R391 (1999).

[61] A. Gambassi, "The Casimir effect: From quantum to critical fluctuations," Journal of Physics: Conference Series **161**, 012037 (2009).

[62] M. Krech, "Casimir forces in binary liquid mixtures," Phys. Rev. E **56**, 1642 (1997).

[63] R. Evans and J. Stecki, "Solvation force in two-dimensional Ising strips," Phys. Rev. B **49**, 8842 (1994).

[64] O. Vasilyev, A. Gambassi, A. Maciołek, and S. Dietrich, "Universal scaling functions of critical casimir forces obtained by monte carlo simulations," Phys. Rev. E **79**, 041142 (2009).

[65] A. Gambassi, A. Maciołek, C. Hertlein, U. Nellen, L. Helden, C. Bechinger, and S. Dietrich, "Critical Casimir effect in classical binary liquid mixtures," Phys. Rev. E **80**, 061143 (2009).

[66] C. Hertlein, L. Helden, A. Gambassi, S. Dietrich, and C. Bechinger, "Direct measurement of critical Casimir forces," Nature **451**, 172 (2008).

[67] O. V. Zvyagolskaya, "Kritischer Casimir-Effekt in kolloidalen Modellsystemen," PhD thesis (University of Stuttgart, 2012).

[68] S. H. Behrens and D. G. Grier, "The charge of glass and silica surfaces," The Journal of Chemical Physics **115**, 6716 (2001).

[69] S. H. Behrens and D. G. Grier, "Pair interaction of charged colloidal spheres near a charged wall," Phys. Rev. E **64**, 050401 (2001).

[70] T. G. Mattos, L. Harnau, and S. Dietrich, "Many-body effects for critical Casimir forces," The Journal of Chemical Physics **138**, 074704 (2013).

[71] T. G. Mattos, L. Harnau, and S. Dietrich, "Three-body critical Casimir forces," Phys. Rev. E **91**, 042304 (2015).

[72] A. Maciołek and S. Dietrich, "Collective behavior of colloids due to critical Casimir interactions," Rev. Mod. Phys. **90**, 045001 (2018).

[73] M. T. Dang, A. V. Verde, V. D. Nguyen, P. G. Bolhuis, and P. Schall, "Temperature-sensitive colloidal phase behavior induced by critical Casimir forces," The Journal of Chemical Physics **139**, 094903 (2013).

[74] S. Paladugu, A. Callegari, Y. Tuna, L. Barth, S. Dietrich, A. Gambassi, and G. Volpe, "Non-additivity of critical Casimir forces," Nature Communications **7**, 10.1038/ncomms11403 (2016).

[75] A. J. Archer, D. Pini, R. Evans, and L. Reatto, "Model colloidal fluid with competing interactions: Bulk and interfacial properties," The Journal of Chemical Physics **126**, 014104 (2007).

[76] J. A. Nelder and R. Mead, "A Simplex Method for Function Minimization," The Computer Journal **7**, 308 (1965).

[77] A. J. Archer, C. Ionescu, D. Pini, and L. Reatto, "Theory for the phase behaviour of a colloidal fluid with competing interactions," Journal of Physics: Condensed Matter **20**, 415106 (2008).

[78] M. Frigo and S. G. Johnson, "The Design and Implementation of FFTW3," Proceedings of the IEEE **93**, 216 (2005).

[79] M. Frigo and S. G. Johnson, *FFTW*, http://www.fftw.org (visited on 2021-02-26).

[80] W. H. Press, S. A. Teukolsky, W. T. Vetterling, and B. P. Flannery, *Numerical Recipes in C, The Art of Scientific Computing*, 2nd ed. (Cambridge University Press, 1992).

[81] D. Stopper and R. Roth, "Massively parallel GPU-accelerated minimization of classical density functional theory," The Journal of Chemical Physics **147**, 064508 (2017).

[82] NVIDIA Corporation, *cuFFT*, https://docs.nvidia.com/cuda/cufft (visited on 2021-02-26).

[83] D. Merrill and NVIDIA Corporation, *CUB*, https://nvlabs.github.io/cub (visited on 2021-02-26).

[84] R. P. Brent, *Algorithms for Minimization Without Derivatives* (Dover Publications, 2013).

[85] H. Serna, E. G. Noya, and W. T. Góźdź, "The influence of confinement on the structure of colloidal systems with competing interactions," en, Soft Matter **16**, 718 (2020).

[86] J. Pękalski, E. Bildanau, and A. Ciach, "Self-assembly of spiral patterns in confined systems with competing interactions," Soft Matter **15**, 7715 (2019).

[87] X. B. Xu, Z. H. Wang, X. N. Xu, G. Y. Fang, and M. Gu, "Structural transitions for 2D systems with competing interactions in logarithmic traps," The Journal of Chemical Physics **152**, 054906 (2020).

[88] Y. H. Liu, L. Y. Chew, and M. Y. Yu, "Self-assembly of complex structures in a two-dimensional system with competing interaction forces," Phys. Rev. E **78**, 066405 (2008).

[89] P. Langevin, "Sur la théorie du mouvement brownien," Comptes rendus de l'Académie des sciences, 530 (1908).

[90] D. S. Lemons and A. Gythiel, "Paul Langevin's 1908 paper 'On the Theory of Brownian Motion'," American Journal of Physics **65**, 1079 (1997).

[91] I. Snook, *The Langevin and Generalised Langevin Approach to the Dynamics of Atomic, Polymeric and Colloidal Systems* (Elsevier, 2007).

[92] M. te Vrugt, H. Löwen, and R. Wittkowski, "Classical dynamical density functional theory: from fundamentals to applications," Advances in Physics **69**, 121 (2020).

[93] U. M. B. Marconi and P. Tarazona, "Dynamic density functional theory of fluids," The Journal of Chemical Physics **110**, 8032 (1999).

[94] U. M. B. Marconi and P. Tarazona, "Dynamic density functional theory of fluids," Journal of Physics: Condensed Matter **12**, A413 (2000).

[95] K. Itô, "Stochastic integral," Proceedings of the Imperial Academy **20**, 519 (1944).

[96] S. Cox and P. Matthews, "Exponential Time Differencing for Stiff Systems," Journal of Computational Physics **176**, 430 (2002).

[97] D. Stopper and R. Roth, "Nonequilibrium phase transitions of sheared colloidal microphases: results from dynamical density functional theory," Phys. Rev. E **97**, 062602 (2018).

[98] Visit `http://www.kevin-marolt.de/dissertation` for supplemental material.

[99] R. Piessens, E. de Doncker-Kapenga, and C. W. Überhuber, *QUADPACK*, `http://nines.cs.kuleuven.be/software/QUADPACK` (visited on 2021-03-30).

[100] GNU Project, *GNU Scientific Library*, `https://www.gnu.org/software/gsl` (visited on 2021-03-30).